Imperial College London

Department Of Civil and Environmental Engineering

Computational models to predict pelvic bone architecture and fracture

---

Dan T. Zaharie

A thesis submitted in part fulfilment of the of the requirements of the degree of Doctor of Philosophy

I declare that, except where explicit reference is made to the work of others, this dissertation is the result of my own work and has not been submitted for any other degree at Imperial College London or any other institution.

The copyright of this thesis rests with the author and is made available under a Creative Commons Attribution Non-Commercial No Derivatives licence. Researchers are free to copy, distribute or transmit the thesis on the condition that they attribute it, that they do not use it for commercial purposes and that they do not alter, transform or build upon it. For any reuse or redistribution, researchers must make clear to others the licence terms of this work.

Acknowledgements

I would like to thank my PhD supervisor, Dr. Andrew Phillips, for the constant support given throughout the duration of this project and for giving me the opportunity to share my findings around the world. His guidance, patience, advice and involvement given in the past four years have been invaluable to this project and doctoral dissertation.

I would like to acknolwedge my two clinical PhD advisors, Prof. Jon Clasper and Davendra Sharma, who provided precious clinical insight for this project.

I would like acknowledge and thank the Royal British Legion for the funding provided for this PhD project.

I wish to thank Claire Villette, Luca Modenese, Clement Favier, Anantharaman Gopalakrishnan for their help and advice on a multitude of aspects of my PhD project.

I am grateful to my colleagues in office 326 for four great years: Clement, Claire, Laura, Ananth, Luca, Josh, Adam and Bran.

I would also like to thank my parents, Daniela and Ioan, without whom I probably would not be here, who have supported me unconditionally throughout my time at Imperial College, and have been loving and encouraging for every day of my journey. Finally, I will be forever grateful to my wife, Tahreem, for being there when it was difficult and for making the past years the best of my life.

Abstract

The pelvic construct is a crucial component of the human musculoskeletal apparatus as it facilitates the transfer of the upper body weight to the lower limb and it protects a number of important blood vessels and organs. Its importance is further highlighted by the high mortality rates associated with pelvic trauma.

As the structure of the pelvic construct has not been studied extensively and the mechanisms of pelvic fractures are not well understood, this project aims to use computational tools to develop a series of predictive models, with the purpose of gaining a deeper understanding of its bone architecture and its behaviour in loading environments associated with pelvic injuries.

A number of predictive structural and continuum finite element models of the pelvic construct were developed and their structure was adapted to a loading environment associated with daily physical activities. The models were compared to a subject specific model derived from medical imaging data to assess the different modelling techniques used. The optimised structural model was used in conjunction with a damage elasto-plasticity material model to predict fracture patterns and fracture loads in dynamic loading scenarios associated with pelvic injuries.

The comparison between adaptive FE models highlights the strengths and weaknesses of each modelling technique implemented. In addition, the ability of the structural model to predict fracture initiation and progression enables the user to obtain more in depth information on the outcome of a simulated injury scenario. The computational models presented in the thesis provide a useful information on the particularities of pelvic bone and can be used in a variety of applications ranging from rehabilitation tools to additive manufacturing of massive endoprostheses or frangible surrogates for ethical and low cost testing of injury scenarios.

Contents

Declaration i

Acknowledgements ii

Abstract iii

Contents iv

List of figures xxvii

List of tables xxix

1 Introduction 1

1.1 Thesis objectives 2

1.2 Summary of chapters 2

2 Background 5

2.1 Pelvis anatomy 6

2.1.1 Bony pelvis 6

2.1.2 Pelvic joints and ligaments 7

2.2 Bone structure 9

2.3 Functional adaptation of bone 13

2.3.1 Bone tissue structure 13

2.3.2 Bone remodelling and adaptation 14

2.4 Pelvic injuries 16

2.4.1 Classification of pelvic injuries 17

2.5 Finite element modelling applied to biomechanics 19

2.5.1 Introduction to finite element modelling 19

2.5.2 Existing FE models of the pelvic construct 20

3 Musculoskeletal and Finite Element modelling of the pelvic construct 23

3.1 Gait data collection and processing 24

3.2 Musculoskeletal modelling 26

3.2.1 Scaling 27

3.2.2 Inverse kinematics 27

3.2.3 Inverse dynamics 30

3.2.4 Hip contact forces and muscle forces 32

3.3 Finite element model development 35

3.3.1 Geometry definition 35

3.3.2 Structural and continuum base models 35

3.3.3 Ligaments and joints modelling 36

3.4 Development of CT scan derived continuum model 40

4 Predictive structural modelling of the pelvic construct 42

4.1 Methods 44

4.1.1 Finite element modelling 44

4.1.1.1 Loading 44

4.1.1.2 Boundary conditions 46

4.1.2 Adaptation algorithm 48

4.1.3 Comparison with a CT scan derived continuum pelvis model . 50

4.2 Results 52

4.2.1 Converged model structure 52

4.2.2 Adaptation to different loading regimes 60

4.2.2.1 Walking 60

4.2.2.2 Stair ascent 62

4.2.2.3 Stair descent 64

4.2.2.4 Sitting and standing 66

4.2.3 Comparison to CT scan derived model 71

4.3 Discussion 75

5 Predictive continuum and hybrid modelling of the pelvic construct 78

5.1 Methods 80

5.1.1 Finite element modelling 80

5.1.2 Bone adaptation algorithm 82

5.1.2.1 Orthotropic adaptation algorithm 82

5.1.2.2 Isotropic adaptation algorithm 87

5.1.3 Adaptation algorithms for hybrid models 88

5.1.3.1 Hybrid orthotropic model 88

5.1.3.2 Hybrid isotropic model 89

5.1.3.3 Hybrid structural model 89

5.2 Results 90

5.2.1 Orthotropic model 90

5.2.1.1 Bone architecture 90

5.2.1.2 Comparison to CT derived model 97

5.2.2 Isotropic model 101

5.2.2.1 Bone architecture 101

5.2.2.2 Comparison to CT derived model 103

5.2.3 Hybrid orthotropic model 107

5.2.3.1 Bone architecture 107

5.2.3.2 Comparison to CT derived model 110

5.2.4 Hybrid isotropic model 114
5.2.4.1 Bone architecture 114
5.2.4.2 Comparison to CT derived model 118
5.2.5 Hybrid structural model 120
5.2.5.1 Bone architecture 120
5.2.5.2 Comparison to CT derived model 123
5.3 Discussion and concluding remarks 125

6 Sensitivity studies **132**

6.1 Sensitivity of ligaments and joints material properties 136
6.2 Mesh sensitivity 140
6.2.1 Structural mesh 140
6.2.2 Continuum mesh 144
6.3 Sensitivity of structural adaptation algorithm 149
6.4 Sensitivity of continuum adaptation algorithm 152
6.5 Discussion and concluding remarks 155

7 Pelvic injury modelling **157**

7.1 Fracture modelling 159
7.1.1 Material model 159
7.1.2 Influence of strain rate and age on failure behaviour of bone . 159

7.2 Lateral compression 162
7.2.1 Loading and boundary conditions 162
7.2.2 Results 164
7.3 Vertical shear 169
7.3.1 Loading and boundary conditions 169
7.3.2 Results 171
7.3.2.1 Unilateral impact 171
7.3.2.2 Bilateral impact 175
7.4 Anterior posterior compression 179
7.4.1 Loading and boundary conditions 179
7.4.2 Results 180
7.4.2.1 Bilateral impact 180
7.4.2.2 Unilateral impact 184
7.4.3 Postures 187
7.5 Concluding remarks 191

8 Conclusions **193**

8.1 Summary of achievements 194
8.2 Current limitations 196
8.3 Future work and applications 198

Appendix **201**

A1 Additional data on structural, continuum and hybrid models 202

A2 Fracture chapter animations 202

A3 Continuum fracture model 203

References **205**

List of Figures

2.1 Anatomical landmarks of the bony pelvis 6

2.2 Ligaments and joints of the pelvis 8

2.3 Trabecular patterns for various human bones proposed by von Meyer (1867). The structure of the proximal femur (6) is compared to Culmann's crane (10). 10

2.4 Illustration of the bone remodelling process at cellular level (image reproduced from *OrthopaedicsOne*) 15

2.5 Illustration of the mechanostat principle proposed by Frost (1987). . . 16

2.6 Young Burgess classification for pelvic fractures (image reproduced from Alton and Gee (2014)) 17

3.1 Lower limb musculoskeletal model in (a) standing and (b) seated positions 26

3.2 Average joint angles at the hip, knee and ankle for five walking trials 28

3.3 Average joint angles at the hip, knee and ankle for four stair ascent trials 28

3.4 Average joint angles at the hip, knee and ankle for two stair descent trials 29

3.5 Average joint angles at the hip, knee and ankle for two sit-to-stand-to-sit trials 29

3.6 Normalized joint moments at the hip, knee and ankle for walking trials 30

3.7 Normalized joint moments at the hip, knee and ankle for stair ascent trials 31

3.8 Normalized joint moments at the hip, knee and ankle for stair descent trials 31

3.9 Normalized joint moments at the hip, knee and ankle for sit-to-stand-to-sit trials 32

3.10 Hip JCFs derived from the musculoskeletal model for cycles of (a) walking, (b) stair ascent, (c) stair descent and (d) sit-to-stand and stand-to-sit are shown in green lines for the right leg and blue lines for the left leg. Hip JCFs recorded and reported by Bergmann et al. Bergmann et al. (2001) for the right leg are shown in red dashed lines for each activity. 34

3.11 Transverse 2.5 mm slice of the pelvis for the base FE model. Shell elements representing cortical bone are shown in grey; truss elements representing trabecular bone are shown in red. 36

3.12 Pelvis model with ligaments included: sacroiliac ligaments in blue, pubic ligament in red, sacrospinous ligaments in yellow, sacrotuberous ligaments in purple and inguinal ligaments in green 38

3.13 Young's modulus (a, b, c) and density (d, e, f) distribution for the CT scan derived model. 41

4.1 Modelling framework used to develop an adaptive structural model of the pelvic construct 43

4.2 (a) Load applicator at the hip and (b) fixator at the top of the sacrum. The elements representing the bone are shown in light grey, with the two layers of soft elements in red and the two layers of stiffer elements in blue (dark blue represents the stiffest layer of elements in the hip applicator). In addition, the black arrow illustrates the peak load applied on the hip joint during walking. 45

4.3 Hip JCFs derived from the musculoskeletal model for cycles of (a) walking, (b) stair ascent, (c) stair descent and (d) sit-to-stand and stand-to-sit are shown in green lines for the right leg and blue lines for the left leg. The frames selected for each activity to be used in the FE simulations are highlighted using solid circles. Hip JCFs recorded and reported by Bergmann et al. (2001) for the right leg are shown in red dashed lines for each activity. 46

4.4 Comparison between reaction forces at the sacrum reported by the musculoskeletal model and FE model for the walking frames. 47

4.5 Loading conditions applied on the adapted structural model and the scan derived continuum model of the right pelvic innominate 51

4.6 Converged structure for the full loading regime. Contours of position dependent cortical thickness ranging from 0.1 mm to 5 mm are shown in the top row: (a) frontal view of pelvis, (b) anterior and (c) medial views of the right innominate. Trabecular elements' radii distribution ranging from 0.1 mm to 2 mm is shown in the bottom row: (d) frontal view, (e) anterior and (f) medial views of the right innominate. Trabecular elements with a radius of 1 μm were excluded for clarity. . . . 54

4.7 Selected 5 mm thick coronal (a, b, e), sagittal (c, d) and transversal (f) slices of the converged pelvic model illustrating the trabecular structure and cortical thickness. Truss elements with a radius > 0.1 mm are shown in red, with elements with a radius of 1 mm shown in blue. Elements with a radius of 1 μm are not shown for clarity. 55

4.8 Figure illustrating transverse slices from the CT scans (a, c, e, g) shown along with corresponding slices of the pelvic model (b, d, f, h) generated using an in-house code developed in MATLAB. Shell elements and truss elements with a radius > 0.1 mm are shown in light grey. Truss elements with a radius of 0.1 mm appear in dark grey. Elements with a radius of 1 μm are not shown for clarity. 56

4.9 Influence of activities on cortical (a, b, c) and trabecular (d, e, f) structure of converged pelvic model. The elements are colour mapped based on the activity which has been most influential in determining their thickness. 58

4.10 Cortical (a,b,e,f,i,j,m,n,q,r) and trabecular (c,d,g,h,k,l,o,p,s,t) strain distributions highlighting the regions with the largest absolute principal strain for each activity. Regions which are highly strained ($\geq 1500\mu\varepsilon$) by a particular activity are shown with a higher intensity in the colour associated with the respective activity as shown in Figure 4.9. 59

4.11 Converged structure for walking. Contours of position dependent cortical thickness ranging from 0.1 mm to 5 mm are shown in the top row: (a) frontal view of pelvis, (b) anterior and (c) medial views of the right innominate. Trabecular elements' radii distribution ranging from 0.1 mm to 2 mm is shown in the bottom row: (d) frontal view, (e) anterior and (f) medial views of the right innominate. Trabecular elements with a radius < 0.1 mm were excluded for clarity. 61

4.12 Cortical, trabecular and total bone volumes for models adapted to each activity separately compared to the full loading regime. The data is available in in the Appendix, in Table A1. 62

4.13 Converged structure for stair ascent. Contours of position dependent cortical thickness ranging from 0.1 mm to 5 mm are shown in the top row: (a) frontal view of pelvis, (b) anterior and (c) medial views of the right innominate. Trabecular elements' radii distribution ranging from 0.1 mm to 2 mm is shown in the bottom row: (d) frontal view, (e) anterior and (f) medial views of the right innominate. Trabecular elements with a radius < 0.1 mm were excluded for clarity. 63

4.14 Converged structure for stair descent. Contours of position dependent cortical thickness ranging from 0.1 mm to 5 mm are shown in the top row: (a) frontal view of pelvis, (b) anterior and (c) medial views of the right innominate. Trabecular elements' radii distribution ranging from 0.1 mm to 2 mm is shown in the bottom row: (d) frontal view, (e) anterior and (f) medial views of the right innominate. Trabecular elements with a radius < 0.1 mm were excluded for clarity. 65

4.15 Converged structure for sit to stand. Contours of position dependent cortical thickness ranging from 0.1 mm to 5 mm are shown in the top row: (a) frontal view of pelvis, (b) anterior and (c) medial views of the right innominate. Trabecular elements' radii distribution ranging from 0.1 mm to 2 mm is shown in the bottom row: (d) frontal view, (e) anterior and (f) medial views of the right innominate. Trabecular elements with a radius < 0.1 mm were excluded for clarity. 67

4.16 Converged structure for stand to sit. Contours of position dependent cortical thickness ranging from 0.1 mm to 5 mm are shown in the top row: (a) frontal view of pelvis, (b) anterior and (c) medial views of the right innominate. Trabecular elements' radii distribution ranging from 0.1 mm to 2 mm is shown in the bottom row: (d) frontal view, (e) anterior and (f) medial views of the right innominate. Trabecular elements with a radius < 0.1 mm were excluded for clarity. 68

4.17 Comparison between cortical, trabecular and total bone volume of the model adapted to the full loading regime and a superimposed model obtained from models adapted to individual activities. 70

4.18 Cortical and trabecular mapping of regions with differences between the superimposed model and the model adapted to the full loading regime based on element thickness/radius. Areas where the superimposed model predicted a greater bone volume than the adapted model are shown in red, and in blue where the superimposed model predicted a lower bone volume than the adapted. Regions where no difference was found are shown in grey. 70

4.19 Absolute maximum principal strain distribution for structural model (a,b,c,d) and scan derived model (e,f,g,h) in response to the loading condition shown in Figure 4.5 72

4.20 Comparison between the minimum (a) and maximum (b) principal strains across the surface of the structural model (x axis) and CT derived model (y axis). Lines of best fit are shown in red for each case and do not differ greatly from the y=x line shown in dashed blue. . . 73

4.21 Bland-Altman plots showing (a) minimum and (b) maximum principal strains as difference between the structural model and CT derived model versus mean. Mean value and crude 95% confidence intervals are shown in blue. Regression lines and V-shaped 95% confidence intervals are shown in red 73

4.22 Lateral views of the hip bone showing regions defined by the ratio of absolute maximum principal strains between the structural model and the CT derived model. A ratio higher than one corresponds to the structural model predicting a higher strain than the CT scan derived model in the highlighted region. 74

4.23 Trabecular trajectories formed in the ilium adapted from (a) walking and (b) all activities. The trajectories highlighted correspond to regions in the ilium with a higher trabecular density caused by walking observed by Macchiarelli et al. (1999): superior bundle (sb), anterior bundle (ab), sacropubic bundle (spb), iliocotyloid bundle (icb), ilioischial bundle (iib), trabecular chiasma (tc). Truss elements with a radius > 0.1 mm are shown in red. Truss elements with a radius of 0.1 mm appear in blue. 75

5.1 Modelling framework used to develop an adaptive continuum model of the pelvic construct 79

5.2 Illustration of the rotation of local coordinate system associated with an element to match the directions of the principal stresses 87

5.3 Distribution of E_1 (MPa), associated with minimum principal strains, across the pelvis 91

5.4 Distribution of E_2 (MPa), associated with medium principal strains, across the pelvis 91

5.5 Distribution of E_3 (MPa), associated with maximum principal strains, across the pelvis 92

5.6 Cube of unit volume with internal cuboids representing the solid phase for each of the three orthotropic directions (x_1, x_2, x_3) 93

5.7 Distributions of mean Young's moduli (MPa) (a,b,c) and density (g/cm^3) (d,e,f) across the continuum orthotropic model 95

5.8 Figure illustrating transverse slices from the CT scans (a, c, e, g) shown along with corresponding slices of the pelvic model (b, d, f, h) generated using an in-house code developed in MATLAB. The shading intensity of each element is based on the dominant Young's modulus (black - low E; white - high E) 96

5.9 Absolute maximum principal strain distribution for continuum orthotropic model (a,b,c,d) and scan derived model (e,f,g,h) in response to the loading condition shown in Figure 4.5 98

5.10 Comparison between the minimum (a) and maximum (b) principal strains across the surface of the continuum orthotropic model (x axis) and CT derived model (y axis). Lines of best fit are shown in red for each case, with y=x line shown in dashed blue. 99

5.11 Bland-Altman plots showing (a) minimum and (b) maximum principal strains as difference between the orthotropic model and CT derived model versus mean. Mean value and crude 95% confidence intervals are shown in blue. Regression lines and V-shaped 95% confidence intervals are shown in red. 100

5.12 Distributions of mean Young's moduli (MPa) (a,b,c) and density (g/cm^3) (d,e,f) across the continuum isotropic model 102

5.13 Absolute maximum principal strain distribution for continuum isotropic model (a,b,c,d) and scan derived model (e,f,g,h) in response to the loading condition shown in Figure 4.5 104

5.14 Comparison between the minimum (a) and maximum (b) principal strains across the surface of the continuum isotropic model (x axis) and CT derived model (y axis). Lines of best fit are shown in red for each case, with y=x line shown in dashed blue. 105

5.15 Bland-Altman plots showing (a) minimum and (b) maximum principal strains as difference between the isotropic model and CT derived model versus mean. Mean value and crude 95% confidence intervals are shown in blue. Regression lines and V-shaped 95% confidence intervals are shown in red. 106

5.16 Cortical thickness distribution for the converged model. 107

5.17 Distributions of mean Young's moduli (MPa) (a,b,c) and density (g/cm^3) (d,e,f) across trabecular bone of the hybrid orthotropic model 109

5.18 Absolute maximum principal strain distribution for hybrid orthotropic model (a,b,c,d) and scan derived model (e,f,g,h) in response to the loading condition shown in Figure 4.5 111

5.19 Comparison between the minimum (a) and maximum (b) principal strains across the surface of the hybrid orthotropic model (x axis) and CT derived model (y axis). Lines of best fit are shown in red for each case, with y=x line shown in dashed blue. 112

5.20 Bland-Altman plots showing (a) minimum and (b) maximum principal strains as difference between the hybrid orthotropic model and CT derived model versus mean. Mean value and crude 95% confidence intervals are shown in blue. Regression lines and V-shaped 95% confidence intervals are shown in red. 113

5.21 Cortical thickness distribution for the converged model. 114

5.22 Distributions of Young's moduli (MPa) (a,b,c) and density (g/cm^3) (d,e,f) across trabecular bone of the hybrid isotropic model 115

5.23 Absolute maximum principal strain distribution for hybrid isotropic model (a,b,c,d) and scan derived model (e,f,g,h) in response to the loading condition shown in Figure 4.5 117

5.24 Comparison between the minimum (a) and maximum (b) principal strains across the surface of the hybrid isotropic model (x axis) and CT derived model (y axis). Lines of best fit are shown in red for each case, with y=x line shown in dashed blue. 118

5.25 Bland-Altman plots showing (a) minimum and (b) maximum principal strains as difference between the hybrid isotropic model and CT derived model versus mean. Mean value and crude 95% confidence intervals are shown in blue. Regression lines and V-shaped 95% confidence intervals are shown in red. 119

5.26 Contours of position dependent cortical thickness ranging from 0.1 mm to 5 mm are shown in the top row: (a) frontal view of pelvis, (b) anterior and (c) medial views of the right innominate. Trabecular elements' radii distribution ranging from 0.1 mm to 2 mm is shown in the bottom row: (d) frontal view, (e) anterior and (f) medial views of the right innominate. Trabecular elements with a radius of 1 μm were excluded for clarity. 121

5.27 Absolute maximum principal strain distribution for hybrid structural model (a,b,c,d) and scan derived model (e,f,g,h) in response to the loading condition shown in Figure 4.5 122

5.28 Comparison between the minimum (a) and maximum (b) principal strains across the surface of the hybrid structural model (x axis) and CT derived model (y axis). Lines of best fit are shown in red for each case, with y=x line shown in dashed blue. 123

5.29 Bland-Altman plots showing (a) minimum and (b) maximum principal strains as difference between the hybrid structural model and CT derived model versus mean. Mean value and crude 95% confidence intervals are shown in blue. Regression lines and V-shaped 95% confidence intervals are shown in red. 124

5.30 Cumulative distributions of predicted density values for the isotropic (blue) and orthotropic (red) models compared to density values extracted from the CT scan (black) in g/cm^3 126

5.31 Frequency distribution of elastic moduli of the three continuum models: CT scan derived, isotropic and orthotropic. 127

5.32 Frequency distribution of trabecular elastic moduli for the hybrid isotropic and hybrid orthotropic models. 128

5.33 Frequency distribution of the cortical thickness for the hybrid isotropic, hybrid orthotropic, hybrid structural and structural models. 129

5.34 Distribution of Young's modulus with respect to density for predictive orthotropic and isotropic models of the right pelvic innominate along with empirical distribution of CT derived model of the right pelvic innominate. For orthotropic model, distribution of mean Young's modulus is shown in (a) and dominant Young's modulus in (b). For each element of the orthotropic model, the data point is colour coded corresponding to the dominant Young's modulus. 130

6.1 Changes in cortical, trabecular and total bone volumes caused by changes in the stiffness of each ligament in the model 138

6.2 Loading conditions applied on beam used for the mesh sensitivity study 141

6.3 Cortical thickness distribution for each of the three meshes. Limits for the three models are 0.1 mm (shown in black) and 2 mm (shown in white). 142

6.4 Trabecular radius distribution for each of the three meshes. Limits for the fine mesh are 0.04 mm (shown in black) and 0.4 mm (shown in white). Limits for the baseline mesh are 0.1 mm (shown in black) and 1 mm (shown in white). Limits for the coarse mesh are 0.17 mm (shown in black) and 1.69 mm (shown in white). 143

6.5 Side and top views of the three meshes illustrating the trabecular structure and cortical thickness. Truss elements with a radius > 0.04 mm for the fine mesh, > 0.1 mm for the baseline mesh and > 0.17 mm for the coarse mesh are shown in red, with elements with a radius of 0.04 mm for the fine mesh, 0.1 mm for the baseline mesh and 0.17 mm for the coarse mesh shown in blue. 143

6.6 Transversal cut views taken at 25mm, 50mm and 75mm from the fixed end illustrating the cortical thickness distribution across the beam for each mesh 144

6.7 Average Young's modulus distribution for each of the three meshes. Limits for all meshes are 10 MPa (shown in black) and 18,000 MPa (shown in white). 146

6.8 Average shear modulus distribution for each mesh. Limits for all meshes are 5 MPa (shown in black) and 10,000 MPa (shown in white). 147

6.9 Density distributions for each mesh. Limits for all meshes are 0.001 g/cm^3 (shown in black) and 2.07 g/cm^3 (shown in white). 148

6.10 Comparison between the minimum (a) and maximum (b) principal strains across the surface of the structural model adapted to a lower target strain (x axis) and CT derived model (y axis). Lines of best fit are shown in red for each case, with y=x line shown in dashed blue. . 151

6.11 Comparison between the minimum (a) and maximum (b) principal strains across the surface of the orthotropic model adapted to a lower target strain (x axis) and CT derived model (y axis). Lines of best fit are shown in red for each case, with y=x line shown in dashed blue. . 154

7.1 Stress-strain curves for (a) 30 year old bone and (b) 75 year old bone across four different strain rates based on the damage elasticity model presented in Villette and Phillips (2018). 161

7.2 Boundary and loading conditions applied to the model to simulate lateral compression fracture 163

7.3 Frontal and side view predicted fracture pattern in lateral compression scenario with an impact velocity of 4m/s. Failed elements are shown in red, elements yielded in tension are shown in light yellow and elements yielded in compression are shown in light blue. 165

7.4 Frontal and side view predicted fracture pattern in lateral compression scenario with an impact velocity of 8 m/s. Failed elements are shown in red, elements yielded in tension are shown in light yellow and elements yielded in compression are shown in light blue. 166

7.5 Force-time plots for both scenarios. Components of reaction force at the sacrum are shown in solid lines and in dash lines at the contralateral femur. 167

7.6 Force-displacement plots for both scenarios. Reaction force at the sacrum is shown in solid red and in dash blue at the contralateral femur. 168

7.7 Boundary and loading conditions applied to the model to simulate unilateral vertical shear fracture 170

7.8 Boundary and loading conditions applied to the model to simulate bilateral vertical shear fracture 171

7.9 Frontal and side view predicted fracture pattern in vertical shear scenario. Failed elements are shown in red, elements yielded in tension are shown in light yellow and elements yielded in compression are shown in light blue. 172

7.10 Frontal and side view predicted fracture pattern in vertical shear scenario. Failed elements are shown in red, elements yielded in tension are shown in light yellow and elements yielded in compression are shown in light blue. 173

7.11 Force-time plots for both scenarios. Components of reaction force at the sacrum are shown in solid lines and in dash lines at the contralateral femur. 174

7.12 Force-displacement plots for both scenarios. Reaction force at the sacrum is shown in red and in dash blue at the contralateral femur. . 175

7.13 Frontal and side view predicted fracture pattern in vertical shear scenario. Failed elements are shown in red, elements yielded in tension are shown in light yellow and elements yielded in compression are shown in light blue. 176

7.14 Reaction force components at the sacral boundary condition for bilateral vertical shear. 177

7.15 Force-displacement for bilateral vertical shear. 178

7.16 Boundary and loading conditions applied to the model to simulate anterior posterior compression fracture 180

7.17 Frontal and side view predicted fracture pattern in anterior posterior compression scenario. Failed elements are shown in red, elements yielded in tension are shown in light yellow and elements yielded in compression are shown in light blue. 181

7.18 Frontal and side view predicted fracture pattern in anterior posterior compression scenario. Failed elements are shown in red, elements yielded in tension are shown in light yellow and elements yielded in compression are shown in light blue. 182

7.19 Force-time plots for both scenarios. 183

7.20 Force-displacement plots for both scenarios. 183

7.21 Frontal and side view predicted fracture pattern in anterior posterior compression scenario. Failed elements are shown in red, elements yielded in tension are shown in light yellow and elements yielded in compression are shown in light blue. 184

7.22 Frontal and side view predicted fracture pattern in anterior posterior compression scenario. Failed elements are shown in red, elements yielded in tension are shown in light yellow and elements yielded in compression are shown in light blue. 185

7.23 Force-time plots for both scenarios. 186

7.24 Force-displacement plots for both scenarios. 186

7.25 Posture obtained by abducting (a) or adducting (b) both femurs by 20 degrees (light blue) shown in comparison to baseline posture (grey) . 187

7.26 Frontal and side view predicted fracture pattern in anterior posterior compression abducted scenario. Failed elements are shown in red, elements yielded in tension are shown in light yellow and elements yielded in compression are shown in light blue. 188

7.27 Frontal and side view predicted fracture pattern in anterior posterior compression adducted scenario. Failed elements are shown in red, elements yielded in tension are shown in light yellow and elements yielded in compression are shown in light blue. 189

7.28 Force-displacement plots (a) and peak forces (b) for neutral, abducted and adducted configurations. In (a), circles indicate moment of fracture initiation. 190

A1 Frontal and side view predicted fracture pattern in lateral compression scenario using an isotropic continuum model. Failed elements are shown in red, elements yielded in tension are shown in light yellow and elements yielded in compression are shown in light blue. 204

A2 Force-time (a) and force-displacement (b) plots for lateral compression of isotropic continuum model 204

List of Tables

3.1 Material properties of the ligaments in tension (taken from Phillips et al. (2007)), with k the ligament stiffness, l the length of the ligament, A the origination area of the ligament, N_l the number of elements forming each ligament, E Young's modulus and r the radius of each truss element. 39

3.2 Material properties of the cartilage in compression (taken from Phillips et al. (2007)), with k the cartilage stiffness, l the length of the cartilage, A the origination area of the cartilage, N_l the number of elements forming each cartilage, E Young's modulus and r the radius of each truss element. 39

5.1 Coefficients of determination and slopes of the line of best fit for each adaptive model compared to the CT scan derived model. A slope value of 1 means a perfect match between models. 127

6.1 Parameters involved in sensitivity study grouped by the type and category of the modelling framework. 135

6.2 Young's modulus of each ligament and joint cartilage for each case . . 136

6.3 Comparison between trabecular, cortical and total bone volumes of baseline model and each case model 139

6.4 Mesh properties for the three models 142

6.5 Comparison between trabecular, cortical and total bone volumes for each of the meshes tested 142

6.6 Comparison between average Young's moduli values across the three meshes. 145

6.7 Comparison between average shear moduli values across the three meshes 146

6.8 Comparison between trabecular, cortical and total bone volumes of baseline model and each case model 150

6.9 Comparison between average Young's moduli values across all case models 153

6.10 Comparison between average shear moduli values across all case models 153

7.1 Material model parameters of 30 year old bone for velocities of 4 m/s and 8 m/s, respectively. 161

A1 Comparison between trabecular, cortical and total bone volumes for each structural model adapted to a different activity 202

1

Introduction

This doctoral research project focuses on bone morhopology and mechanical behaviour of the pelvic construct. In this Chapter, the main objectives of the thesis are outlined.

1.1 Thesis objectives

The main objective of this thesis was to use computational modelling techniques to develop a set of novel models of the pelvic ring that would provide further insight on its bony morphology and behaviour under non-standard loads that can lead to injuries. The aims of the thesis are listed below:

- Develop a structural finite element (FE) model of the pelvic construct and optimise its structure based on experimental data to provide a numerical model of the pelvis with a physiologically relevant bone architecture.
- Develop continuum orthotropic and isotropic FE models of the pelvic ring and implement a similar pipeline to predict a realistic material property distribution.
- Assess the sensitivity of the continuum and structural FE models and the robustness of the adaptation algorithms to gain insight in the two different modelling approaches.
- Implement a damage elasto-plasticity material model in the optimised structural model to predict fracture initiation, progression and load for injury scenarios commonly associated with complex pelvic bone injuries and a risk of mortality.

1.2 Summary of chapters

This thesis is organised in eight chapters, including the Introduction.

In Chapter 2, a background of the research project is presented. The anatomy and functional characteristics of the pelvic region are described, along with an introduction

to bone tissue and bone remodelling. Previous research on the methods used in this thesis is presented as well.

In Chapter 3, human motion data capture, processing and a musculoskeletal modelling framework are presented along with the results obtained. The generation of the FE model of the pelvic ring including ligaments and cartilage is described.

In Chapter 4, a predictive framework for a structural mesoscale model of the pelvic ring is developed. A strain driven adaptation algorithm developed by Phillips et al. (2015) based on the Mechanostat principle (Frost, 2003) is used to iteratively adapt the thickness and cross-sectional area of the shells and trusses in the structural base FE model presented in Chapter 3 in response to the loading environment produced by the joint reaction forces and muscle forces derived from the musculoskeletal simulations described in Chapter 3.

In Chapter 5, a predictive framework for a continuum model of the pelvic ring is developed. A number of continuum models were developed based on the type of constitutive material properties assigned to elements: orthotropic and isotropic. A strain drived adaptation algorithm based similarly on the Mechanostat principle (Frost, 2003) inspired from the work done by Geraldes and Phillips (2010) on the femur is used to iteratively adapt the material properties (and material orientations for the orthotropic model) in response to the loading environment caused by the joint reaction forces and muscle forces derived from musculoskeletal simulations, described in Chapter 3.

In Chapter 7, a strain rate and age dependent damage elasto-plasticity bone model developed by Villette (2016) was used to predict fracture onset and progression in the pelvic construct in scenarios generally associated with lateral compression, vertical shear and antero-posterior compression. The predicted fracture patterns and fracture loads were compared to experimental and clinical data from literature.

Chapter 6 reports a sensitivity study performed to assess the sensitivity of the

models and adaptation algorithms developed in Chapters 3 and 4 to material properties of the ligaments, mesh density and parameters associated with the adaptation algorithms.

Finally, concluding remarks are made in Chapter 8.

2

Background

This Chapter outlines the context of this research project in terms of anatomy of the pelvic ring, the structure of bone and presents an overview of the mechanisms of functional bone adaptation in the first three sections. The last two sections of this Chapter offer an overview of pelvic injuries and finite element techniques applied to skeletal biomechanics.

2.1 Pelvis anatomy

2.1.1 Bony pelvis

The pelvic girdle is a ring shaped structure located in the lower part of the trunk, connecting the lower limbs to the axial skeleton of the upper body. The bony pelvis serves a number of important functions:

- transfers and distributes the weight from the upper body to the lower limbs;
- houses and protects the pelvic viscera;
- provides attachment for muscles and ligaments used in locomotion.

The pelvic ring consists of three bones: the sacrum and two innominate (hip) bones (Figure 2.1). Each hip bone is made of three fused parts (ilium, ischium and pubis) which are initially separated by hyaline cartilage. The fusion process commences at the age of eleven years in females and fourteen years in males.

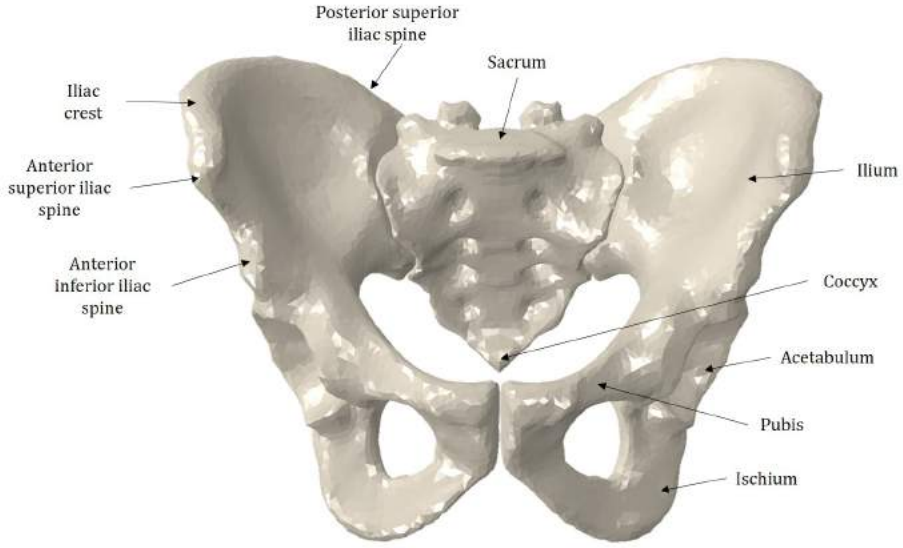


Figure 2.1: Anatomical landmarks of the bony pelvis.

2.1.2 Pelvic joints and ligaments

The three bones are joined together by a set of strong joints and ligaments in order to ensure little mobility between them, illustrated in Figure 2.2. The pubic symphisis is a cartilaginous joint connecting the two innominates anteriorly. The joint is surrounded above and below by a layer of fibrous ligaments. Posteriorly, the hip bones are connected to the sacrum by the sacroiliac joints and three bundles of ligaments to provide additional stability: anterior sacroiliac, posterior sacroiliac and interosseous sacroiliac. The anterior sacroiliac ligament extends from the auricular surface of the ilium to the anterolateral part of the sacrum. The posterior sacroiliac ligament is a very strong ligament connecting the posterior superior iliac spine to the third and fourth segments of the sacrum. The interosseous ligament is a short and strong ligament lying deep to the posterior sacroiliac ligament.

Three other ligaments further stabilise the pelvic ring: sacrotuberous, sacrospinous and inguinal. The sacrotuberous ligament is attached to to the sacrum and coccyx, with the fibers converging into the medial ischial tuberosity. The sacrospinous ligament is attached to the ischial spine and the lateral region of the sacrum. The inguinal ligament runs from the pubic tubercle to the anterior superior iliac crest of the ilium. The bony pelvis is connected to the skeletal system through a lumbosacral joint connecting the last lumbar vertebra and the first sacral segment and through two hip joints connecting each femur to the respective hip bones.

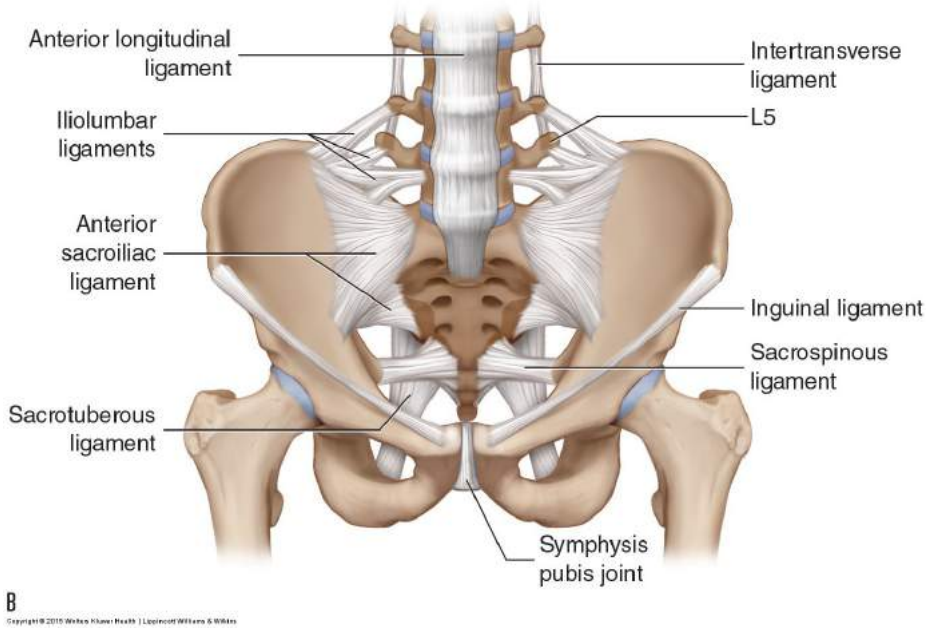


Figure 2.2: Ligaments and joints of the pelvis (image reproduced from https://learnmuscles.com/blog/2017/08/30/ligaments-of-the-lumbar-spine-and-pelvis/)

2.2 Bone structure

Bone structure has been studied extensively across history, with an emphasis on long bones. As early as the 16^{th} century, Galilei made a number of observations on the mechanical function and shape of long bones across different species, proposing a dimensional scaling law. One of his conclusive remarks was that the size of bones could not only grow linearly for larger animals as they would have to maintain the same strength (Galilei, 1638).

The notion of architectural structures in the cancellous bone was first introduced by Bourgery in 1832, with his observations being indicative of bone achieving 'maximum strength with minimum construction material' (Roesler, 1987). Later that century, anatomist von Meyer (1867) published a paper describing cancellous bone architecture in a number of bones (Figure 2.3).

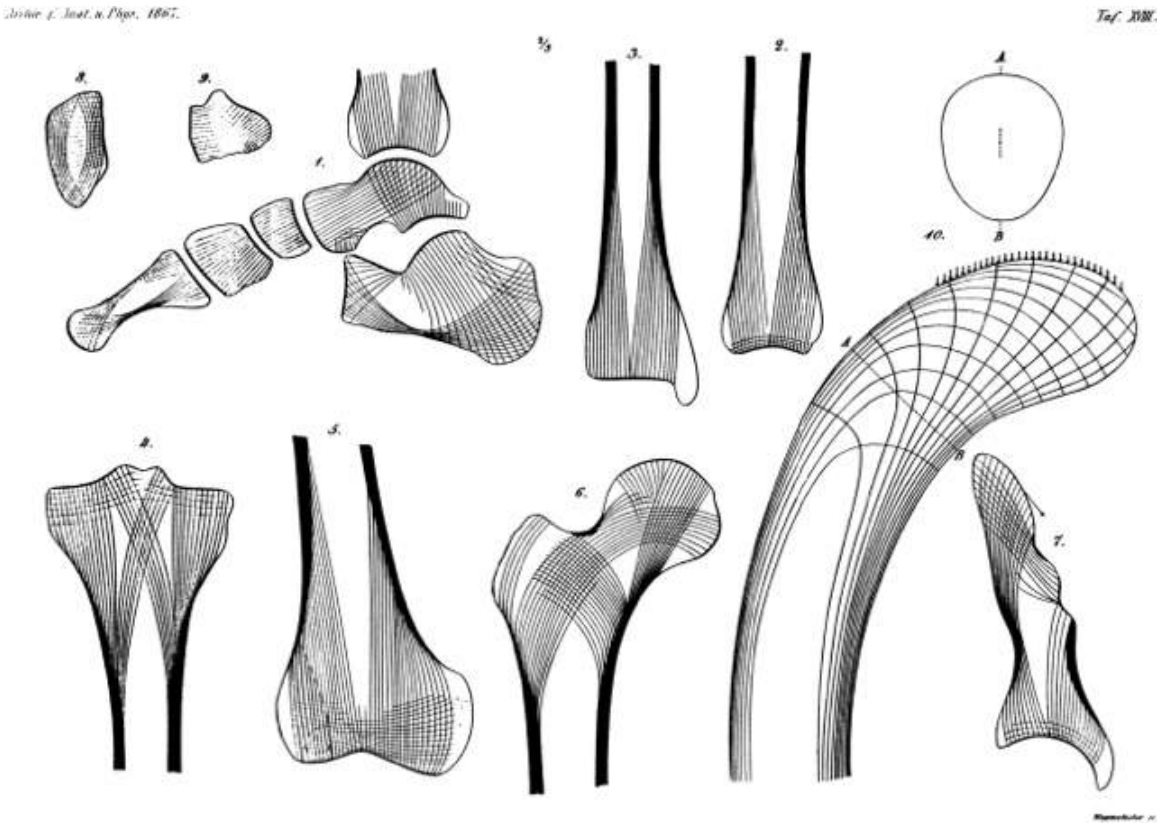


Figure 2.3: Trabecular patterns for various human bones proposed by von Meyer (1867). The structure of the proximal femur (6) is compared to Culmann's crane (10).

An interesting aspect was noted by structural engineer Karl Culmann, who observed that the depicted structures resemble the maximum internal stress lines in cantilever beams subjected to analogous loading conditions. In particular, the cancellous architecture of the proximal femur seemed to correspond to the principal stress trajectories of a Fairbairn crane (Culmann, 1866). This view of trabecular trajectories was expanded upon by Julius Wolff, who believed that the principal stress directions dictate the resulting structure of cancellous bone, implying that these trajectories crossed orthogonally. He hypothesised that a mathematical relationship exists between skeletal loads and bone structure and any change in those loads would result in changes to the cancellous structure:

"Every change in the form and function of the bones, or of their function alone, is followed by certain definite changes in their internal architecture, and equally definite

secondary alterations of their external conformation, in accordance with mathematical laws." (Skedros and Baucom, 2007)

Wolff's theory of bone tissue adapting to the mehanical environment surrounding it, along with Roux's functional adaptation principle (1895), which stated that undifferentiated connective tissue would differentiate into, cartilage, fibrous tissue or bone depending on the mechanical stress experienced, later became 'Wolff's Law' (Roesler, 1987).

Although it is generally accepted that an orthogonal trabecular configuration is optimal for simple loading cases (Koch, 1917; Pedersen, 1989), more recent studies have suggested that acute intersections between trajectories might be better suited to resist shear stresses generated by complex loading scenarios (Pidaparti and Turner, 1997; Skedros and Baucom, 2007).

As opposed to the femur, the mechanics and structure of pelvic bone have not been studied as extensively. A potential explanation for this gap could be the difference in complexity between the geometries of the pelvis and femur (Dalstra, 1993). Pelvic bone resembles a sandwich construction consisting of two thin layers of cortical bone surrounding cancellous bone, designed to withstand high stresses and maintain a low weight (Jacob et al., 1976). Dalstra (1993) hypothesised that the majority of loads are transferred along the cortex, with trabecular bone stopping cortical bone from buckling.

Macchiarelli et al. (1999) compared trabecular bone structure in the adolescent and adult South African australopithecines ilium with the human counterpart using advanced digital image processing techniques on radiographs. In the human ilium, they qualitatively identified a number of gait-related trabecular trajectories which were consistent with the observations of Correnti (1955). The particularities of the iliac trabecular structure found by them are highlighted and discussed in Chapter 4.

Anderson et al. (2005) reconstructed the geometry of a pelvis from CT imaging data to investigate the spatial distribution of cortical bone thickness and trabecular

bone elastic modulus. They found cortical thickness to vary between 0.44 and 4 mm (mean: 1.41 mm) and identified the iliac crest, ascending pubic ramus, gluteal surface and the acetabular rim to be the regions with high cortical thickness. Regions with thin cortical bone were found at the acetabular cup, ischial tuberosity, iliac fossa and area surrounding the pubic tubercle. The elastic modulus of trabecular bone varied between 2.5 and 3829 MPa (mean: 338 MPa). They identified the muscle insertion areas and the subchondral bone region surrounding the acetabulum to have high modulus. The interior of the ilium, ischial tuberosity and the regions near the sacroiliac and pubic joints were found to have low elastic modulus.

2.3 Functional adaptation of bone

2.3.1 Bone tissue structure

Bone is a complex tissue with different material structures across length scales (Rho et al., 1998; Reznikov et al., 2014). The hierarchical levels of bone are:

- cancellous and cortical bone - macrostructure
- haversian systems, osteons, single trabeculae - microstructure
- lamellae - sub-microstructure
- fibrillar collagen and embedded minerals - nanostructure
- molecular structures of constituent elements - sub-nanostructure

At the macrostructure (1 to 5 mm), bone can be separated in two types: trabecular or cancellous bone, and cortical bone. Cancellous bone forms a porous structure made of rod and plate-like elements with thicknesses ranging from 100 to 300 μm, with bone marrow filling the remaining void (Rho et al., 1998; Keaveny et al., 2004). On the other hand, cortical bone is dense and encloses the trabecular bone, with thicknesses ranging from 0.1 mm to 5 mm in the pelvis (Anderson et al., 2005). At the microstructure and sub-microstructure, both types of bone have similar characteristics.

Structural units called lamellae are thin sheets (6 μm thick) made of unidirectionally oriented mineralized collagen fibrils (50 nm in diameter) (Rho et al., 1998; Keaveny et al., 2004; Reznikov et al., 2014). In the cortex, lamellae are organised in concentric rings around a 50 μm wide Haversian canal containing blood vessel, nerve and bone cells. Between them, the lamellae contain osteocytes, which are connected through canaliculi. This assembly is typically 200 μm wide and 1 to 3 mm long and

is called an osteon. In trabecular bone, lamellae are organised into 'lamellar packets' (Reznikov et al., 2015). As opposed to cortical bone, lamellae are aligned locally within each packet but across multiple packets orientation varies (Reznikov et al., 2015).

It is generally accepted that bone is a highly anisotropic material and it presents a number of unique characteristics. At apparent level, cortical bone can be treated as an orthotropic material (Knets, 1977; Cowin and Mehrabadi, 1989), as it is stiffer and stronger in the longitudinal than in the transverse direction (Reilly and Burstein, 1975; Gibson and Ashby, 1999). In addition, it is tougher in compression than in tension (Reilly and Burstein, 1975). Mechanical properties of bone are heavily influenced by age (McCalden et al., 1993) and loading rate (Hansen et al., 2008).

An interesting aspect on trabecular bone is that its porosity plays a major role in defining the mechanical behaviour. At tissue level, the stiffness of trabecular bone is similar to cortical bone, with Young's modulus for cancellous bone falling between longitudinal and transverse Young's moduli for cortical bone (Turner et al., 1999). This indicates the importance of the structural arrangement of individual trabecular and the resulting porosity (Keaveny et al., 2004). Strength and elastic properties of cancellous bone are also dependent on other factors: loading mode (Keaveny et al., 1994), age and bone health (Goldstein et al., 1983) and loading direction (Ciarelli et al., 1991).

2.3.2 Bone remodelling and adaptation

Osteoclasts, osteoblasts and osteocytes are the three main bone cells that drive bone remodelling. From a biological perspective, bone remodelling consists of four phases (Hill and Orth, 1998), as shown in Figure 2.4. In the activation phase, lining cells at the bone surface differentiate into osteoclasts. In the resorption phase, osteoclasts dissolve the bone tissue. Osteoclasts then undergo apoptosis while macrophage-like

cells appear on the bone surface that can stimulate the formation of osteoblasts as part of the reversal phase. Finally, the bone formation phase occurs when the recruited osteoblasts produce the new bone matrix and promote its mineralization, followed by their maturation into osteocytes (Hill and Orth, 1998; Rucci, 2008; Kular et al., 2012). The notion that osteocytes regulate the activity of osteoblasts and osteoclasts

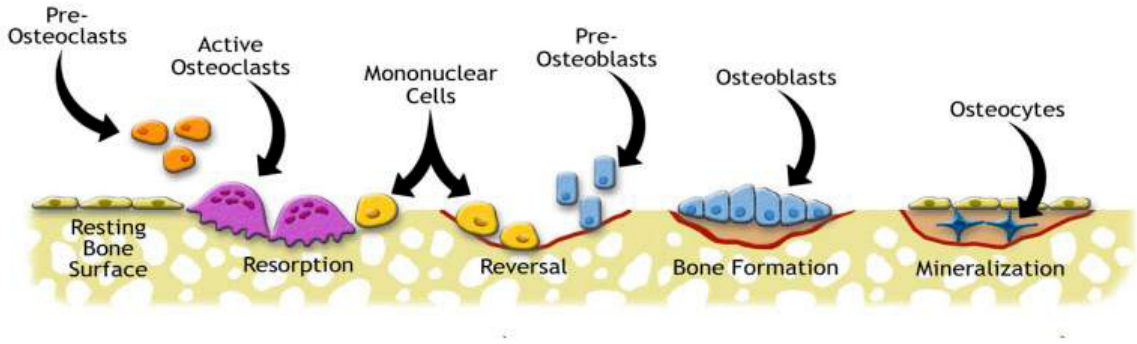


Figure 2.4: Illustration of the bone remodelling process at cellular level (image reproduced from *OrthopaedicsOne*)

in response to mechanical loading of the surrounding environment is now commonly accepted (Hill and Orth, 1998; Robling et al., 2006; Rucci, 2008; Kular et al., 2012). Frost (1987; 2003) formulated a principle that refers to bone adaptation towards a local target mechanical stimulus state, driven by stress or strain. Thus, bone resorption and apposition would be triggered by lower and higher strains, respectively, compared to the target. In addition, he hypothesised the presence of a lazy zone around the target, in which bone remodelling would not be triggered. The process is illustrated in Figure 2.5. This hypothesised process is consistent with observations of functional adaptations such as: spaceflight and bed rest leading to a decrease in bone density (Donaldson et al., 1970; Bloomfield, 1997; LeBlanc et al., 2000; Lang et al., 2004), and physical activity leading to an increase in local bone density (eg. dominant arm of tennis players was found to have a higher bone mineral density than contralateral arm) (Kannus et al., 1995; Bennell et al., 1997; Pollock et al., 1997; Andreoli et al., 2001).

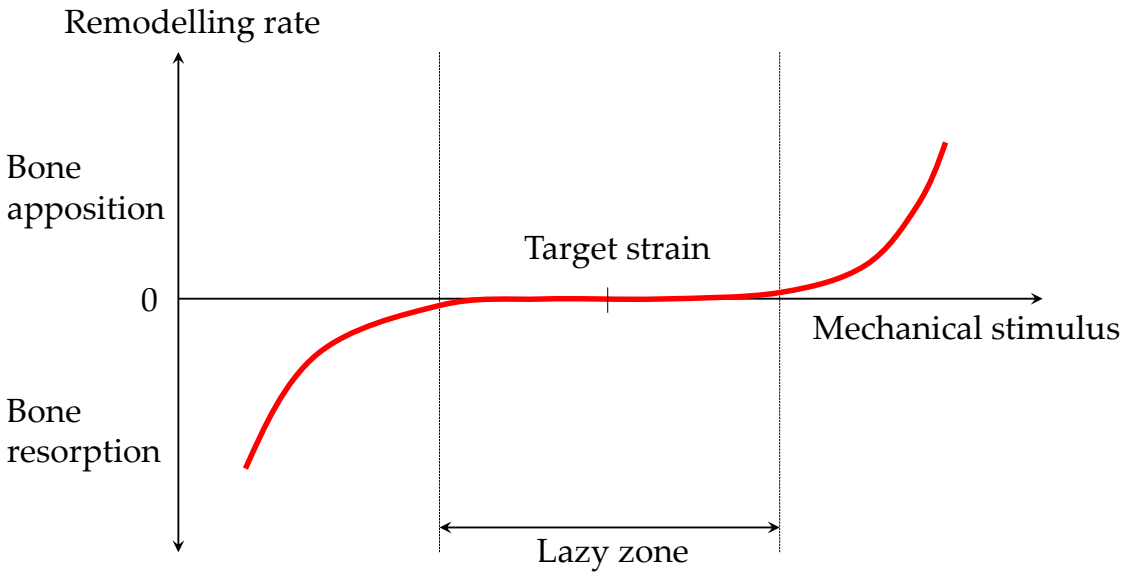


Figure 2.5: Illustration of the mechanostat principle proposed by Frost (1987).

2.4 Pelvic injuries

Pelvic injuries encountered both in civilian and military environments are generally complex in nature and associated with high rates of morbidity and mortality (Mucha and Farnell, 1984; Poole et al., 1992; Pohlemann et al., 1996; Van Vugt and Van Kampen, 2006; Mossadegh et al., 2012; Sathy et al., 2009). As the pelvic ring requires a considerable force to disrupt it (Van Vugt and Van Kampen, 2006), pelvic injuries are generally associated with additional trauma to other regions in the body (Chong et al., 1997). The severity of pelvic fractures ranges from minor to high-energy, which can cause prehospital death (Balogh et al., 2007). Mortality from pelvic injury is primarily caused by haemorrhage in the pelvic cavity (Cryer et al., 1988; Balogh et al., 2007).

2.4.1 Classification of pelvic injuries

Pelvic injuries were initially classified by Tile and Pennal (1980), followed by a modification proposed by Burgess et al. (1990) to relate the direction of the force applied to the pelvis to the fracture pattern. The proposed classification has three categories: lateral compression (LC), vertical shear (VS) and anterior-posterior compression (APC). The fracture patterns are shown in Figure 2.6, with each category further divided based on severity. APC injuries occur typically from high energy impacts,

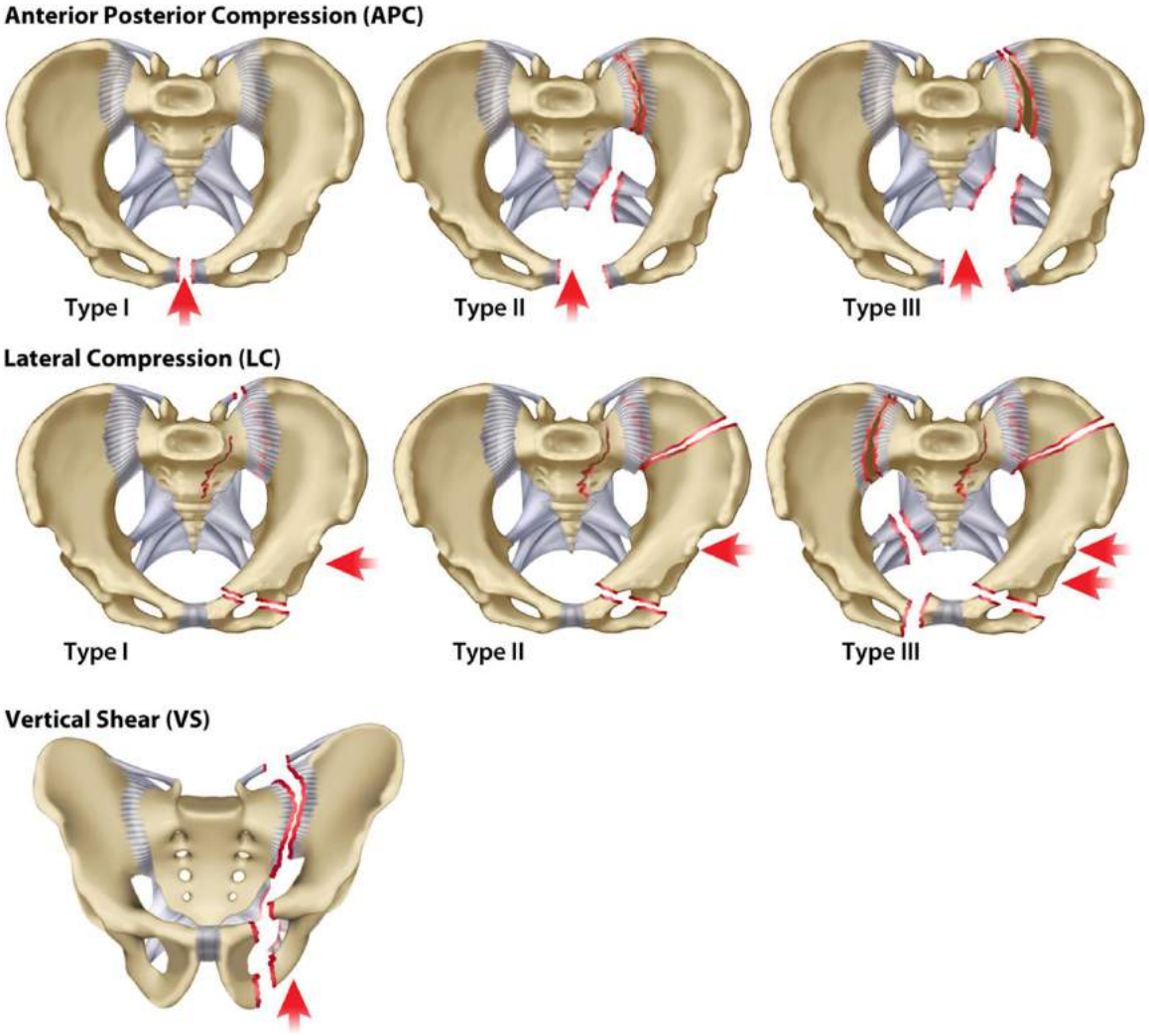


Figure 2.6: Young Burgess classification for pelvic fractures (image reproduced from Alton and Gee (2014))

with one iliac blade being externally rotated, causing disruption at the pubic symph-

ysis and sacroiliac joint. The three severity grades are differentiated by the amount of widening in both joints, ranging from a slight widening of the pubic symphysis (<25 mm) and sacroiliac joint to complete separation of the hemipelvis from the pelvic ring.

LC injuries are caused by a lateral force causing an inward rotation of the pelvis, typically occuring in motor vehicle accidents (MVA) (Dalal et al., 1989). They are classified in three subgroups (I, II and III) based on injury severity (Burgess et al., 1990). Type I is usually caused by a force directed to the posterior side of the pelvis and leads to a transverse fracture across the pubic rami and a compression fracture of the sacrum. The ligaments are rarely disrupted, meaning that it is a stable injury. Type II fractures are generally caused by forces directed at the anterior side of the pelvis, leading to inward rotation of the iliac crest. In addition to fractured pubic rami, a crescent fracture occurs near the anterior sacroiliac joint. Type III fractures are the most severe, with one hip being projected onto the contralateral hip, causing disruption of the sacroiliac joints (Burgess et al., 1990).

VS injuries are caused by an axial shear force being transmitted through the pelvis, often from landing feet first in a fall from height. This scenario usually leads to a disruption anteriorly at the pubic symphysis and posteriorly around the sacroiliac joint, with the occasional vertically displaced iliac wing and fractured sacrum (Burgess et al., 1990).

In the past decades, efforts have been made to improve the outcome of these injuries by attempting to understand the mechanism associated with them, generally by designing appropriate experimental studies. Details on the experimental studies focusing on each fracture mechanism can be found in the corresponding sections in Chapter 5.

2.5 Finite element modelling applied to biomechanics

2.5.1 Introduction to finite element modelling

The finite element method (FEM) is a numerical technique used to solve typically engineering or physics problems which can be described by a set of partial differential equations, which would be too complex to solve analytically. In the case of continuum solids, the method consists of discretising the volume into a finite number of elements connected through nodes. This enables solving the approximated equilibrium equations associated with each element based on an overall equilibrium between forces at each node, imposed boundary conditions and any applied loads. In addition, to identify solutions at positions within a given element, shape functions are used to interpolate between the two nodes surrounding the point of interest. This also provides a continuity between adjoining elements.

This method was first introduced in a paper published in 1956 (Turner, 1956) and was initially used in the aerospace industry. During the 1950s and 1960s, the technique was transferred to a wider range of engineering applications. One of the first applications of FEM in biomechanics was to derive the stresses within a human femur (Rybicki et al., 1972). The extensive work of Zienekiewick (1967; 1977; 2000) provides detailed explanations of the concepts associated with this method.

The main advantage FE modelling has over clinical investigations and physical experiments is that it enables investigation of a large number of scenarios with few constraints on the design space and no risk of material shortage. In addition, there are multiple modelling approaches that can be applied to a biomechanical problem. Two such approaches refer to the use of continuum or structural elements, which are discussed in the next Section.

2.5.2 Existing FE models of the pelvic construct

Early pelvic models were either 2D (Vasu et al., 1982; Carter et al., 1982; Rapperport et al., 1985; Oonishi et al., 1986), axisymmetric (Pedersen et al., 1982; Huiskes, 1987), or used simplified geometries (Goel et al., 1978; Oonishi et al., 1983; Landjerit et al., 1992; Schuller et al., 1993). Goel et al. (1978) have developed one of the first FE models of the hip bone with the aim to investigate stresses across it as a result of forces in the muscles and ligaments acting on it. The main aim of the first FE models of the pelvis were to bridge the gap in understanding its behaviour under loading compared to the femur, which had been studied more extensively at the time. This would enable designing appropriate hip implants. Several early studies have focused on investigating the mechanical behaviour of the hip region with an implant (Carter et al., 1982; Pedersen et al., 1982; Oonishi et al., 1983; Huiskes, 1987).

A common approach over the past three decades has been to develop models based on geometries and material properties extracted from medical imaging data (eg. computed tomography (CT)) and to build them using continuum solid elements. Dalstra et al. (1993) used dual-energy quantitative computer tomography (DEQCT) to investigate the distribution of bone densities throughout pelvic bone and tested cubic samples of pelvic trabecular bone to extract Young's moduli and Poisson's ratios in three orthogonal directions, concluding that trabecular bone in the pelvis is not highly anisotropic. The study also provided insight in the distribution of pelvic trabecular bone density.

The first computational model of the bony pelvis developed using subject specific geometry and material properties from medical imaging data was developed by Dalstra et al. (1995b). The authors validated the model against experimentally obtained strains from a cadaveric pelvis loaded at the hip joint, although the specimen used for the experiment was different from the one used for generating the FE model.

Similarly, Anderson et al. (2005) developed a FE model of the pelvis by obtaining

location dependent cortical thickness and trabecular elastic modulus information from medical imaging data. The model was validated against experimental data by comparing cortical bone strains resulting from applying a load through the acetabulum and fixing the superior ilium. In addition, the authors performed a set of sensitivity studies to assess the impact of certain parameters (eg. elastic modulus, cortical bone thickness) on the model's response. The majority of published models only partially represent the pelvic ring, focusing primarily on either the hip joint (Goel et al., 1978; Oonishi et al., 1983; Rapperport et al., 1985; Schuller et al., 1993; Thompson et al., 2002; Zant et al., 2008; Cilingir et al., 2007; Anderson et al., 2008) or the hemi-pelvis (Schuller et al., 1993; Dalstra et al., 1995b; Phillips et al., 2004; Anderson et al., 2005; Phillips et al., 2006; Ghosh et al., 2013; Clarke et al., 2013; Fernandez et al., 2014). For the purpose of investigating the structural response of the pelvis in a variety of loading conditions, the development of a complete model of the pelvic construct is considered to provide an improved understanding of its behaviour in complex loading scenarios, compared to models which represent an isolated part of the construct.

As discussed in §2.1, an important aspect of the pelvic girdle are the joints holding the three components of the pelvis (sacrum and two pelvic innominates) together, the sacroiliac joint and the pubic symphysis. A number of other ligaments (sacrospinous, sacrotuberous, iliolumbar, inguinal) provide additional stability to the pelvic ring under load (Vrahas et al., 1995). Phillips et al. (2007) developed a model of the pelvis including both hemipelves, the corresponding ligaments and joints, a structure representing the sacrum, and the muscles attached to the pelvis in an explicit manner to eliminate the need of using fixed boundary conditions on the bone. They observed that the use of ligaments and muscles in the model resulted in a more even stress distribution across bone as opposed to fixed boundary conditions.

A number of FE models of the pelvic ring have been developed and used to investigate injury mechanisms (Renaudin et al., 1993b; Dawson et al., 1999; Majumder et al., 2004, 2007; Li et al., 2007). Dawson et al. (1999) developed and validated a FE model of the pelvic ring with spatially-varying material properties for bone and

included ligaments and joints using linear springs. The model was used to investigate the pelvic response in side impact (eg. car-to-car side crash) by applying forces in the range [5520 N, 15,550 N], corresponding to previous experimental studies on side impact (Cesari et al., 1980; Cesari and Ramet, 1982; Nusholtz et al., 1982). The fracture criterion was defined as the ratio between von Mises stress and strength for each element. The model predicted fracture onset at a load of around 8.6 kN with an impulse of 129 N/s, corresponding to an impact velocity of approximately 41 km/h.

Similarly, Majumder et al. (2004) developed a FE model from CT data and assigned homogeneous material properties to trabecular bone and a uniform thickness to cortical bone based on the observations made by Dalstra et al. (1995b). The model was used to simulate side impact for 25 dynamic load cases by varying the peak impact force (1 kN to 5 kN) and the duration of impact (0.5 ms to 15 ms). Von Mises stress was used to predict local bone failure based on the compressive strength of cortical bone. They reported that, for peak impact forces higher than 3 kN, a fracture would occur. Although the results were consistent with experimental findings (Guillemot et al., 1998; Beason et al., 2003) for the loading interval, the homogeneous material properties and independence of Young's modulus and strength with respect to strain rate could explain the discrepancy with the results reported by Dawson et al. (1999).

An alternative approach to continuum FE modelling is to look at bone from a structural perspective and represent its architecture using a combination of idealized structural elements such as trusses, beams and shells. An important aspect of this method is the increased computational efficiency (van Lenthe et al., 2006), while maintaining the ability to capture the overall structural behaviour of bone (Phillips et al., 2015). Furthermore, structural modelling allows for directionality to be included in modelling trabecular bone, which can have a mechanical significance (Miller et al., 2002). Using this technique to model and predict bone morphology enables the use of such models to predict fracture initiation and progression (Villette and Phillips, 2018). To the authors' knowledge, the structural approach to model bone morphology has not been applied to the pelvic construct.

3

Musculoskeletal and Finite Element modelling of the pelvic construct

This Chapter presents the process of obtaining the relevant loading environment to apply to the adaptive models presented in Chapters 4 and 5. In addition, the creation of the initial structural and continuum FE models and the development of a FE model with varying material properties based on clinical CT imaging data is presented.

3.1 Gait data collection and processing

Full body kinematic data for five common daily physical activities (walking, stair ascent, stair descent, sit-to-stand and stand-to-sit) (Morlock et al., 2001) were collected from a healthy male volunteer well known to the author (age: 23 years, weight: 93 kg, height: 188 cm) in the Biodynamics Lab in the Imperial College Research Labs at Charing Cross Hospital. 59 spherical reflective markers (⌀=14 mm) were attached directly on the volunteer's skin on bony landmarks based on the recommendations of the International Society of Biomechanics for lower and upper extremities (Wu et al., 2002). Clusters of markers were placed on the mid-thigh laterally and mid-shank medially on both legs. A Vicon system (Oxford Metrics, Oxford, UK) equipped with 10 infrared cameras was used to track the markers motion at sampling rate of 100 Hz.

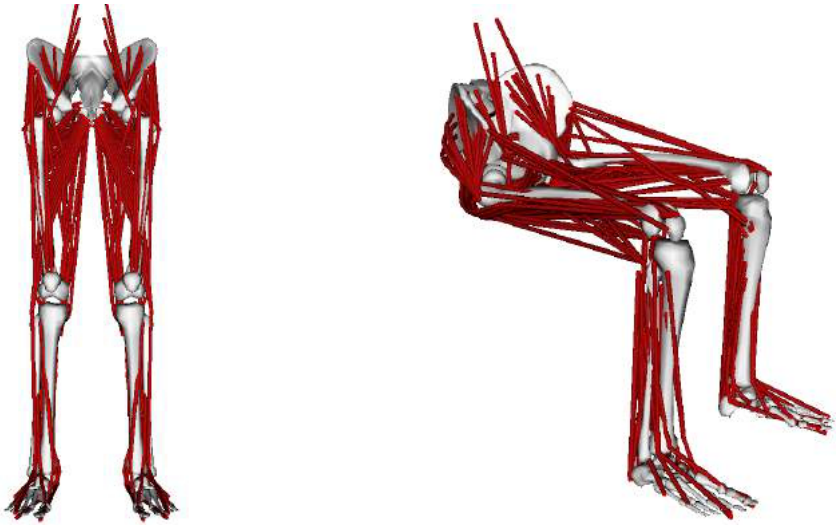
Three force plates (Type 9286BA, sampling rate 1000 Hz, Kistler Instruments Ltd, Hook, UK) were used to measure the ground reaction forces (GRFs). The force plates were positioned to form a walkway which was used to record GRFs during walking (speed: 1.34 m/s, stride length: 0.64 m, cadence: 115.54 steps/min). To measure stair ascent and descent GRFs, the three force plates were positioned on consecutive steps on a staircase (step height 15 cm and step depth 25 cm, with a step inclination of 36.8 degrees). A stool with a height of 52.5 cm from the floor was used to record GRFs during sit-to-stand and stand-to-sit. Force plates were placed on the seat and at both feet.

Trajectories of the markers were labeled, gap filled and filtered using a 4^{th} order zero lag low-pass Butterworth filter with a cutoff frequency of 6 Hz (Winter et al., 1974) in Vicon Nexus (version 1.8.5). The c3d files produced in Vicon Nexus were further processed in Matlab using the Biomechanical ToolKit (Barre and Armand, 2014) to generate input files compatible with OpenSim. Marker data were saved in trc format, analog signals from the force plates were filtered using a zero lag low-pass

Butterwoth filter with a cuttoff frequency of 30 Hz (Eng and Winter, 1995). Gait events (heel strike and toe off) were automatically identified using a 30 N vertical force threshold. For walking,the length of the processed trial was set to include a full gait cycle for each leg.

3.2 Musculoskeletal modelling

A bilateral musculoskeletal model based on an ipsilateral model developed by Modenese et al. (2011) and validated at the hip joint was used (Modenese et al., 2013). The model was based on an anatomical dataset published by Horsman et al. (2007) and implemented in OpenSim (Delp et al., 2007). It includes thirteen body segments: pelvis, two femurs, two patellas, two tibias, two hindfeet, two midfeet and two sets of phalanges (Figure 3.1). The segments are connected by nine joints: pelvis-ground (6 degrees of freedom (DOF)), hip joints (3 DOF each), knee joints (1 DOF each), patellofemoral joints (1 DOF each) and ankle joints (1 DOF each). The local reference systems of the segments were defined in accordance with the recommendations of the International Society of Biomechanics (Wu et al., 2002). The anatomical muscle attachment points on the right side of the model were the same as in Modenese et al. (2011), while those on the left side were obtained by mirroring the right side points with respect to the sagittal plane. Thus, the total number of muscles and actuators in the bilateral model was 76 and 326, respectively.



(a) (b)

Figure 3.1: Lower limb musculoskeletal model in (a) standing and (b) seated positions

3.2.1 Scaling

The segments of the generic bilateral model were linearly scaled based on the ratios between the distance of pairs of experimental markers located on the segment in question and corresponding pairs of virtual markers located on the unscaled model. Each body segment was linearly scaled based on its length. The inertial properties were updated according to the regression equations of Dumas et al. (2007). The virtual markers on the generic model were positioned according to the coordinates reported by Horsman et al. (2007).

3.2.2 Inverse kinematics

Joints angles describing the kinematics of trials for all activities were obtained using the OpenSim inverse kinematics tool. This tool identifies joint angles that minimize the error between experimental and virtual markers, similar to the global optimization method described by Lu and O'Connor (1999).

Joint angles for complete cycles on both legs for walking, stair ascent, stair descent and sit-to-stand-to-sit are shown in Figures 3.2, 3.3, 3.4 and 3.5, respectively. The inverse kinematics results for walking and stair ascent trials were in good agreement with previously published data using a unilateral version of the musculoskeletal model (Modenese et al., 2013).

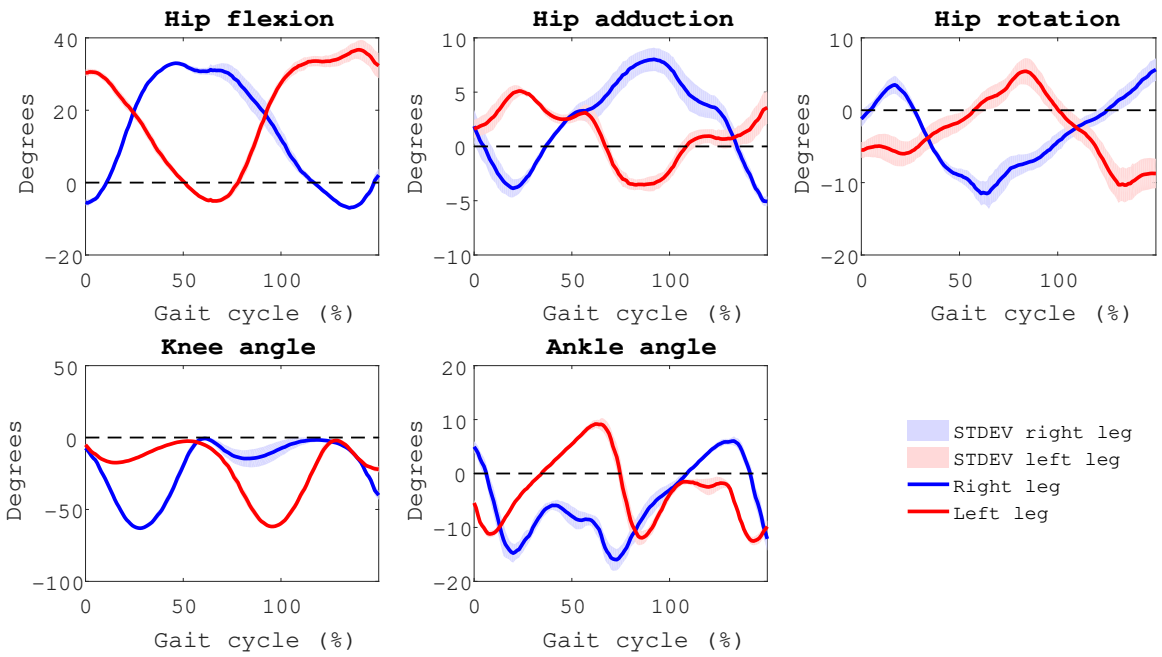


Figure 3.2: Average joint angles at the hip, knee and ankle for five walking trials

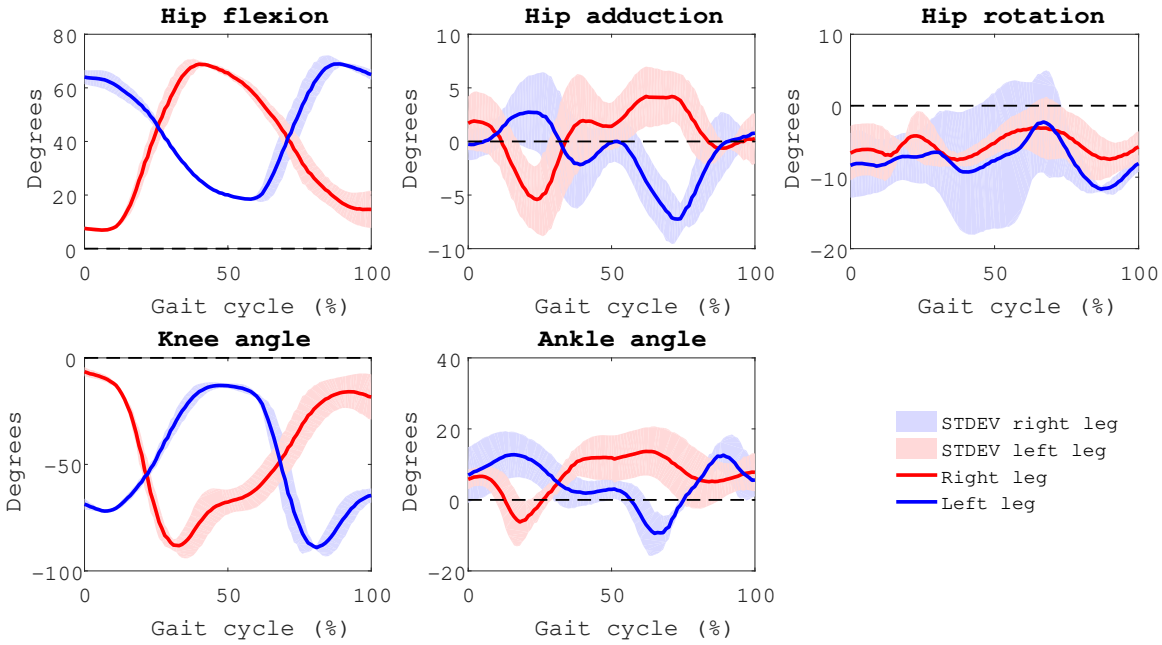


Figure 3.3: Average joint angles at the hip, knee and ankle for four stair ascent trials

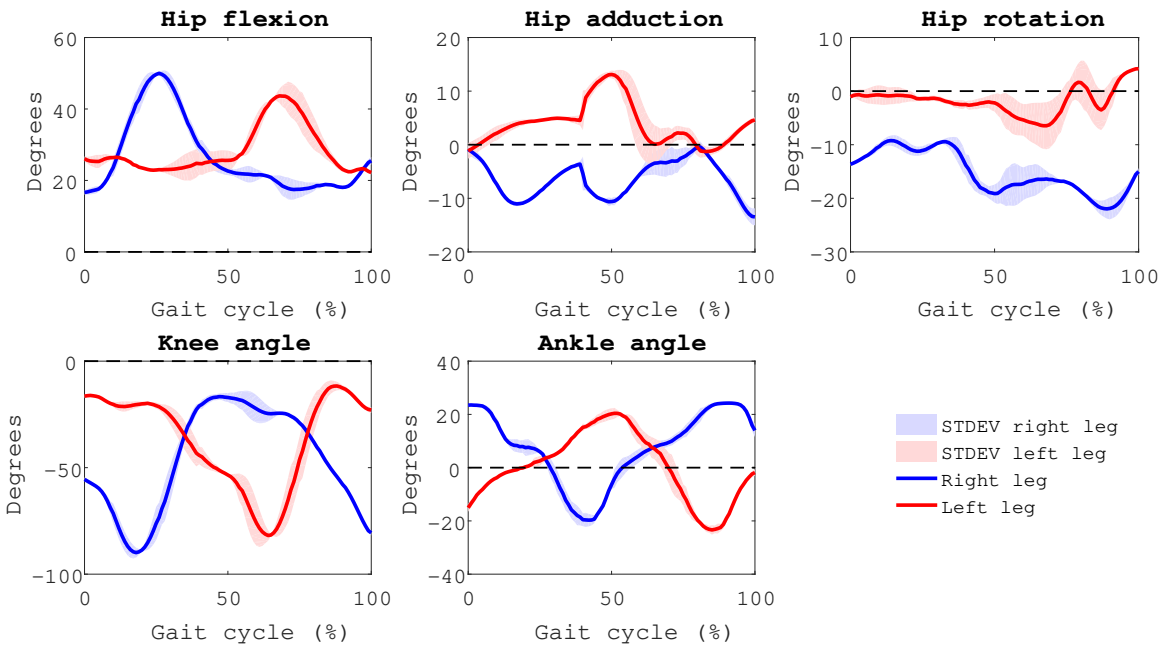


Figure 3.4: Average joint angles at the hip, knee and ankle for two stair descent trials

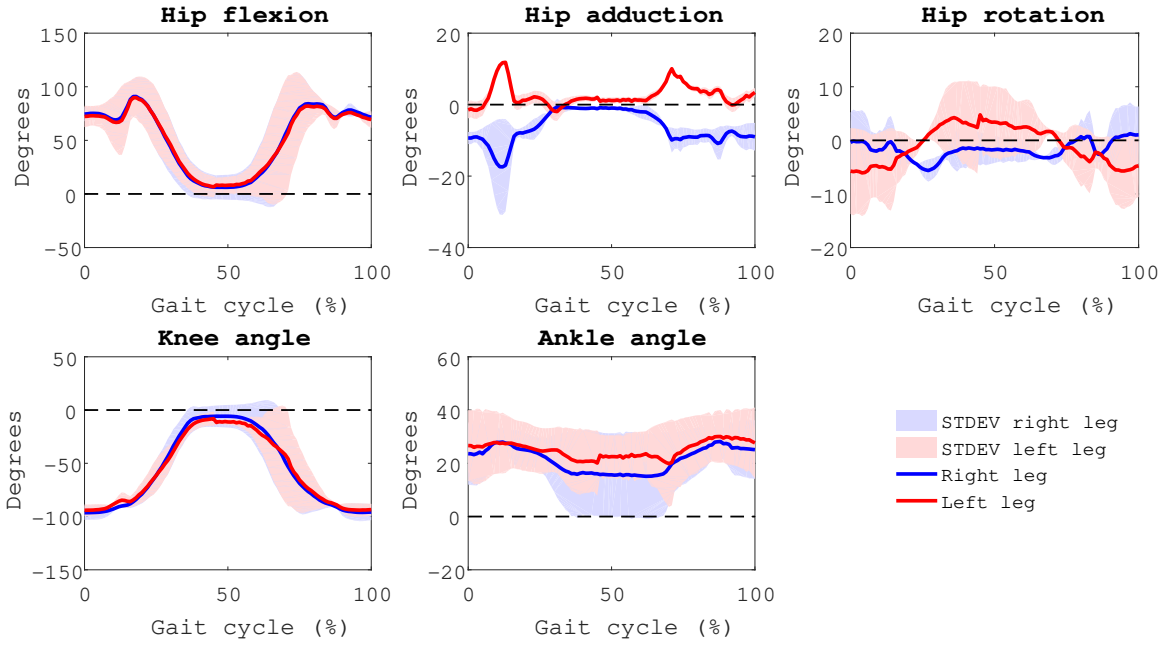


Figure 3.5: Average joint angles at the hip, knee and ankle for two sit-to-stand-to-sit trials

3.2.3 Inverse dynamics

Net joint moments were calculated using the OpenSim inverse dynamics tool (ID) by soving equations of motion in a bottom up approach (Winter, 2009).

Normalized joint moments for complete cycles of both legs for walking, stair ascent, stair descent and sit-to-stand-to-sit are shown in Figures 3.6, 3.7, 3.8 and 3.9, respectively. The inverse dynamics results for walking and stair ascent trials were in good agreement with previously published data using a unilateral version of the musculoskeletal model (Modenese et al., 2013).

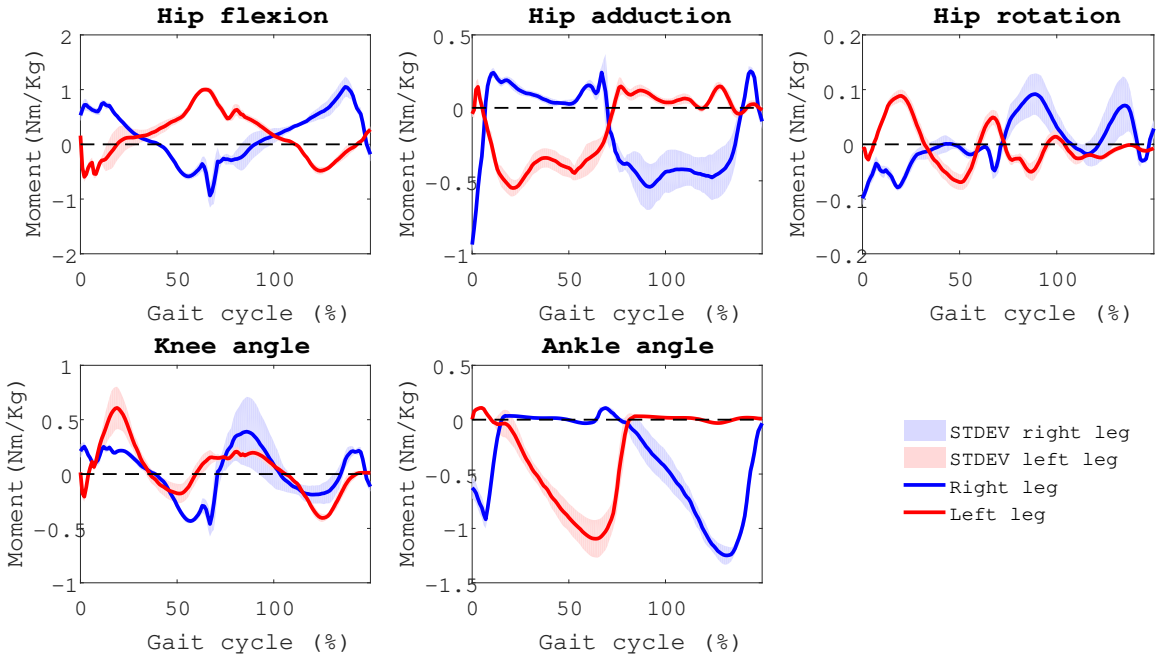


Figure 3.6: Normalized joint moments at the hip, knee and ankle for walking trials

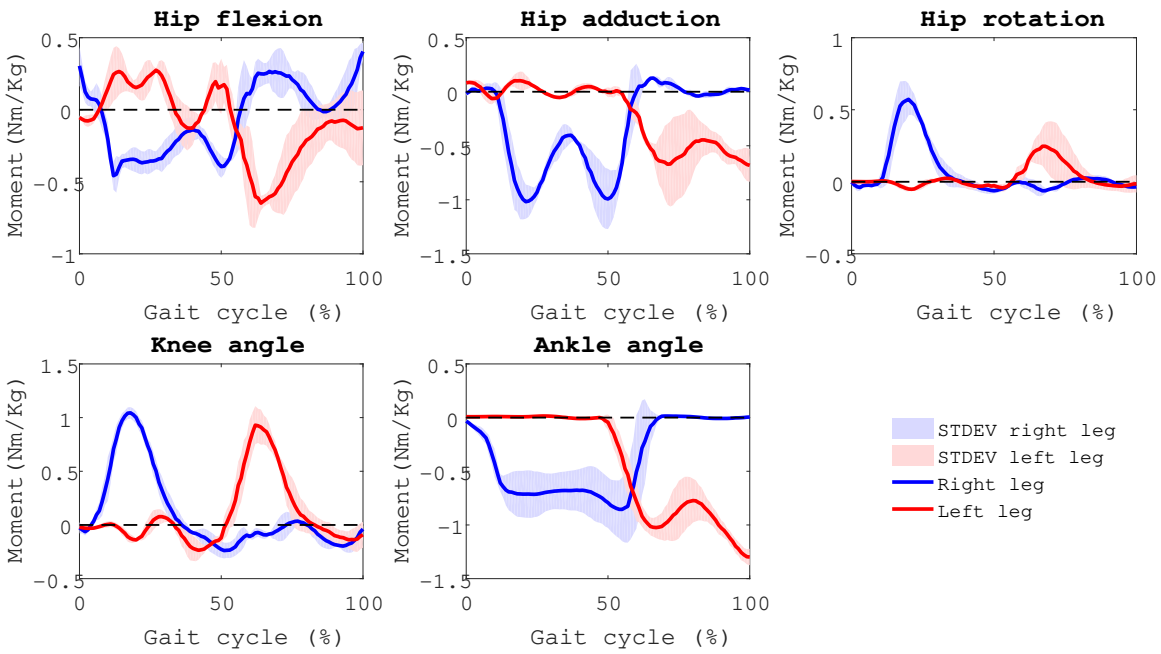


Figure 3.7: Normalized joint moments at the hip, knee and ankle for stair ascent trials

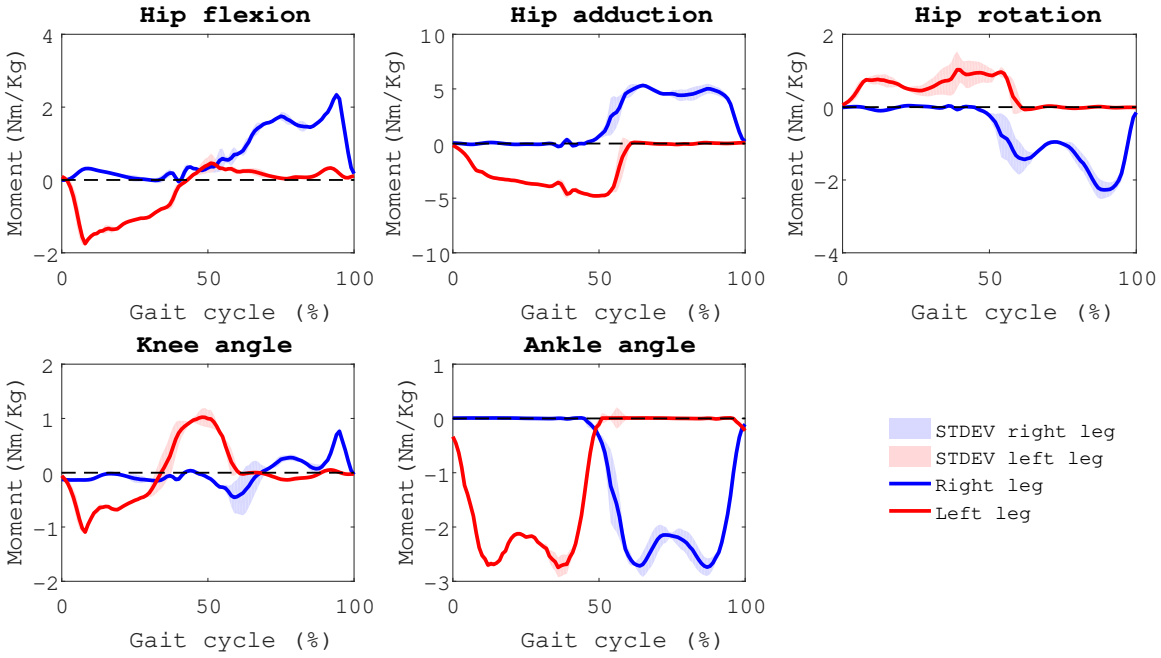


Figure 3.8: Normalized joint moments at the hip, knee and ankle for stair descent trials

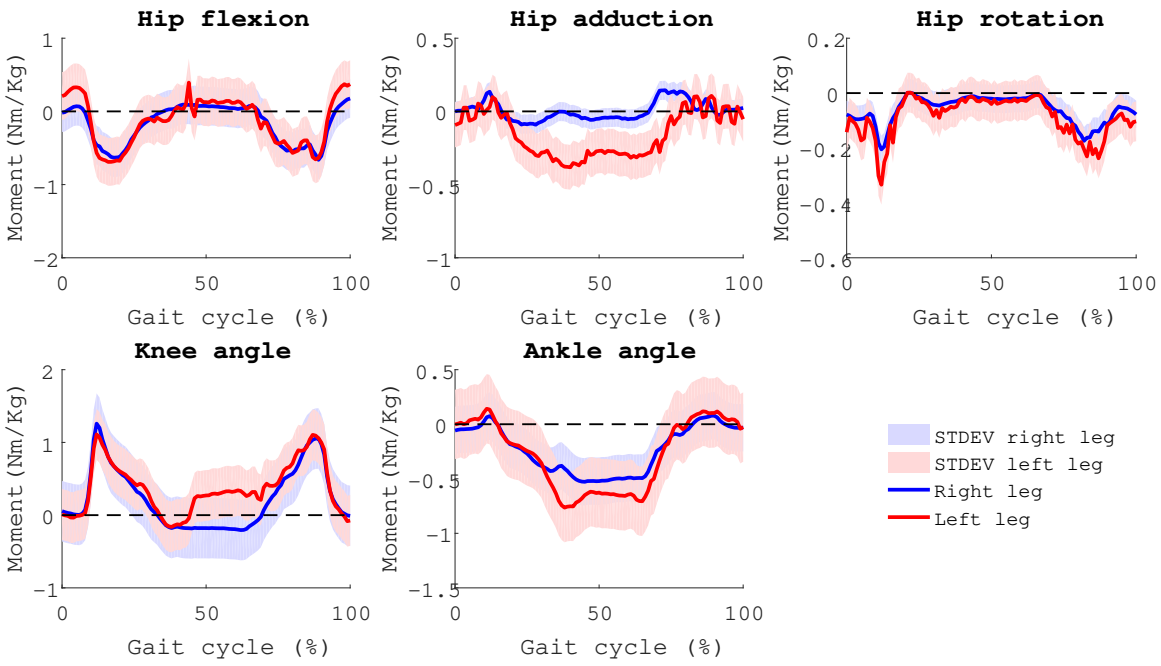


Figure 3.9: Normalized joint moments at the hip, knee and ankle for sit-to-stand-to-sit trials

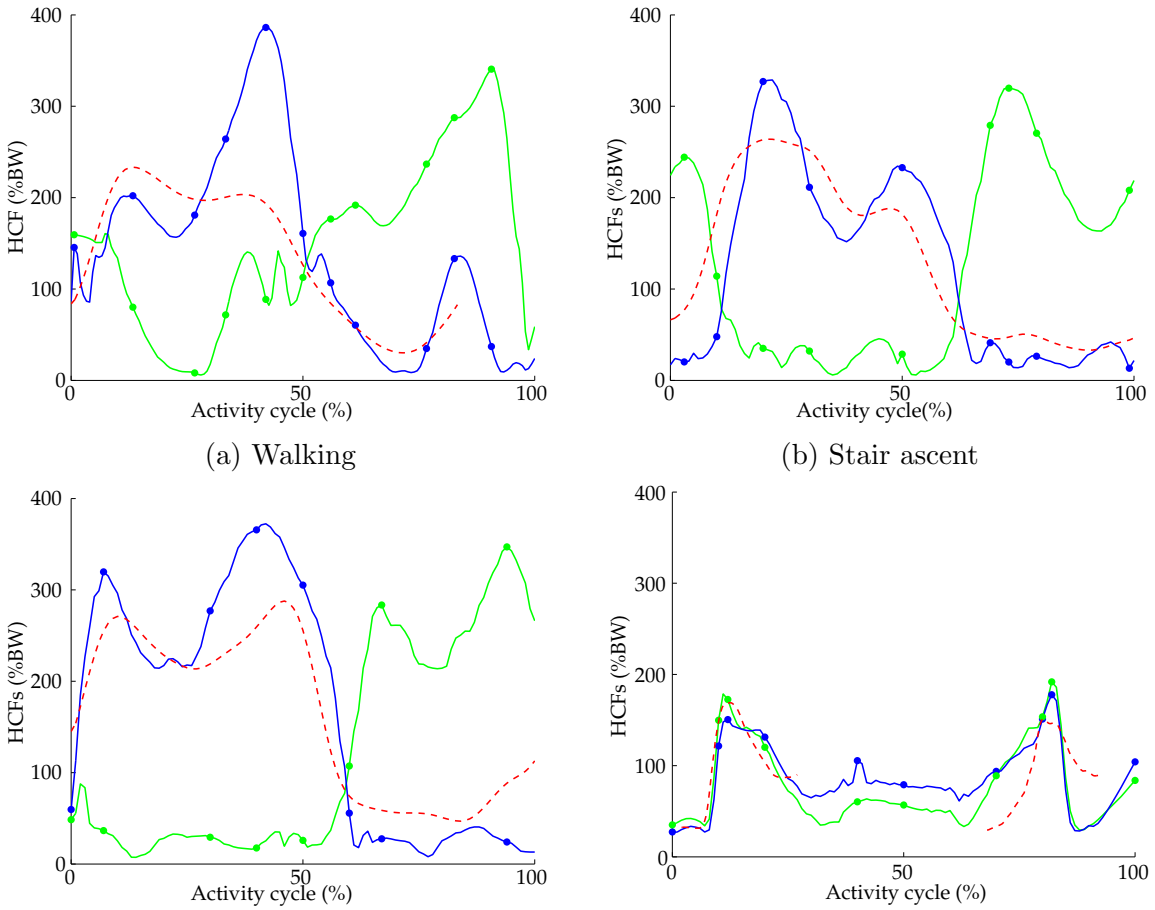
3.2.4 Hip contact forces and muscle forces

Muscle forces were estimated using the static optimization tool. The optimization problem was solved by minimising the sum of squared muscle activations for each frame of the kinematics under the constraints of joint moment equilibrium and physiological limits of the muscle forces (Modenese et al., 2011; Modenese and Phillips, 2012; Modenese et al., 2013). The hip joint contact forces were calculated from the muscle forces using the JointReaction tool available in OpenSim (Steele et al., 2012). All simulations were performed in OpenSim (Version 3.3) (Delp et al., 2007).

For each activity, the loads applied on the pelvis throughout the duration of the gait cycle (joint reaction forces and muscle forces) were determined in order to be applied to the FE model. The muscle insertion points' coordinates on the pelvis along with the direction and magnitude of each muscle force were extracted from the musculoskeletal model using the MuscleForceDirection (v1.0) plugin (van Arkel et al.,

2013; Phillips et al., 2015).

Reaction forces for both hips for all activities are shown in Figure 3.10. Data reported by Bergmann et al. (2001) for the same activities are included for comparison. The derived JCFs show a reasonable match for stair ascent, descent and sit-to-stand-to-sit. During walking, the second peak was higher compared to the range reported by Bergmann et al. (2001). Similar differences were reported by Modenese (2013) and Horsman et al. (2007) and this seems to be a consitent feature in musculoskeletal modelling predictions using static optimisation. This difference can be justified by the magnitude of the hip joint flexor moments calculated for the current model being greater than the analogous moments in the Bergmann et al. (2001) dataset (Heller et al., 2001).



(a) Walking

(b) Stair ascent

(c) Stair descent

(d) Sit-to-stand and stand-to-sit

Figure 3.10: Hip JCFs derived from the musculoskeletal model for cycles of (a) walking, (b) stair ascent, (c) stair descent and (d) sit-to-stand and stand-to-sit are shown in green lines for the right leg and blue lines for the left leg. Hip JCFs recorded and reported by Bergmann et al. Bergmann et al. (2001) for the right leg are shown in red dashed lines for each activity.

A limitation of the musculoskeletal framework in the context of its use in the next Chapters is that the muscle actuators contained in the musculoskeletal model do not take into account contraction dynamics and force-length-velocity relationships (Modenese et al., 2011). Although it was shown that these assumptions do not influence the predicted outcome for walking (Anderson and Pandy, 2001), they might have an impact on other activities.

3.3 Finite element model development

3.3.1 Geometry definition

An ethically obtained computed tomography (CT) scan (399×3 mm thick slices, 512×512 pixels, 0.91 mm/pixel) of a cadaveric pelvis and lower limbs (Male, age: 55, weight: 94.3 kg, height: 188 cm) provided by the Royal British Legion Centre for Blast Injury Studies of Imperial College London was processed in Mimics (Materialise, Leuven, Belgium) to generate a 3D surface of the two innominates and sacrum. The surface was imported in 3-matics (Materialise, Leuven, Belgium) and meshed with a maximum allowable edge length of 4 mm, resulting in a volumetric mesh composed of 377,362 four noded tetrahedral elements with an average edge length of 3.76 mm. The geometry of pelvis was not mirrored with respect to the sagittal plane as the musculoskeletal model did not predict symmetric results for the two sides of the pelvis. In addition, the CT scan from which the model was derived did not have a symmetric density distribution (3.13).

3.3.2 Structural and continuum base models

For structural modelling, the external surface of the mesh was used to define three-noded linear triangular shell elements, representing cortical bone. These were arbitrarily assigned an initial thickness of 0.1 mm. The internal nodes were used to define two-noded truss elements connecting each node to its nearest 16 neighbouring nodes. The trusses were arbitrarily assigned an initial radius of 0.1 mm. The resulting network is taken to represent trabecular bone. The initial minimum connectivity of each node was 16, with a maximum of 62 and mean value of 21.32. Previous work in the research group has shown that a nodal connectivity of 16 provides a sufficient range of element directionalities to enable trabecular trajectories to develop during adaptation (Villette, 2016).

The base mesh consisted of 33,466 cortical shell elements (12,601 for each innominate and 8,264 for the sacrum) and 588,028 trabecular truss elements (247,268 for each innominate and 93,492 for the sacrum). A transverse slice of the base structural mesh is shown in Figure 3.11. The initial structural model was generated from the tetrahedral mesh using MATLAB (The MathWorks Inc., USA). The shell and truss elements were assigned linear isotropic material properties with Young's modulus and Poisson's ratio values of E=18,000 MPa and ν=0.3 respectively (Turner et al., 1999; Anderson et al., 2005; Phillips et al., 2007).

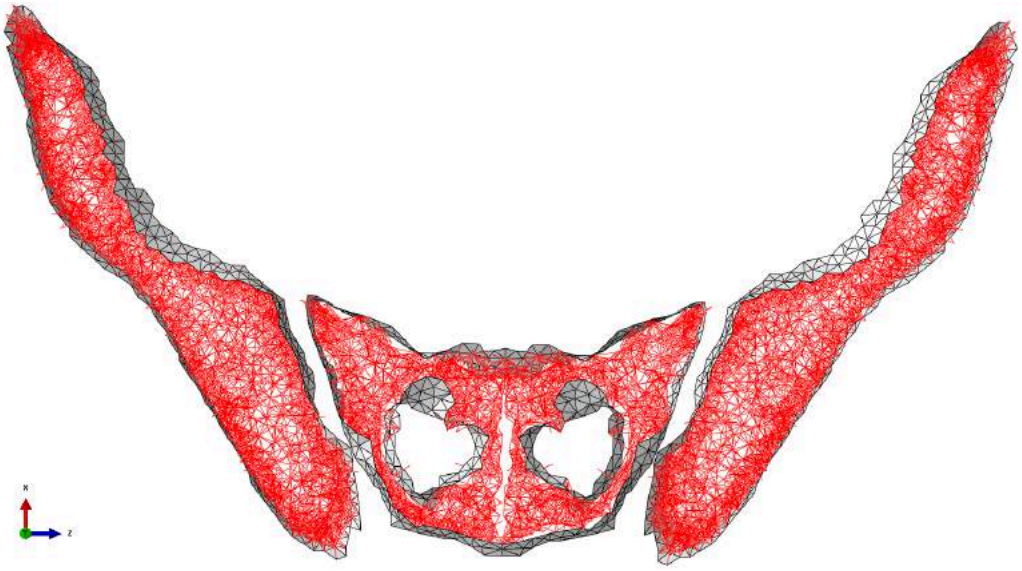


Figure 3.11: Transverse 2.5 mm slice of the pelvis for the base FE model. Shell elements representing cortical bone are shown in grey; truss elements representing trabecular bone are shown in red.

3.3.3 Ligaments and joints modelling

As described in Chapter 2, §2.1, the three pelvic bones are joined together by a set of strong joints and ligaments to stabilise the pelvic ring. The sacroiliac and pubic joints are composed of ligament and cartilage to ensure mechanical resistance in tension and compression, respectively. The joints and ligaments were modelled using truss elements. Anatomical attachment areas for each ligament and joint were visually defined on the mesh as node sets, based on descriptions in literature (Phillips

et al., 2007; Hammer et al., 2009, 2010; Moore et al., 2015). Truss elements were constructed between pairs of node sets by attaching each node in one set with the closest node in the corresponding set. Truss elements representing the joints were set to provide resistance only in tension for the ligament component and only in compression for the cartilage component. The ligaments and joints are shown in Figure 3.12.

The behaviour of ligaments is complex and models which aim to capture their biphasic and viscoelastic nature focus on soft tissue behaviour or joint mechanics (Suh and Bai, 1998; Almeida and Spilker, 1998; Ehlers and Markert, 2001), rather than the behaviour of the pelvis as a whole. Ligaments included in previous pelvic models were either assigned linear elastic material properties (Phillips et al., 2007; Dawson et al., 1999) or modelled as hyperelastic components (Li et al., 2006, 2007; Majumder et al., 2007; Leung et al., 2009).

Given that the focus of this study is to analyze the structural behaviour of the pelvic construct as a whole and nonlinear modelling of the ligaments would result in an increased computational cost, they were assigned linear elastic material properties and were modelled using truss elements by connecting each surface node on an origin area to the closest node on the corresponding insertion area. The material properties of each ligament were derived from previously published data on ligament stiffnesses (Zheng et al., 1997; Dakin et al., 2001) which were used in another computational study (Phillips et al., 2007). The Young's moduli were derived from the stiffnesses, with E being Young's modulus, k the stiffness of the ligament, l the length and A the origination area of the ligament (Eq. 3.1).

$$E = \frac{kl}{A} \tag{3.1}$$

$$r = \sqrt{\frac{A}{\pi N_l}} \tag{3.2}$$

The radius of each truss element, r, was calculated based on the origination area of the

ligaments, A, and the number of truss elements, N_l, forming each ligament (Eq. 3.2). In the case of the pubic symphysis and sacroiliac joints, truss elements taking only tension were used to model the pubic and sacroiliac ligaments, and truss elements taking only compression were used to model the cartilage contained in the joints. As ligaments do not have compressive stiffness, they were overlayed with identical sets of elements given a low Young's modulus value of 0.1 MPa in compression to ensure numerical stability. Similarly, elements representing cartilage were overlayed with identical elements given a low Young's modulus of 0.1 MPa in tension to ensure numerical stability. The tensile and compressive material properties assigned to the ligaments and cartilage are shown in Tables 3.1 and 3.2.

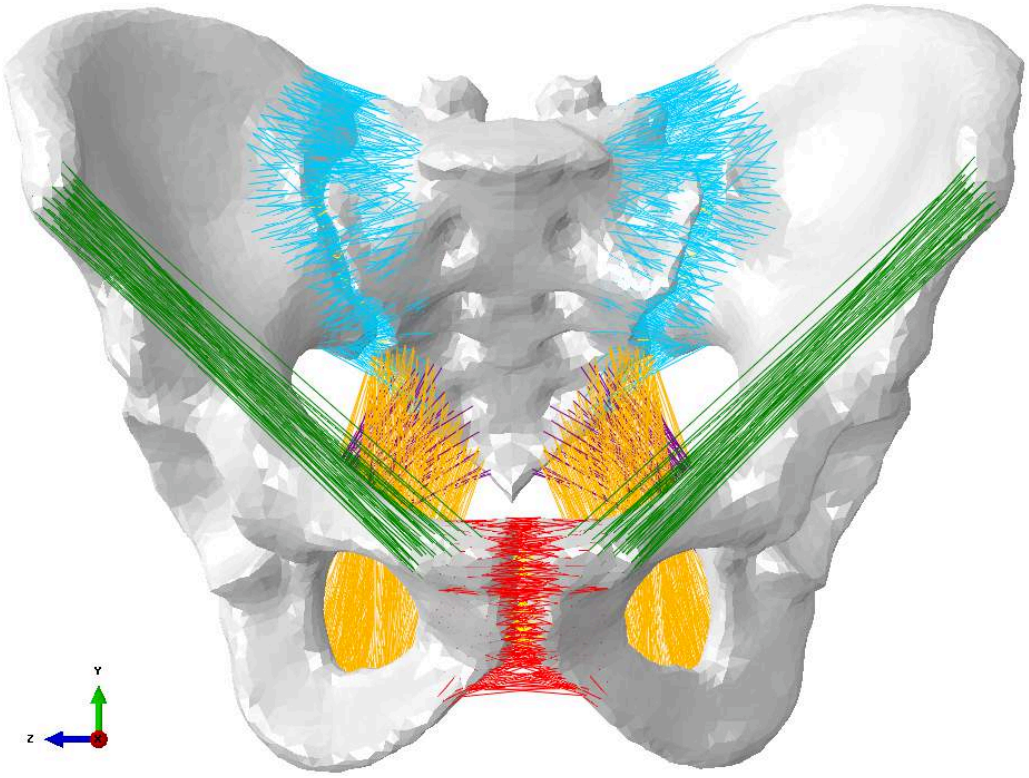


Figure 3.12: Pelvis model with ligaments included: sacroiliac ligaments in blue, pubic ligament in red, sacrospinous ligaments in yellow, sacrotuberous ligaments in purple and inguinal ligaments in green

Ligament	k (N/mm)	l (mm)	A (mm^2)	N_l	E (MPa)	r (mm)
Sacroiliac	5000	27.8	4824.2	918	28.8	0.72
Pubic	1000	27.6	2732.7	582	15.9	0.68
Inguinal	250	147.6	303.8	64	121.5	0.69
Sacrospinous	1500	68.1	647.8	102	105.1	0.80
Sacrotuberous	1000	125.6	1764.5	344	106.8	0.73

Table 3.1: Material properties of the ligaments in tension (taken from Phillips et al. (2007)), with k the ligament stiffness, l the length of the ligament, A the origination area of the ligament, N_l the number of elements forming each ligament, E Young's modulus and r the radius of each truss element.

Cartilage	k (N/mm)	l (mm)	A (mm^2)	N_l	E (MPa)	r (mm)
Sacroiliac	3000	8.5	2191.7	328	11.6	0.82
Pubic	1500	7.7	728.4	176	10.1	0.64

Table 3.2: Material properties of the cartilage in compression (taken from Phillips et al. (2007)), with k the cartilage stiffness, l the length of the cartilage, A the origination area of the cartilage, N_l the number of elements forming each cartilage, E Young's modulus and r the radius of each truss element.

3.4 Development of CT scan derived continuum model

A subject specific FE model was derived from the CT scans used to generate the geometries of the adaptive models. The geometry extracted from imaging data was used to develop a continuum FE model comprising of linear tetrahedral elements with varying material properties using Bonemat (Taddei et al., 2007). Assuming a linear relationship between the Hounsfield values in the scans and bone ash density (Les et al., 1994), bone ash density distribution was derived from the medical images. Young's modulus for each element was derived from the ash density using a power relationship, shown in Equation 3.3 (Keller, 1994).

$$E = 10.5\rho_{ash}^{2.29} \tag{3.3}$$

In the FE model, Young's modulus values for each element were discretised into 100 materials to maintain the computational efficiency. Young's modulus distribution on one hip bone is shown in Figure 3.13.

A potential limitation of this model is the lack of calibration of the CT data prior to assigning varying material properties based on Hounsfield values. Furthemore, the use of a clinical CT scan reduces the potential of capturing bone architecture particularities that can potentially play an important role in dictating the mechanical behaviour of the model.

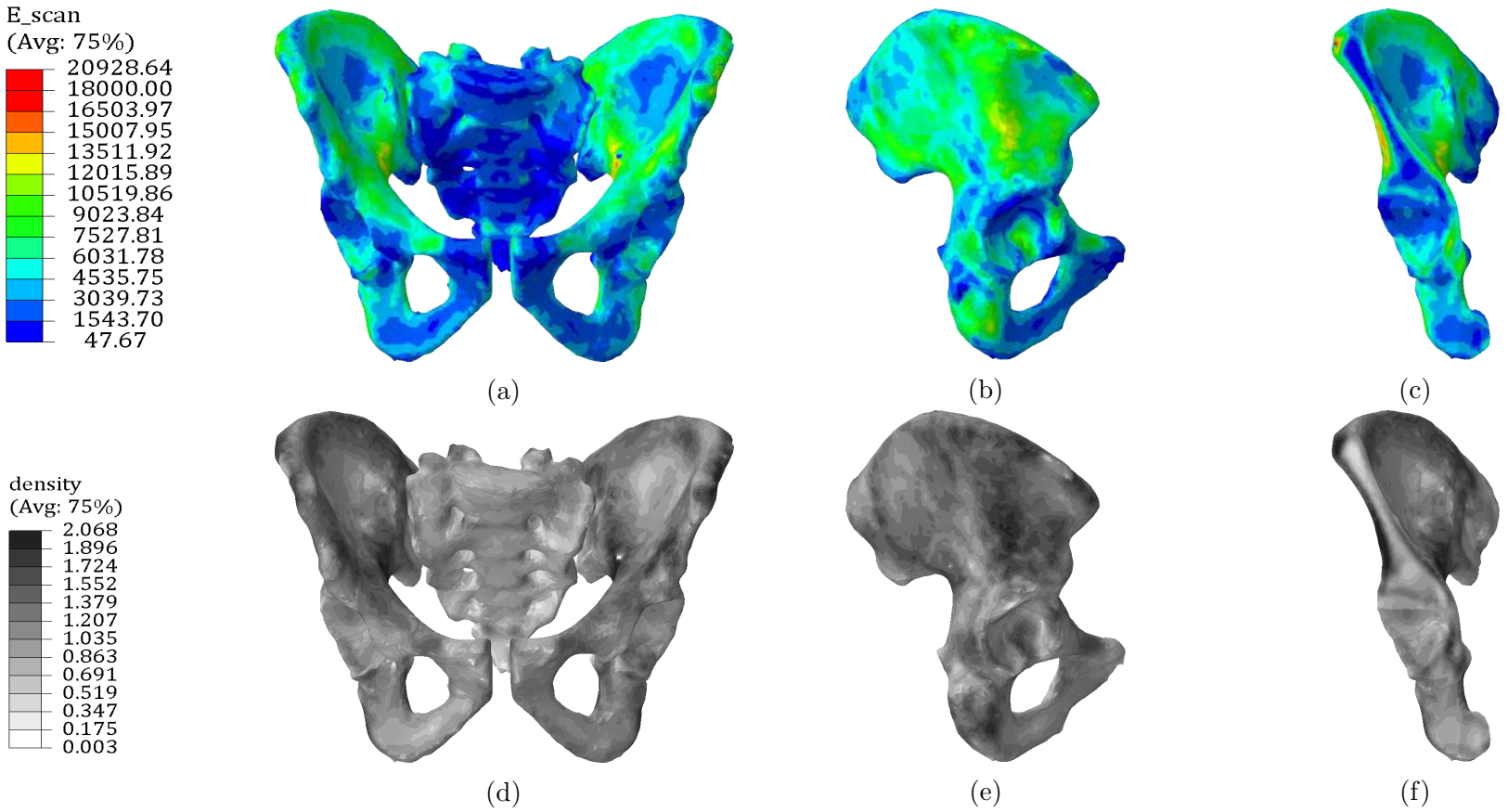


Figure 3.13: Young's modulus (a, b, c) and density (d, e, f) distribution for the CT scan derived model.

4

Predictive structural modelling of the pelvic construct

The author wishes to thank Claire Villette for providing the adaptation algorithm used in this chapter.

Note: A large portion of this chapter has been published in the journal article: Zaharie, D. T., & Phillips, A. T. (2018). Pelvic construct prediction of trabecular and cortical bone structural architecture. *Journal of Biomechanical Engineering*, 140(9), 091001.

Chapter 2 highlighted a lack of information on the bone architecture of the pelvis in contrast to long bones such as the femur. This chapter presents the framework used to develop a structural model of the pelvic construct that was adapted to a physiological loading regime corresponding to the most common daily physical activities, described in Chapter 3. The resulting structures of the converged model adapted to the full loading regime and individual activities are investigated qualitatively along with a quantitative comparison between the model and a continuum model derived from the CT imaging data. The modelling framework is shown in Figure 4.1.

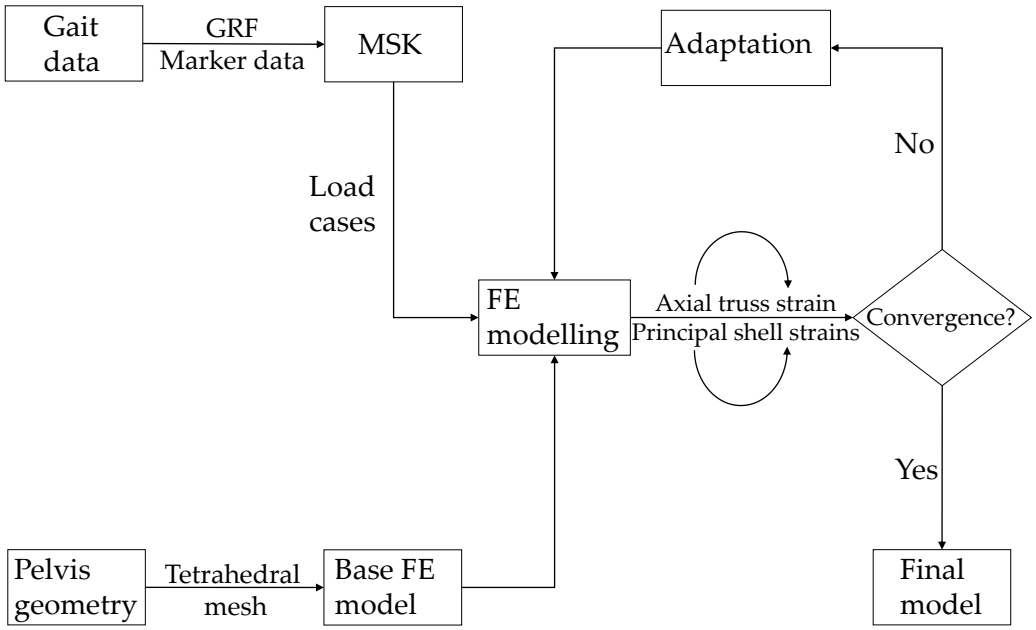


Figure 4.1: Modelling framework used to develop an adaptive structural model of the pelvic construct

4.1 Methods

4.1.1 Finite element modelling

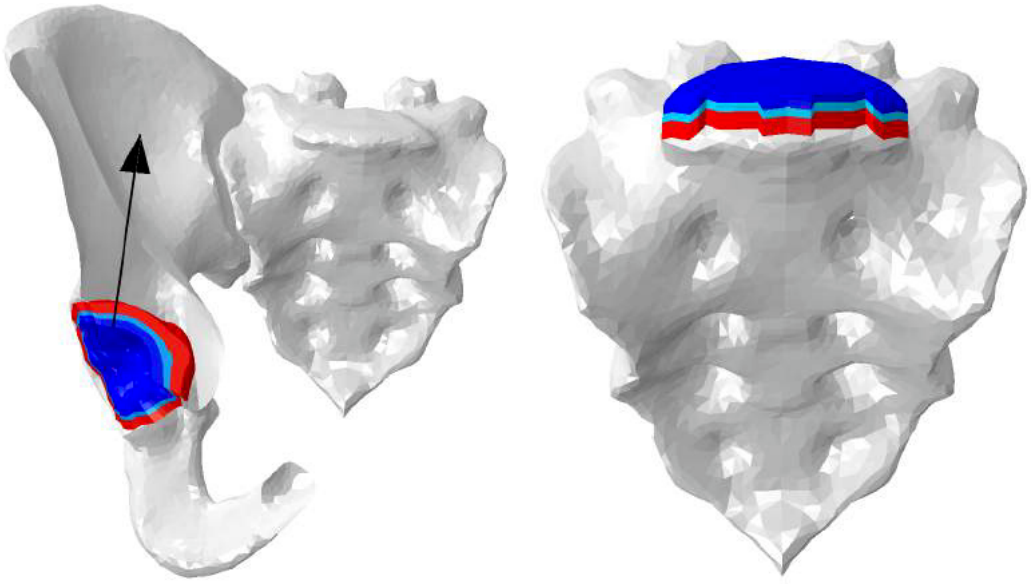
4.1.1.1 Loading

The muscle forces obtained from the musculoskeletal model were applied as point loads distributed on the closest three surface nodes to each muscle insertion point, extracted from the musculoskeletal model (§3.2). The hip joint contact forces and the inertial loads were calculated at the joint centres and the centre of mass of the pelvic segment. In addition, for sit to stand and stand to sit, the reaction load from the seat was applied at the inferior ischium. To spread these loads over the corresponding bone surface, they were applied using 'load applicators' and an 'inertia applicator', as they allow for a reduction in CPU time in comparison to modelling contact at each joint.

The load applicators were built by first projecting each node on the surface of the hip joint along the direction defined by the point and the joint centre four times with a distance of 2 mm between them. Subsequently, four layers of six-noded linear continuum wedge elements were created using the newly generated nodes and the initial surface nodes. The overall structure was taken to represent the bone-cartilage-bone interface at the hip joint. Thus, the bottom two layers (closest to the bone surface) were assigned E=10 MPa and ν=0.49, representative of cartilage. The outermost 2 layers were assigned stiffnesses of 10 MPa (ν=0.3) and 500 MPa (ν=0.3), respectively. The material properties were adopted based on a sensitivity study performed by Villette (2016).

The loads derived from the musculoskeletal model were applied to the outside node closest to the direction of the load vector for each load case, as shown in Figure 4.2a. The load applicators implemented enable an appropriate distribution of the hip

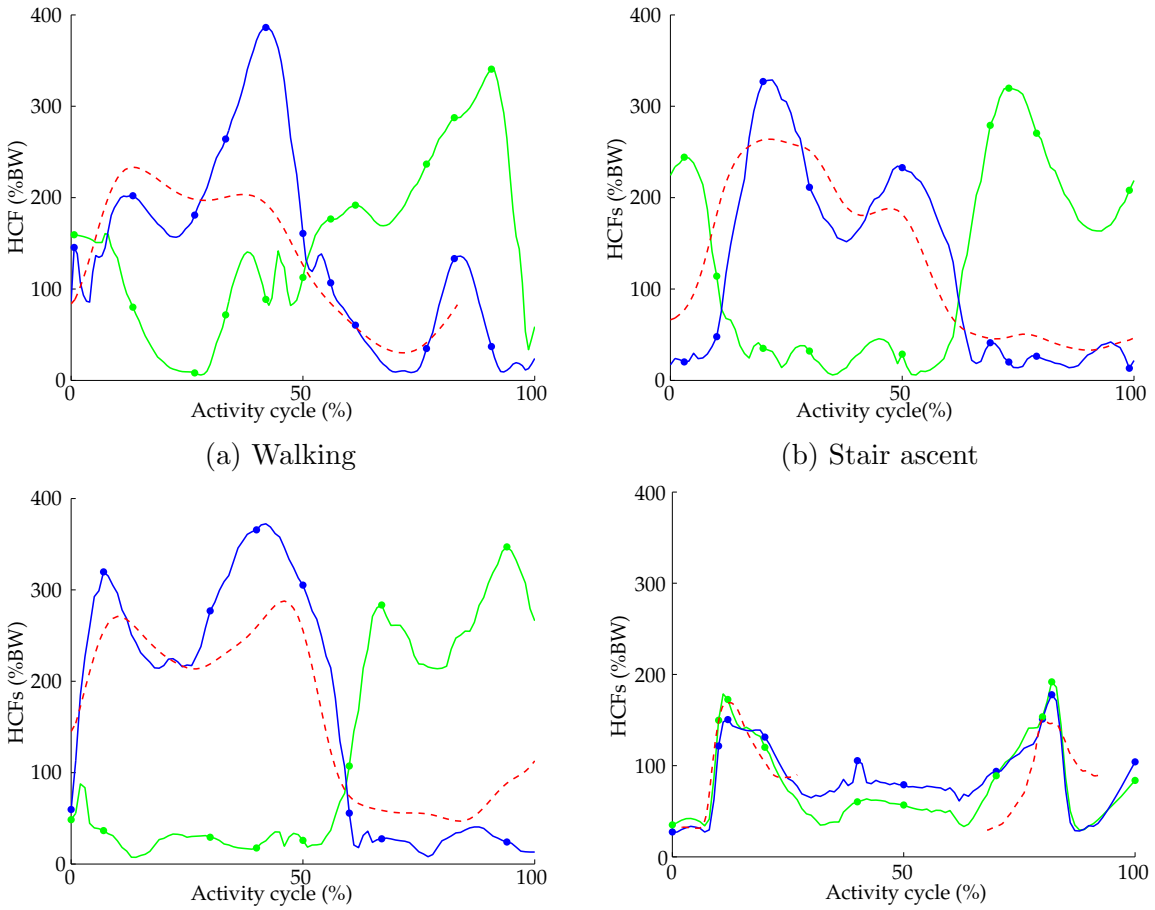
contact force across the acetabular surface (Villette, 2016). An 'inertia applicator' was included to spread the inertial load of the pelvis over the whole construct. It was designed by linking a node positioned at the centre of mass of the pelvis to every node of the model using truss elements of circular cross section with a radius of 0.1 mm and low stiffness (E=0.1MPa, ν=0.3) to prevent artificial stiffening of the model. The inertial loads derived from the musculoskeletal simulations were applied at the control node.



(a) (b)

Figure 4.2: (a) Load applicator at the hip and (b) fixator at the top of the sacrum. The elements representing the bone are shown in light grey, with the two layers of soft elements in red and the two layers of stiffer elements in blue (dark blue represents the stiffest layer of elements in the hip applicator). In addition, the black arrow illustrates the peak load applied on the hip joint during walking.

The load cases obtained from the musculoskeletal model were subsampled to maintain computational efficiency. The subset of frames were selected such that the difference between the integrated hip joint contact forces (JCF) for the full set of frames and the selected set of frames was lower than 5%. The joint contact forces and the subsampled set of values are shown in Figure 4.3. The resulting 39 load cases were applied in consecutive steps to the FE model.



(a) Walking

(b) Stair ascent

(c) Stair descent

(d) Sit-to-stand and stand-to-sit

Figure 4.3: Hip JCFs derived from the musculoskeletal model for cycles of (a) walking, (b) stair ascent, (c) stair descent and (d) sit-to-stand and stand-to-sit are shown in green lines for the right leg and blue lines for the left leg. The frames selected for each activity to be used in the FE simulations are highlighted using solid circles. Hip JCFs recorded and reported by Bergmann et al. (2001) for the right leg are shown in red dashed lines for each activity.

4.1.1.2 Boundary conditions

To ensure numerical stability, a boundary condition was enforced at the sacral joint. The reaction force components at the sacral joint predicted by the FE model and the musculoskeletal model for the walking activity were found to be similar in magnitude (Figure 4.4). The differences in the magnitude of the forces can be attributed to the deformability of the FE model. Similar to the load applicators, four layers of wedge

elements were constructed on the top of the sacrum, representing the L5S1 interface between the lumbar spine and the sacrum. The construct facilitating the application of the boundary conditions at the sacrum is shown in Figure 4.2b. The two layers closer to bone were assigned a Young's modulus of 10 MPa (ν=0.49) to represent cartilage, while the outermost two were assigned stiffnesses of 10 MPa (ν=0.3) and E=500 MPa (ν=0.3). The boundary conditions of the model were applied at the top of the sacrum by constraining the nodes on the outermost layer of the construct in the three translational DOF. This was done to avoid fixing nodes on the bone, which would potentially lead to stress concentrations developing over the surface of the sacrum.

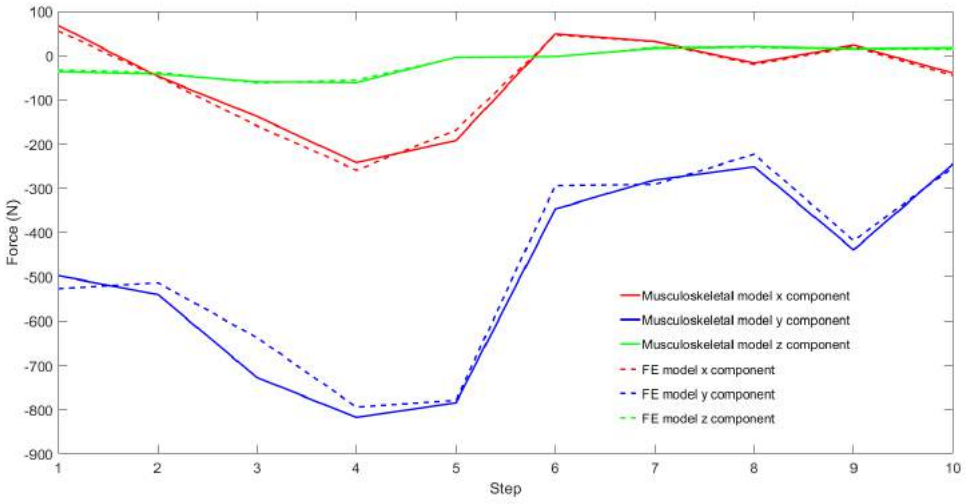


Figure 4.4: Comparison between reaction forces at the sacrum reported by the musculoskeletal model and FE model for the walking frames.

4.1.2 Adaptation algorithm

Based on the Mechanostat principle (Frost, 2003), the base structural pelvis model was subjected iteratively to the load cases obtained from the musculoskeletal model for the activities mentioned in the previous section (methodology adapted from Phillips et al. (2015)). At each iteration, the thickness of each shell element and cross-sectional area of each truss element were adjusted according to a strain criterion. The iterative process was implemented using MATLAB and Python (Python Software Foundation, Beaverton, OR, USA) scripts, and the succesive FE models were run using the Abaqus/Standard solver (Dassault Systèmes Simulia, Johnston, RI, USA) until convergence was achieved.

For each iteration i, the absolute maximum normal strain value for the j^{th} truss element and j^{th} shell element over all load cases ($\lambda = 1, ..., n$) was defined using Equations 4.1 and 4.2, respectively.

$$|\varepsilon_{i,j}|_{\max} = \max(|\varepsilon_{11,j,\lambda}|) \tag{4.1}$$

with $\varepsilon_{11,j,\lambda}$ being the axial strain in the j^{th} truss element for load case λ.

$$|\varepsilon_{i,j}|_{\max} = \max(|\varepsilon^{t}_{\max,j,\lambda}|, |\varepsilon^{t}_{\min,j,\lambda}|, |\varepsilon^{b}_{\max,j,\lambda}|, |\varepsilon^{b}_{\min,j,\lambda}|) \tag{4.2}$$

with $\varepsilon^{t}_{\max,j,\lambda}, \varepsilon^{t}_{\min,j,\lambda}, \varepsilon^{b}_{\max,j,\lambda}, \varepsilon^{b}_{\min,j,\lambda}$ being the maximum and minimum principal strains in the top and bottom surfaces of the j^{th} shell element for load case λ.

The strain ranges associated with, bone resorption, the lazy zone and bone apposition (Frost, 2003; Aamodt et al., 1997; Phillips, 2012) are given in Equation 4.3:

$$\phi_{i,j} = \begin{cases} 1, & \text{if } 0 \leq |\varepsilon_{i,j}|_{\max} < 1000\mu\varepsilon \qquad \text{(Bone resorption)} \\ 0, & \text{if } 1000 \leq |\varepsilon_{i,j}|_{\max} \leq 1500\mu\varepsilon \qquad \text{(Lazy zone)} \\ 1, & \text{if } |\varepsilon_{i,j}|_{\max} > 1500\mu\varepsilon \qquad \text{(Bone apposition)} \end{cases} \tag{4.3}$$

For the subsequent iteration $(i+1)$, the cross-sectional area of the j^{th} truss element $(A_{i+1,j})$ was modified using Equation 4.4 based on the value of $\phi_{i,j}$. The thickness of the j^{th} shell element $(T_{i+1,j})$ was modified using Equation 4.5. The target strain, ε_t, was given a value of 1250 $\mu\varepsilon$, corresponding to the middle of the lazy zone.

$$A_{i+1,j} = \begin{cases} A_{i,j}\dfrac{|\varepsilon_{i,j}|_{\max}}{\varepsilon_t}, & \text{if } \phi_{i,j} = 1 \\ A_{i,j}, & \text{if } \phi_{i,j} \neq 1 \end{cases} \tag{4.4}$$

$$T_{i+1,j} = \begin{cases} \frac{T_{i,j}}{2}\left(1 + \dfrac{|\varepsilon_{i,j}|_{\max}}{\varepsilon_t}\right), & \text{if } \phi_{i,j} = 1 \\ T_{i,j}, & \text{if } \phi_{i,j} \neq 1 \end{cases} \tag{4.5}$$

The adaptation equations for the two types of elements were defined such that trabecular bone adapts in preference to cortical bone. This is important in particular during the first few iterations as it prevents the oscillation of the shell elements thicknesses. In addition, truss elements with a strain lower than 250 $\mu\varepsilon$ were considered to be in the dead zone.

To increase computational efficiency, the thicknesses of the shell elements were linearly discretised into 256 categories. Based on CT scans, cortical thickness throughout the pelvis has been reported to vary between 0.5 and 4 mm (Dalstra et al., 1995b; Anderson et al., 2005; Zhang et al., 2010). The thickness range for the shell elements in this model was set between 0.1 mm and 5 mm as for a thickness lower than 0.5 mm the accuracy of clinical CT scanners decreases, meaning that there could be areas with a cortical thickness lower than 0.5 mm which would not be captured due to the image resolution (Prevrhal et al., 1999).

Similarly, the cross-sectional areas of the truss elements were linearly discretised in 255 categories. The range for the truss elements was set between $\pi(0.1)^2\text{mm}^2$ and $\pi(2)^2\text{mm}^2$, which is considered reasonable to characterise trabecular bone at mesoscale level (Phillips et al., 2015; Nägele et al., 2004). In addition, a 256^{th} category with a cross-sectional area of $\pi(0.001)^2\text{mm}^2$ was added to allow for effective removal

of the elements in the dead zone while maintaining numerical stability. The elements in the dead zone were assigned a radius of 1 μm, making their stiffness contribution to the model negligible. This enabled regeneration of the elements in the dead zone as they could be reassigned in one of the other 255 categories at a later iteration.

4.1.3 Comparison with a CT scan derived continuum pelvis model

The response of the CT scan derived model described in Chapter 3, §3.4 to a simple loadcase representing a vertical two-legged standing position was compared to the behaviour of the optimised structural model in an analogous case. As simulating the behaviour of the entire pelvic construct for a simple loading scenario was not necessary, both models were reduced to the right hemipelvis. Both models were subjected to a vertical load of $2kN$ applied at the acetabulum using the load applicator described in §4.1.1.1. The boundary conditions applied to the model consisted of restraining the sacroiliac and pubic joints surfaces in all degrees of freedom (Figure 4.5). In addition to the continuum elements in the CT scan derived model, shell elements identical to those used in the structural model were added and assigned a uniform thickness of 1 mm and a low Young's modulus (E=0.01 MPa). The purpose of including low stiffness shell elements was to provide a more robust way of comparing the resulting surface strains between the models.

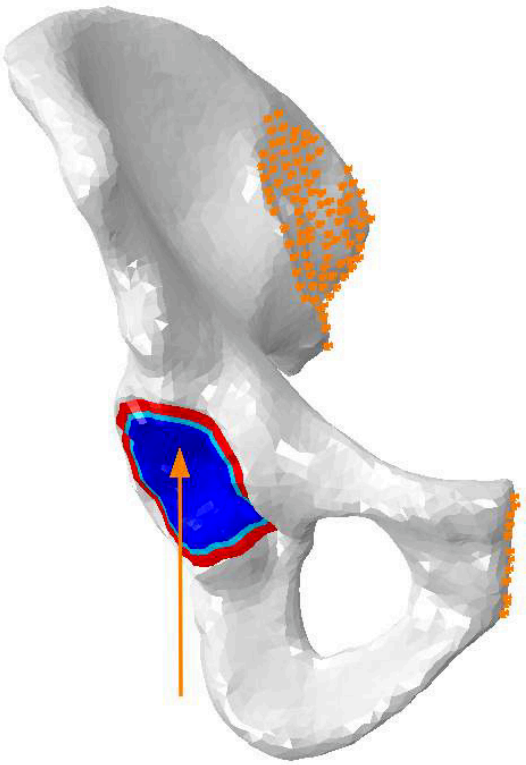


Figure 4.5: Loading conditions applied on the adapted structural model and the scan derived continuum model of the right pelvic innominate

4.2 Results

4.2.1 Converged model structure

The structural model converged after 39 iterations. Cortical thickness and trabecular radius distributions are shown in Figure 4.6. Cortical thickness was highest at the superior sacrum, along the gluteal surface, around the sacroiliac joint, superior pubic ramus, posterior iliac crest and greater sciatic notch. Cortical bone had a thickness between 0.1mm and 0.5mm at the ischium, acetabulum, pubic tubercle, iliac fossa and posterior superior iliac spine. The results for the cortical thickness distribution across the hip bone compare well with the study published by Anderson et al. (2005).

Clusters of trabecular elements with large radii were found at the superior sacrum, supra acetabular region, pubic tubercle and greater sciatic notch. High trabecular density in these regions was also reported in a previous study (Dalstra et al., 1995a). Regions with a small number of active elements were found at the iliac fossa, ischial tuberosity and inferior sacrum (Figure 4.6). Distinct trajectories were formed in the supra acetabular region (Figure 4.7a, c), around the sacroiliac joint extending from the ilium to the sacrum (Figure 4.7d-f) and along the direction between the two locations mentioned above (Figure 4.7b-c).

To obtain a more comprehensive view of the optimised bone architecture, a number of transverse slices of the model were qualitatively compared to the corresponding CT scans used to define the initial surface geometry, as shown in Figure 4.8. Across the acetabulum, the model predicted a thickening of the cortex at the ascending pubis ramus and a thin cortex along the acetabular notch, which is in agreement with the CT scan (Figure 4.8a and 4.8b). Another similarity can be found along the inferior gluteal line, where the model showed a distinct thickening of the cortex, which is also present in the scan (Figure 4.8g-h). The region around the sacroiliac joint compares well with the scan for both the sacrum and the hip bones (Figure 4.8e-f). The main

discrepancies in terms of cortical thickness between the model and scan can be seen between the anterior superior iliac spine and anterior inferior iliac spine (Figure 4.8c-h), towards the greater sciatic notch (Figure 4.8g-h) and ischial body (Figure 4.8a-b). On the other hand, the areas mentioned have a higher trabecular density compared to the CT scan, meaning that the stiffness of the regions could still be considered similar to the scan. Although an attempt was made to quantitatively compare cortical bone thickness and trabecular bone structure, the resolution of the CT scan used in this study was not high enough to enable the comparison.

In terms of trabecular architecture, a number of trajectories were clearly formed. In the region surrounding the sacroiliac joint, thick trabecular elements were formed following trajectories which intersect both hip bones and the sacrum (Figure 4.7e-f). As a consequence, the highest trabecular density in the sacrum was found on the load-bearing S1 segment (Figure 4.7d-e), which is in agreement with previous findings (Peretz et al., 1998; Mahato, 2010). Another region with high trabecular density was identified above the acetabulum (Figure 4.7a-c). Given that the loads are transmitted from the hip joint towards the lumbar spine through the sacroiliac joint and sacrum, the presence of these trabecular trajectories seems justified.

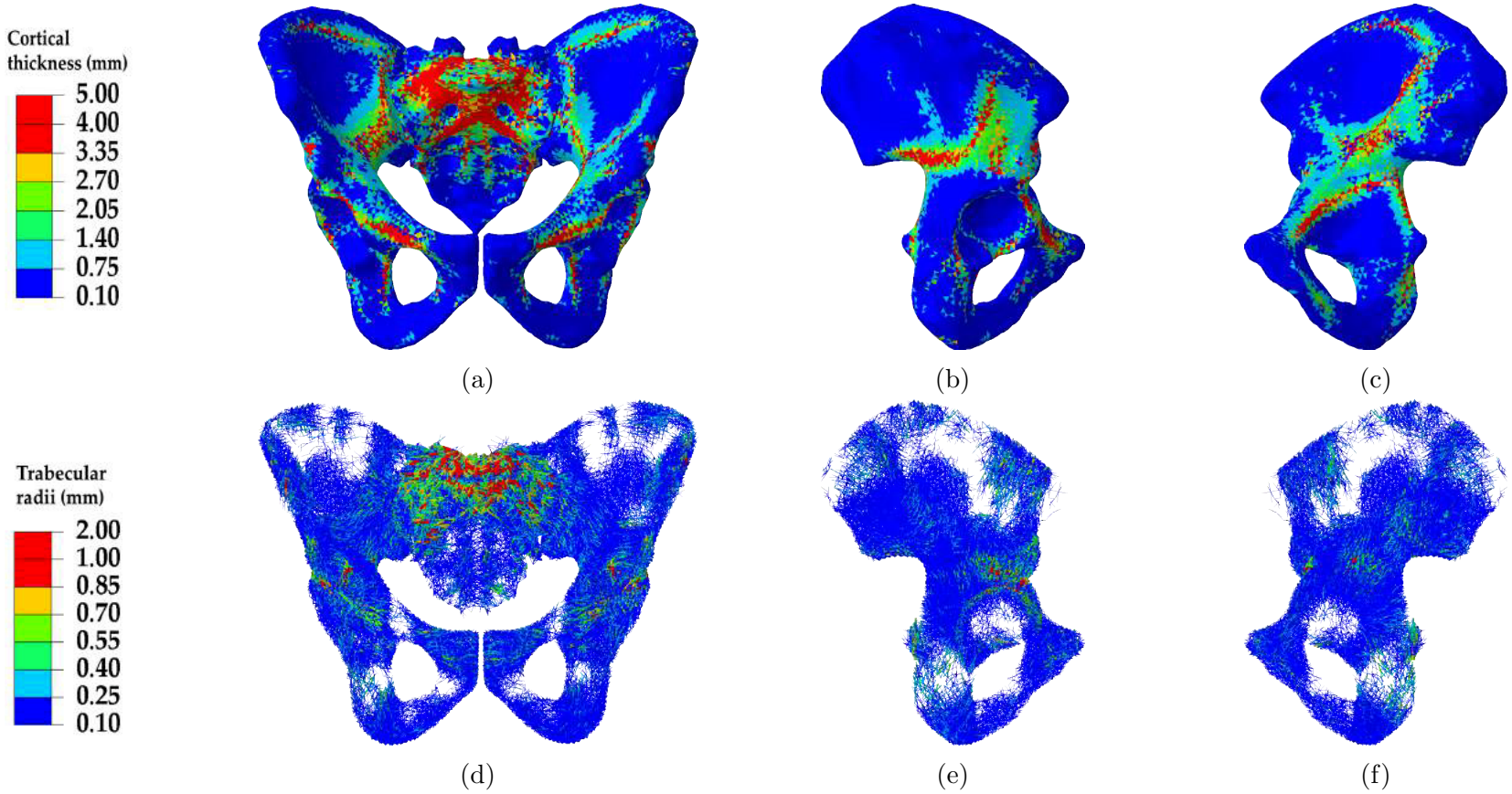


Figure 4.6: Converged structure for the full loading regime. Contours of position dependent cortical thickness ranging from 0.1 mm to 5 mm are shown in the top row: (a) frontal view of pelvis, (b) anterior and (c) medial views of the right innominate. Trabecular elements' radii distribution ranging from 0.1 mm to 2 mm is shown in the bottom row: (d) frontal view, (e) anterior and (f) medial views of the right innominate. Trabecular elements with a radius of 1 μm were excluded for clarity.

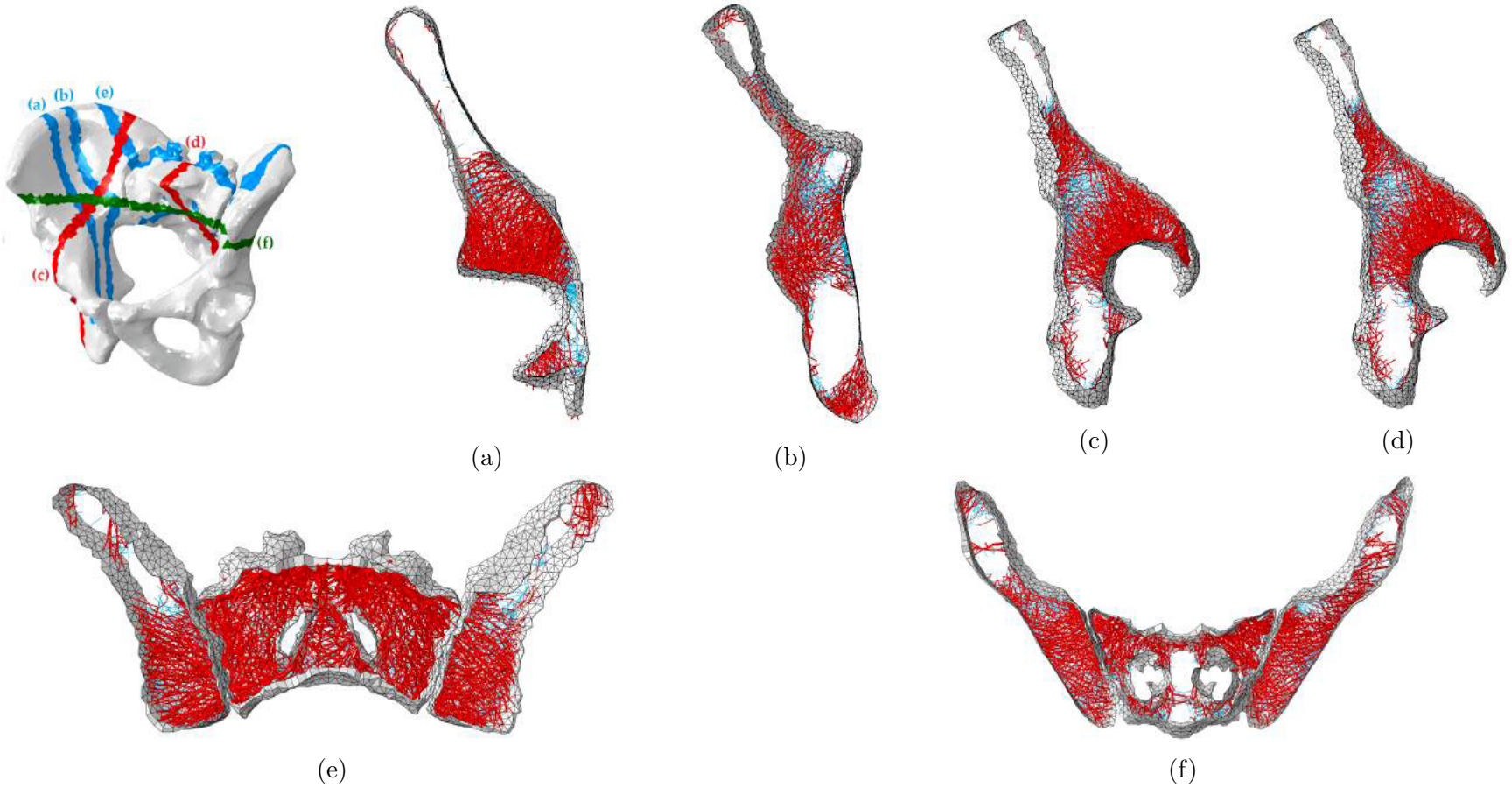


Figure 4.7: Selected 5 mm thick coronal (a, b, e), sagittal (c, d) and transversal (f) slices of the converged pelvic model illustrating the trabecular structure and cortical thickness. Truss elements with a radius > 0.1 mm are shown in red, with elements with a radius of 1 mm shown in blue. Elements with a radius of 1 μm are not shown for clarity.

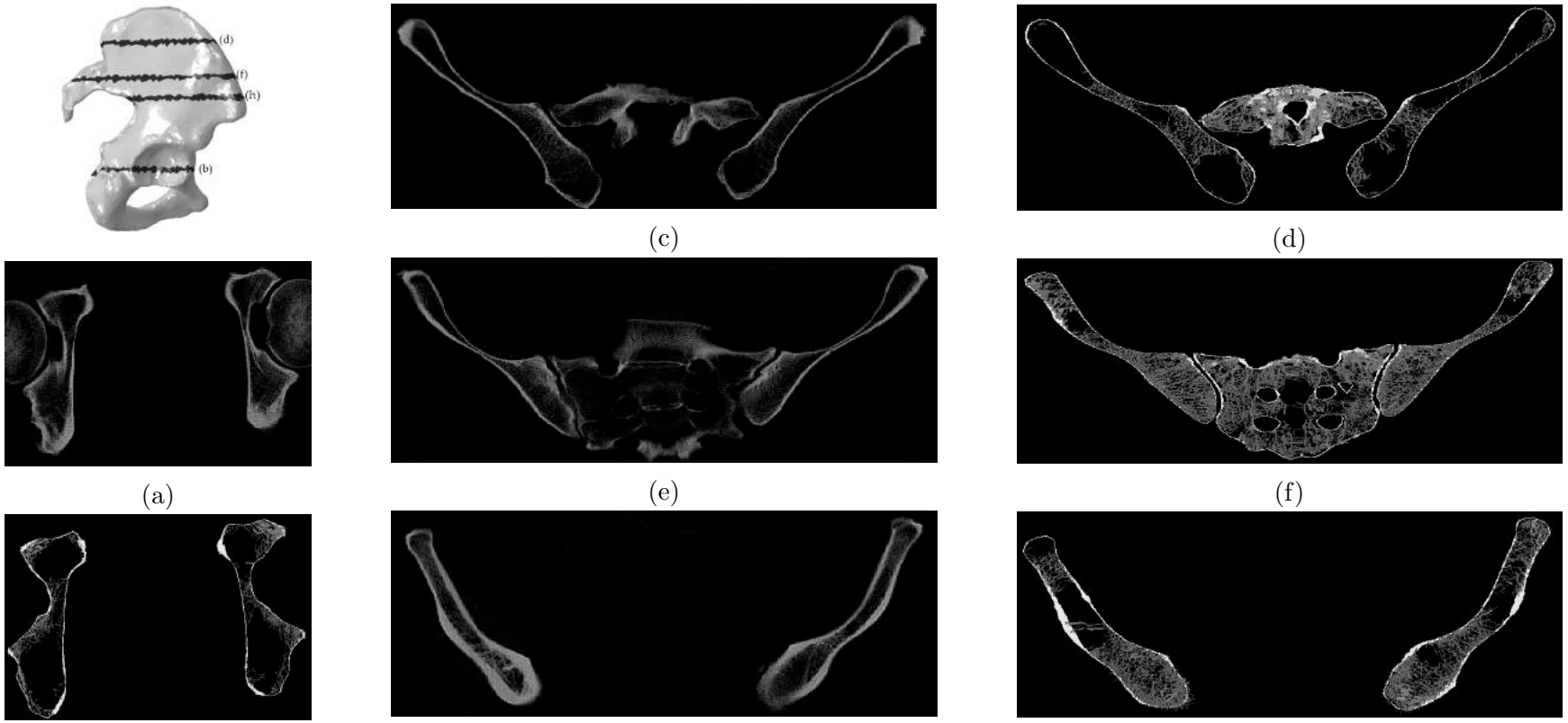


Figure 4.8: Figure illustrating transverse slices from the CT scans (a, c, e, g) shown along with corresponding slices of the pelvic model (b, d, f, h) generated using an in-house code developed in MATLAB. Shell elements and truss elements with a radius > 0.1 mm are shown in light grey. Truss elements with a radius of 0.1 mm appear in dark grey. Elements with a radius of 1 μm are not shown for clarity.

The influence of each physical activity on bone architecture is shown in Figure 4.9. For each activity modelled, the absolute maximum strain value occuring during the activity for each element was plotted as a colour intensity to highlight the influence of a given activity on the resulting bone morphology for the full loading regime. Strain distributions for each activity are shown in Figure 4.10. Walking was primarily responsible for the thickening of the cortex along the ischial spine, the inferior ramus of the pubis and the posterior part of the iliac fossa. The cortex development between the anterior inferior iliac spine and the iliac crest and along the superior pubic ramus was primarily influenced by stair ascent, while stair descent was the main factor in the thickening of the cortex accross the sacrum, between the anterior and posterior gluteal lines, at the ischium and along the posterior superior iliac spine. The increased trabecular structure present at the upper sacrum was influenced by both stair ascent and descent. Walking was mainly responsible for the appearance of trabecular structures along the superior pubic ramus, around the acetabulum, at the anterior inferior iliac spine and anterior gluteal line. The asymmetric distribution of activity influence can be attributed to the subject specific geometry and gait used in the musculoskeletal model.

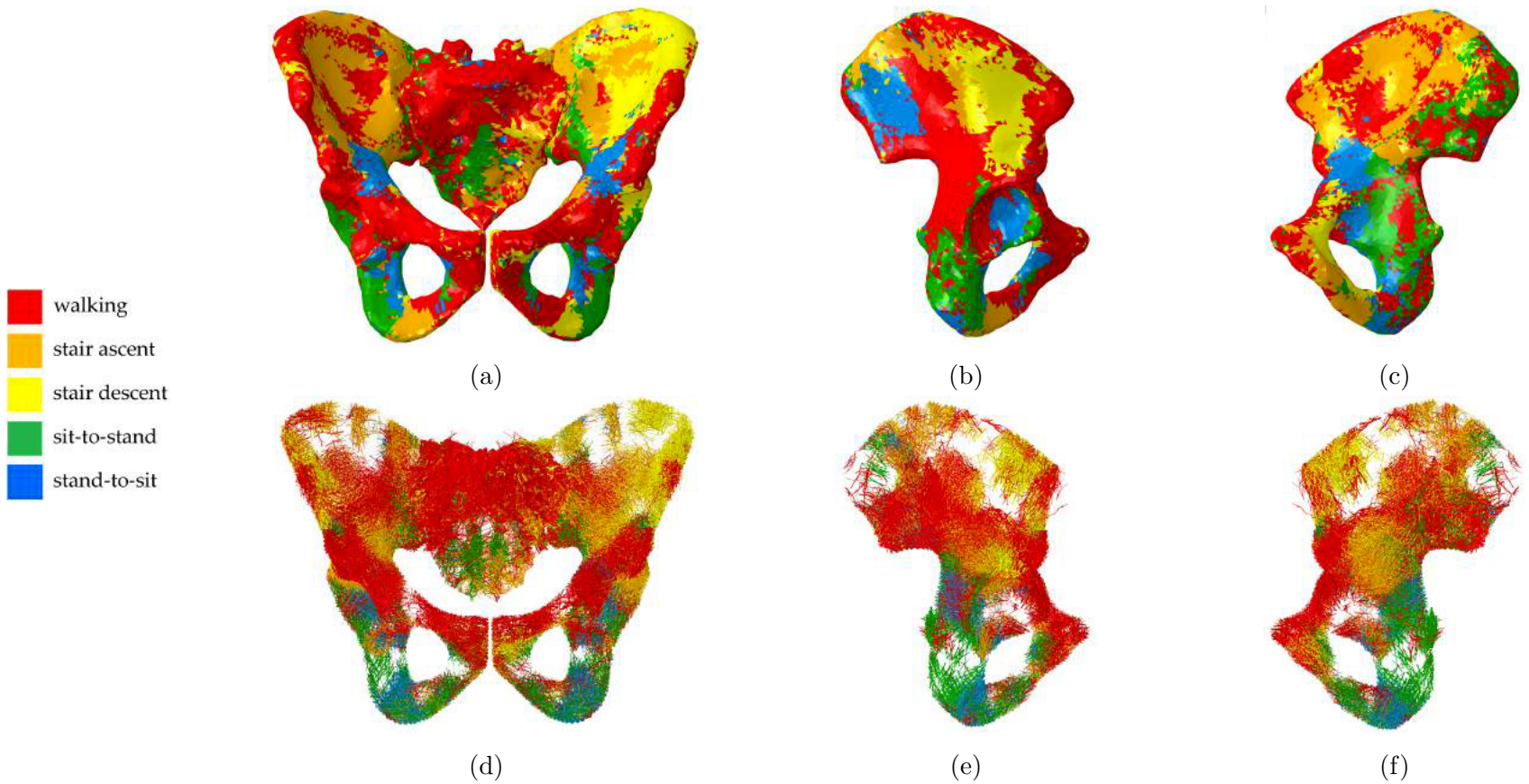
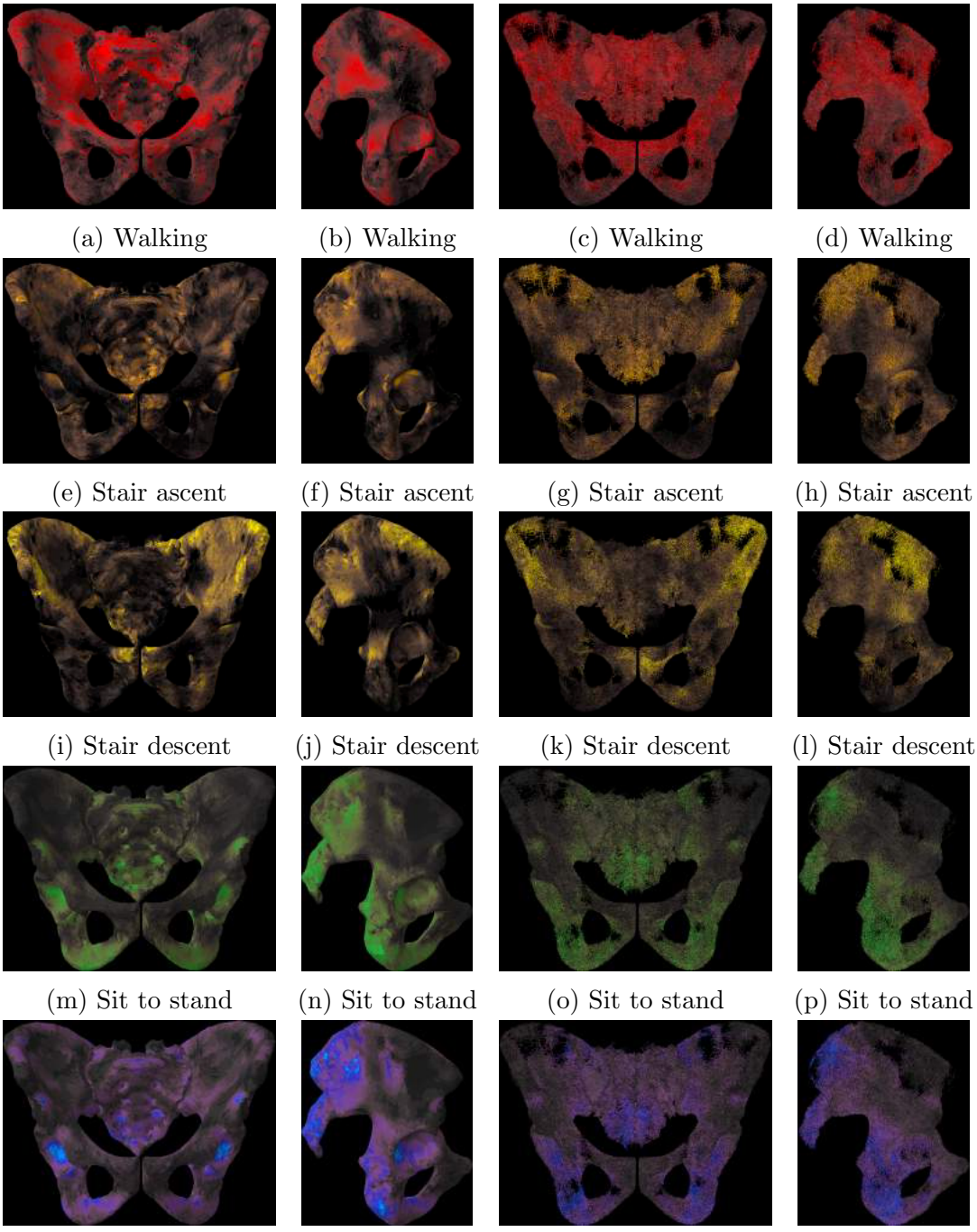


Figure 4.9: Influence of activities on cortical (a, b, c) and trabecular (d, e, f) structure of converged pelvic model. The elements are colour mapped based on the activity which has been most influential in determining their thickness.



(a) Walking (b) Walking (c) Walking (d) Walking

(e) Stair ascent (f) Stair ascent (g) Stair ascent (h) Stair ascent

(i) Stair descent (j) Stair descent (k) Stair descent (l) Stair descent

(m) Sit to stand (n) Sit to stand (o) Sit to stand (p) Sit to stand

(q) Sit to stand (r) Stand to sit (s) Stand to sit (t) Stand to sit

Figure 4.10: Cortical (a,b,e,f,i,j,m,n,q,r) and trabecular (c,d,g,h,k,l,o,p,s,t) strain distributions highlighting the regions with the largest absolute principal strain for each activity. Regions which are highly strained ($\geq 1500\mu\varepsilon$) by a particular activity are shown with a higher intensity in the colour associated with the respective activity as shown in Figure 4.9.

4.2.2 Adaptation to different loading regimes

The structural model was subjected to five separate loading regimes, each corresponding to one of the physical activities selected for this study. This was done to investigate differences in the resulting bone architectures from adapting the model to individual activities as opposed to adapting in response to a complete loading regime. Cortical thickness and trabecular radii distribution for load cases associated with each individual activity are shown in Figures 4.11 to 4.16. he bone volumes of each adapted model are shown in Figure 4.12. The comparison was made to highlight the importance of a loading regime associated with multiple physical activites, as opposed to singular physical activities.

4.2.2.1 Walking

The cortical thickness distribution of the model adapted to walking was broadly similar to the model adapted to all activities. The main discrepancies found were a thinner cortex along the line between the iliac spine and greater sciatic notch, along the anterior side of the sacroiliac joint on the hip bone and along the inner ischial ramus (Figure 4.11a-c). The trabecular architecture resulting from adaptation to walking had a lower density of trabecular elements compared to the benchmark model at the ischial tuberosity, lesser sciatic notch and posterior iliac spine (Figure 4.11d-f). The difference between the two models in terms of bone architecture was further highlighted by comparing the cortical and trabecular volumes, with the model adapted only to walking having 17% less cortical bone and 24% less trabecular bone (Figure 4.12).

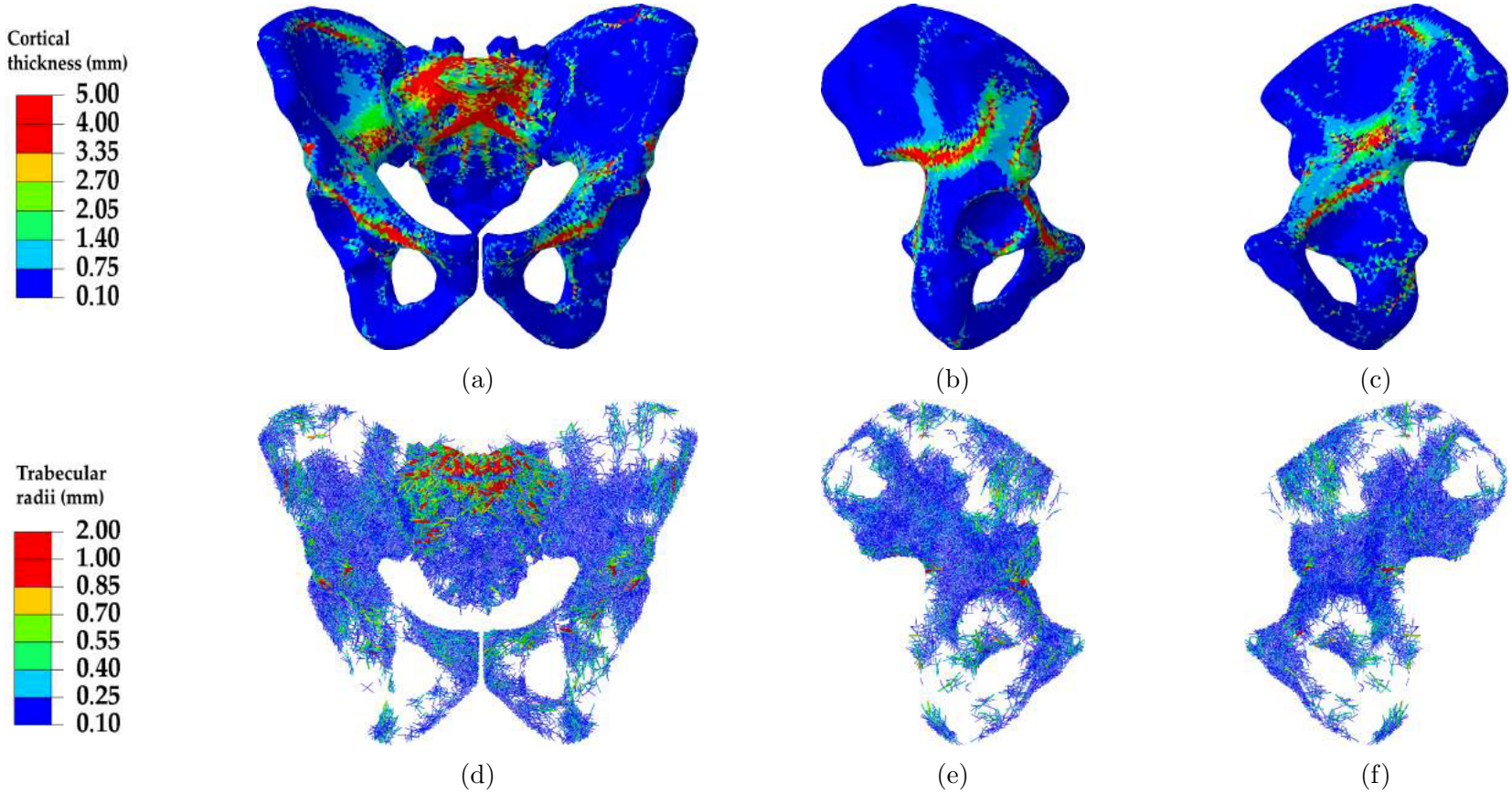


Figure 4.11: Converged structure for walking. Contours of position dependent cortical thickness ranging from 0.1 mm to 5 mm are shown in the top row: (a) frontal view of pelvis, (b) anterior and (c) medial views of the right innominate. Trabecular elements' radii distribution ranging from 0.1 mm to 2 mm is shown in the bottom row: (d) frontal view, (e) anterior and (f) medial views of the right innominate. Trabecular elements with a radius < 0.1 mm were excluded for clarity.

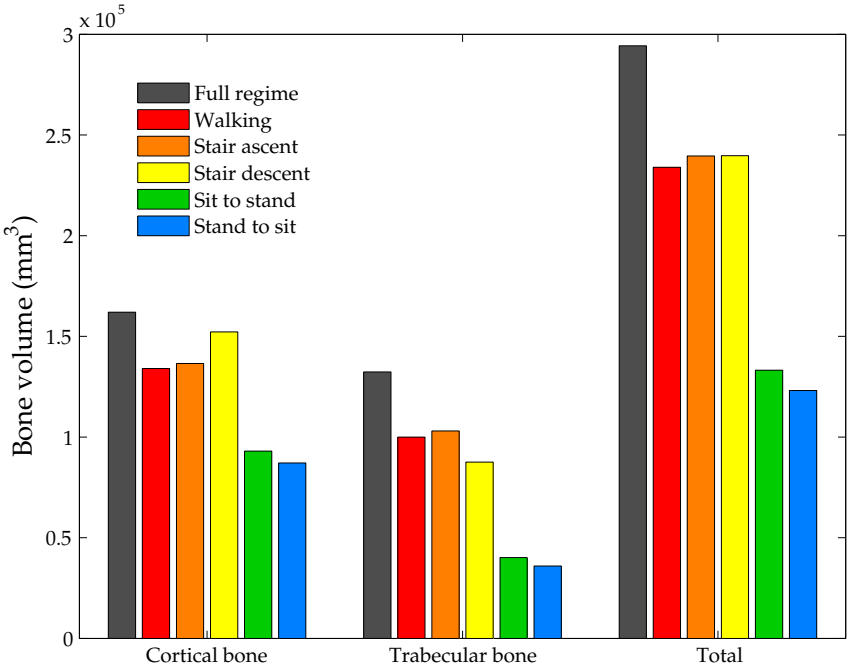


Figure 4.12: Cortical, trabecular and total bone volumes for models adapted to each activity separately compared to the full loading regime. The data is available in in the Appendix, in Table A1.

4.2.2.2 Stair ascent

The cortical thickness distribution of the model adapted only to stair ascent showed a clear loss of cortical thickness compared to the benchmark model, especially along the gluteal surface of the ilium and arcuate line (Figure 4.13a-c). Similarly, the density of trabecular elements in the area above the acetabulum rising to the anterior iliac crest was much lower than for the benchmark model (Figure 4.13d-f). Although the differences in terms of cortical and trabecular architecture were more evident than for the model adapted to walking from a visual perspective, the cortical and trabecular bone volumes were slightly higher. The model adapted to stair ascent had 15% less cortical bone and 22% less trabecular bone than the benchmark model (Figure 4.12).

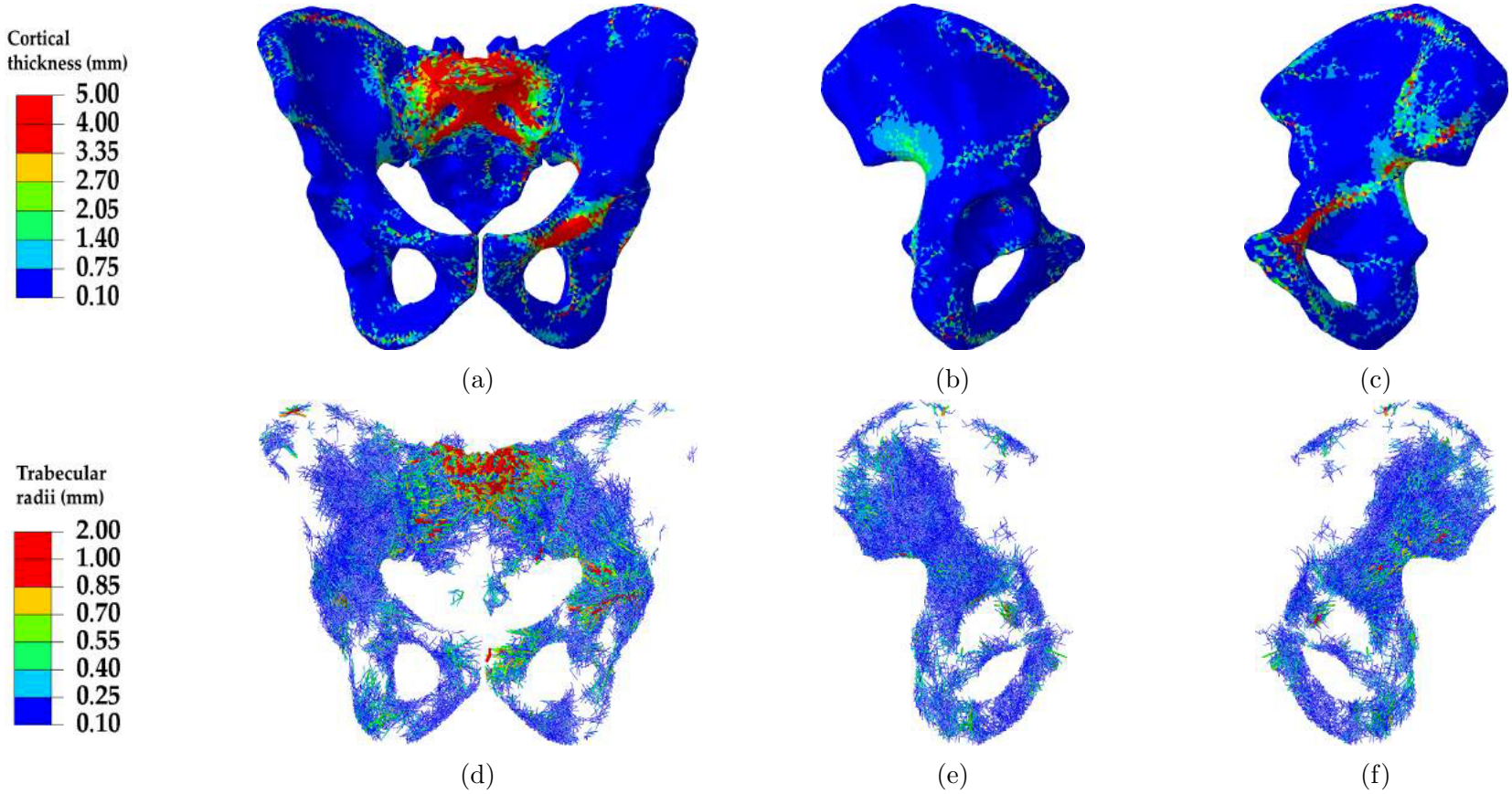


Figure 4.13: Converged structure for stair ascent. Contours of position dependent cortical thickness ranging from 0.1 mm to 5 mm are shown in the top row: (a) frontal view of pelvis, (b) anterior and (c) medial views of the right innominate. Trabecular elements' radii distribution ranging from 0.1 mm to 2 mm is shown in the bottom row: (d) frontal view, (e) anterior and (f) medial views of the right innominate. Trabecular elements with a radius < 0.1 mm were excluded for clarity.

4.2.2.3 Stair descent

The thickness distribution of cortex of the model adapted to stair descent, in contrast to the model adapted to stair ascent, was more similar to the benchmark model. The main difference was the thinner cortex along the gluteal surface near the greater sciatic notch (Figure 4.14a-c). In terms of trabecular architecture, the inferior pubic ramus, the ischial tuberosity and large areas in the superior ilium were regions where few or no trabecular elements had radii greater than 0.1 mm, in contrast to the benchmark model (Figure 4.14d-f). These particularities were confirmed by the differences in bone volume, with the model adapted to stair descent having 6% less cortical bone and 33% less trabecular bone (Figure 4.12).

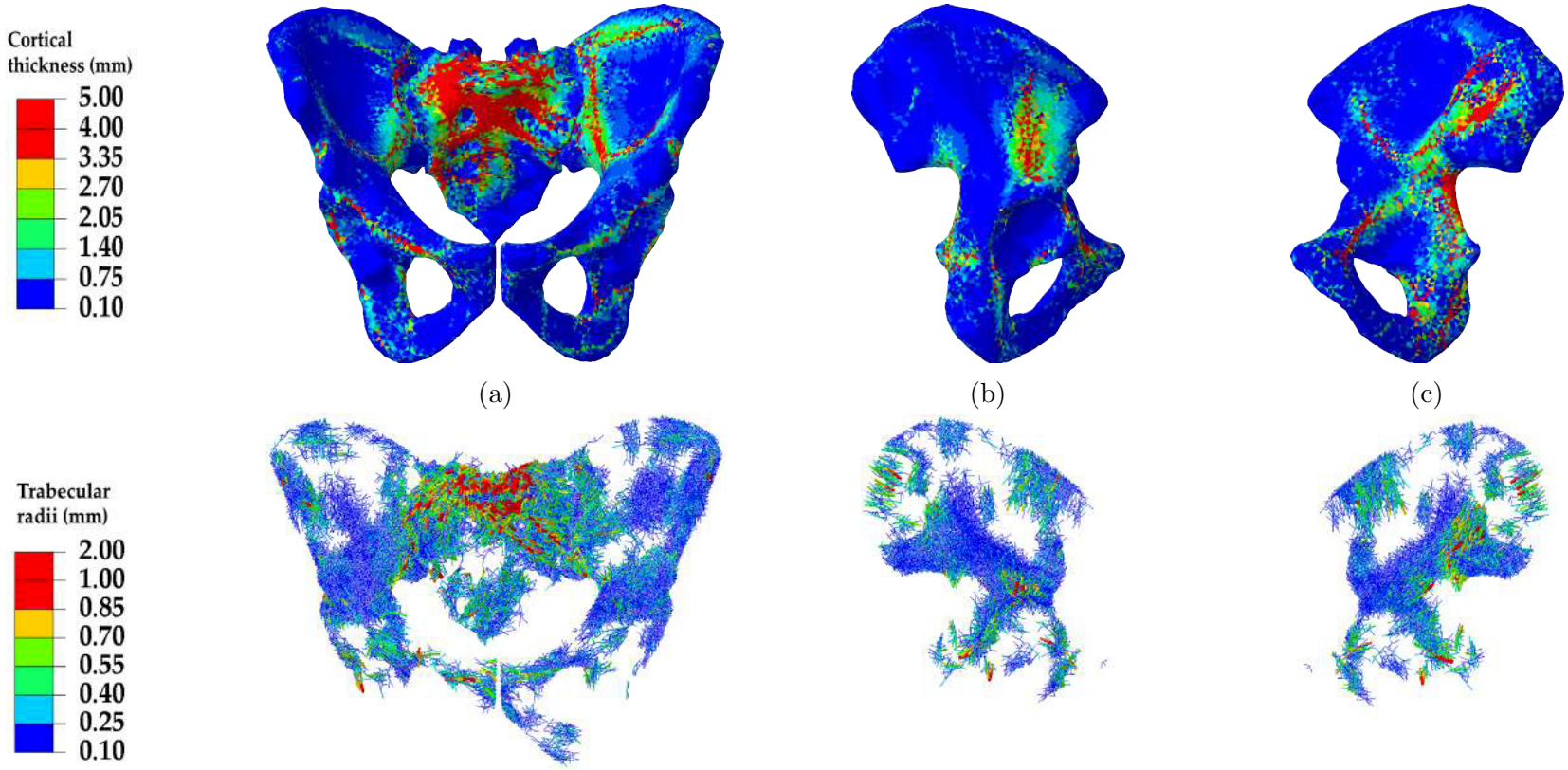


Figure 4.14: Converged structure for stair descent. Contours of position dependent cortical thickness ranging from 0.1 mm to 5 mm are shown in the top row: (a) frontal view of pelvis, (b) anterior and (c) medial views of the right innominate. Trabecular elements' radii distribution ranging from 0.1 mm to 2 mm is shown in the bottom row: (d) frontal view, (e) anterior and (f) medial views of the right innominate. Trabecular elements with a radius < 0.1 mm were excluded for clarity.

4.2.2.4 Sitting and standing

The models which showed the greatest differences in bone architecture were the models adapted to sit to stand and stand to sit. The cortex of both models was generally thin across the hip bones, with thicker cortex being around the superior sacroiliac joint and along the middle of the sacrum (Figures 4.15a-c and 4.16a-c). Across the superior ilium, anterior superior iliac spine and superior pubic ramus trabecular architecture was very sparse compared to the benchmark model (Figures 4.15d-f and 4.16d-f). The distinct differences are highlighted by the bone volumes of both models in comparison to the model adapted to the full loading regime. The model adapted to sit to stand had 42% less cortical bone volume and 69% less trabecular bone volume than the benchmark model. The cortical and trabecular bone volumes in the model adapted to stand to sit were 46% and 72% less than in the model adapted to all activities, respectively.

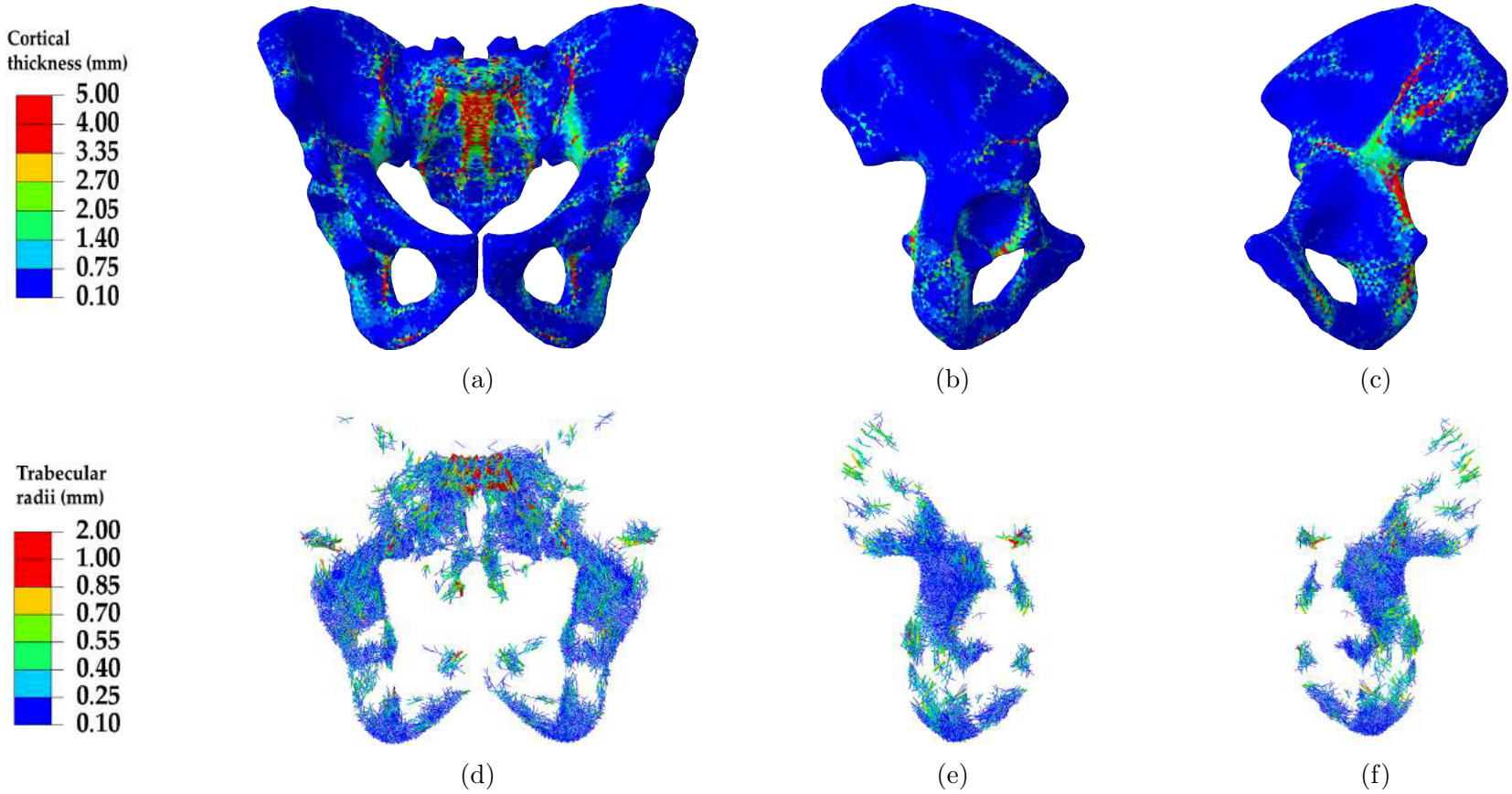


Figure 4.15: Converged structure for sit to stand. Contours of position dependent cortical thickness ranging from 0.1 mm to 5 mm are shown in the top row: (a) frontal view of pelvis, (b) anterior and (c) medial views of the right innominate. Trabecular elements' radii distribution ranging from 0.1 mm to 2 mm is shown in the bottom row: (d) frontal view, (e) anterior and (f) medial views of the right innominate. Trabecular elements with a radius < 0.1 mm were excluded for clarity.

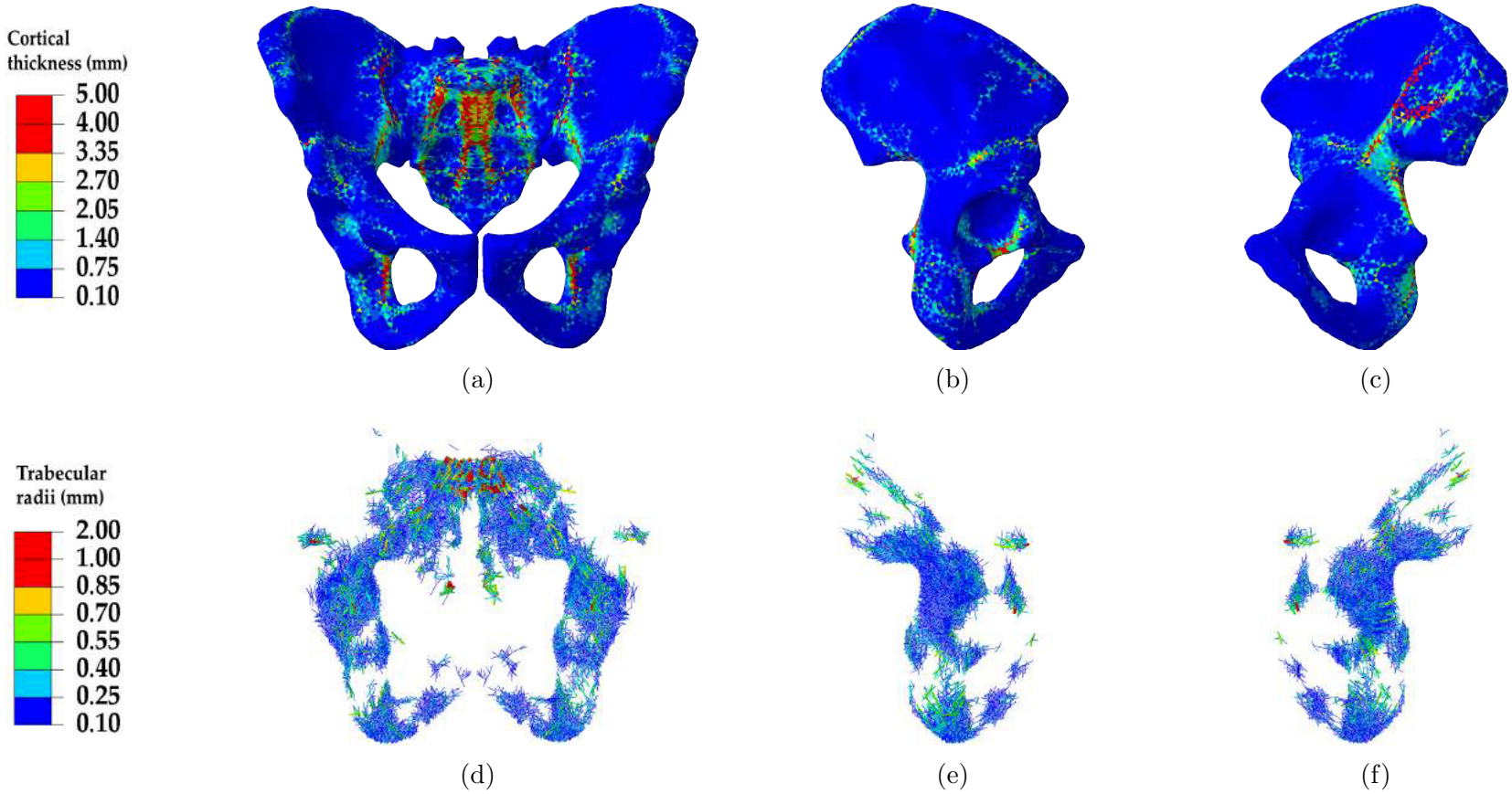


Figure 4.16: Converged structure for stand to sit. Contours of position dependent cortical thickness ranging from 0.1 mm to 5 mm are shown in the top row: (a) frontal view of pelvis, (b) anterior and (c) medial views of the right innominate. Trabecular elements' radii distribution ranging from 0.1 mm to 2 mm is shown in the bottom row: (d) frontal view, (e) anterior and (f) medial views of the right innominate. Trabecular elements with a radius < 0.1 mm were excluded for clarity.

Adapting the model to individual activities has shown that, whilst they caused the development of similar cortical and trabecular architecture in certain regions, they each contributed to distinct structural features across the pelvis. However, that does not necessarily mean that superimposing the effects of these activities would produce version of bone optimised to resist the complete loading spectrum. The superimposed model was obtained by selecting for each element i the largest thickness or cross-sectional area from all activities (a_k=walking, stair ascent, stair descent, sit to stand, stand to sit) (Equations 4.6 and 4.7). A comparison between the cortical, trabecular and total bone volumes of a model obtained by superimposing the singular activities and a model adapted to all activities is shown in Figure 4.17. A mapping of the cortical and trabecular regions where regions were highlighted based on the difference in bone volume between the two models is shown in Figure 4.18.

$$T_i^{superimposed} = \max(T_i^{a_1}, T_i^{a_2}, T_i^{a_3}, T_i^{a_4}, T_i^{a_5}) \tag{4.6}$$

$$A_i^{superimposed} = \max(A_i^{a_1}, A_i^{a_2}, A_i^{a_3}, A_i^{a_4}, A_i^{a_5}) \tag{4.7}$$

The cortical and trabecular bone volumes of the superimposed model were 37% and 40% greater than the corresponding volumes of the model adapted simultaneously to the full loading regime. These results indicate that adaptation to a loading regime consisting of multiple activities leads to a structure that can withstand loads corresponding to each activity whilst having a lower material volume, hence a more optimised structure.

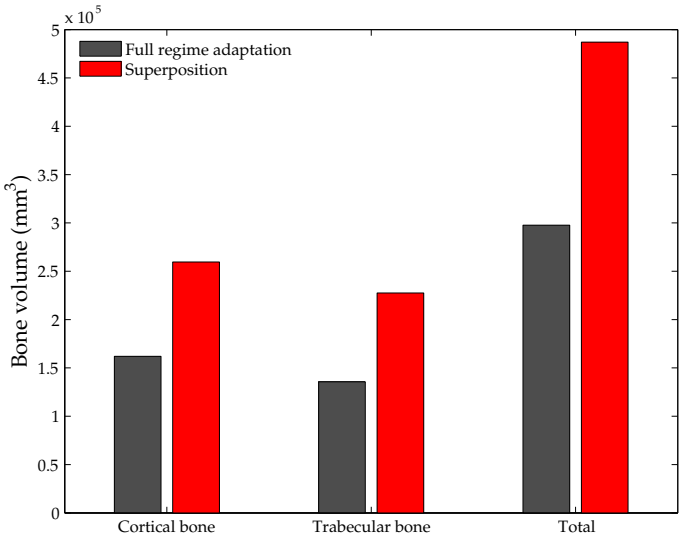


Figure 4.17: Comparison between cortical, trabecular and total bone volume of the model adapted to the full loading regime and a superimposed model obtained from models adapted to individual activities.

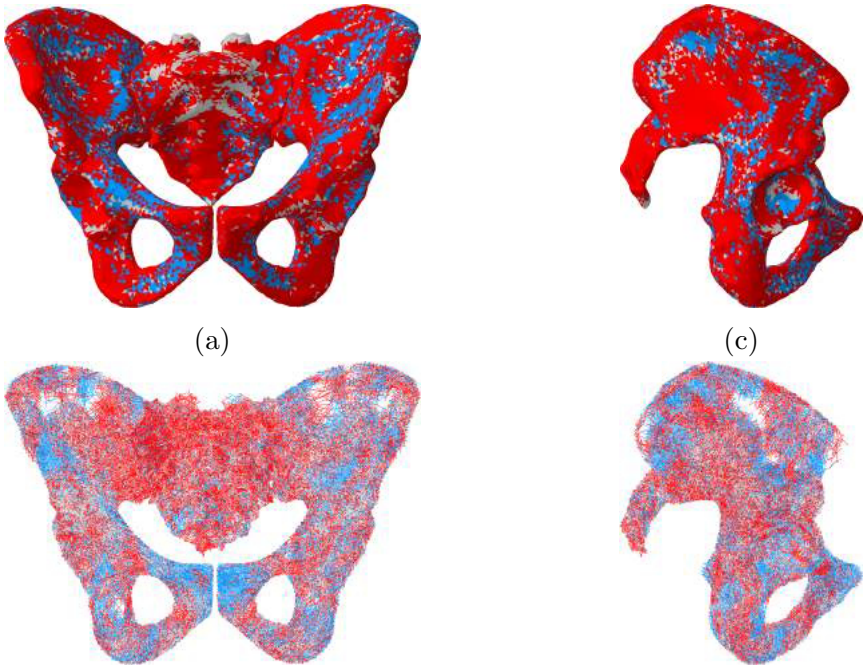


Figure 4.18: Cortical and trabecular mapping of regions with differences between the superimposed model and the model adapted to the full loading regime based on element thickness/radius. Areas where the superimposed model predicted a greater bone volume than the adapted model are shown in red, and in blue where the superimposed model predicted a lower bone volume than the adapted. Regions where no difference was found are shown in grey.

4.2.3 Comparison to CT scan derived model

The absolute maximum principal strains on the surface of the structural model adapted to the complete loading regime and the CT scan derived model are shown in Figure 4.19. The maximum and minimum principal strains across the surface of the structural model and continuum model derived from the CT data were compared (Figure 4.20). The coefficients of correlation for both minimum (0.813) and maximum (0.809) principal strains show a fairly good agreement between the strains predicted by the structural model and CT derived model.

In addition to the standard correlation plots, Bland-Altman plots (Bland and Altman, 1999) were used to compare the strain difference between models and the average strain (Figure 4.21). The mean differences between the structural model and the CT scan derived model were found to be $-68.42\mu\epsilon$ for minimum principal strains and $83.81\mu\epsilon$ for maximum principal strains. Linear regression lines fitting the data show a proportional bias ($p<0.05$) and indicate that using crude 95% confidence intervals would not be appropriate. V-shaped limits of agreement were constructed.

The limits of agreement indicated that the structural model is less stiff than the CT scan derived model in some areas. The surface of the hemipelvis was separated into regions based on the strain ratio between the two models to highlight these differences (Figure 4.22). The regions where the structural model was not in agreement with the CT scan derived model were identified to either have a sparse trabecular architecture or a low cortical thickness, whereas the continuum model has a minimum stiffness across the whole geometry. In addition, these regions corresponded to a large extent with regions undergoing low strain in both models.

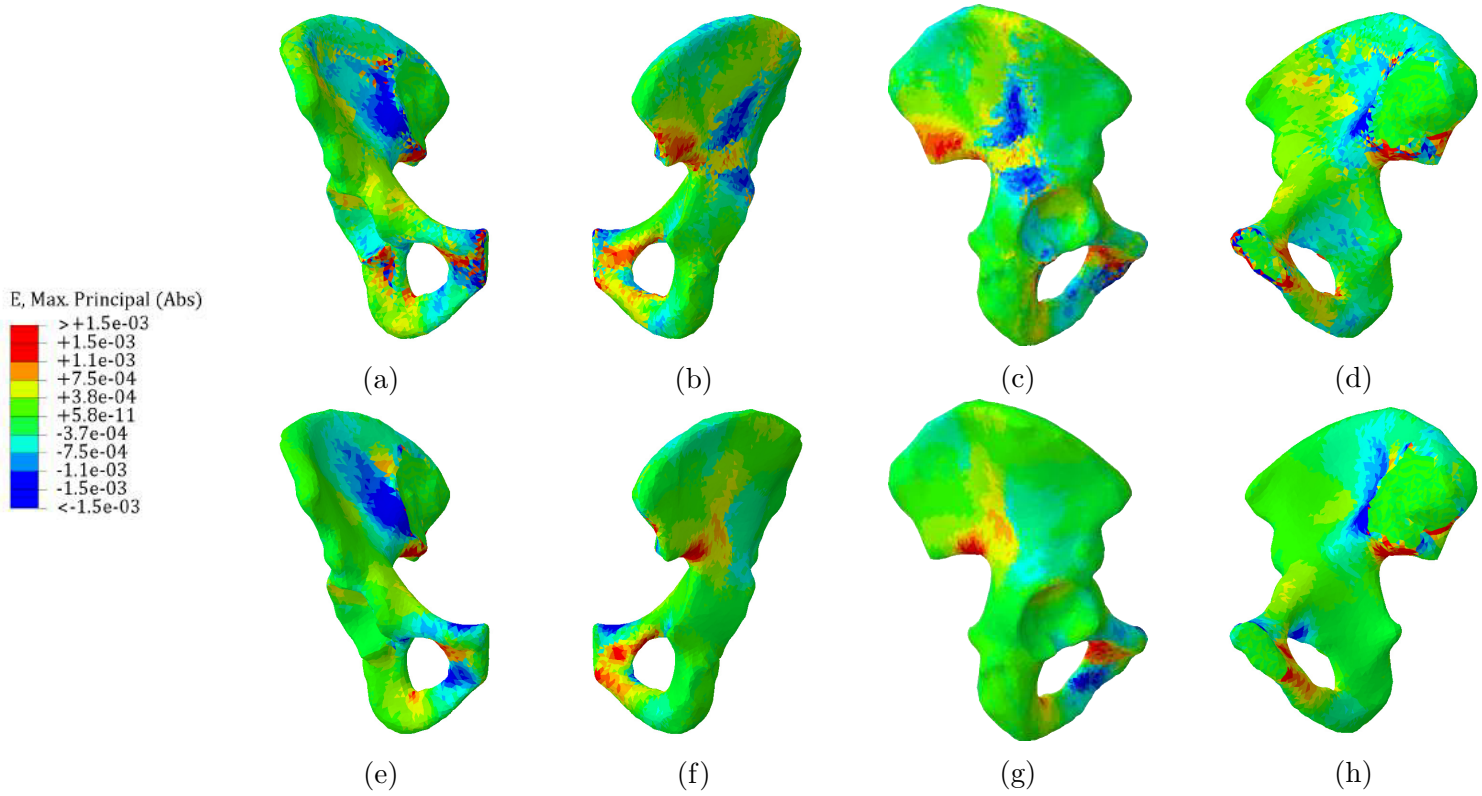
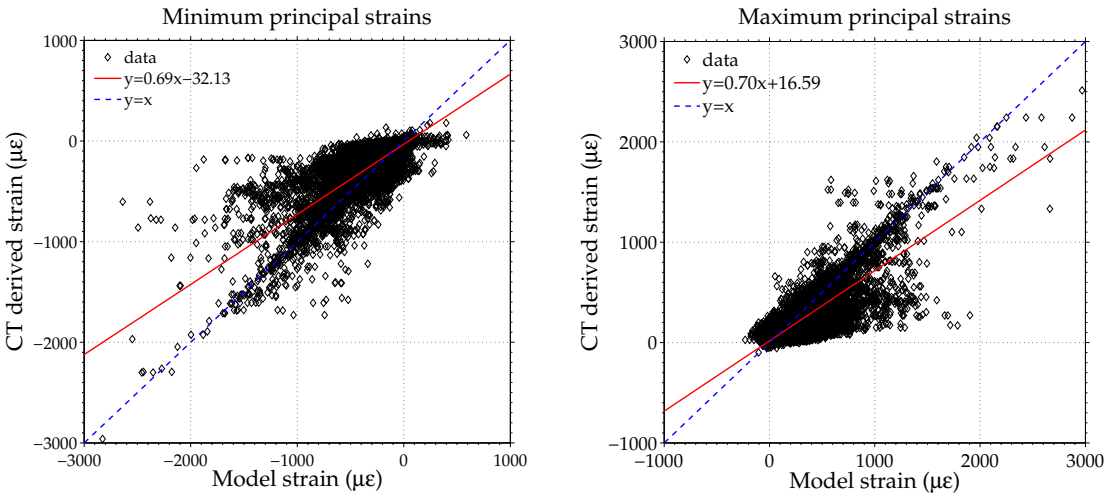
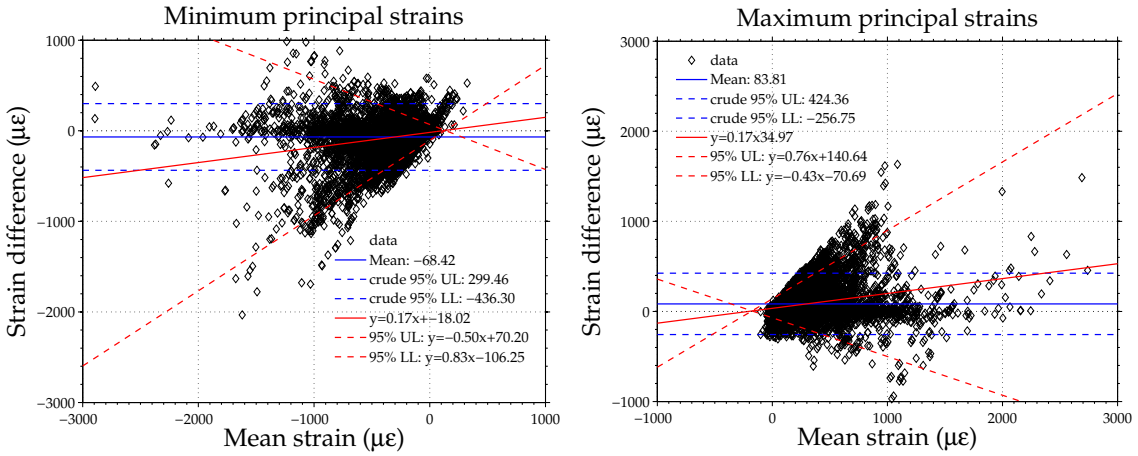


Figure 4.19: Absolute maximum principal strain distribution for structural model (a,b,c,d) and scan derived model (e,f,g,h) in response to the loading condition shown in Figure 4.5



(a) Correlation coefficient: 0.813 (b) Correlation coefficient: 0.809

Figure 4.20: Comparison between the minimum (a) and maximum (b) principal strains across the surface of the structural model (x axis) and CT derived model (y axis). Lines of best fit are shown in red for each case and do not differ greatly from the y=x line shown in dashed blue.



(a) (b)

Figure 4.21: Bland-Altman plots showing (a) minimum and (b) maximum principal strains as difference between the structural model and CT derived model versus mean. Mean value and crude 95% confidence intervals are shown in blue. Regression lines and V-shaped 95% confidence intervals are shown in red

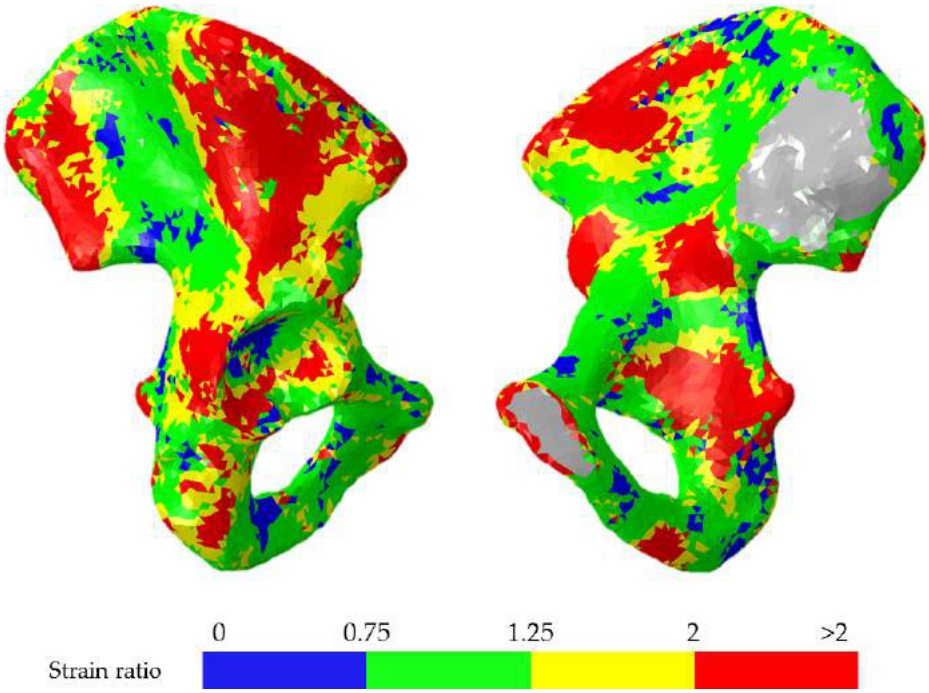
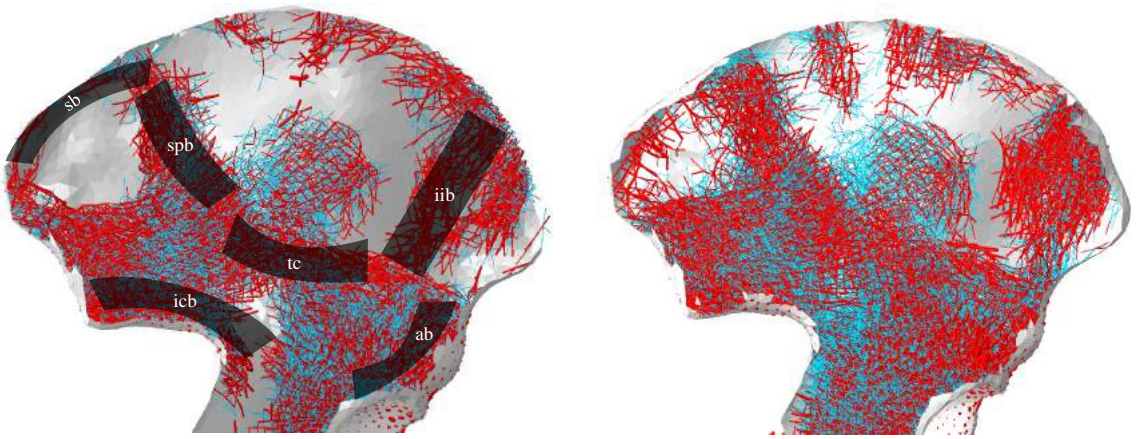


Figure 4.22: Lateral views of the hip bone showing regions defined by the ratio of absolute maximum principal strains between the structural model and the CT derived model. A ratio higher than one corresponds to the structural model predicting a higher strain than the CT scan derived model in the highlighted region.

4.3 Discussion

The architecture and structural features of the bony pelvis has not been studied extensively compared to other bones, as highlighted in Chapter 2. Macchiarelli et al. (1999) investigated the gait-related trabecular architecture of the ilium and hypothesized that a number of distinct trabecular trajectories form as a consequence of the joint and muscle loads applied on the hip during gait. The trajectories proposed by the authors were: superior bundle (sb), anterior bundle (ab), sacropubic bundle (spb), iliocotyloid bundle (icb), ilioischial bundle (iib), trabecular chiasma (tc). These trajectories can be quite clearly identified in the trabecular architecture of the model adapted to walking as clusters of elements with large radii, shown in Figure 4.23a. The trabecular structure in the ilium of the model adapted to the full loading regime is shown in Figure 4.23b, with a more developed structure and trabecular groups appearing in addition to the trajectories identified by Macchiarelli et al. (1999).



(a) (b)

Figure 4.23: Trabecular trajectories formed in the ilium adapted from (a) walking and (b) all activities. The trajectories highlighted correspond to regions in the ilium with a higher trabecular density caused by walking observed by Macchiarelli et al. (1999): superior bundle (sb), anterior bundle (ab), sacropubic bundle (spb), iliocotyloid bundle (icb), ilioischial bundle (iib), trabecular chiasma (tc). Truss elements with a radius > 0.1 mm are shown in red. Truss elements with a radius of 0.1 mm appear in blue.

The response of the converged structural model to a loading scenario was compared to an analogous continuum model with varying material properties derived from the CT data. Although the comparison showed that the two models were in fairly good agreement, the correlation was not found to be as strong as reported in previous studies which have compared continuum models with experimental data (Anderson et al., 2005; Leung et al., 2009). However, the sample size used for comparison in the studies mentioned was limited to the number of strain gauges used, meaning that a comparison between strains across the whole bone surface was not possible. Differences between the structural model and CT derived model could be attributed to trabecular bone in the CT derived model having a minimum stiffness of 50 MPa based on the conversion from the HU values, while corresponding regions in the structural model had very sparse trabecular architecture.

The structural model of the pelvis comprised of 691,852 elements and 235,914 design variables was found to have a run time of 153 s on a workstation PC with one Intel Xeon E5-2630 v2 2.60 GHz and 64 GB of RAM. The run time for adapting the model to the full loading regime was around 24 h. A direct comparison to another adaptive model of the pelvis cannot be made due to lack of availability in the literature. Continuum models of the pelvis were developed from CT scans and used in simulating loading scenarios with the number of elements varying between 190,000 and 1.2 million (Anderson et al., 2005; Li et al., 2007; Leung et al., 2009), with the run times not being reported. A potentially better comparison can be made with adaptive models of the femur. Boyle and Kim (2011) developed a microscale model of the proximal femur (23.3 million elements) reporting a runtime of around 343 h for a single combined load case. Phillips et al. (2015) reported a run time of 52 s for their mesoscale structural model of the femur (229,113 elements) and a duration of 10 h for the full adaptation regime. Although the current model has not been implemented at the microscale, it is reasonable to conclude that it has a low computational cost, comparable to a similar computationally efficient structural model of the femur.

A limitation of the combined modelling approach is that the loads applied on the

FE model are derived from a rigid multibody system, meaning that the equilibrium condition satisfied in the musculoskeletal model is compromised by the deformation and displacement occuring in the FE model. Furthermore, the muscle forces are not spread over attachment areas and the muscle compression forces onto bone are not accounted for. The musculoskeletal model partially overcomes this limitation by having a high number of actuators for muscles.

A limitation associated with the loading conditions applied on the model is that they were derived from one subject. Having experimental data from multiple subjects with similar anthropometric characteristics could have provided an envelope of loading conditions associated with the physical activities selected for this study. This could provide insight into the asymmetric bone structure observed for adapting the model to a set of loading conditions derived from a singular subject.

An additional limitation is that the CT scan which was used to define the initial model geometry originated from a different subject to the one used to derive the loading conditions from. However, this limitation was partially overcome by having similar anthropometric characteristics (height and weight) for both subjects. Although the physical activites selected to drive bone adaptation are the most commonly encountered in daily life (Morlock et al., 2001), adapting the model to additional activities (eg. cardiovascular exercise, strength exercise) could provide potentially valuable insight into the effect of more strenuous physical activities on the pelvic bone architecture.

Finally, the model was developed to contain only the pelvic bones and ligaments. Although the main focus in this Chapter was on bone adaptation, the lack of internal organs and soft tissue connected to the pelvis can have an impact on bone adaptation as loads in certain regions are not spread and compressive loads caused by the presence of muscles and organs are not taken into account.

5

Predictive continuum and hybrid modelling of the pelvic construct

In this chapter, the framework developed by Geraldes et al. (2016) was adapted to simulate bone adaptation in a continuum model of the pelvic construct, using orthotropic and isotropic material models, respectively. The continuum models were subjected to loading conditions associated with daily physical activities, derived from the musculoskeletal model described in Chapter 3, §3.2, and the material properties of each element were iteratively adapted using an adaptation algorithm based on the Mechanostat (Frost, 2003). In addition, a number of hybrid FE models comprising of both structural and continuum elements were developed and run through the adaptation pipeline to assess the effect of different modelling approaches on bone architecture. The modelling framework is illustrated in Figure 5.1.

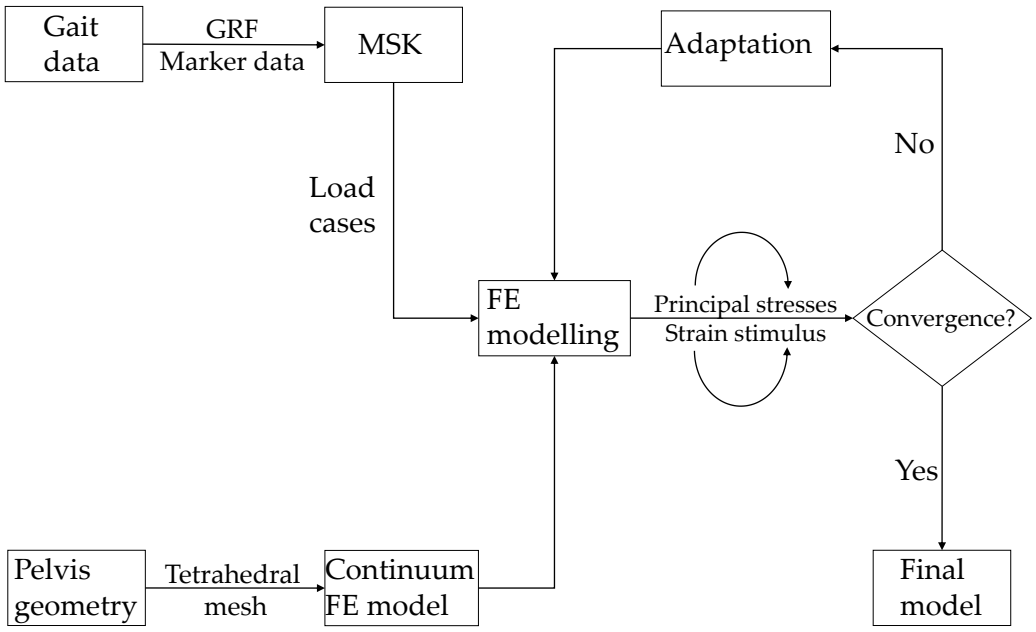


Figure 5.1: Modelling framework used to develop an adaptive continuum model of the pelvic construct

5.1 Methods

5.1.1 Finite element modelling

The base FE mesh of the continuum model originated from the same CT scan used to develop the structural model presented in Chapter 4. The FE model consisted of 377,362 first order linear tetrahedral elements (C3D4) with an average edge length of 3.76 mm.

Ligaments, cartilage, load applicators, fixators and inertia applicator were added to the model using the methodology described in Chapter 3, §3.3.3. Briefly, five ligaments (sacro-iliac, pubic, sacrospinous, scarotuberous and inguinal) and cartilage at two joints (sacro-iliac and pubic) were built. Load applicators and fixators were designed comprising four layers of continuum elements superposed onto the desired bone surface. The two first layers were assigned material properties akin to cartilage (E=10 MPa, ν=0.49), with the furthest two being assigne dstiffnesses of 10 MPa ($\nu = 0.3$) and 500 MPa ($\nu = 0.3$), respectively Villette (2016). Lastly, an inertia applicator was designed to spread the inertial load of the pelvis over the whole construct by linking its centre of mass to every node of the model with truss elements with a radius of 0.1 mm and low stiffness (E=0.1 MPa, ν=0.3).

The musculoskeletal model and the kinematics data described in Chapter 3, §3.2, were used to apply to the model joint contact forces, muscle forces and inertial loading experienced during daily physical activities: walking, stair ascent, stair descent, sit to stand and stand to sit, resulting in 39 loading frames.

A total of five FE models were developed in this chapter: an orthotropic model, an isotropic model, two combined models where cortical bone was represented by shell elements and trabecular model was represented by orthotropic and isotropic continuum elements, respectively, and a combined structural model where cortical

bone was modelled using shell elements, trabecular bone using truss elements and continuum elements were added to provide a background stiffness to the model.

Continuum elements were assigned individual material properties using the distribution table in Abaqus as follows: orthotropic material properties were introduced by defining a local coordinate system and assigning three sets of Young's modulus, Poisson's ratio and shear modulus values; isotropic material properties were defined by Young's modulus and a Poisson's ratio value of 0.3. The exception was for the combined structural model, where the continuum elements were assigned homogenous isotropic material properties.

5.1.2 Bone adaptation algorithm

5.1.2.1 Orthotropic adaptation algorithm

The adaptation algorithm developed by Geraldes and Phillips (2014) and Geraldes et al. (2016) has been adapted for the finite element model of the pelvis. The algorithm is based on the hypothesis that each orthotropic element adapts its material orientations depending on the principal stress directions and material properties depending on the stresses and strains resulting from the loading regime applied. Initially, each element was assigned a Young's modulus value of 3000 MPa, a Poisson's ratio of 0.3 and a shear modulus value of 1500 MPa. The local coordinate system of each element was aligned with the global coordinate system.

At each iteration i, the guiding frame (λ) was selected from the loading regime as the frame in which the absolute normal strain had the largest value for the j^{th} element (Equation 5.1).

$$\varepsilon_{i,j}^{max} = \max(|\varepsilon_{kk}|_{\lambda}), \lambda = 1, ..., n \tag{5.1}$$

This was then used to extract the stress tensor, σ_{kl}^{λ}, associated with the guiding frame for each element (Equation 5.2).

$$\sigma_{kl}^{\lambda} = \begin{pmatrix} \sigma_{11}^{\lambda} & \sigma_{12}^{\lambda} & \sigma_{13}^{\lambda} \\ \sigma_{21}^{\lambda} & \sigma_{22}^{\lambda} & \sigma_{23}^{\lambda} \\ \sigma_{31}^{\lambda} & \sigma_{32}^{\lambda} & \sigma_{33}^{\lambda} \end{pmatrix}, k, l = 1, 2, 3 \tag{5.2}$$

The stress tensor was then used to calculate the principal stresses, σ_{p}^{λ}, and vectors associated with the principal stress directions, σ_{pv}^{λ}, by performing an eigenanalysis (Equation 5.3).

$$eig(\sigma_{kl}^{L}) = \left(\begin{pmatrix} \sigma_{pv1}^{min} & \sigma_{pv1}^{med} & \sigma_{pv1}^{max} \\ \sigma_{pv2}^{min} & \sigma_{pv2}^{med} & \sigma_{pv2}^{max} \\ \sigma_{pv3}^{min} & \sigma_{pv3}^{med} & \sigma_{pv3}^{max} \end{pmatrix}, \begin{pmatrix} \sigma_{p}^{min} & 0 & 0 \\ 0 & \sigma_{p}^{mid} & 0 \\ 0 & 0 & \sigma_{p}^{max} \end{pmatrix} \right) \tag{5.3}$$

The maximum absolute values for component of the strain tensor, ε_{kl}^{max}, were chosen from all loading frames (λ) for each element (Equation 5.4).

$$\varepsilon_{kl}^{max} = \max(|\varepsilon_{kl}|_{\lambda}), \lambda = 1, ..., n \tag{5.4}$$

Thus, the maximum strain matrix, $\underline{\varepsilon}^{max}$, can be defined using Equation 5.5.

$$\underline{\varepsilon}^{max} = \begin{pmatrix} \varepsilon_{11}^{max} & \varepsilon_{12}^{max} & \varepsilon_{13}^{max} \\ \varepsilon_{21}^{max} & \varepsilon_{22}^{max} & \varepsilon_{23}^{max} \\ \varepsilon_{31}^{max} & \varepsilon_{32}^{max} & \varepsilon_{33}^{max} \end{pmatrix} \tag{5.5}$$

The bone adaptation driver was defined as a strain stimulus matrix, $\underline{\varepsilon}^{*}$, associated with both the maximum strain matrix, $\underline{\varepsilon}^{max}$, and the directions of the principal stresses, σ_{pv}^{λ} (Equation 5.6).

$$\underline{\varepsilon}^{*} = {\sigma_{pv}^{\lambda}}^{T} \underline{\varepsilon}^{max} \sigma_{pv}^{\lambda} \tag{5.6}$$

Geraldes et al. (2016) have argued that orthotropic bone adaptation using $\underline{\varepsilon}^{*}$ as the driving stimulus comes in agreement with both the Mechanostat (Frost, 2003) and bone trajectory (Skedros and Baucom, 2007) theories.

The material properties of each element were adjusted to bring the local strains within the lazy zone. As discussed in Chapter 2, the normal target strain, ε_{nt}, was assigned a value of $1250\mu\varepsilon$, with the lazy zone ranging from $1000\mu\varepsilon$ to $1500\mu\varepsilon$. The normal strain ranges associated with the dead zone, bone resorption, the lazy zone

and bone apposition for the j^{th} element at iteration i are shown in Equation 5.7. The Young's moduli in each orthogonal direction ($E^k_{i,j}$, $k = 1, 2, 3$) were adjusted proportionally as a function of the normal stimulus strains and the target strain (Equation 5.8), limited between 10 MPa and 18 GPa (Dalstra et al., 1995b). Elements with all normal strains corresponding to the dead zone were assigned the minimum stiffness values and were not re-adjusted in the subsequent iterations of the adaptation process.

$$\phi_{i,j} = \begin{cases} -1, & \text{if } |\varepsilon^*_{kk}| < 250\mu\varepsilon \qquad \text{(Dead zone)} \\ 1, & \text{if } 250\mu\varepsilon \leq |\varepsilon^*_{kk}| < 1000\mu\varepsilon \qquad \text{(Bone resportion)} \\ 0, & \text{if } 1000\mu\varepsilon \leq |\varepsilon^*_{kk}| \leq 1500\mu\varepsilon \qquad \text{(Lazy zone)} \\ 1, & \text{if } |\varepsilon^*_{kk}| > 1500\mu\varepsilon \qquad \text{(Bone apposition)} \end{cases} \tag{5.7}$$

$$E^k_{i,j} = \begin{cases} 10\text{MPa}, & \text{if } \phi_{i,j} = -1 \\ E^k_{i-1,j}\dfrac{|\varepsilon^*_{kk}|}{\varepsilon_{nt}}, & \text{if } \phi_{i,j} = 1 \\ E^k_{i-1,j}, & \text{if } \phi_{i,j} = 0 \end{cases} \tag{5.8}$$

The Poisson's ratios for the j^{th} element at iteration i, $\nu^{i,j}_{kl}$, were limited to an upper value of 0.3 and were altered to satisfy the thermodynamic restrictions on the elastic constants of bone (Cowin and Van Buskirk, 1986) (Equation 5.9) and to ensure that the compliance matrix was always positive definite.

$$\frac{E^{i,j}_k}{E^{i,j}_l} > (\nu^{i,j}_{kl})^2 \tag{5.9}$$

To maintain the equality in Equation 5.10, one of $\nu^{i,j}_{kl}$ and $\nu^{i,j}_{lk}$ was altered whilst the other was kept at 0.3.

$$\frac{\nu_{lk}^{i,j}}{E_l^{i,j}} = \frac{\nu_{kl}^{i,j}}{E_k^{i,j}} \tag{5.10}$$

The resistance of trabecular bone to shear strains in the case of multiple complex loading scenarios has been highlighted in previous studies (Skedros and Baucom, 2007; Geraldes et al., 2016). Albeit the authors made these observations when studying the proximal femur, it can be argued that shear strains play an important role in areas of the pelvic construct that are subjected to complex loading conditions.

To adapt the shear moduli of each element, a target shear strain was used, ε_{st}, the value of which was calculated using the octahedral shear strain, γ_o, defined according to Equation 5.11.

$$\gamma_o = \frac{2}{3}\sqrt{(\varepsilon_{11}-\varepsilon_{22})^2 + (\varepsilon_{22}-\varepsilon_{33})^2 + (\varepsilon_{33}-\varepsilon_{11})^2 + 6(\varepsilon_{12}^2 + \varepsilon_{23}^2 + \varepsilon_{13}^2)} \tag{5.11}$$

Octahedral shear strain has been used in previous studies as a bone remodelling driver (Carter et al., 1998; Shefelbine et al., 2005). Equation 5.11 can be simplified for the cases of pure axial loading ($\varepsilon_{11} = \varepsilon_{nt}; \varepsilon_{22} = \varepsilon_{33} = \varepsilon_{12} = \varepsilon_{13} = \varepsilon_{23} = 0$) (Equation 5.12) and pure shear loading ($\varepsilon_{12} = \varepsilon_{st}; \varepsilon_{11} = \varepsilon_{22} = \varepsilon_{33} = \varepsilon_{13} = \varepsilon_{23} = 0$) (Equation 5.13).

$$\gamma_o = \frac{2\sqrt{2}}{3}\varepsilon_{nt} \tag{5.12}$$

$$\gamma_o = \frac{2\sqrt{6}}{6}\varepsilon_{st} \tag{5.13}$$

Equating Equation 5.12 and Equation 5.13, the equivalent engineering shear target strain can be found (Equation 5.14). For a normal target strain value of $1250\mu\varepsilon$, the

shear target strain is $1443\mu\varepsilon$.

$$\gamma_{st} = 2\varepsilon_{st} = 2\frac{\sqrt{2}}{\sqrt{6}}\varepsilon_{nt} \tag{5.14}$$

The shear moduli of each element, G_{ij}^{n}, were updated proportionally at every iteration, n, as a function of the shear stimulus strain and the target shear strain, γ_{st}, with a lazy zone ranging from 1154 μstrain to 1732 μstrain. The shear strain ranges associated with bone resorption, the lazy zone and bone apposition for the j^{th} element at iteration i are given in Equation 5.15. The shear moduli are updated using Equation 5.16.

$$\phi_{i,j}^{s} = \begin{cases} 1, & \text{if } |\varepsilon_{kl}^{*}| < 1154\mu\varepsilon \qquad \text{(Bone resorption)} \\ 0, & \text{if } 1154\mu\varepsilon \leq |\varepsilon_{kl}^{*}| \leq 1732\mu\varepsilon \qquad \text{(Lazy zone)} \\ 1, & \text{if } |\varepsilon_{kl}^{*}| > 1732\mu\varepsilon \qquad \text{(Bone apposition)} \end{cases} \tag{5.15}$$

$$G_{kl}^{i,j} = \begin{cases} G_{kl}^{i,j}\dfrac{|\varepsilon_{kl}^{*}|}{\gamma_{st}}, & \text{if } \phi_{i,j}^{s} = 1 \\ G_{kl}^{i,j}, & \text{if } \phi_{i,j}^{s} = 0 \end{cases} \tag{5.16}$$

At each iteration, the material orientations of each element were rotated to match the local principal stress directions obtained by performing an eigen-analysis of the stress tensor associated with each element (Equation 5.3) (Geraldes and Phillips, 2010). The three orthotropic axes, x_1, x_2 and x_3 were associated to with the minimum, σ_{pv}^{min}, medium, σ_{pv}^{med} and maximum, σ_{pv}^{max}, principal stress directions, respectively (Figure 5.2).

The association of the first orthotropic axis with the minimum principal stress direction is based on the hypothesis that the predominant loading mode of the pelvis is compression, similar to the femur (Taylor et al., 1996; Sverdlova and Witzel, 2010; Geraldes et al., 2016). To avoid flic-flac of the local material orientations, the elements

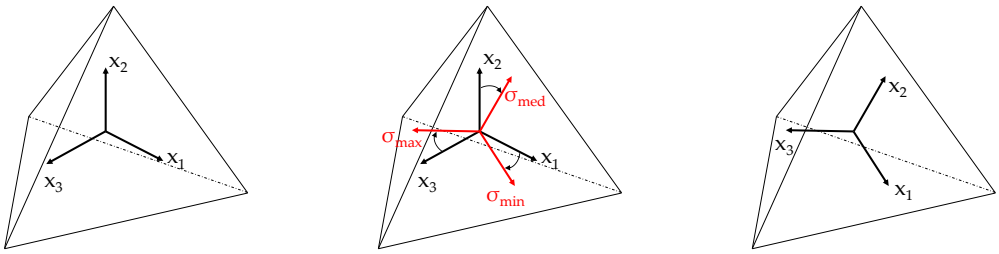


Figure 5.2: Illustration of the rotation of local coordinate system associated with an element to match the directions of the principal stresses

for which between successive iterations the angle between the old minimum principal axis and new minimum principal axis was lower than 5° or greater than 175° were kept with the local orientation from the previous iteration.

The convergence criterion was defined as when the average change in Young's moduli of elements with absolute normal strain values above 250 $\mu\varepsilon$ and Young's moduli greater than 10 MPa (outside the dead zone) was less than 2% between successive iterations (Geraldes and Phillips, 2010).

5.1.2.2 Isotropic adaptation algorithm

As isotropic adaptation does not require directional material properties, at iteration i, the Young's modulus of element j was updated proportionally to the maximum absolute principal strain (ε_{max}) taken across all loading frames (λ) and the normal target strain (Equations 5.17 - 5.19). The target strain and Young's modulus range used were the same as in the orthotropic adaptation algorithm. Each element's Poisson's ratio was assigned a constant value of 0.3. Initially, each element was assigned a Young's modulus value of 3000 MPa and a Poisson's ratio of 0.3, similar to the orthotropic model. It should be noted that in the case of isotropic adaptation, the values for Poisson's ratio were not changed.

$$\varepsilon_{i,j}^{max} = \max(|\varepsilon_{max}|_{\lambda}), \lambda = 1, ...n \tag{5.17}$$

$$\phi_{i,j} = \begin{cases} -1, & \text{if } |\varepsilon_{i,j}^{max}| < 250\mu\varepsilon \qquad \text{(Dead zone)} \\ 1, & \text{if } 250\mu\varepsilon \leq |\varepsilon_{i,j}^{max}| < 1000\mu\varepsilon \qquad \text{(Bone resportion)} \\ 0, & \text{if } 1000\mu\varepsilon \leq |\varepsilon_{i,j}^{max}| \leq 1500\mu\varepsilon \qquad \text{(Lazy zone)} \\ 1, & \text{if } |\varepsilon_{i,j}^{max}| > 1500\mu\varepsilon \qquad \text{(Bone apposition)} \end{cases} \tag{5.18}$$

$$E_{i,j} = \begin{cases} 10\text{MPa}, & \text{if } \phi_{i,j} = -1 \\ E_{i-1,j}\dfrac{|\varepsilon_{i,j}^{max}|}{\varepsilon_{nt}}, & \text{if } \phi_{i,j} = 1 \\ E_{i-1,j}, & \text{if } \phi_{i,j} = 0 \end{cases} \tag{5.19}$$

The convergence criterion for isotropic adaptation was the same as the criterion used for orthotropic adaptation.

5.1.3 Adaptation algorithms for hybrid models

All three combined models were subjected to the same loading environment used in adapting the continuum and structural models.

5.1.3.1 Hybrid orthotropic model

The orthotropic material properties and shell thickness were iteratively updated using a combination of the orthtoropic continuum and structural adaptation algorithms. Initially, each continuum element was assigned a Young's modulus value of 300 MPa, a Poisson's ratio of 0.3 and a shear modulus value of 150 MPa. The upper limit for Young's modulus was set to 2 GPa (Dalstra et al., 1995b). The local coordinate systems of each element were aligned initially with the global coordinate system. Each shell element was assigned a Young's modulus value of 18 GPa, a Poisson's ratio of

0.3 and an initial thickness of 0.1 mm.

After each iteration, continuum orthotropic elements were adapted using the algorithm presented in §5.1.2.1 and the thickness of shell elements was adapted using a part of the algorithm presented in Chapter 4, §4.1.2. Convergence was achieved when both criteria for continuum orthotropic adaptation and structural shell adaptation were satisfied simultaneously.

5.1.3.2 Hybrid isotropic model

Similarly, the isotropic material properties and shell thickness were iteratively updated using a combination of the isotropic continuum and structural adaptation algorithms. Initially, each element was assigned a Young's modulus value of 300 MPa with an upper limit of 2 GPa, and a Poisson's ratio of 0.3. Each shell element was assigned a Young's modulus value of 18 GPa, a Poisson's ratio of 0.3 and an initial thickness of 0.1 mm.

After each iteration, continuum isotropic elements were adapted using the algorithm presented in §5.1.2.2 and the thickness shell elements was adapted using the algorithm presented in Chapter 4, §4.1.2. Convergence was achieved when both criteria for continuum isotropic adaptation and structural shell adaptation were satisfied simultaneously.

5.1.3.3 Hybrid structural model

The hybrid structural model was adapted using the algorithm presented in Chapter 4, §4.1.2, as the continuum elements had a constant elastic modulus throughout the adaptation process. The structural elements were assigned the same initial properties as in the purely structural model, whereas the continuum elements, which would maintain the same elastic modulus throughout the adaptation process, were assigned

isotropic material properties, with a Young's modulus value of 50 MPa, and a Poisson's ratio of 0.3, matching the minimum elastic modulus value in the CT scan derived model.

5.2 Results

5.2.1 Orthotropic model

5.2.1.1 Bone architecture

The continuum orthotropic model of the pelvis was found to converge after 60 iterations, when the average change in Young's moduli of elements outside the dead zone was less than 2%. The distributions of directional Young's moduli are shown in Figures 5.3, 5.4 and 5.5. For all three Young's moduli, large values were found mainly across the sacrum, around the sacroiliac joint on the ilium, along the arcuate line and in the region of the greater sciatic notch. Albeit more sparsely, stiff elements were identified along the superior and inferior pubic rami, at the anterior inferior iliac spine and in the acetabulum. Interestingly, there were no clear differences between distributions of the three Young's moduli. In addition, regions with stiff elements appeared to also contain elements with low stiffness, rather than a continuous area of elements with large Young's moduli. These results suggest that there are no distinct regions in the pelvis that exhibit exclusively compressive or tensile behaviours under loading scenarios associated with daily physical activities. In contrast, long bones, such as the femur, were found to have distinct regions which are loaded mainly in compression or tension (Geraldes et al., 2016).

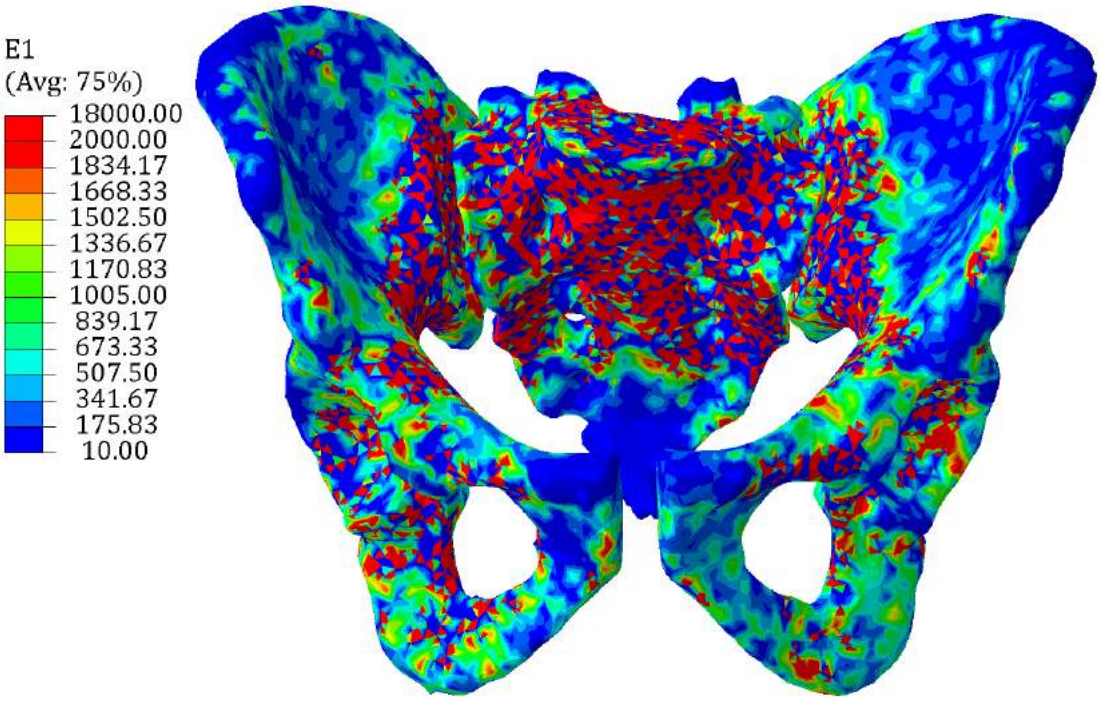


Figure 5.3: Distribution of E_1 (MPa), associated with minimum principal strains, across the pelvis

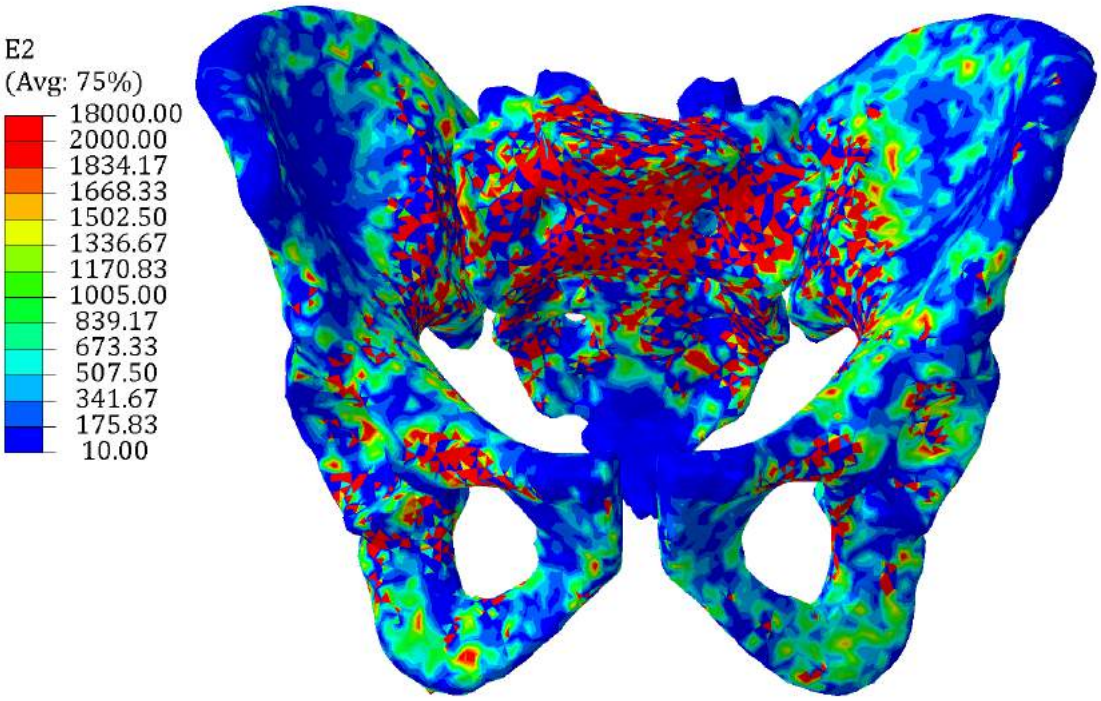


Figure 5.4: Distribution of E_2 (MPa), associated with medium principal strains, across the pelvis

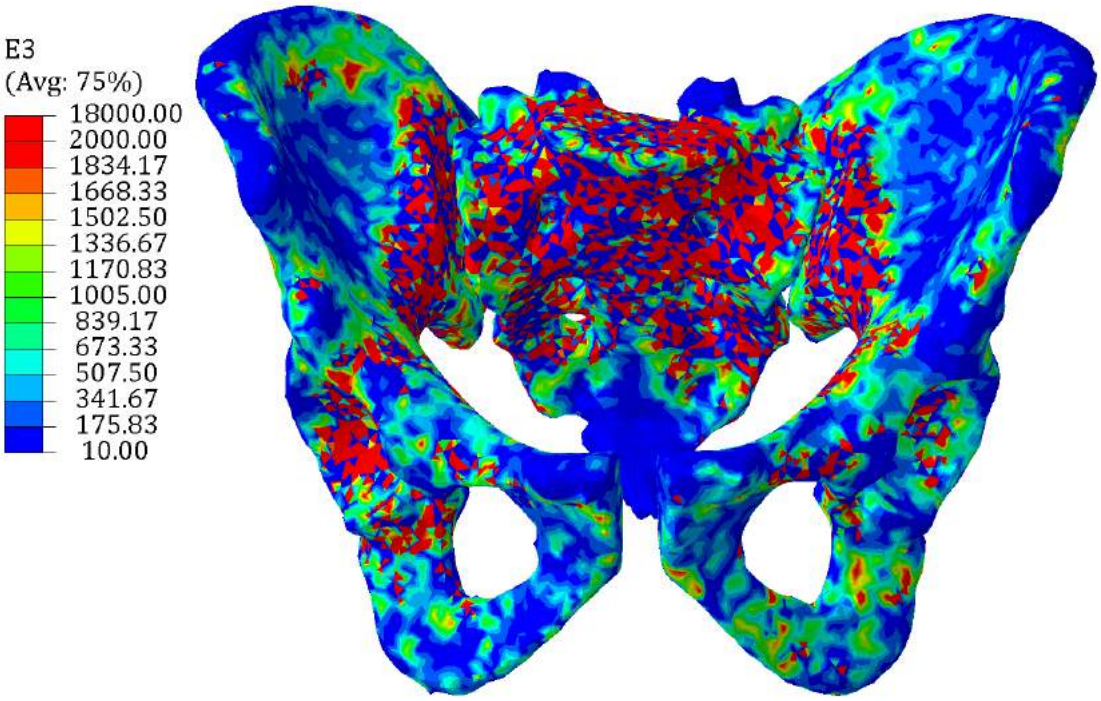


Figure 5.5: Distribution of E_3 (MPa), associated with maximum principal strains, across the pelvis

The density of each element was calculated using a method developed by Geraldes et al. (2016), described in full the the electronic supplementary material of the journal article. Briefly, the method considers a cube of unit volume to calculate the relative density (ratio of solid volume to total volume) based on the dimensions of each internal cuboid representing the solid phase, assumed to be isotropic (Figure 5.6). The thickness of each cuboid was calculated based on the ratios between the orthotropic Young's moduli and shear moduli compared to the maximum permissible values. The maximum thickness of each cuboid was limited to 0.7286, which was obtained by taking into account the minimum bone porosity (p_{min} =0.02). Each thickness was calculated using Equation 5.20, where E_{max} and G_{max} are the maximum value of Young's modulus and shear modulus, respectively.

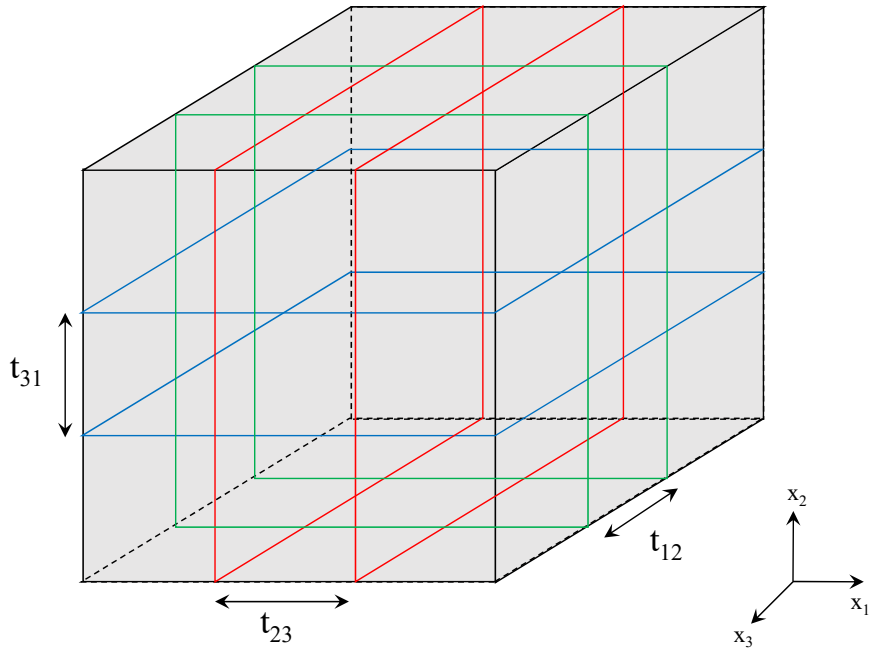


Figure 5.6: Cube of unit volume with internal cuboids representing the solid phase for each of the three orthotropic directions (x_1, x_2, x_3)

$$t_{ij} = \max\left(\frac{E_i}{E_{max}}, \frac{G_{ij}}{G_{max}}\right) t_{max} \tag{5.20}$$

The relative density of each element was obtained using Equation 5.21. Finally, the values were then multiplied by a tissue density value of 2.11 g/cm^3 (Geraldes et al., 2016).

$$\overline{\rho} = t_{12} + (1 - t_{12})(t_{23} + t_{31} - t_{23}t_{31}) \tag{5.21}$$

The distribution of the mean of Young's moduli along with the density distribution across the model is shown in Figure 5.7. The mean Young's modulus for each element

was calculated as the average between the three directional Young's moduli (Eq. 5.22).

$$E_{mean} = \frac{E_1 + E_2 + E_3}{3} \tag{5.22}$$

Regions with large mean Young's modulus and high density were found around the sacroiliac joint, along the arcuate line, around the top of the sacrum, along the superior pubis ramus, in the acetabulum and between the posterior inferior iliac spine and greater sciatic notch. Low mean Young's modulus and low densities were found at the iliac fossa, ischial tuberosity and inferior sacrum.

To obtain a clearer view of the distribution of element orientations, a number of transverse slices of the model were visualised by plotting the dominant orientation of each element within the slice. In addition, the shading intensity of each element is based on the dominant Young's modulus value of the element. The slices were visually compared to corresponding transverse slices from the CT data (Figure 5.8). Across all slices, it can be observed that cortical bone has developed as elements near the surface of bone have high Young's moduli and the dominant orientations appear to be somewhat aligned with the surface of bone. In terms of trabecular bone, the model and CT images share similar region with low or high stiffness.

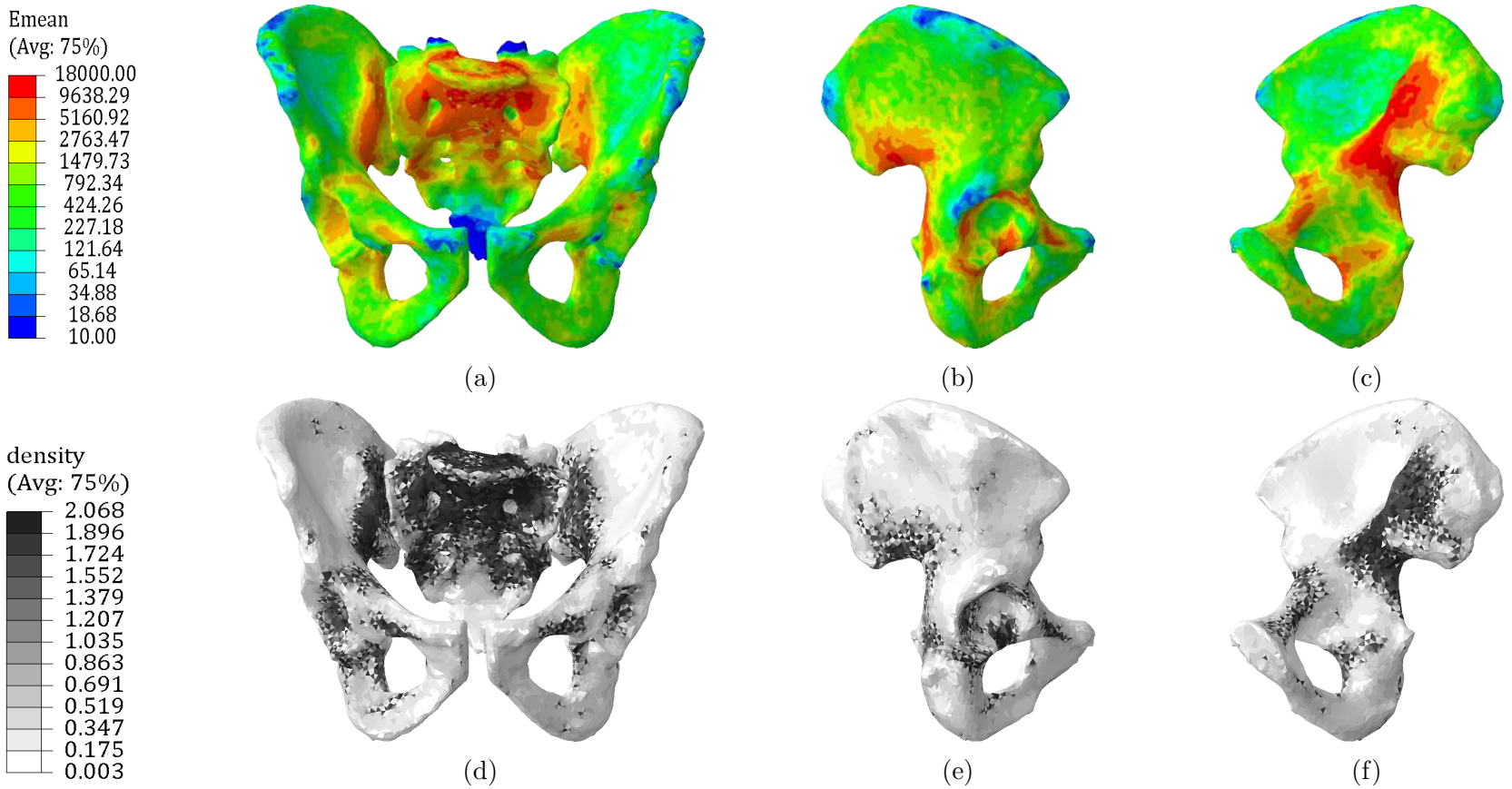


Figure 5.7: Distributions of mean Young's moduli (MPa) (a,b,c) and density (g/cm^3) (d,e,f) across the continuum orthotropic model

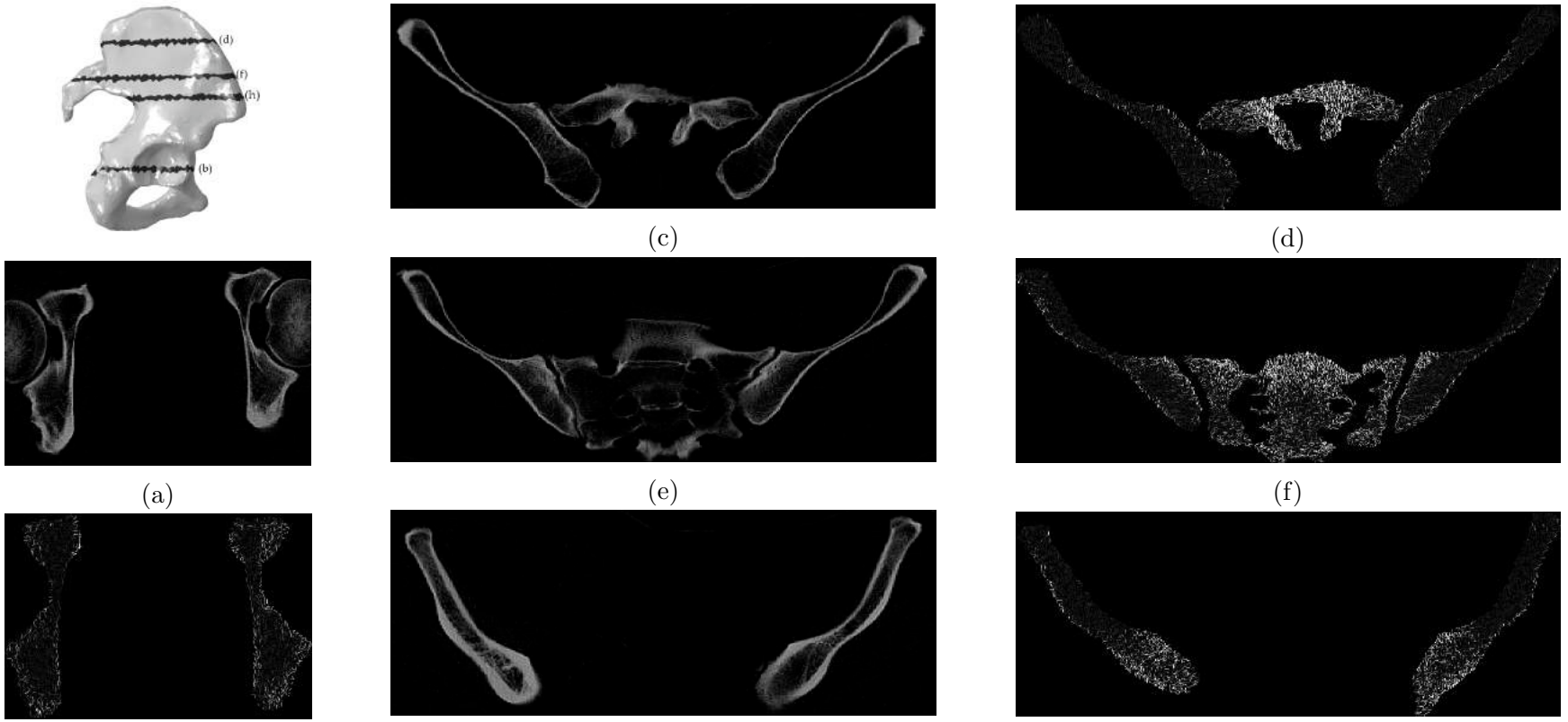


Figure 5.8: Figure illustrating transverse slices from the CT scans (a, c, e, g) shown along with corresponding slices of the pelvic model (b, d, f, h) generated using an in-house code developed in MATLAB. The shading intensity of each element is based on the dominant Young's modulus (black - low E; white - high E)

5.2.1.2 Comparison to CT derived model

The response of the converged orthotropic model to a simple load case was compared to the subject specific model described in Chapter 3, §3.4. To compare the surface strains of both models in a consistent, a layer of shell elements with a uniform thickness of 1 mm and low stiffness (E=0.1MPa) were included in the orthotropic model. The absolute maximum principal strains on the surface of both models are shown in Figure 5.9. The maximum and minimum principal strains across the surface of the orthotropic model and subject specific model were compared (Figure 5.10).

The coefficients of correlation for both minimum (0.881) and maximum (0.886) principal strains show a good agreement between the strains predicted by the orthotropic model and CT derived model.

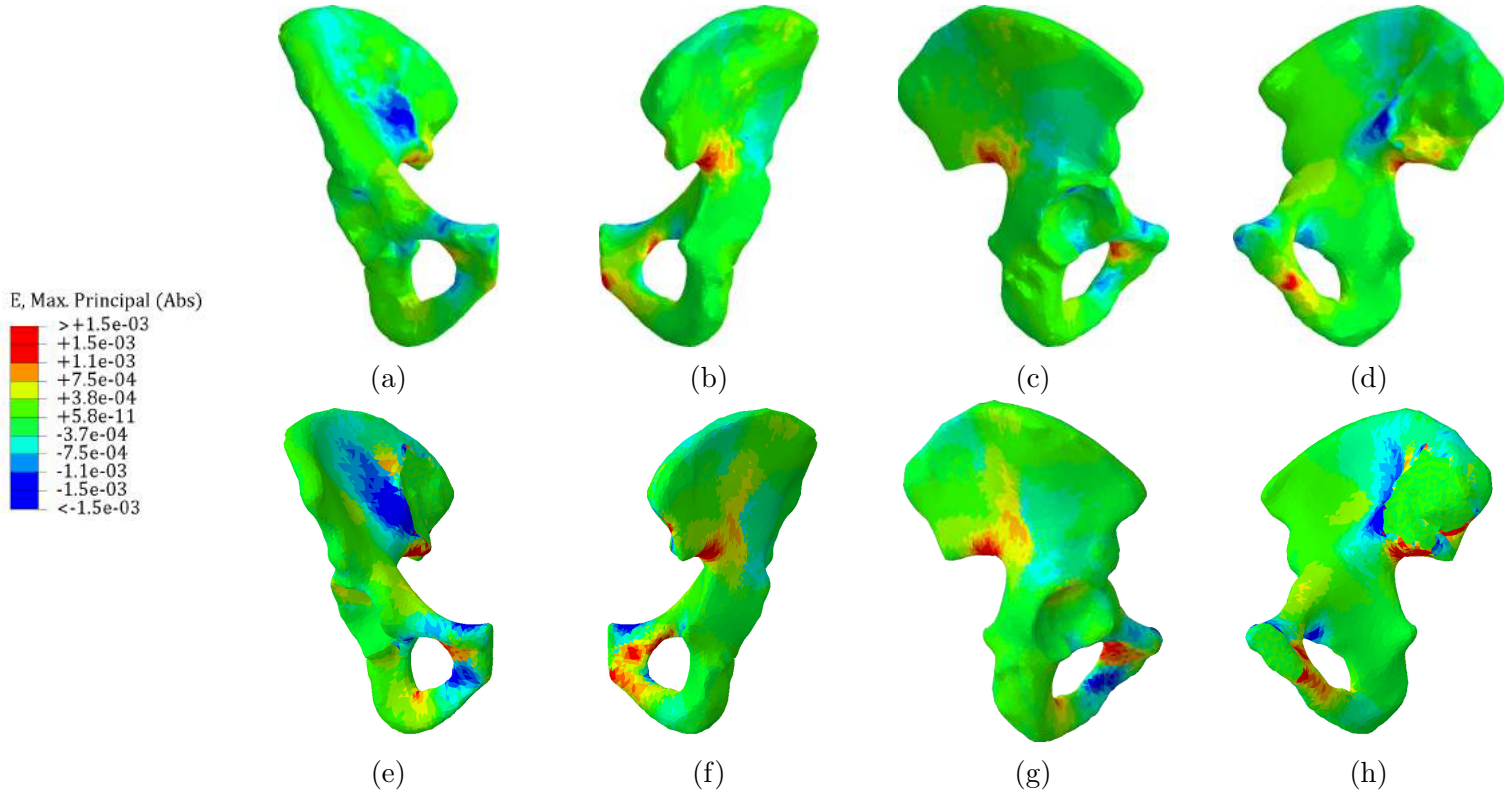
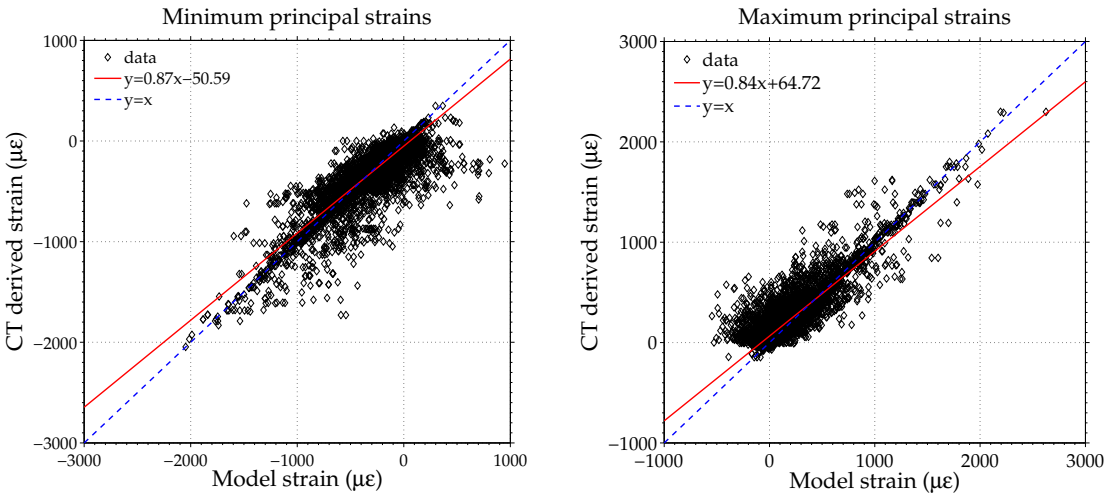


Figure 5.9: Absolute maximum principal strain distribution for continuum orthotropic model (a,b,c,d) and scan derived model (e,f,g,h) in response to the loading condition shown in Figure 4.5

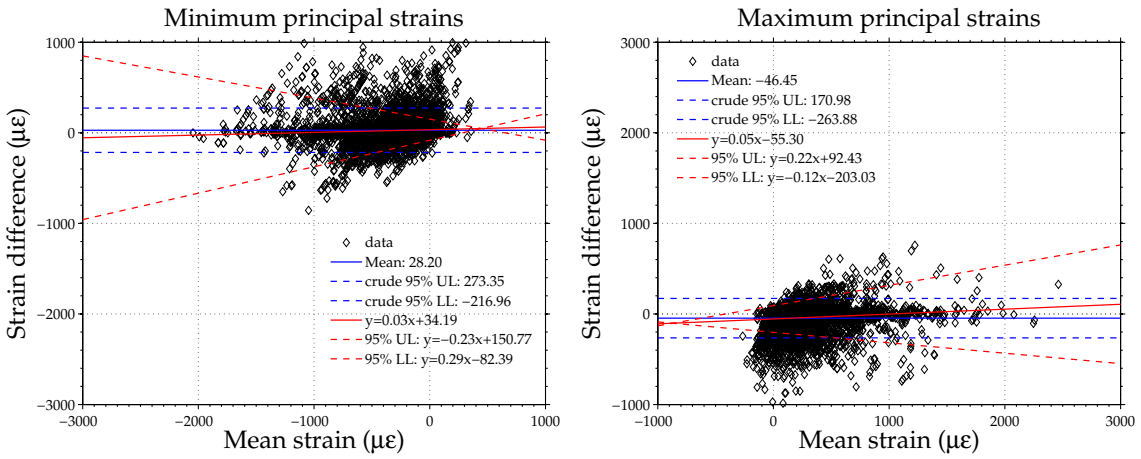


(a) Correlation coefficient: 0.881

(b) Correlation coefficient: 0.886

Figure 5.10: Comparison between the minimum (a) and maximum (b) principal strains across the surface of the continuum orthotropic model (x axis) and CT derived model (y axis). Lines of best fit are shown in red for each case, with y=x line shown in dashed blue.

Bland-Altman plots (Bland and Altman, 1999) were used to compare the strain difference between models and the average strain (Figure 5.11). The mean differences between the orthotropic model and the CT scan derived model were found to be $28.20\mu\epsilon$ for minimum principal strains and $-46.45\mu\epsilon$ for maximum principal strains. Linear regression lines fitting the data show a proportional bias ($p<0.05$) and indicate that using crude 95% confidence intervals would not be appropriate. V-shaped limits of agreement were constructed. Both types of agreement limits indicate a good match between the orthotropic model and the CT scan derived model.



(a) (b)

Figure 5.11: Bland-Altman plots showing (a) minimum and (b) maximum principal strains as difference between the orthotropic model and CT derived model versus mean. Mean value and crude 95% confidence intervals are shown in blue. Regression lines and V-shaped 95% confidence intervals are shown in red.

5.2.2 Isotropic model

5.2.2.1 Bone architecture

The continuum isotropic model reached a state of convergence after 25 iterations. The density of each element was calculated using the method presented in §5.2.1.1, adapted to an isotropic material. The Young's modulus and density distributions of the converged isotropic model are shown in Figure 5.12. Regions with high density and stiffness were found along the arcuate line, anterior superior sacrum, superior pubis ramus, acetabulum and near the greater sciatic notch. Conversely, large parts of the ilium, inferior pubis ramus and inferior sacrum were found to have a low density and stiffness.

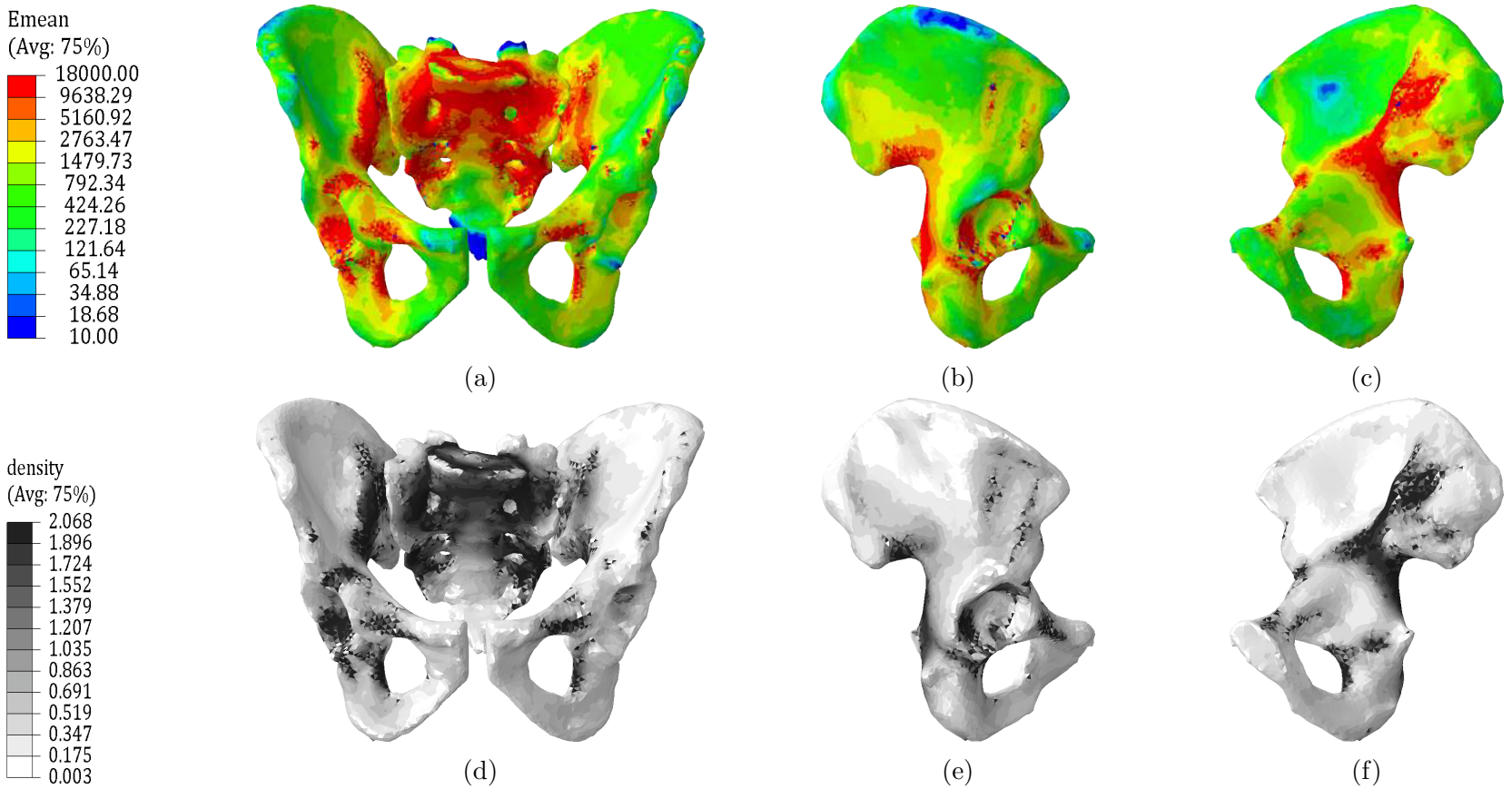


Figure 5.12: Distributions of mean Young's moduli (MPa) (a,b,c) and density (g/cm^3) (d,e,f) across the continuum isotropic model

5.2.2.2 Comparison to CT derived model

The response of the converged isotropic model to a simple load case was compared to the subject specific model described in Chapter 3, §3.4. To compare the surface strains of both models correctly, a layer of shell elements with a uniform thickness of 1 mm and low stiffness (E=0.1MPa) were included in the isotropic model. The absolute maximum principal strains on the surface of both models are shown in Figure 5.13. The maximum and minimum principal strains across the surface of the isotropic model and subject specific model were compared (Figure 5.14).

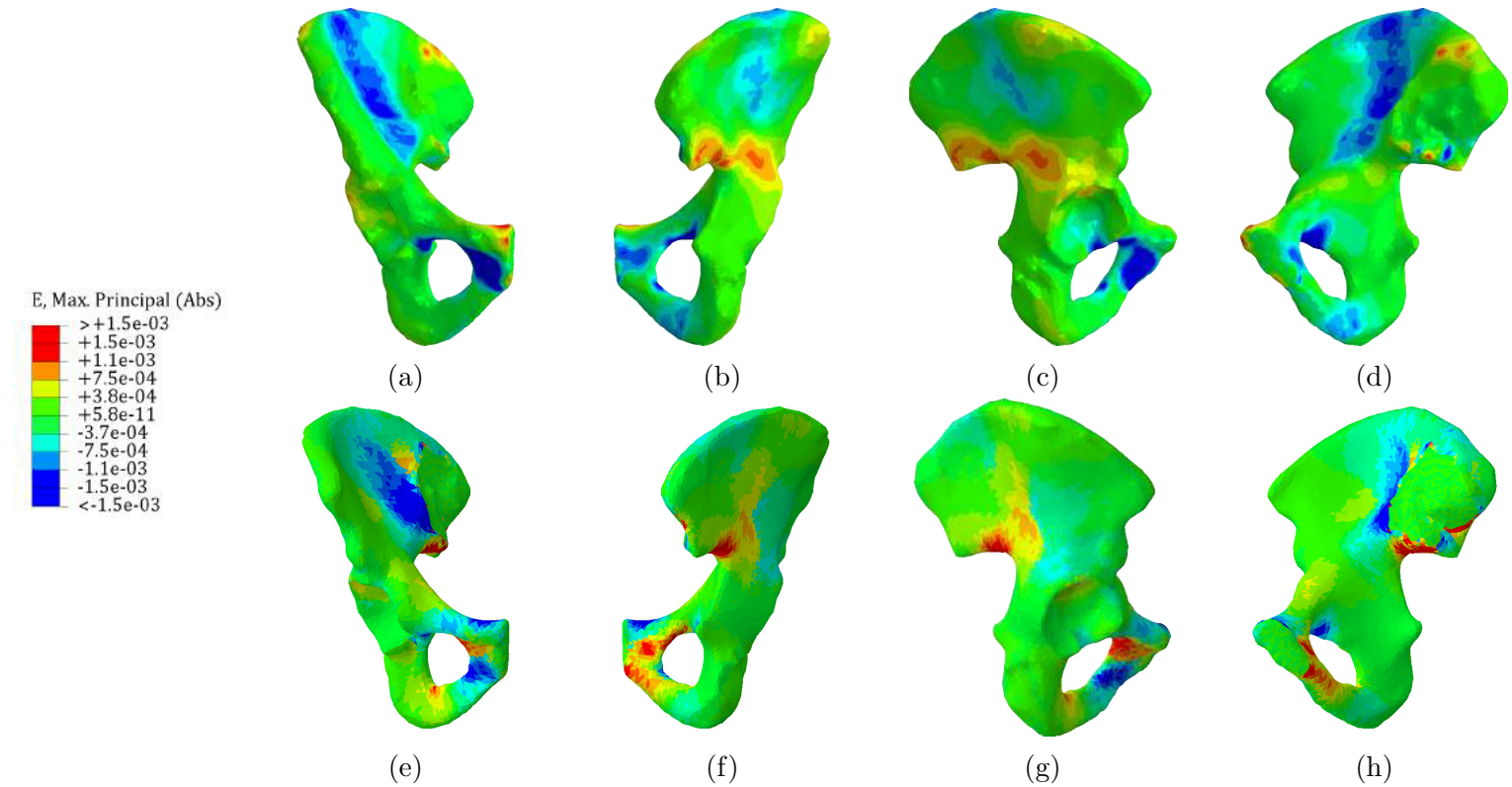
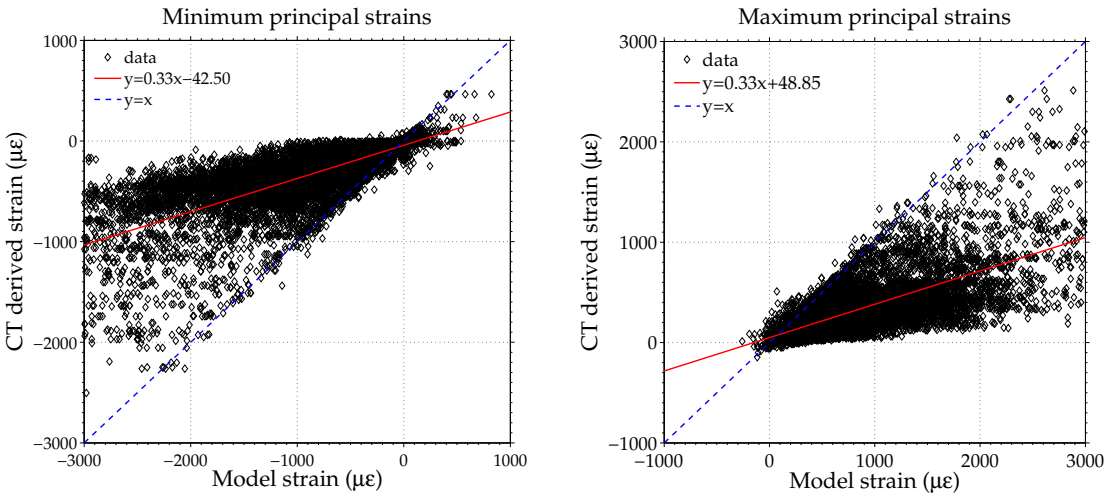


Figure 5.13: Absolute maximum principal strain distribution for continuum isotropic model (a,b,c,d) and scan derived model (e,f,g,h) in response to the loading condition shown in Figure 4.5

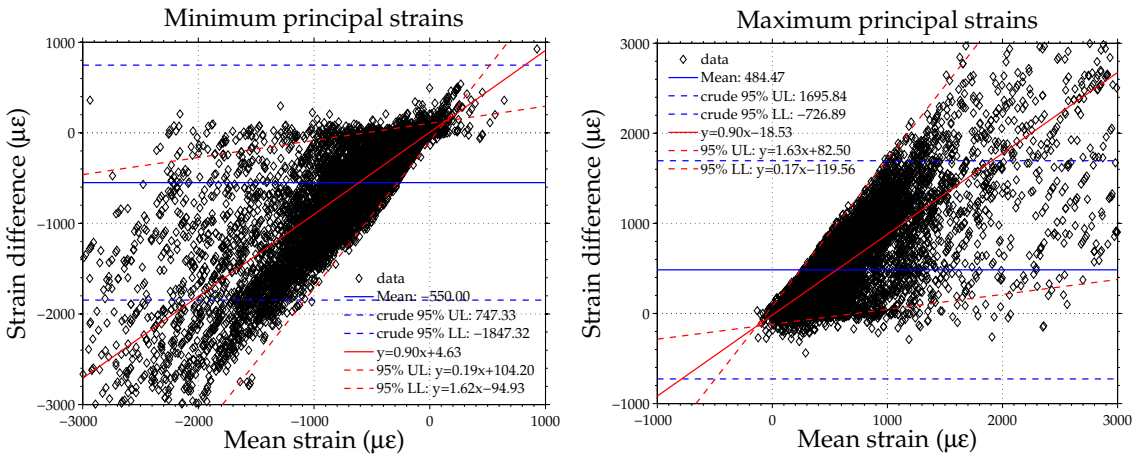


(a) Correlation coefficient: 0.798

(b) Correlation coefficient: 0.794

Figure 5.14: Comparison between the minimum (a) and maximum (b) principal strains across the surface of the continuum isotropic model (x axis) and CT derived model (y axis). Lines of best fit are shown in red for each case, with y=x line shown in dashed blue.

Bland-Altman plots were used to compare the strain difference between models and the average strain (Figure 5.15). The mean differences between the isotropic model and the CT scan derived model were found to be $-550\mu\epsilon$ for minimum principal strains and $484.87\mu\epsilon$ for maximum principal strains. Linear regression lines fitting the data show a proportional bias ($p<0.05$) and indicate that using crude 95% confidence intervals would not be appropriate. V-shaped limits of agreement were constructed and indicate that the isotropic model is less stiff than the CT scan derived model in most of the regions.



(a) (b)

Figure 5.15: Bland-Altman plots showing (a) minimum and (b) maximum principal strains as difference between the isotropic model and CT derived model versus mean. Mean value and crude 95% confidence intervals are shown in blue. Regression lines and V-shaped 95% confidence intervals are shown in red.

5.2.3 Hybrid orthotropic model

5.2.3.1 Bone architecture

The hybrid orthotropic model of the pelvis was found to converge after 44 iterations. The cortical thickness distribution is illustrated in Figure 5.16. Thick shell elements appeared at the superior sacrum, around the sacroiliac joint, along the superior pubic ramus and in the region of the greater sciatic notch. Areas with thin shell elements were found on the superior ilium, inferior pubic ramus, ischial tuberosity and supraacetabular region.

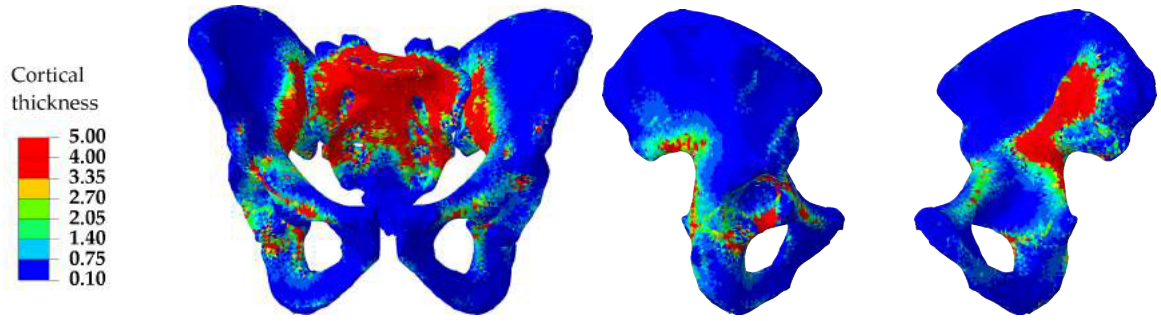


Figure 5.16: Cortical thickness distribution for the converged model.

The distribution of mean Young's moduli along with the density distribution of the continuum elements of the hybrid orthotropic model is shown in Figure 5.17. The mean Young's modulus for each element was calculated as the average between the three directional Young's moduli (Eq. 5.22). The density of each element was calculated using the method presented in §5.2.1.1.

Regions with large mean Young's modulus and high density were found around the sacroiliac joint, on the arcuate line close to the sacrum, around the top of the sacrum, along the superior pubis ramus, around the superior acetabulum and between the posterior inferior iliac spine and greater sciatic notch. Low mean Young's modulus and low densities were found at the iliac fossa, ischial tuberosity, inferior sacrum and

superior ilium.

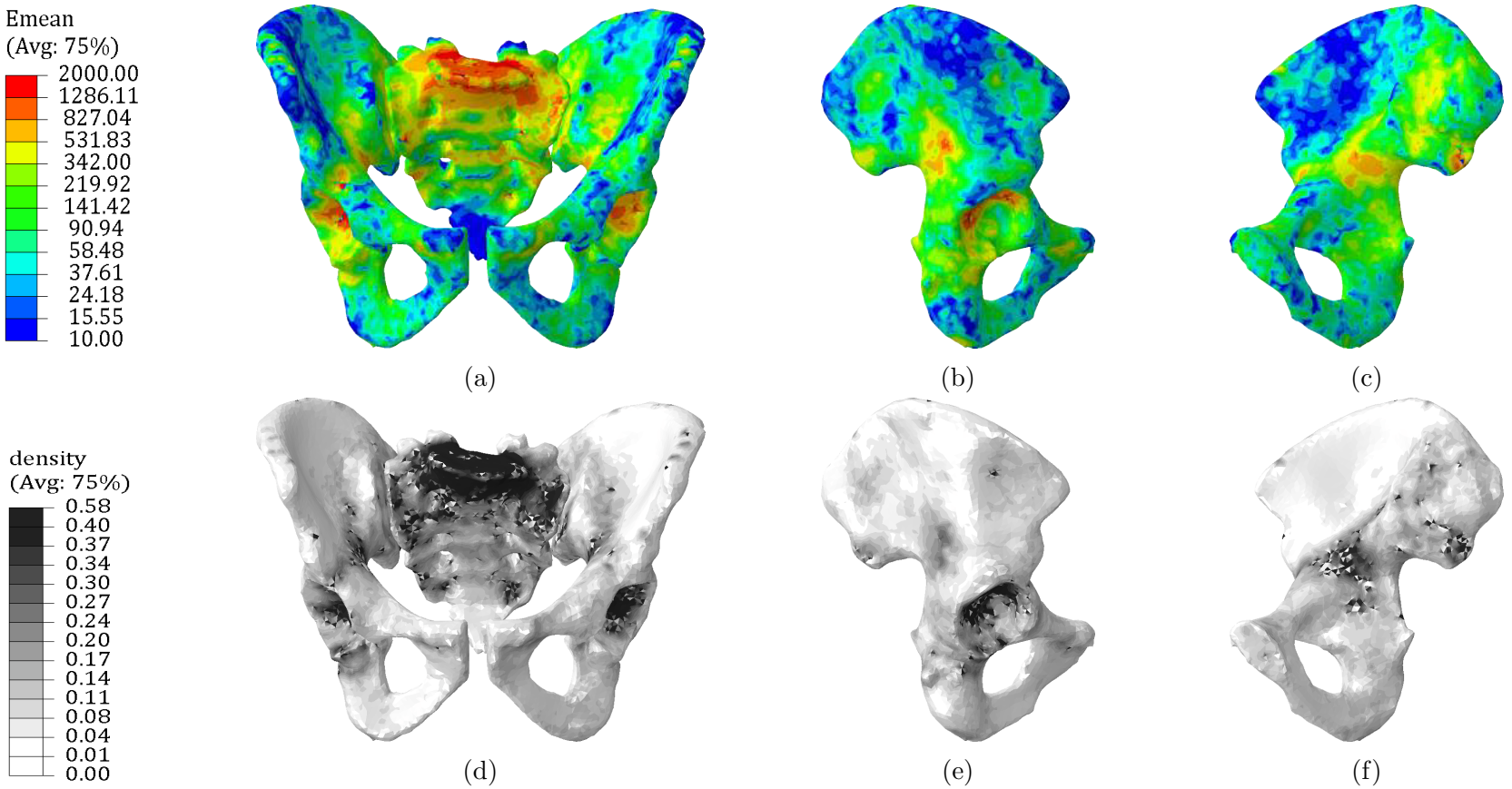


Figure 5.17: Distributions of mean Young's moduli (MPa) (a,b,c) and density (g/cm^3) (d,e,f) across trabecular bone of the hybrid orthotropic model

5.2.3.2 Comparison to CT derived model

The response of the converged hybrid orthotropic model to a simple load case was compared to the subject specific model described in Chapter 3, §3.4. As opposed to the previous two models, the current model already had a layer of shell elements. The absolute maximum principal strains on the surface of both models are shown in Figure 5.18. The maximum and minimum principal strains across the surface of the hybrid orthotropic model and subject specific model were compared (Figure 5.19).

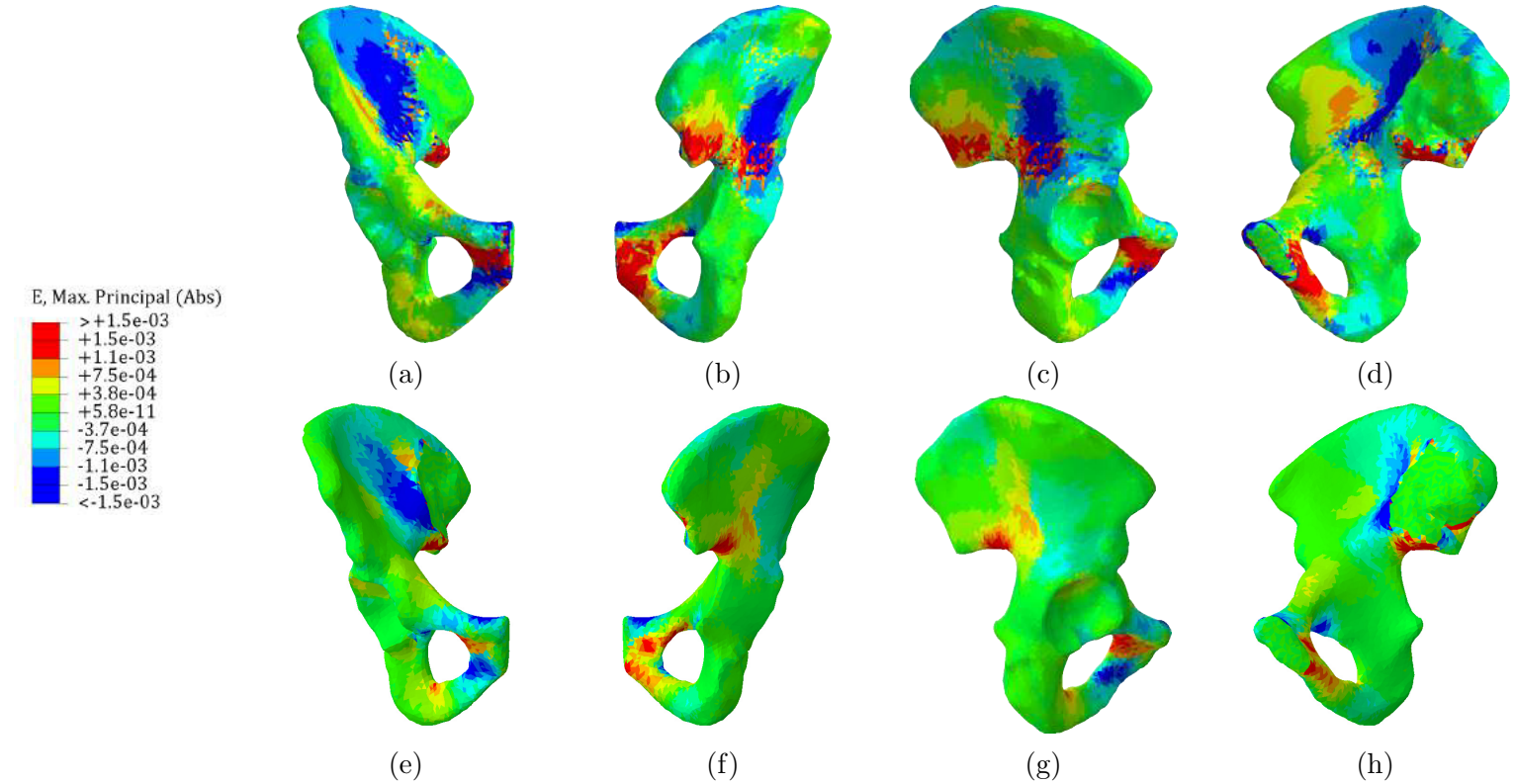
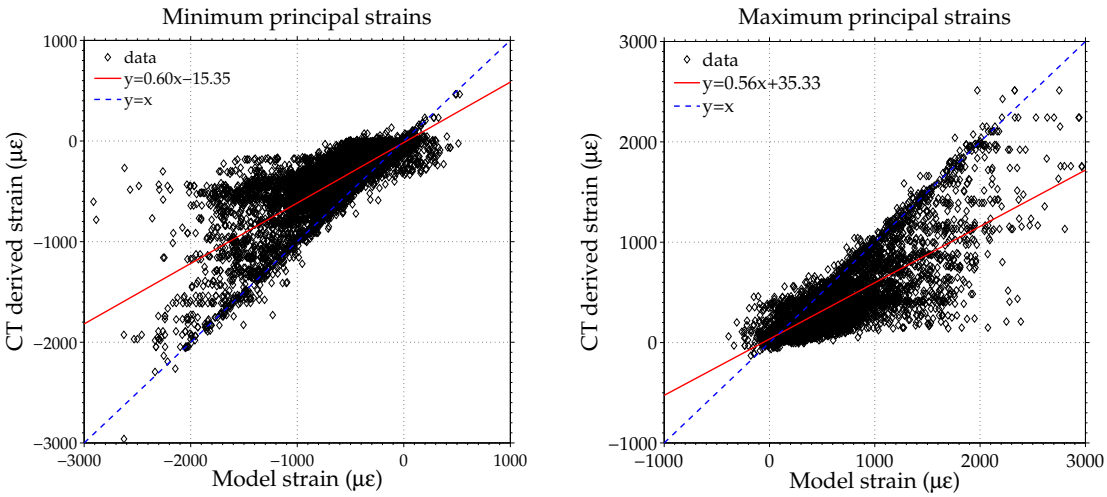


Figure 5.18: Absolute maximum principal strain distribution for hybrid orthotropic model (a,b,c,d) and scan derived model (e,f,g,h) in response to the loading condition shown in Figure 4.5



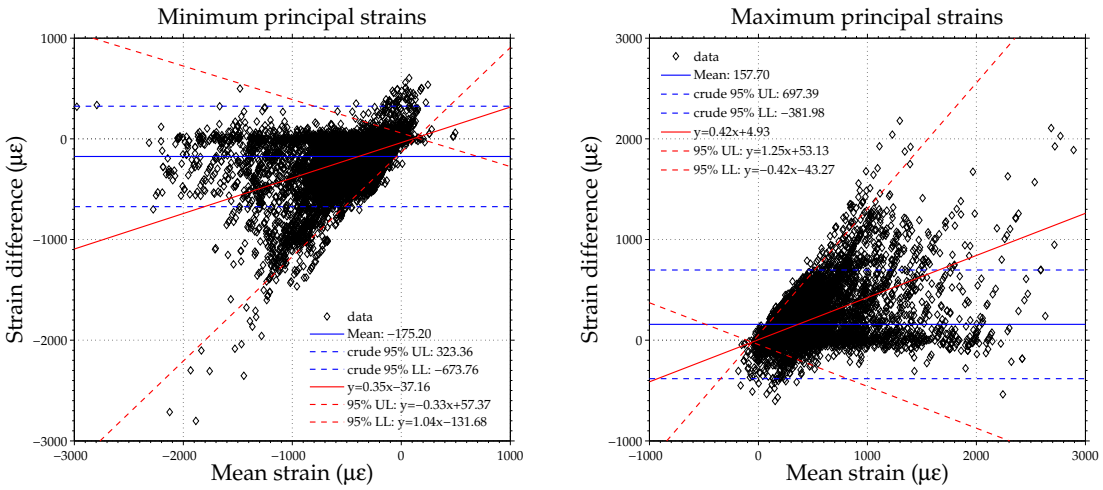
(a) Correlation coefficient: 0.837

(b) Correlation coefficient: 0.828

Figure 5.19: Comparison between the minimum (a) and maximum (b) principal strains across the surface of the hybrid orthotropic model (x axis) and CT derived model (y axis). Lines of best fit are shown in red for each case, with y=x line shown in dashed blue.

Bland-Altman plots were used to compare the strain difference between models and the average strain (Figure 5.20). The mean differences between the hybrid orthotropic model and the CT scan derived model were found to be $-175.2\mu\epsilon$ for minimum principal strains and $157.7\mu\epsilon$ for maximum principal strains. Linear regression lines fitting the data show a proportional bias ($p<0.05$) and indicate that using crude 95% confidence intervals would not be appropriate.

V-shaped limits of agreement were constructed and indicate that the hybrid orthotropic model is less stiff than the CT scan derived model in most of the regions



(a) (b)

Figure 5.20: Bland-Altman plots showing (a) minimum and (b) maximum principal strains as difference between the hybrid orthotropic model and CT derived model versus mean. Mean value and crude 95% confidence intervals are shown in blue. Regression lines and V-shaped 95% confidence intervals are shown in red.

5.2.4 Hybrid isotropic model

5.2.4.1 Bone architecture

The hybrid isotropic model reached a state of convergence after 24 iterations. The cortical thickness distribution is shown in Figure 5.21. Shell elements were the thickest at the superior sacrum, along the arcuate line, around the sacroiliac joint, along the superior pubic ramus and in the region of the greater sciatic notch. Areas with thin shell elements were found on the superior ilium, inferior pubic ramus, ischial tuberosity, pubic tubercle and supraacetabular region.

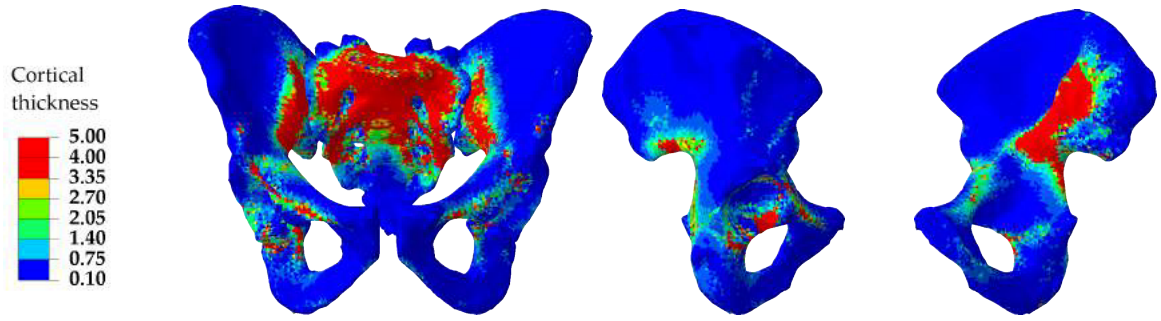


Figure 5.21: Cortical thickness distribution for the converged model.

The Young's modulus and density distributions of the continuum elements in the hybrid isotropic model are shown in Figure 5.22. The density of each element was calculated using the method presented in §5.2.1.1, adapted to an isotropic material. Regions with high density and stiffness were found along the arcuate line, anterior superior sacrum, superior pubis ramus, acetabulum and near the greater sciatic notch. Conversely, large parts of the ilium, inferior pubis ramus and inferior sacrum were found to have a low density and stiffness.

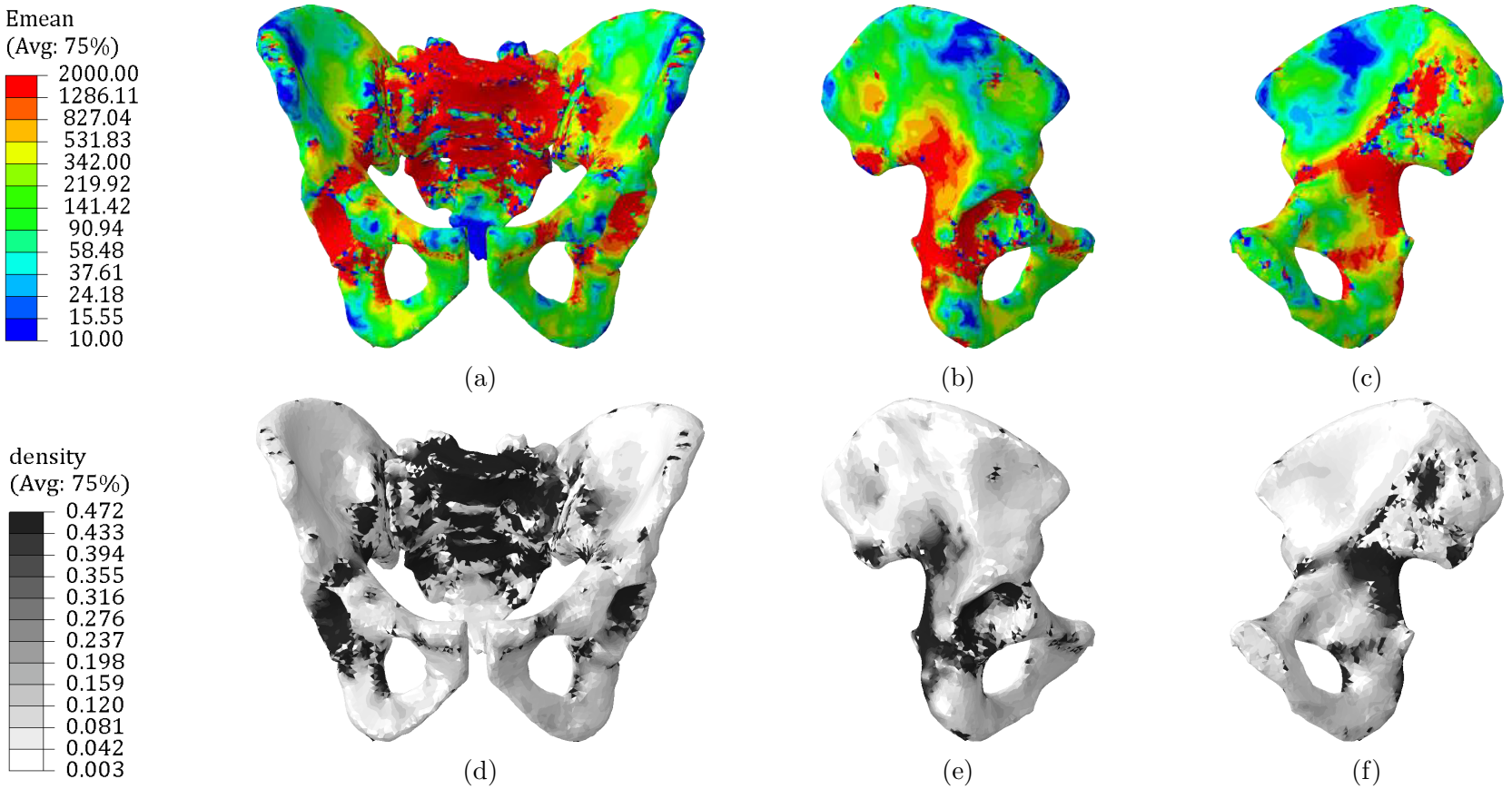


Figure 5.22: Distributions of Young's moduli (MPa) (a,b,c) and density (g/cm^3) (d,e,f) across trabecular bone of the hybrid isotropic model

The response of the converged hybrid isotropic model to a simple load case was compared to the subject specific model described in Chapter 3, §3.4. As opposed to the purely continuum models, the current model already had a layer of shell elements. The absolute maximum principal strains on the surface of both models are shown in Figure 5.23. The maximum and minimum principal strains across the surface of the isotropic model and subject specific model were compared (Fig. 5.24).

In contrast to the orthotropic model, the strains predicted by the hybrid isotropic model showed a weaker agreement to the strains predicted by the subject specific model, with a correlation coefficient of 0.84 for both minimum principal strains and maximum principal strains.

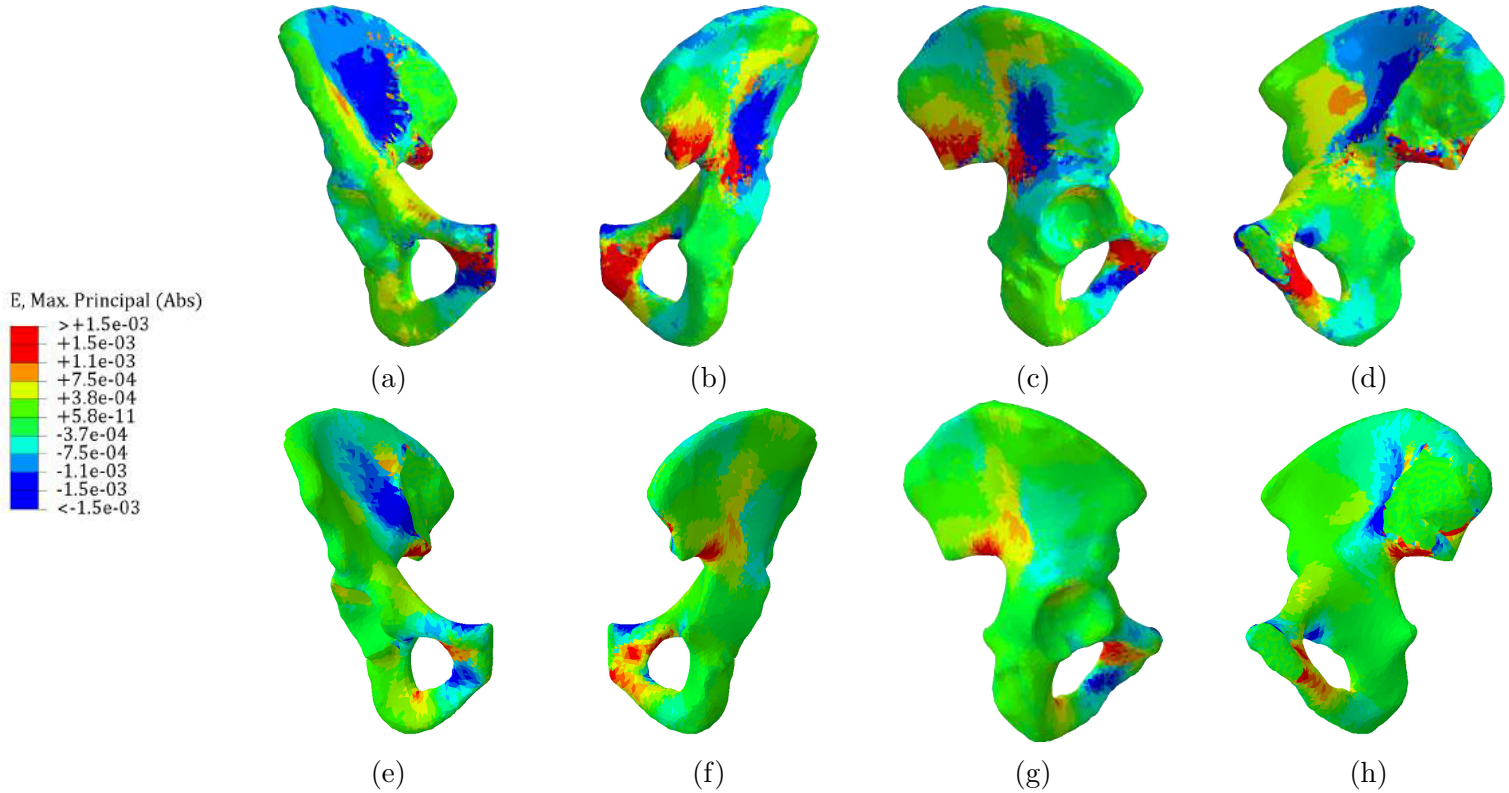
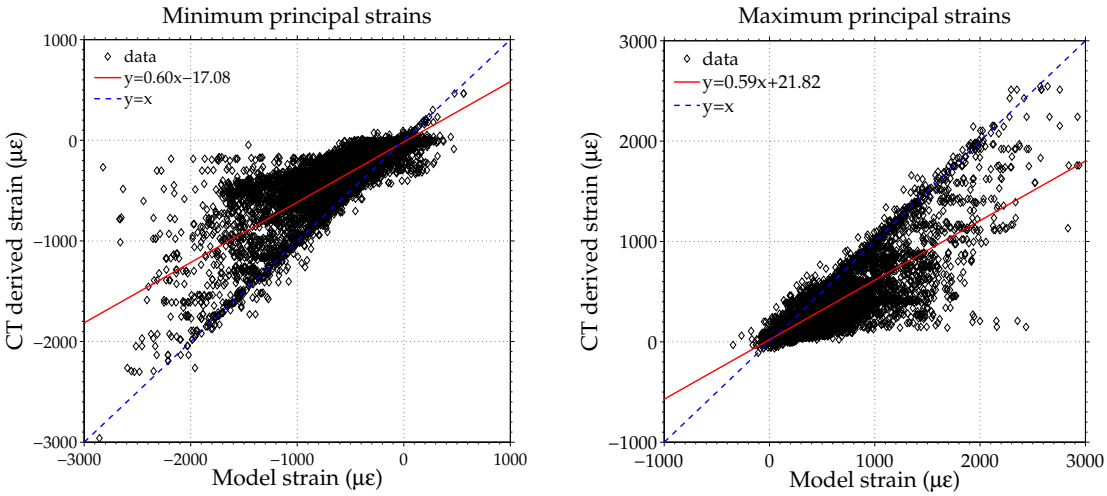


Figure 5.23: Absolute maximum principal strain distribution for hybrid isotropic model (a,b,c,d) and scan derived model (e,f,g,h) in response to the loading condition shown in Figure 4.5

5.2.4.2 Comparison to CT derived model



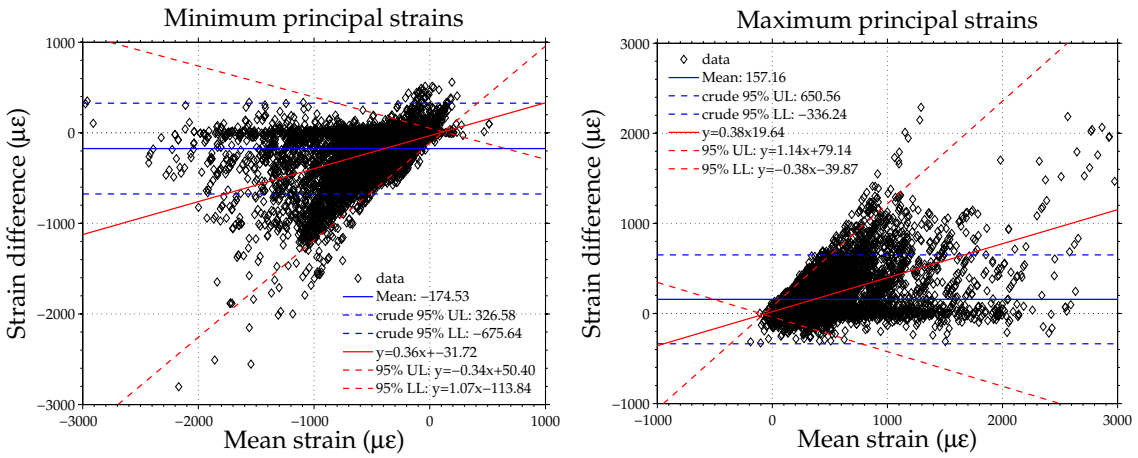
(a) Correlation coefficient: 0.844

(b) Correlation coefficient: 0.846

Figure 5.24: Comparison between the minimum (a) and maximum (b) principal strains across the surface of the hybrid isotropic model (x axis) and CT derived model (y axis). Lines of best fit are shown in red for each case, with y=x line shown in dashed blue.

Bland-Altman plots were used to compare the strain difference between models and the average strain (Figure 5.25). The mean differences between the hybrid isotropic model and the CT scan derived model were found to be $-174.5\mu\epsilon$ for minimum principal strains and $157.2\mu\epsilon$ for maximum principal strains. Linear regression lines fitting the data show a proportional bias ($p<0.05$) and indicate that using crude 95% confidence intervals would not be appropriate.

V-shaped limits of agreement were constructed and indicate that the hybrid isotropic model is less stiff than the CT scan derived model in most of the regions.



(a) (b)

Figure 5.25: Bland-Altman plots showing (a) minimum and (b) maximum principal strains as difference between the hybrid isotropic model and CT derived model versus mean. Mean value and crude 95% confidence intervals are shown in blue. Regression lines and V-shaped 95% confidence intervals are shown in red.

5.2.5 Hybrid structural model

5.2.5.1 Bone architecture

The hybrid structural model was found to converge after 34 iterations. Cortical thickness and trabecular radius distributions are shown in Figure 5.26. Regions with thick cortical elements were found at the superior sacrum, superior pubic ramus, along the gluteal surface, along the arcuate line and around the greater sciatic notch. Thin regions (0.1-0.5 mm) were identified on the ilium, inferior pubic ramus, ischial tuberosity and posterior superior iliac spine.

Regions with thick trabecular elements developed at the superior sacrum, supra acetabular region and along the arcuate line. The iliac fossa, inferior acetabulum, inferior pubic ramus and inferior sacrum were found to have few and thin (0.1-0.25 mm) trabecular elements.

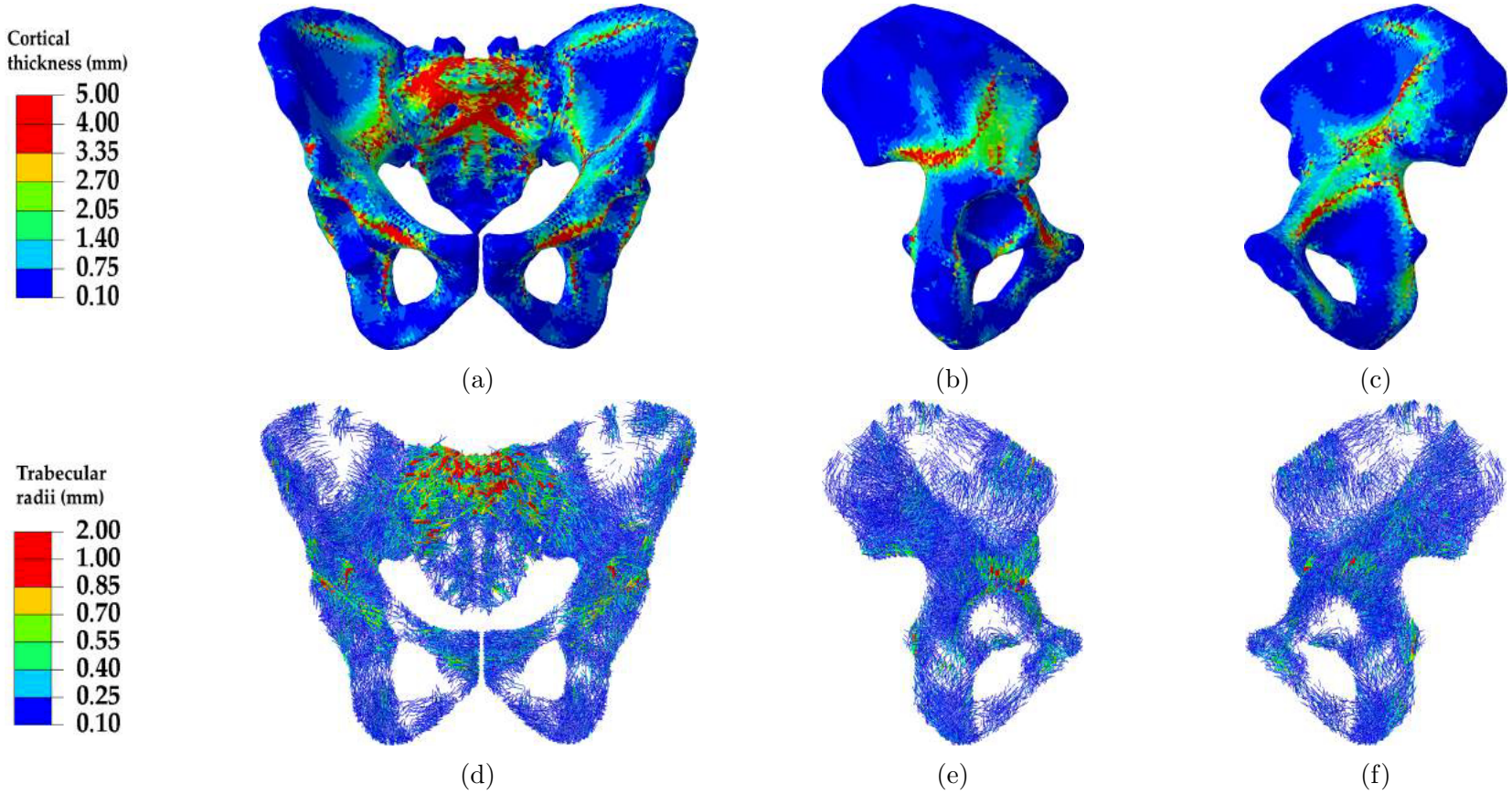


Figure 5.26: Contours of position dependent cortical thickness ranging from 0.1 mm to 5 mm are shown in the top row: (a) frontal view of pelvis, (b) anterior and (c) medial views of the right innominate. Trabecular elements' radii distribution ranging from 0.1 mm to 2 mm is shown in the bottom row: (d) frontal view, (e) anterior and (f) medial views of the right innominate. Trabecular elements with a radius of 1 μm were excluded for clarity.

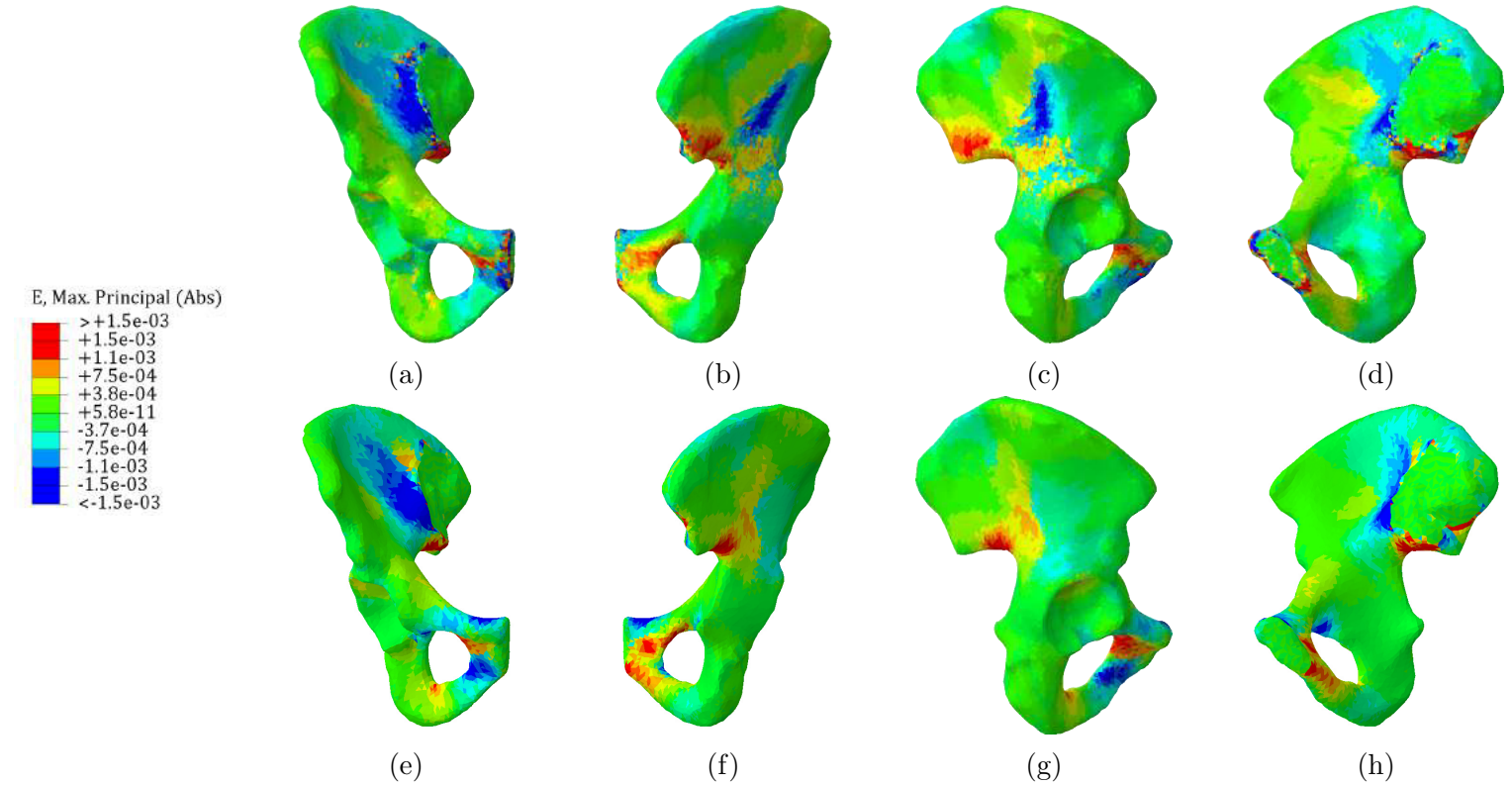
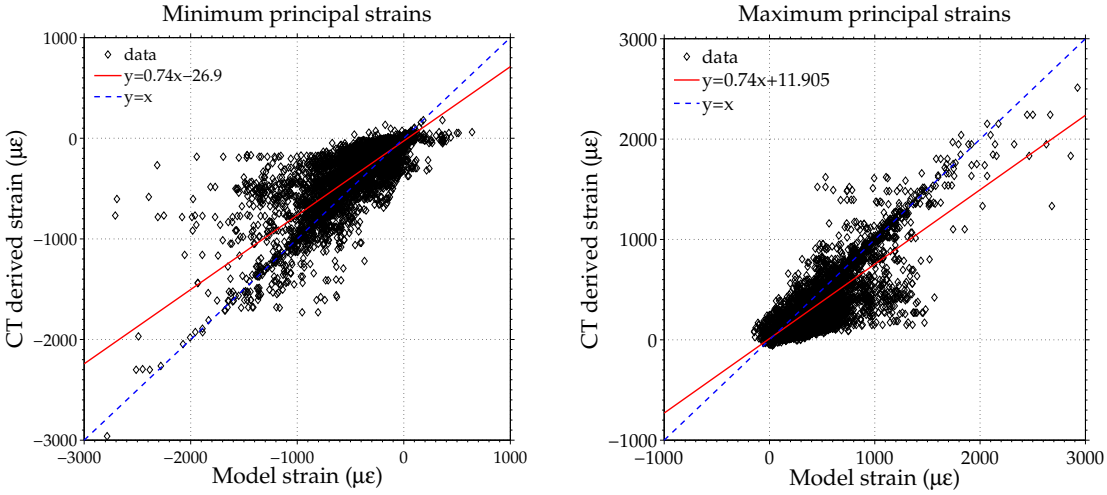


Figure 5.27: Absolute maximum principal strain distribution for hybrid structural model (a,b,c,d) and scan derived model (e,f,g,h) in response to the loading condition shown in Figure 4.5

5.2.5.2 Comparison to CT derived model

The response of the converged hybrid structural model to a simple load case was compared to the subject specific model described in Chapter 3, §3.4. The absolute maximum principal strains on the surface of both models are shown in Figure 5.27. The maximum and minimum principal strains across the surface of the isotropic model and subject specific model were compared (Figure 5.28).

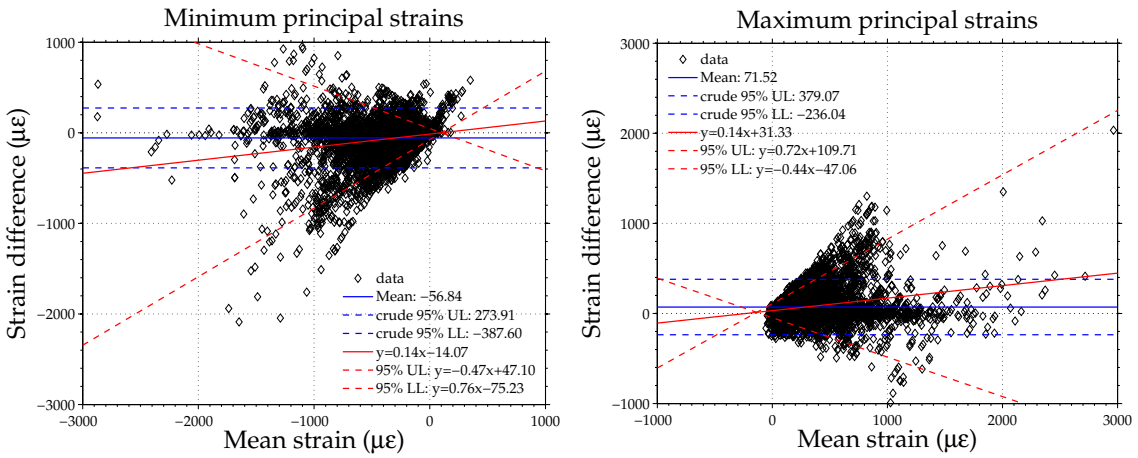
The coefficients of correlation for minimum and maximum principal strains were 0.846 and 0.848, respectively, indicating a good agreement between models.



(a) Correlation coefficient: 0.846 (b) Correlation coefficient: 0.848

Figure 5.28: Comparison between the minimum (a) and maximum (b) principal strains across the surface of the hybrid structural model (x axis) and CT derived model (y axis). Lines of best fit are shown in red for each case, with y=x line shown in dashed blue.

Bland-Altman plots were used to compare the strain difference between models and the average strain (Figure 5.29). The mean differences between the hybrid isotropic model and the CT scan derived model were found to be $-56.84\mu\epsilon$ for minimum principal strains and $71.52\mu\epsilon$ for maximum principal strains. Linear regression lines fitting the data show a proportional bias ($p<0.05$) and indicate that using crude 95% confidence intervals would not be appropriate.



(a) (b)

Figure 5.29: Bland-Altman plots showing (a) minimum and (b) maximum principal strains as difference between the hybrid structural model and CT derived model versus mean. Mean value and crude 95% confidence intervals are shown in blue. Regression lines and V-shaped 95% confidence intervals are shown in red.

5.3 Discussion and concluding remarks

This chapter presented a predictive framework for two continuum FE models of the pelvic construct with orthotropic and isotropic material properties. In addition, three combined continuum-structural models were developed and assessed to provide a comprehensive image of the capabilities of the modelling approaches presented in Chapter 4 and the present Chapter. In each case, the FE models were adapted to a loading environment corresponding to five physical activities common in daily life. The converged models were visually assessed in terms of bone architecture and compared to a CT scan derived FE model to quantitatively compare their mechanical response.

The cumulative density distributions predicted by the isotropic and orthotropic models were compared to the CT data (Figure 5.30). The main difference between the distributions is a much greater number of low density elements present in both predictive models compared to the CT data. In addition, the distribution of the orthotropic model shows an almost vertical increase at 1.5 g/cm^3, corresponding to stiff regions in the cortex.

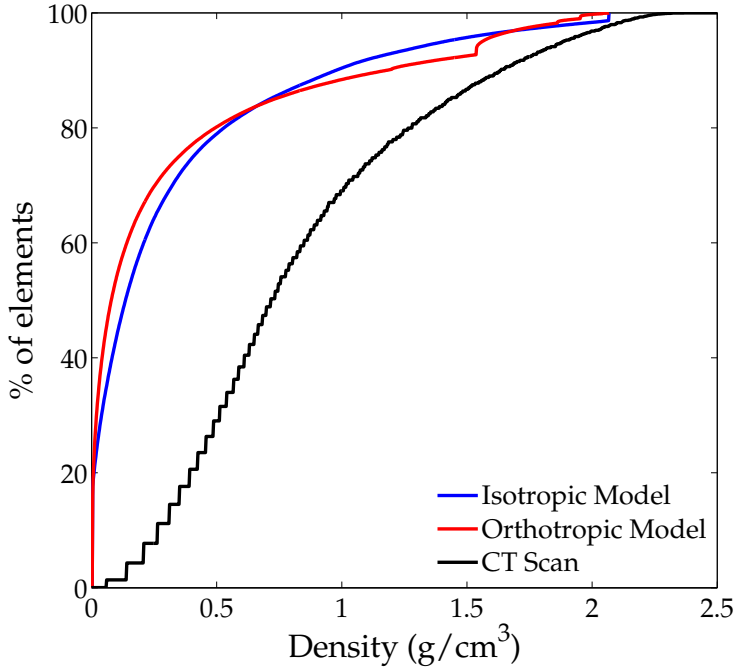


Figure 5.30: Cumulative distributions of predicted density values for the isotropic (blue) and orthotropic (red) models compared to density values extracted from the CT scan (black) in g/cm^3

A frequency distribution of Young's modulus values for the CT derived model, orthotropic model and isotropic model is shown in Figure 5.31. Both predictive models have a similar distribution of elastic moduli, with over 70% of elements having a stiffness lower than 2 GPa. Conversely, the CT scan derived model has approximately 40% low stiffness elements and a greater number of elements from 2 GPa up to 16 GPa compared to the predictive models.

The average Young's moduli of the orthotropic, isotropic and CT scan derived models were 819.2 MPa (median = 47.3 MPa), 1688 MPa (median = 541.6 MPa) and 3728.5 MPa (median = 2148.4 MPa), respectively. An interesting aspect is that, despite the orthotropic model having the lowest average stiffness, its behaviour under loading was more similar to the CT scan derived model than the isotropic model, as shown in Table 5.1. An explanation for this are the directional material properties associated with the orthotropic model, which enable regions of bone to

have a higher stiffness in a certain direction. Directional stiffness enables the use of less bone material whilst maintaining a higher overall stiffness, as opposed to an isotropic approach.

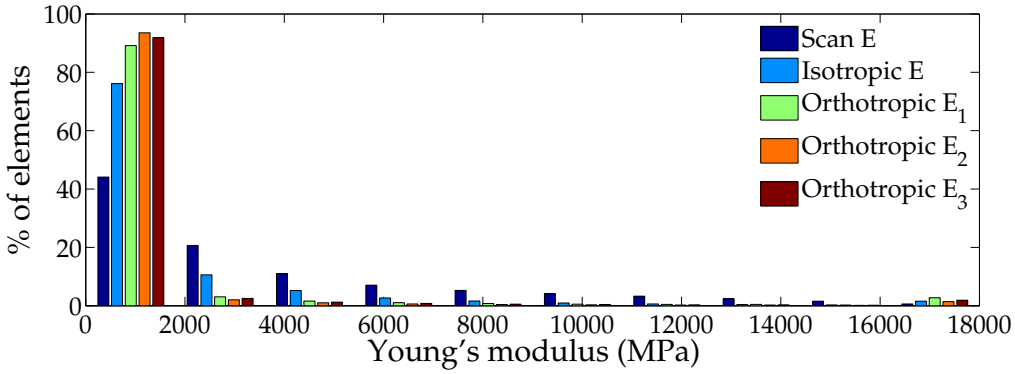


Figure 5.31: Frequency distribution of elastic moduli of the three continuum models: CT scan derived, isotropic and orthotropic.

Model	$\varepsilon_{\min}(R^2)$	$\varepsilon_{\max}(R^2)$	$\varepsilon_{\min}$ (slope)	$\varepsilon_{\max}$(slope)
Orthotropic	0.78	0.79	0.87	0.84
Isotropic	0.64	0.63	0.33	0.33
Hybrid orthotropic	0.70	0.69	0.60	0.59
Hybrid isotropic	0.71	0.72	0.60	0.59
Hybrid structural	0.72	0.72	0.74	0.74
Structural	0.66	0.65	0.69	0.70

Table 5.1: Coefficients of determination and slopes of the line of best fit for each adaptive model compared to the CT scan derived model. A slope value of 1 means a perfect match between models.

Frequency distributions of trabecular elastic moduli for the hybrid isotropic and hybrid orthotropic models are shown in Figure 5.32. Similar to the purely orthotropic model, over 80% of elements had at least one directional elastic modulus lower than 200 MPa. Young's moduli of the isotropic model were more distributed, with fewer low stiffness elements and consistently more elements than the orthotropic counterpart for values ranging from 200 MPa to 2000 MPa. Interestingly, both models compared

similarly to the CT derived model (Table 5.1), meaning that adding a layer of shell elements to represent the cortex improved the performance of the isotropic model, but caused the orthotropic model to have a less favourable response.

The frequency distribution of cortical shell thicknesses for the hybrid isotropic and orthotropic models, along with the hybrid structural and purely structural models is shown in Figure 5.33. The hybrid continuum models predicted a similar distribution of cortical thickness, which suggests that the drastic change in trabecular elastic modulus distribution for the hybrid isotropic model was the key factor in improving its performance with respect to the purely isotropic model when compared to the CT scan derived model.

The hybrid structural model performed slightly better than the purely structural model when compared to the CT scan derived model, suggesting that using background stiffness even at the start of the adaptation process can have an impact on the overall stiffness of the resulting model.

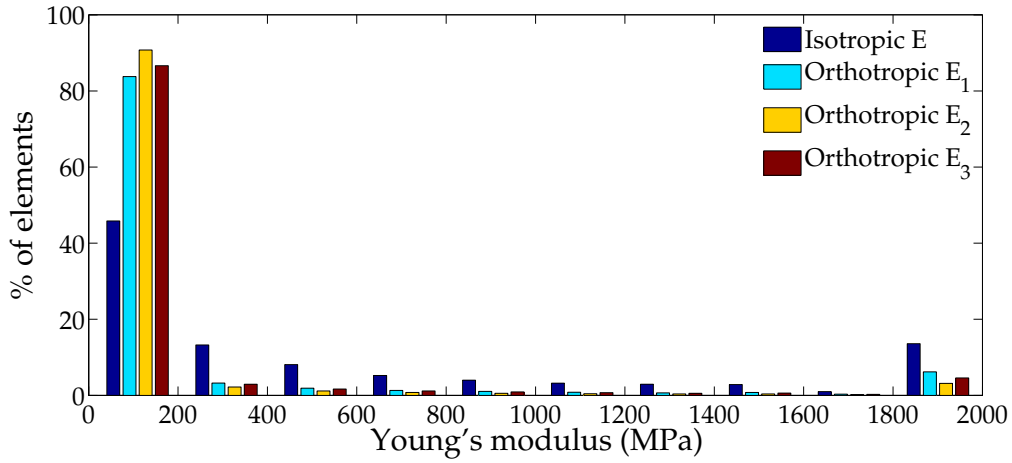


Figure 5.32: Frequency distribution of trabecular elastic moduli for the hybrid isotropic and hybrid orthotropic models.

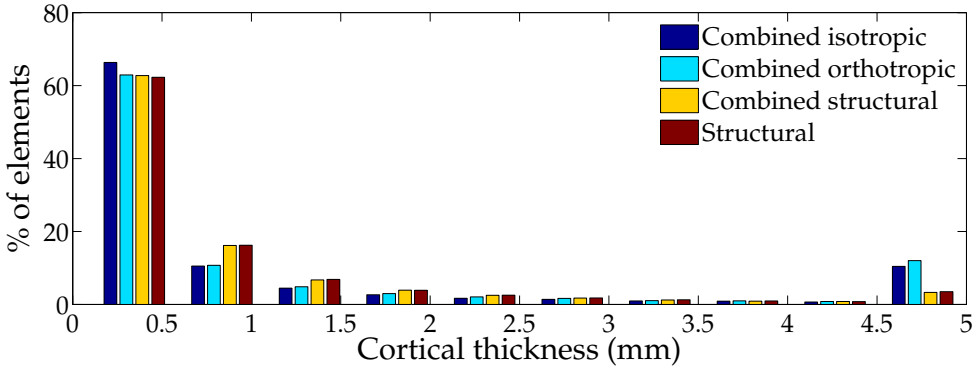


Figure 5.33: Frequency distribution of the cortical thickness for the hybrid isotropic, hybrid orthotropic, hybrid structural and structural models.

A distribution of Young's modulus with respect to density for the predictive orthotropic and isotropic models of the right pelvic innominate along with the empirical relationship for the CT scan derived model is shown in Figure 5.34.

The distributions of the three models can explain the reason for the orthotropic model having a more similar overall stiffness as the CT scan derived model as opposed to the isotropic model. The plots highlight how the dominant Young's modulus values (largest value of the three Young's moduli) in the elements of the orthotropic model increase its stiffness compared to the isotropic model as the mean Young's modulus values would suggest a less stiff model compared to the isotropic model.

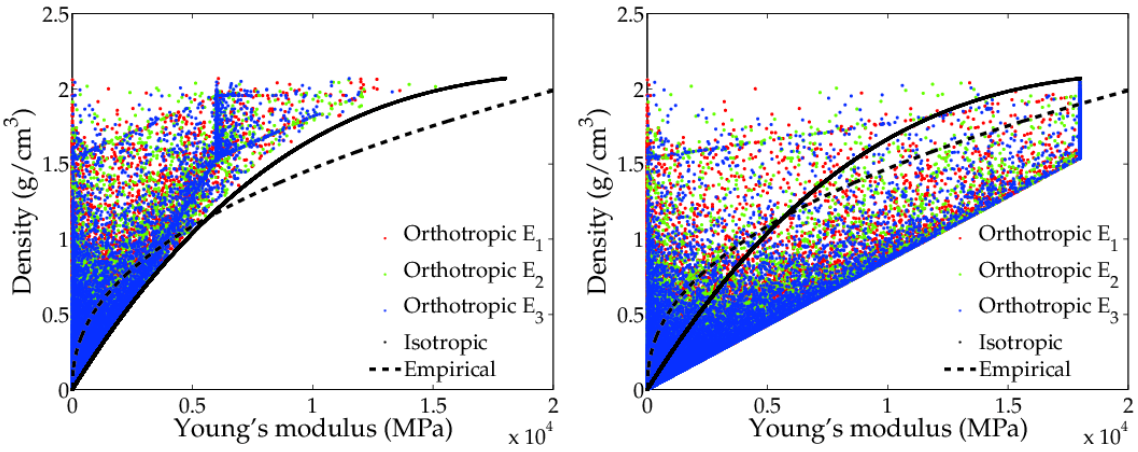


Figure 5.34: Distribution of Young's modulus with respect to density for predictive orthotropic and isotropic models of the right pelvic innominate along with empirical distribution of CT derived model of the right pelvic innominate. For orthotropic model, distribution of mean Young's modulus is shown in (a) and dominant Young's modulus in (b). For each element of the orthotropic model, the data point is colour coded corresponding to the dominant Young's modulus.

A potential limitation of the continuum models developed is the scale at which they were developed. The average edge length of each element was 3.76 mm, suggesting a model closer to macroscale rather than microscale. This can lead to errors in predicting the stiffness of elements in areas where complex loads occur. In addition, modelling bone void is not realistic at this scale. However, an important factor in deciding the scale of the models was computational efficiency. Further details on mesh resolution impact on continuum adaptation and computational efficiency are presented in Chapter 6.

All models were found to have run times of approximately 3 minutes for a single loadcase on a workstation PC with one Intel Xeon E5-2630 v2 2.60 GHz and 64 GB of RAM. The overall run times for adapting the models to the full loading regime were approximately 40 hours for the orthotropic model, 24 hours for the isotropic model, 38 hours for the hybrid orthotropic model, 25 hours for the hybrid isotropic model and 28 hours for the hybrid structural model. The isotropic, hybrid isotropic and hybrid structural models were comparable to the structural model presented in

Chapter 4 in terms of computational efficiency. The main factor in slowing down the adaptation of the orthotropic and hybrid orthotropic models was post-processing. Adapting a model with a much finer mesh to the same loading regime would result in a run time which would not be reasonable. Thus, although the scale poses a limitation, the models present a good balance between accuracy and computational efficiency as they provide valuable information on bone architecture while running in a reasonable amount of time.

In terms of use of the models presented in this Chapter, the purely continuum models were shown to lack the capability of distinguishing between cortical and trabecular bone as they do not predict cortical thickness. This can be a hindrance in the cases when bone architecture needs to be assessed locally. Although the combined continuum models overcome this limitation, they do not provide sufficient information on bone architecture.

The combined orthotropic model provides trabecular bone directionality in addition to the combined isotropic model, but it does not allow for an assessment of trabecular bone architecture locally, such as investigating inter-trabecular angles. This capability is provided by the purely structural and combined structural models. When investigating the effects of a rehabilitation regime on bone architecture, the combined continuum models can be used with the caveat that the combined isotropic model only provides information on bone mineral density. In addition, the structural model is more appropriate for fracture modelling given its capabilities to predict fracture onset and progression.

The models presented in this Chapter served as a tool to benchmark the structural model against continuum modelling approaches.

6

Sensitivity studies

A portion of this chapter is included as supplementary material in the journal article: Zaharie, D. T., & Phillips, A. T. (2018). Pelvic construct prediction of trabecular and cortical bone structural architecture. *Journal of Biomechanical Engineering*, 140(9), 091001.

This chapter investigates the sensitivity of the structural and continuum modelling pipelines presented in Chapters 2 and 3. A sensitivity study is a useful approach to gain insight on the effects parameters or characteristics of a model have on its predictions. Several previous studies concerning the development of an FE model of the pelvic construct have used a sensitivity study to gain a better understanding on how sensitive the models developed were to the chosen parameters (Anderson et al., 2005; Li et al., 2007; Leung et al., 2009).

Anderson et al. (2005) assessed the sensitivity of their model to variations in cortical and trabecular bone Poisson's ratio, cartilage elastic modulus and cortical and trabecular bone elastic modulus, and cortical thickness. They applied vertically oriented loads (0.25, 0.5, 0.75 and 1.0 $\times$ body weight) through the hip joint to simulate upright standing posture. To quantify the effects of alterations, they compared the predicted cortical strains. They found that cortical surface strains were ten and fifteen times more sensitive to changes in cortical thickness and cortical bone elastic modulus, respectively, compared to changes in trabecular elastic modulus. The authors suggested that the FE predicted strains were not very sensitive to changes in cartilage modulus, cartilage thickness, cortical and trabecular bone Poisson's ratio.

Li et al. (2007) conducted a sensitivity study under drop tower lateral impact conditions to quantify the sensitivity of their FE model to changes in material properties of cortical and trabecular bone, as well as the soft tissue defining the pubic symphysis. Similar to the findings of Anderson et al. (2005), they noted that cortical bone stresses were more sensitive to changes in cortical elastic modulus, as opposed to trabecular elastic modulus. They found that two fold increases of the linear elastic material properties assigned to hip ligaments and sacroiliac ligaments had a small effect on predicted cortical stresses (less than 5%). They also suggested that doubling the parameters concerned with the hyperelastic material properties used for the pubic symphysis lead to a decrease in deformation of the pubic disc of 16 %.

Leung et al. (2009) varied the elastic moduli of trabecular and cortical bone by

±10 % and ±20 % with respect to their baseline values and applied vertical loading (0.25, 0.5 and 0.75 × body weight) through the sacral joint while constraining the proximal femurs. They reported changes in predicted principal strains of around 15 % and 9 % when varying cortical bone elastic modulus and trabecular bone elastic modulus by 20 %, respectively. When changing both cortical and trabecular material properties simultaneously, they reported a variation of around 31 % in predicted principal strains.Their conclusions were in agreement with previous work by Anderson et al. (2005), reporting that cortical bone thickness has a greater effect on predicted surface strains than trabecular bone density.

This study is organised in four main sections: ligaments sensitivity, mesh sensitivity, structural adaptation algorithm sensitivity and continuum adaptation sensitivity. In each section, the approach used was to vary one parameter at a time while keeping all others at their baseline values. Depending on the parameter in question, the base model or adaptation algorithm were modified accordingly and the model was adapted to the full loading regime. The parameters analyzed in each section are shown in Table 6.1. An advantage of this approach (one-at-a-time) is that any changes in the resulting model compared to the baseline model can be attributed to the variation of the parameter in question. To investigate the effect of each parameter, the bone volume or average stiffness of the resulting model was compared to the baseline value. Total bone volume was chosen as a measure of comparison as it gives a good indication of the effect of each parameter modified in the sensitivity analysis. The results for each analysis category are presented in the following sections.

Section	Type	Parameter
Joints	Sacroiliac Joint	Young's modulus
	Pubic joint	
Ligaments	Inguinal ligament	Young's modulus
	Sacrospinous ligament	
	Sacrotuberous ligament	
	All ligaments	
Mesh	Structural mesh density	Element edge length
	Continuum mesh density	
Structural adaptation	Cortical thickness	Initial thickness
		Upper thickness limit
	Trabecular radii	Initial radius
		Upper radius limit
	Adaptation	Target strain
		Discretization categories
Continuum adaptation	Bone	Initial Young's modulus and shear modulus
	Adaptation	Target strain

Table 6.1: Parameters involved in sensitivity study grouped by the type and category of the modelling framework.

6.1 Sensitivity of ligaments and joints material properties

The sensitivity of the model to the material properties of the ligaments and joints used to connect the three bones of the pelvic ring was investigated by varying their Young's modulus (50% increase and 50% decrease) while maintaining all other values at their baseline. The sacroiliac and pubic joints were defined as a unit comprising of the corresponding ligament and cartilage defined using the same element type. Stiffnesses for each case are shown in Table 6.2.

Case	Sacroiliac cartilage (MPa)	Pubic carti-lage (MPa)	Inguinal ligament (MPa)	Sacrospinous ligament (MPa)	Sacrotuberous ligament (MPa)
Baseline model	28.8	15.9	121.5	105.1	106.8
Sacroiliac +50%	43.2	15.9	121.5	105.1	106.8
Sacroiliac -50%	14.4	15.9	121.5	105.1	106.8
Pubic +50%	28.8	23.9	121.5	105.1	106.8
Pubic -50%	28.8	7.9	121.5	105.1	106.8
Inguinal +50%	28.8	15.9	182.3	105.1	106.8
Inguinal -50%	28.8	15.9	60.8	105.1	106.8
Sacrospinous +50%	28.8	15.9	121.5	157.7	106.8
Sacrospinous -50%	28.8	15.9	121.5	52.6	106.8
Sacrotuberous +50%	28.8	15.9	121.5	105.1	160.2
Sacrotuberous -50%	28.8	15.9	121.5	105.1	53.4
All +50%	43.2	23.9	182.3	157.7	160.2
All -50%	14.4	7.9	60.8	52.6	53.4

Table 6.2: Young's modulus of each ligament and joint cartilage for each case

Each case model was subjected to the iterative adaptation algorithm for the full loading regime. The changes in trabecular and cortical bone volumes of each converged model with respect to corresponding values obtained for the baseline model are shown for each case in Figure 6.1. When modifying the stiffness of one ligament or cartilage region, the greatest difference in trabecular bone volume was found when increasing the stiffness of the sacroiliac joint by 50%, with a value of -0.74%. Decreasing the stiffness of the sacroiliac joint resulted in the maximum difference in cortical and total bone volume, with values of 3.18% and 1.92%, respectively. Increasing the stiffness of all ligaments and joints by 50% resulted in the greatest change in trabecular bone volume of -0.86%. Conversely, decreasing the stiffness of all ligaments resulted in an increase of cortical bone volume of 3.59%, the largest of all cases tested. All values are shown in Table 6.3.

Overall, the material properties associated with the pelvic ligaments and joint cartilage did not have a large effect on the adaptation process, with the greatest impact being recorded when the stiffness of all ligaments and cartilage was decreased by 50%, when the volume of cortical bone increased by 3.59%.

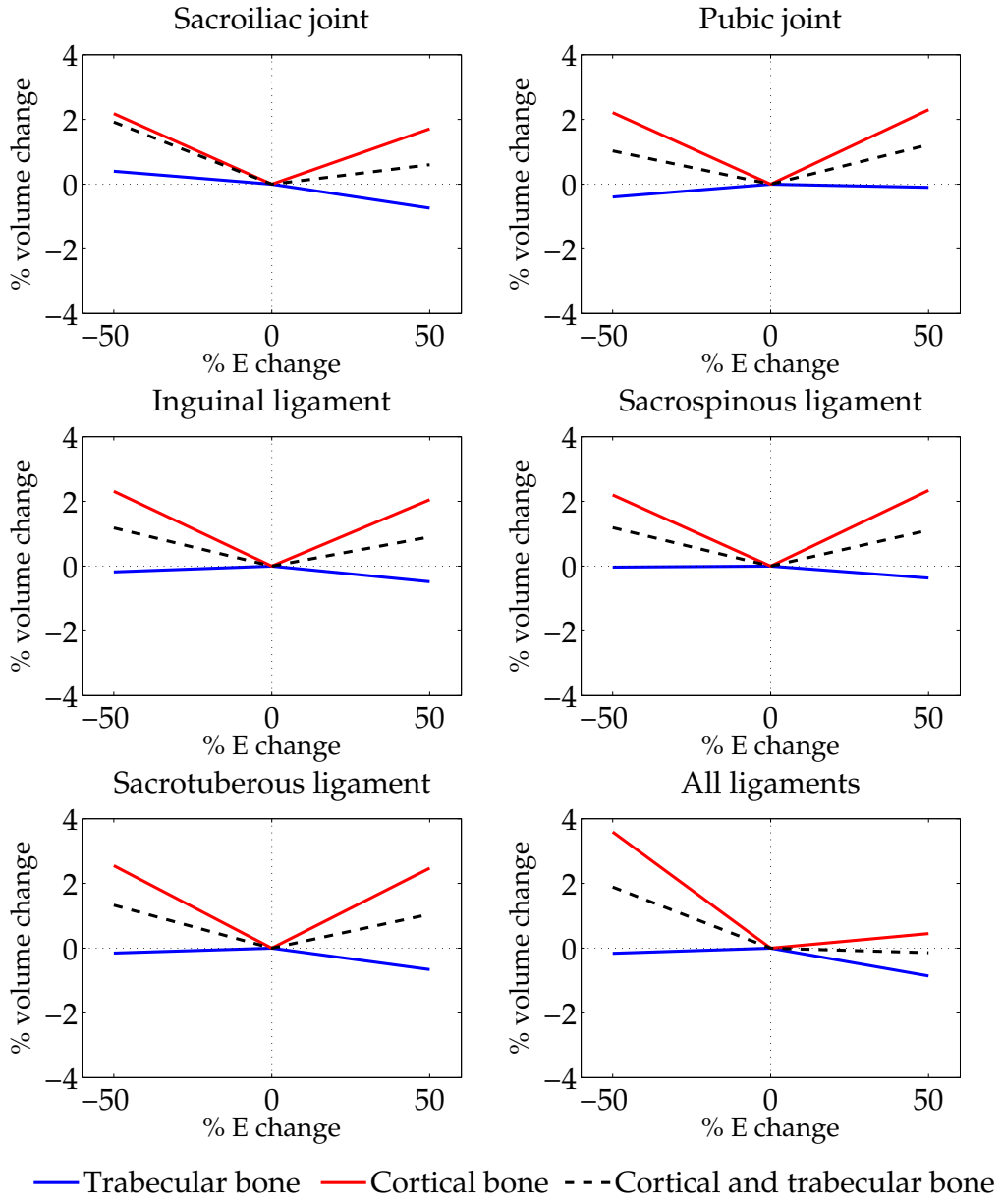


Figure 6.1: Changes in cortical, trabecular and total bone volumes caused by changes in the stiffness of each ligament in the model

Case	Trabecular (mm^3)	Cortical (mm^3)	Total (mm^3)	$\Delta_{trab}(\%)$	$\Delta_{cort}(\%)$	$\Delta_{tot}(\%)$
Baseline model	127433	154426	281859	N/A	N/A	N/A
Sacroiliac joint: +50%	126489	157062	283550	-0.74	1.71	0.60
Sacroiliac joint: -50%	127946	159339	287285	0.40	3.18	1.92
Pubic joint: +50%	127309	157988	285298	-0.10	2.30	1.22
Pubic joint: -50%	126924	157844	284769	-0.40	2.21	1.03
Inguinal ligament: +50%	126822	157584	284406	-0.48	2.05	0.90
Inguinal ligament: -50%	127198	157998	285196	-0.18	2.31	1.18
Sacrospinous ligament: +50%	126965	158046	285011	-0.37	2.34	1.12
Sacrospinous ligament: -50%	127392	157818	285211	-0.03	2.20	1.19
Sacrotuberous ligament: +50%	126587	158240	284827	-0.66	2.47	1.05
Sacrotuberous ligament: -50%	127248	158364	285612	-0.15	2.55	1.33
All +50%	126332	155121	281453	-0.86	0.45	-0.14
All -50%	127219	159972	287190	-0.16	3.59	1.89

Table 6.3: Comparison between trabecular, cortical and total bone volumes of baseline model and each case model

6.2 Mesh sensitivity

6.2.1 Structural mesh

A mesh sensitivity study was conducted to assess whether the mesh density has an impact on the adaptation process of the structural model. Given the size of the standard pelvis mesh, testing a finer mesh would have a very high computational cost. An analogous structural beam model with a length of 100 mm, height of 10 mm and depth of 20 mm was used instead. The baseline mesh was built using the same characteristics defining the pelvis mesh, with shell elements representing cortical bone and truss elements representing trabecular bone. Two additional meshes, one fine and one coarse, were defined by changing the maximum element edge length by ±50%.

Similar to the pelvis model, the three models were subjected to a loading case (Figure 6.2) and iteratively adapted until convergence was achieved using the algorithm described in Chapter 4, §4.1.2. The ranges for the radii of trusses were varied according to the mesh density to maintain the ratio compared to element length (Table 6.4). The shell thickness ranges were the same for all three models ([0.1 mm, 2 mm]).

The trabecular and cortical bone volumes of the finer and coarse meshes were compared to the baseline mesh (Table 6.5). In addition, the cortical thickness and trabecular radius distributions of each model were compared visually (Figures 6.3 and 6.4). The resulting structures for all three models are similar for both trabecular and cortical bone (Figures 6.5 and 6.6).

In terms of computational efficiency, the total times required for each model to converge were compared. The time required for the coarse mesh model to converge was 36.8 % shorter than for the baseline model, whereas it took the fine mesh model

394 % longer to converge with respect to the baseline model.

The results of the sensitivity study indicate that a finer mesh would not be required to model the pelvis as the coarser mesh has a similar architecture to the baseline model in terms of bone volume and trajectories. The baseline mesh provides enough directionality for trajectories to be formed in response to the loading regime. The coarse mesh produced similar results to the baseline mesh in terms of bone volume, although the fact that the average trabecular element length is greater than the maximum edge element length (Table 6.4) suggests that it may not provide a wide enough range of directionalities. Based on the results of the mesh sensitivity study and considering the computational cost of each mesh, it is considered that a structural mesh of the pelvis at the mesoscale is appropriate for this study.

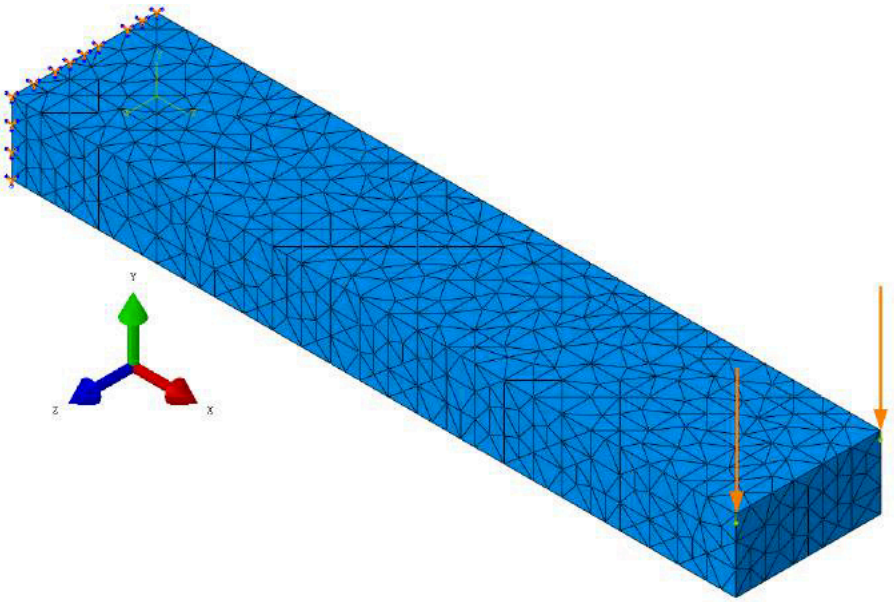


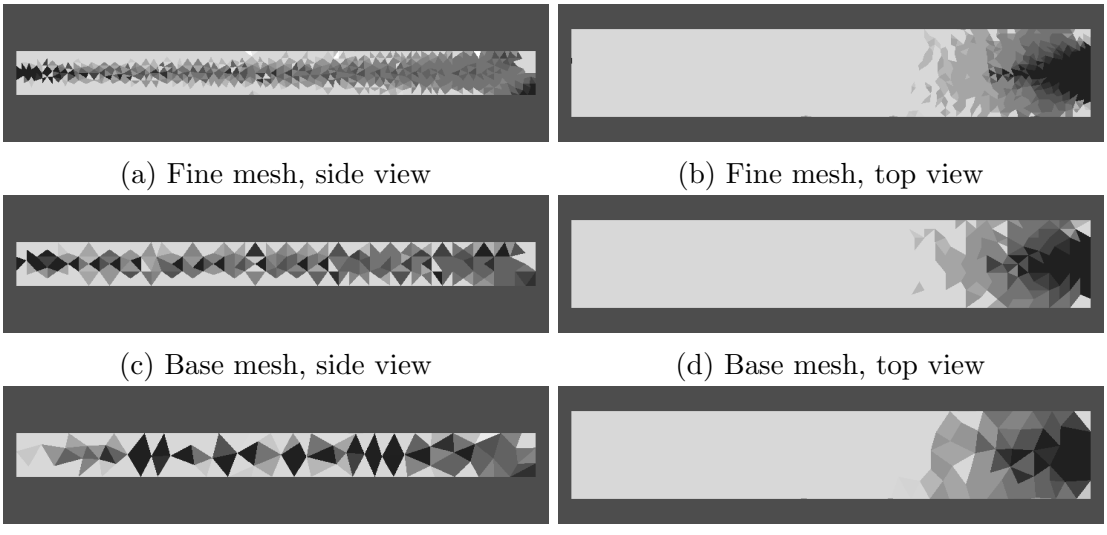
Figure 6.2: Loading conditions applied on beam used for the mesh sensitivity study

Case	Avg. element length (mm)	Max. edge length (mm)	Number of truss elements	Truss radii range (mm)	Number of shell elements
Baseline mesh	3.97	4	24649	[0.1, 1]	1836
Fine mesh	1.78	2	150019	[0.04, 0.4]	6936
Coarse mesh	6.63	6	798	[0.17, 1.69]	8598

Table 6.4: Mesh properties for the three models

Case	Trabecular (mm^3)	Cortical (mm^3)	Total (mm^3)	$\Delta_{trab}(\%)$	$\Delta_{cort}(\%)$	$\Delta_{tot}(\%)$
Baseline mesh	7492	9437	16929	N/A	N/A	N/A
Fine mesh	7560	9714	17274	0.91	2.93	2.04
Coarse mesh	7015	9266	16281	-6.36	-1.82	-3.83

Table 6.5: Comparison between trabecular, cortical and total bone volumes for each of the meshes tested

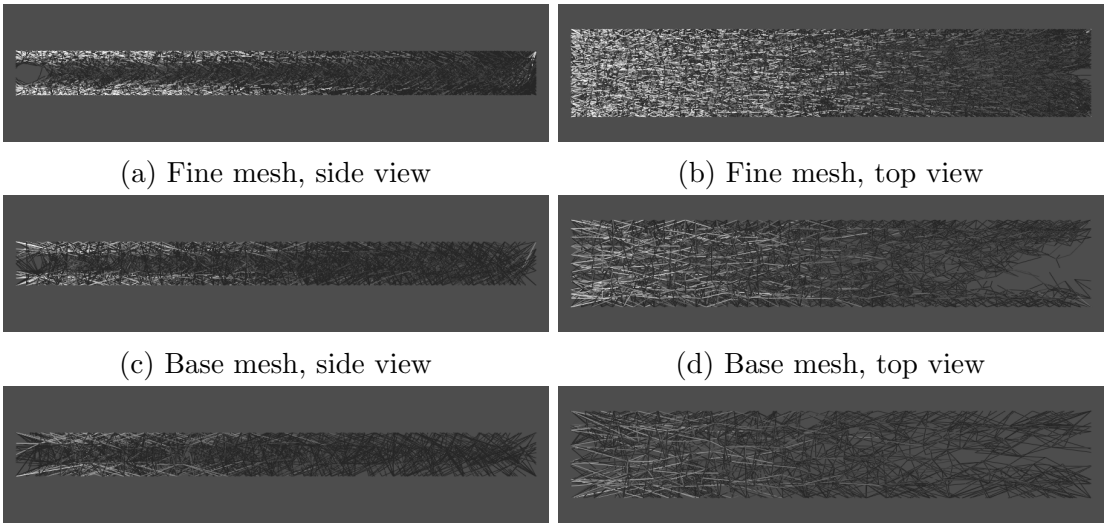


(a) Fine mesh, side view (b) Fine mesh, top view

(c) Base mesh, side view (d) Base mesh, top view

(e) Coarse mesh, side view (f) Coarse mesh, top view

Figure 6.3: Cortical thickness distribution for each of the three meshes. Limits for the three models are 0.1 mm (shown in black) and 2 mm (shown in white).

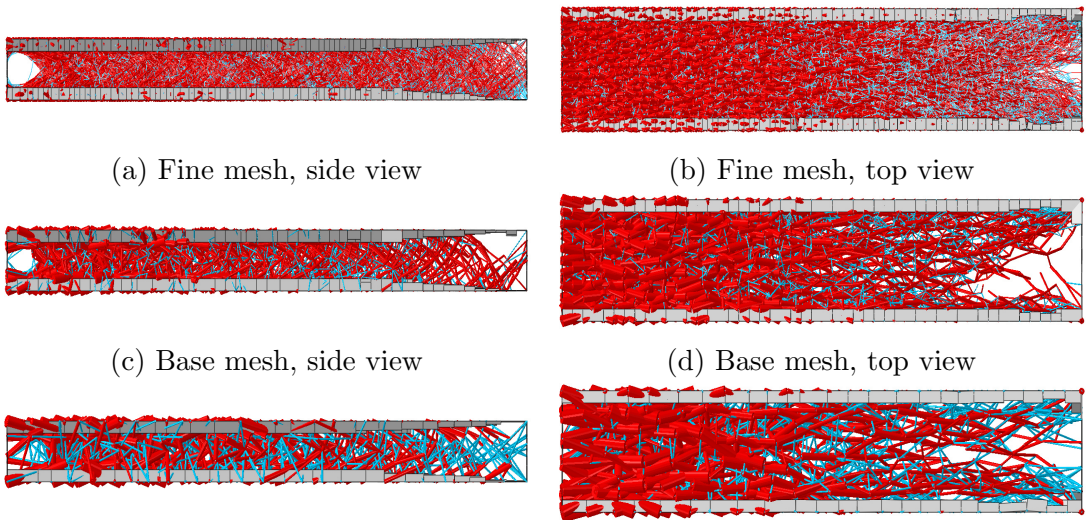


(a) Fine mesh, side view (b) Fine mesh, top view

(c) Base mesh, side view (d) Base mesh, top view

(e) Coarse mesh, side view (f) Coarse mesh, top view

Figure 6.4: Trabecular radius distribution for each of the three meshes. Limits for the fine mesh are 0.04 mm (shown in black) and 0.4 mm (shown in white). Limits for the baseline mesh are 0.1 mm (shown in black) and 1 mm (shown in white). Limits for the coarse mesh are 0.17 mm (shown in black) and 1.69 mm (shown in white).

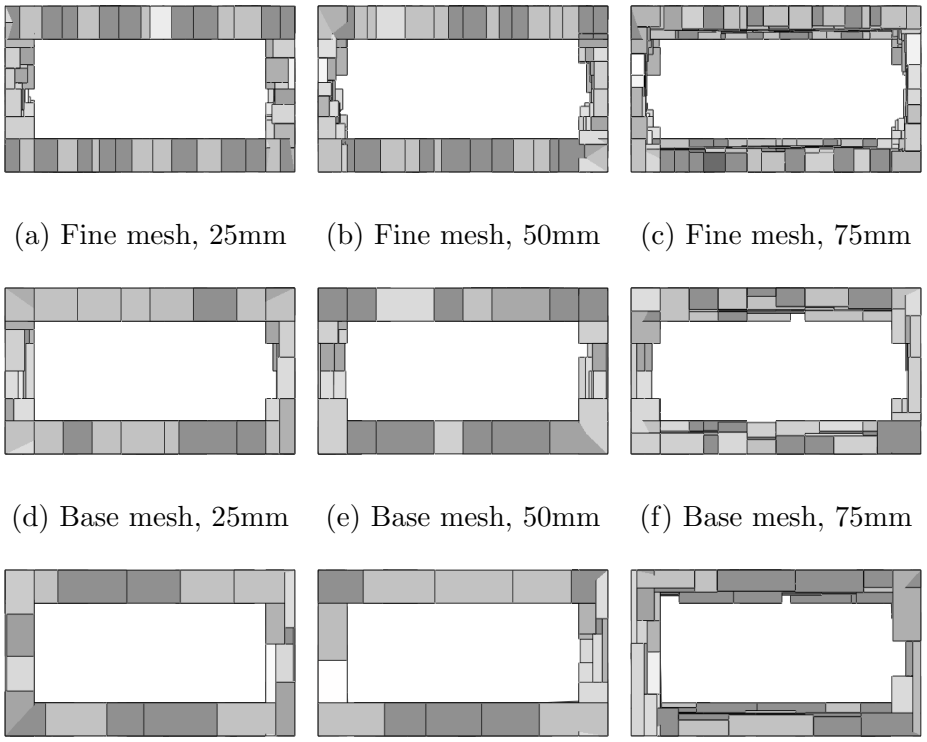


(a) Fine mesh, side view (b) Fine mesh, top view

(c) Base mesh, side view (d) Base mesh, top view

(e) Coarse mesh, side view (f) Coarse mesh, top view

Figure 6.5: Side and top views of the three meshes illustrating the trabecular structure and cortical thickness. Truss elements with a radius $>$ 0.04 mm for the fine mesh, $>$ 0.1 mm for the baseline mesh and $>$ 0.17 mm for the coarse mesh are shown in red, with elements with a radius of 0.04 mm for the fine mesh, 0.1 mm for the baseline mesh and 0.17 mm for the coarse mesh shown in blue.



(a) Fine mesh, 25mm (b) Fine mesh, 50mm (c) Fine mesh, 75mm

(d) Base mesh, 25mm (e) Base mesh, 50mm (f) Base mesh, 75mm

(g) Coarse mesh, 25mm (h) Coarse mesh, 50mm (i) Coarse mesh, 75mm

Figure 6.6: Transversal cut views taken at 25mm, 50mm and 75mm from the fixed end illustrating the cortical thickness distribution across the beam for each mesh

6.2.2 Continuum mesh

Similarly, the sensitivity of the continuum mesh was analyzed by using a continuum beam with a length of 100 mm, height of 10 mm and depth of 20 mm. The analogous model comprised of first order tetrahedral elements, as used in the continuum pelvis model. From the baseline mesh, the maximum element edge length was varied by $\pm 50\%$ to obtain a coarse and fine mesh, respectively. The elements were assigned initial orthotropic material properties with identical Young's moduli, shear moduli and Poisson's ratios in all three directions: 300 MPa, 150 MPa and 0.3, respectively. The resulting models were subjected to the loading case shown in Figure 6.2 and iteratively adapted until convergence was achieved using the algorithm described in Chapter 5, §5.1.2.1.

Average values of directional Young's moduli and shear moduli for each case are shown in Tables 6.6 and 6.7. Average Young's modulus and shear modulus distributions for the three meshes are shown in Figures 6.7 and 6.8, respectively.

The average overall Young's modulus, E_1 and E_3 increased for the fine mesh and decreased for the coarse mesh. Conversely, E_2 decrease for the fine mesh and increased for the coarse mesh. Average overall and all three components of shear modulus were found to decrease for the fine mesh and decrease for the coarse mesh. In addition, the variation of the average shear modulus is much greater than the variation of the average Young's modulus across cases.

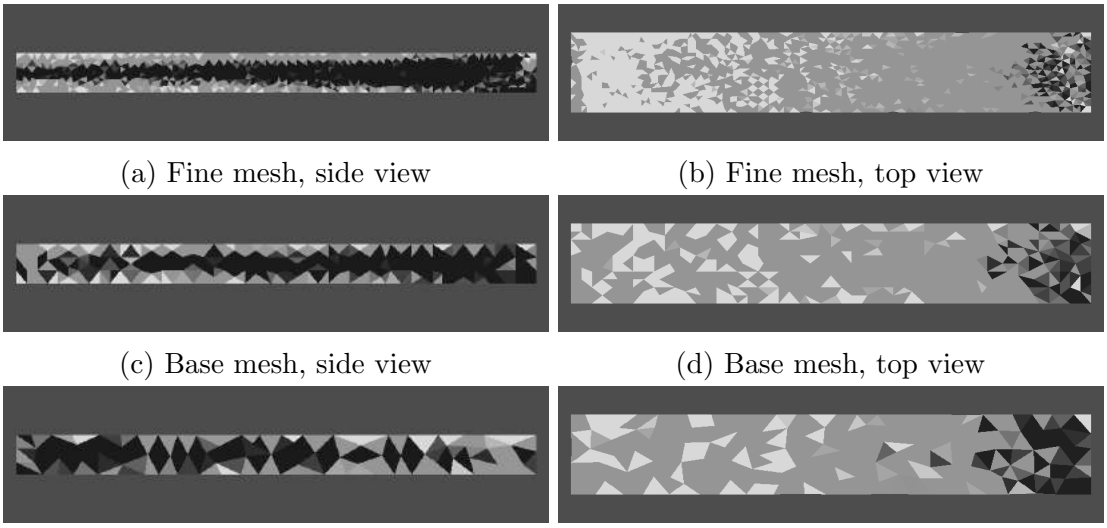
Visually, the distributions of Young's moduli for all three cases (Figure 6.7) are consistent with the distributions of shell thickness and truss radii from the structural meshes. The fine mesh produced a slightly smoother distribution of average Young's modulus compared to the other two, meaning that it can potentially capture more accurately the spatial stiffness variation.

Mesh	$E_{1,mean}$ (MPa)	$E_{2,mean}$ (MPa)	$E_{3,mean}$ (MPa)	E_{mean} (MPa)	$\Delta_{E_1}(\%)$	$\Delta_{E_2}(\%)$	$\Delta_{E_3}(\%)$	$\Delta_{E_{mean}}(\%)$
Baseline	3587.3	827.5	3980.3	2798.4	N/A	N/A	N/A	N/A
Fine	3802.5	741.1	4384.4	2976.0	5.99	-10.44	10.15	6.35
Coarse	2998.6	1152.6	3789.0	2646.7	-16.41	39.28	-4.81	-5.42

Table 6.6: Comparison between average Young's moduli values across the three meshes.

Mesh	$G_{12,mean}$ (MPa)	$G_{31,mean}$ (MPa)	$G_{23,mean}$ (MPa)	G_{mean} (MPa)	$\Delta_{G_{12}}(\%)$	$\Delta_{G_{31}}(\%)$	$\Delta_{G_{23}}(\%)$	$\Delta_{G_{mean}}(\%)$
Baseline	477.9	977.7	674.8	710.1	N/A	N/A	N/A	N/A
Fine	343.4	777.2	506.6	542.4	-28.15	-20.51	-24.93	-23.62
Coarse	639.9	1120.7	814.9	858.5	33.89	14.63	20.77	20.89

Table 6.7: Comparison between average shear moduli values across the three meshes

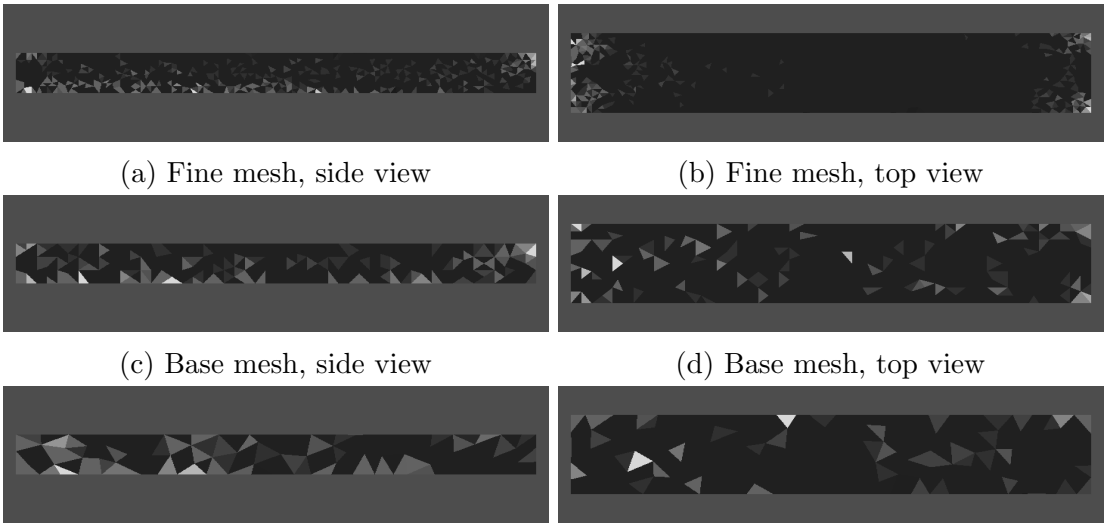


(a) Fine mesh, side view (b) Fine mesh, top view

(c) Base mesh, side view (d) Base mesh, top view

(e) Coarse mesh, side view (f) Coarse mesh, top view

Figure 6.7: Average Young's modulus distribution for each of the three meshes. Limits for all meshes are 10 MPa (shown in black) and 18,000 MPa (shown in white).



(a) Fine mesh, side view (b) Fine mesh, top view

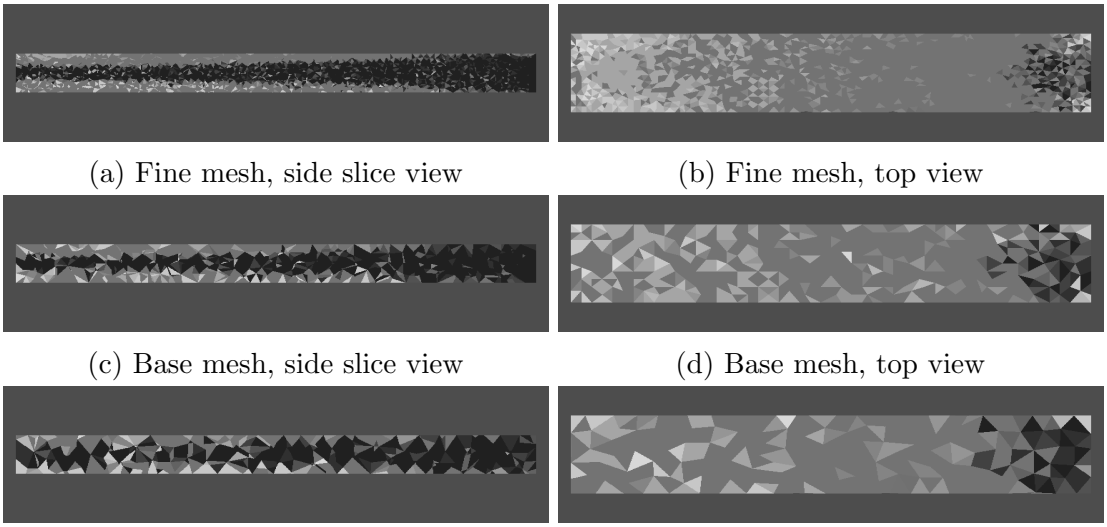
(c) Base mesh, side view (d) Base mesh, top view

(e) Coarse mesh, side view (f) Coarse mesh, top view

Figure 6.8: Average shear modulus distribution for each mesh. Limits for all meshes are 5 MPa (shown in black) and 10,000 MPa (shown in white).

Density distributions for each mesh are shown in Figure 6.9. The density of each element was calculated using the method presented in Chapter 5, §5.2.1.1. Bone volumes were calculated for each mesh by multiplying the relative density of each element to its volume, as shown in Equation 6.1. Compared to the base mesh (7456mm^3), the coarse mesh predicted a decrease in volume of 1.26% (7359mm^3), while the fine mesh predicted an increase in volume of 45 % (10812mm^3). Given the smaller variation in volume for the structural model (Table 6.5), these results further suggest that the continuum model is more sensitive to mesh properties and using a structural approach is reasonable. To establish the accuracy of these models, micro and macro CT scans of the same specimen would be required to quantitatively assess the predicted bone architecture of the approaches presented in this thesis.

$$V_{total} = \sum_{i=1}^{n} \overline{\rho} V_i \tag{6.1}$$



(a) Fine mesh, side slice view

(b) Fine mesh, top view

(c) Base mesh, side slice view

(d) Base mesh, top view

(e) Coarse mesh, side slice view

(f) Coarse mesh, top view

Figure 6.9: Density distributions for each mesh. Limits for all meshes are 0.001 g/cm^3 (shown in black) and 2.07 g/cm^3 (shown in white).

In terms of computational cost, the time to convergence for the coarse mesh was found to be 5.5 % shorter than for the baseline model, with the time required for the fine mesh model to converge 263 % longer than for the baseline model. Thus, given the considerable increase in computational cost associated with a fine mesh, using a mesh with the characteristics of the baseline mesh presented in this section seems to be an appropriate trade-off between accuracy and computational cost.

6.3 Sensitivity of structural adaptation algorithm

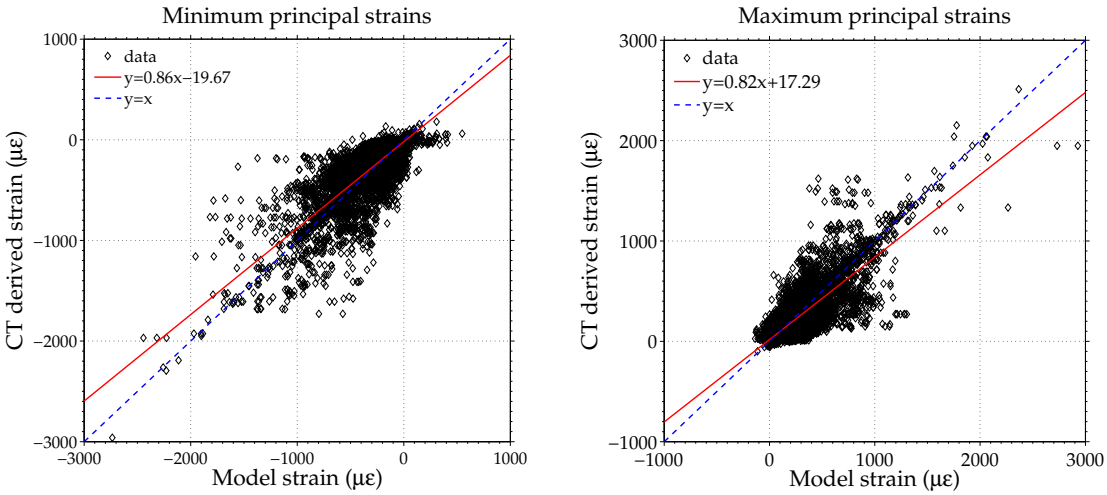
The robustness of the structural adaptation algorithm was assessed by varying the following parameters: number of attachment points per muscle (1 and 5; baseline value: 3), initial cortical thickness (1 mm; baseline value: 0.1 mm), initial trabecular radius (1 mm; baseline value: 0.1 mm), cortical thickness upper limit (10 mm; baseline value: 5 mm), trabecular radii upper limit (4 mm; baseline value: 2 mm), target strain (1000 $\mu\epsilon$ and 1500 $\mu\epsilon$; baseline value: 1250 $\mu\epsilon$) and number of discrete section categories (128 and 512; baseline value: 256). In each case, the model was run through the adaptation process until convergence was achieved.

Similar to Section 6.1, for the sensitivity cases regarding adaptation related parameters, the total trabecular and cortical volumes were compared to the baseline model. The results are shown in Table 6.8. The model was most sensitive to the target strain value. For a target strain of 1000 $\mu\epsilon$, the model predicted a gain of trabecular and cortical bone of 32.70% and 18.51%, respectively. For a target strain of 1500 $\mu\epsilon$, the model predicted a loss of trabecular and cortical bone of 19.28% and 13.88%, respectively. The other parameters were found to have little effect on the resulting bone structure. The model adapted to a lower target strain was quantitatively compared to the CT scan derived model in the same manner as the predictive models presented in Chapters 4 and 5 were assessed.

Case	Trabecular (mm^3)	Cortical (mm^3)	Total (mm^3)	$\Delta_{trab}(\%)$	$\Delta_{cort}(\%)$	$\Delta_{tot}(\%)$
Baseline model	127433	154426	281859	N/A	N/A	N/A
One attachment point per muscle	127318	154314	281632	-0.09	-0.07	-0.08
Five attachment points per muscle	127568	154581	282149	0.11	0.10	0.10
Higher initial cortical thickness	130170	153964	284134	2.15	-0.30	0.81
Higher initial trabecular radius	132148	151646	283795	3.70	-1.80	0.69
Higher cortical thickness limit	140623	147584	288207	-5.99	8.80	1.04
Higher trabecular radii limit	140792	145714	286506	-5.88	7.42	0.45
Lower target strain	169109	183005	352114	32.71	18.51	24.93
Higher target strain	102867	132988	235855	-19.27	-13.88	-16.32
128 section categories	124653	157931	282584	-2.18	2.27	0.26
512 section categories	129358	152486	281845	1.51	-1.25	-0.01

Table 6.8: Comparison between trabecular, cortical and total bone volumes of baseline model and each case model

The minimum and maximum principal strains for the models are shown in Figure 6.10. As the model was adapted to a lower target strain, it was expected to be stiffer than the baseline predictive model, as shown by the total volume of bone. This aspect is further highlighted by the slopes of the lines of best fit for both cases are slightly greater than for the case when the baseline structural model was compared to the CT derived model (Figure 4.20).



(a) Correlation coefficient: 0.881

(b) Correlation coefficient: 0.886

Figure 6.10: Comparison between the minimum (a) and maximum (b) principal strains across the surface of the structural model adapted to a lower target strain (x axis) and CT derived model (y axis). Lines of best fit are shown in red for each case, with y=x line shown in dashed blue.

6.4 Sensitivity of continuum adaptation algorithm

A sensitivity study was run to assess the robustness of the continuum adaptation algorithm by varying the initial material properties of the FE model (E=10000 MPa, G=5000 MPa; E=300 MPa, G=150 MPa; baseline values: E=3000 MPa, G=1500 MPa) and the target strains used to drive adaptation (normal strain: 1000 $\mu\epsilon$ and 1500 $\mu\epsilon$; baseline value: 1250 $\mu\epsilon$; shear strain: 1154 $\mu\epsilon$ and 1731 $\mu\epsilon$; baseline value: 1443 $\mu\epsilon$).

For each case, the model was run through the adaptation process until convergence was achieved. The resulting models were assessed by comparing the average Young's moduli and shear moduli in each direction to the baseline model. The results are shown in Tables 6.9 and 6.10. The model was found to be insensitive to changes in initial assigned Young's modulus and shear modulus. Similar to the structural adaptation algorithm presented in Section 1.3, the continuum adaptation algorithm was found to be sensitive to changes in target strains. A higher target strain produced a 17.11 % decrease in average Young's modulus and a 18.09 % decrease in average shear modulus. Conversely, a lower target strain resulted in a 23.22 % increase in average Young's modulus and 27.17 % increase in average shear modulus. The model adapted to a lower target strain was quantitatively compared to the CT scan derived model in the same manner as the predictive models presented in Chapters 4 and 5 were assessed.

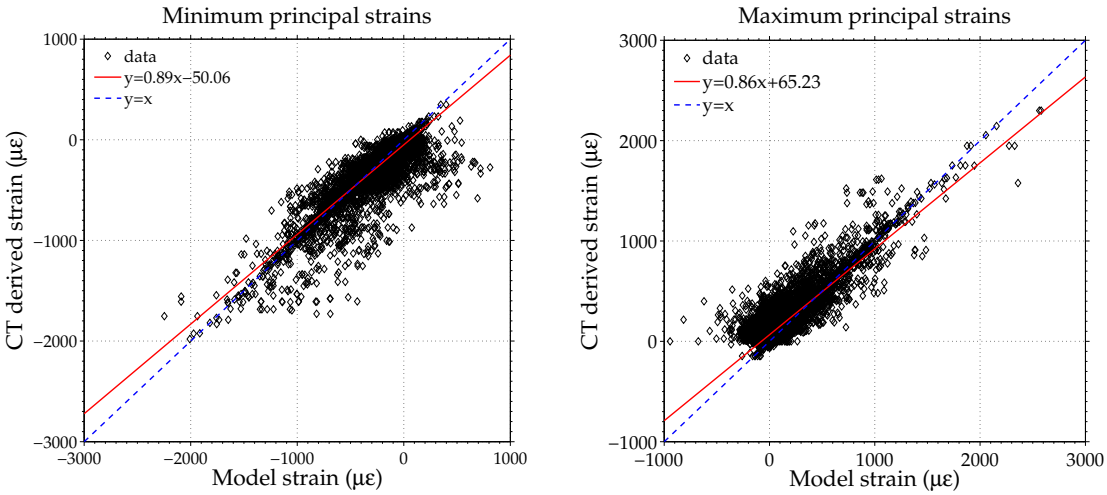
Case	$E_{1,mean}$ (MPa)	$E_{2,mean}$ (MPa)	$E_{3,mean}$ (MPa)	E_{mean} (MPa)	$\Delta_{E_1}(\%)$	$\Delta_{E_2}(\%)$	$\Delta_{E_3}(\%)$	$\Delta_{E_{mean}}(\%)$
Baseline model	1064.8	636.9	784.9	828.9	N/A	N/A	N/A	N/A
Higher initial E and G	1052.1	639.6	779.2	823.6	-1.19	0.41	-0.72	-0.63
Lower initial E and G	1048.5	637.2	777.9	821.2	-1.54	0.04	-0.89	-0.93
Higher target strain	896.7	513.8	650.7	687.1	-15.79	-19.33	-17.09	-17.11
Lower target strain	1305.4	771.5	987.2	1021.3	22.59	21.12	25.78	23.22

Table 6.9: Comparison between average Young's moduli values across all case models

Case	$G_{1,mean}$ (MPa)	$G_{2,mean}$ (MPa)	$G_{3,mean}$ (MPa)	G_{mean} (MPa)	$\Delta_{G_{12}}(\%)$	$\Delta_{G_{31}}(\%)$	$\Delta_{G_{23}}(\%)$	$\Delta_{G_{mean}}(\%)$
Baseline model	567.0	585.8	538.8	563.8	N/A	N/A	N/A	N/A
Higher initial E and G	568.9	585.2	537.6	563.9	0.33	-0.06	-0.23	0.01
Lower initial E and G	563.6	592.6	539.1	565.1	-0.60	1.20	0.05	0.23
Higher target strain	465.9	491.2	428.4	461.8	-17.83	-16.12	-20.50	-18.09
Lower target strain	719.9	765.2	665.8	717.0	26.97	30.67	23.60	27.17

Table 6.10: Comparison between average shear moduli values across all case models

The minimum and maximum principal strains for the models are shown in Figure 6.11. As the model was adapted to a lower target strain, it was expected to be stiffer than the baseline predictive model, as shown by the average directional Young's modulus values. This aspect is further highlighted by the slopes of the lines of best fit for both cases are slightly greater than for the case when the baseline orthotropic model was compared to the CT derived model (Figure 5.10).



(a) Correlation coefficient: 0.877

(b) Correlation coefficient: 0.883

Figure 6.11: Comparison between the minimum (a) and maximum (b) principal strains across the surface of the orthotropic model adapted to a lower target strain (x axis) and CT derived model (y axis). Lines of best fit are shown in red for each case, with y=x line shown in dashed blue.

6.5 Discussion and concluding remarks

This chapter presented a sensitivity analysis of selected parameters associated with the two finite element models and adaptation algorithms presented in Chapters 1 and 2. The results presented in this chapter have shown that both the continuum and structural model along with the corresponding adaptation algorithms are robust and the chosen parameters are appropriate for the objective set out in each case.

The chosen mesh density for both the structural and continuum models was found to be appropriate in terms of balancing accuracy and computational cost, albeit the continuum model was found to be more sensitive to changes in mesh density. In particular, the resulting shear moduli were impacted the most by changing the mesh density. The findings suggest that, when using the orthotropic continuum model to simulate complex multi-directional loading conditions, greater attention should be directed towards selecting a mesh density. Although there is a sensitivity to mesh density, the orthtropic model still gives information on bone directionality as opposed to a model using an isotropic material definition. However, the sensitivity of the continuum mesh can be a hindrance when predicting the onset and progression of fracture patterns, suggesting that, for simulating fracture scenarios, the structural model is more appropriate.

Although the current version of the structural mesh does not allow for network reorganisation, this aspect is currently investigated and future versions of this model could be set up to predict reorganisation of the local trabecular networks, which can lead to a more physiologically relevant representation of bone architecture in the pelvis. Material properties of the ligaments were found to have little influence on the resulting structural model. These results show the FE models of the pelvic construct to be robust for the purpose of the study.

The structural and continuum adaptation algorithms were not found to be sensitive to parameters related to the initial definitions of the models with these having

small effects on the resulting structures. Target strain was identified as the most sensitive parameter in both cases, which was expected as it was the main driver of adaptation.

A limitation associated with the one-at-a-time approach used to perform the sensitivity study is that it is based on the assumption that parameters affecting the response of the model are independent of one another. Assessing only one value above and below the baseline is not enough to establish any potential non-linear relationships between the parameter in question and its effect on the model. Although the FE models investigated are computationally efficient relative to similar models presented in literature, a sensitivity study base on a full factorial design and assessing multiple levels in order to capture potential non-linear relationships would greatly increase the total computational time. In addition, introducing a further level of change would likely not provide further information for the parameters changes which were found to have little effect on the resulting models.

Despite these limitations, the sensitivity study has identified the parameters which have the most significant effect on the model and backed up the decisions made when developing the structural and continuum FE models in terms of mesh density and material properties assignment.

7

Pelvic injury modelling

The author wishes to thank Claire Villette for providing the structural fracture algorithm used in this chapter (Villette and Phillips, 2018).

As described in Chapter 2, §2.4, fractures of the pelvic ring are generally complex injuries that can lead to death due to exsanguination (Cryer et al., 1988; Balogh et al., 2007). The mechanism that causes blood vessel rupture in cases of high energy pelvic fractures is not well understood. A hypothesis is that bony fracture leads to a destabilization of the pelvic ring which in turn can tear blood vessels causing fatal haemorrhage.

Although pelvic fractures have been classified in the past based on injury mechanism and clinical outcome, fracture initiation and progression has not been studied extensively. Knowledge of fracture progression for the different injury mechanisms could provide a better understanding of how the pelvic region responds to injury scenarios and be a platform for improving prevention and mitigation strategies of combined hard and soft tissue pelvic injuries.

In this chapter, the optimised structural pelvic model presented in Chapter 4 was used along with a damage elaso-plasticity material model of bone (Villette and Phillips, 2018) to predict fracture initiation and progression for three injury scenarios relevant to three classes of pelvic fractures: lateral compression, vertical shear and anterior-posterior compression.

The scenarios simulated were set up in a generic manner, rather than replicating a particular experimental study from literature. The objective of these simulations was to investigate the structural model's ability to predict fracture progression and to broadly compare fracture loads with literature data on similar loading scenarios.

7.1 Fracture modelling

7.1.1 Material model

A damage elasto-plasticity model for bone developed by Villette and Phillips (2018), implemented using an *Abaqus* subroutine, was used to predict fracture in the structural model of the pelvic construct presented in Chapter 2. The model comprises of an elastic and plastic regime, in both tension and compression. The plastic behaviour of bone has been previously reported in literature (Reilly and Burstein, 1975; Gibson, 1985; Hansen et al., 2008; Prot et al., 2016) The plastic regime was incorporated as a plateau between the yield strains in compression, and tension, and the ultimate strains in compression and tension, respectively. Upon reaching one of the yield criteria, each material point was assigned an 'effective' Young's modulus value different to the original value. Thus, the element in question has a reduced load-bearing ability, allowing for elements to be effectively removed from the model without numerical instabilities or potential loss of computational efficiency. All models were run using the dynamic explicit simulation option in Abaqus.

7.1.2 Influence of strain rate and age on failure behaviour of bone

Two factors which can influence the mechanical behaviour of bone are loading rate and bone age. A number of studies have investigated the effect that age can have on the mechanical behaviour of bone, generally at tissue level (Lindahl and Lindgren, 1967; Burstein et al., 1976; Evans, 1976; McCalden et al., 1993; Zioupos and Currey, 1998). The ultimate tensile strain of bone has been shown to decrease by around 10 % every ten years after a threshold age (Lindahl and Lindgren, 1967; McCalden et al., 1993; Keaveny et al., 2004). Bone mass density (BMD) was also found to

decrease with age, and in cases concerning osteoporotic patients BMD can decrease at a rate of up to 10.2 mg/cm^2 per year (Nguyen et al., 1998; Kado et al., 2000). With age, bone tends to become more brittle, which is hypothesised to be due to collagen changes (McCalden et al., 1993; Keaveny et al., 2004). Factors which can lead to bone loss are hormonal changes (specifically for post-menopausal women) (Riggs et al., 1998; Ahlborg et al., 2003) lifestyle (eg. tobacco consumption) (Nguyen et al., 1994; Burger et al., 1998; Hannan et al., 2000), or a decrease in the frequency of daily physical activities (Drinkwater, 1993; Joseph et al., 1988; Nguyen et al., 1998; Hannan et al., 2000).

The effect of loading rate on Young's modulus was found to be moderate by several studies (Keaveny et al., 2004; Hansen et al., 2008; Prot et al., 2016), with a variation in Young's modulus of a factor of two over a six order magnitude increase in strain rate (Keaveny et al., 2004). On the other hand, failure properties are more sensitive to strain rate (Carter and Hayes, 1976; Hansen et al., 2008). Yield and ultimate strains were found to vary by factors of two and three respectively over a three order of magnitude increase in strain rate (Hansen et al., 2008).

Stress-strain curves can be obtained for a given combination of bone age and strain rate. Curves representing the mechanical behaviour of 30 and 75 years old bone for strain rates ranging from quasi-static to dynamic are shown in Figure 7.1.

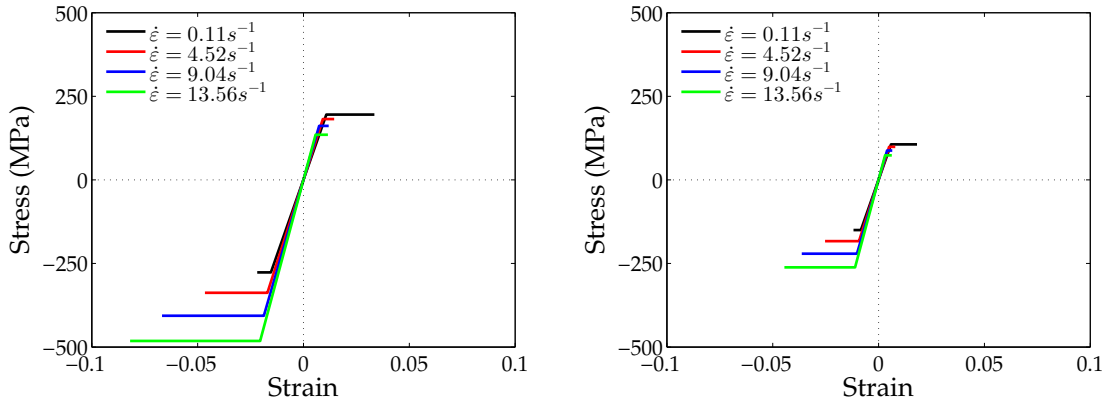


Figure 7.1: Stress-strain curves for (a) 30 year old bone and (b) 75 year old bone across four different strain rates based on the damage elasticity model presented in Villette and Phillips (2018).

In the following sections of this chapter, bone was assumed to have an age of 30 years and the strain rates used in simulations correspond to velocities of 4 m/s and 8 m/s, respectively. The velocity/strain rate relationships were derived by calculating the average strain rate over the model for two test simulations for the selected velocities. Although each element had a different strain rate during the simulations, the purpose of this exercise was to associate the selected impact velocities with an approximate strain rate. The parameters associated with the two bone models are shown in Table 7.1. The material model was applied only to elements comprising the pelvic ring, meaning that femoral elements in the models presented in the following sections were not allowed to fracture. All models were run using the dynamic explicit simulation option in Abaqus. The time step parameters in this type of simulation are set automatically by the solver throughout the simulation.

Case	Strain rate (s^{-1})	Age (years)	$\varepsilon_{y,c}$	$\varepsilon_{y,t}$	$\varepsilon_{u,c}$	$\varepsilon_{u,t}$
4 m/s	4.52	30	-0.01702	0.00916	-0.04653	0.01545
8 m/s	9.04	30	-0.01873	0.00745	-0.06679	0.01191

Table 7.1: Material model parameters of 30 year old bone for velocities of 4 m/s and 8 m/s, respectively.

7.2 Lateral compression

The first fracture mechanism investigated in this chapter is lateral compression. As described in Chapter 2, §2.4, lateral compression fractures are generally caused by a lateral force which drives the impacted hip inward (eg. motor vehicle accidents).

Multiple experimental studies have been done to investigate this injury mechanism and establish a fracture tolerance criterion. The majority of studies focused on peak impact force as the criterion for injury. The average peak load varied between 6.5 and 13 kN for full cadaver tests (Cesari et al., 1980; Cesari and Ramet, 1982; Nusholtz et al., 1982; Nusholtz and Kaiker, 1986; Viano et al., 1989; Viano, 1989; Cavanaugh et al., 1990; Zhu et al., 1993; Matsui et al., 2003) and between 1.75 and 5.5 kN for isolated pelvis tests (Renaudin et al., 1993a; Guillemot et al., 1997; Molz et al., 1997; Guillemot et al., 1998; Arbelaez et al., 1998; Beason et al., 2001, 2003; Salzar et al., 2009).

In addition to experimental testing, some studies focused on developing numerical models to simulate lateral impact on the pelvic construct (Renaudin et al., 1993a; Plummer et al., 1996, 1998; Dawson et al., 1999; Beason et al., 2001; Majumder et al., 2007; Li et al., 2007).

7.2.1 Loading and boundary conditions

The scenario for lateral compression was modelled by including a structural model of the femur, developed previously in the research group based on the adaptation algorithm presented in Chapter 3 (Villette, 2016). The femur was reduced to the proximal part to reduce computational cost and mirrored with respect to a plane perpendicular on the line comprising the two hip joint centres. Both femurs were placed in the coordinate frame recommended by the International Society of Biomechanics (Wu et al., 2002), to be consistent with the coordinate frame of the pelvis. The model

was placed in a two legged stance.

A layer of cartilage was added on the surfaces of the acetabulum and femoral head to facilitate contact between bones. Cartilage was modelled using a layer of wedge elements, 1 mm thick, assigned linear elastic material properties (E = 10 MPa, $\nu = 0.3$). If needed, the positions of both femurs were readjusted to avoid intersections between geometries and to avoid numerical issues when modelling contact between the two surfaces. In addition, the fixator described in Chapter 3 was included at the top of the sacrum to enable the addition of a boundary condition.

To simulate side impact, a lateral displacement of 30 mm was applied on the right femur, with fixed boundary conditions applied on the sacral load fixator and the greater trochanter of the contralateral femur, as shown in Figure 7.2. The loading conditions and boundary conditions were set to resemble a lateral impact on the greater trochanter and lateral pelvis. The displacement was applied at two different velocities (4 m/s and 8 m/s), to investigate the effect of strain rate on fracture initiation and progression.

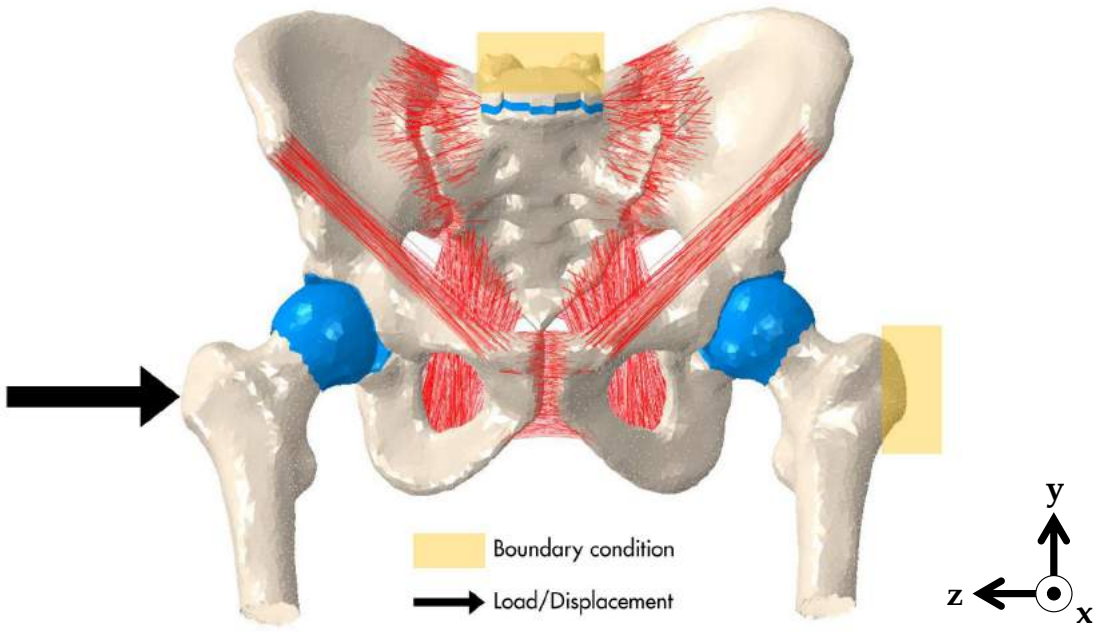


Figure 7.2: Boundary and loading conditions applied to the model to simulate lateral compression fracture

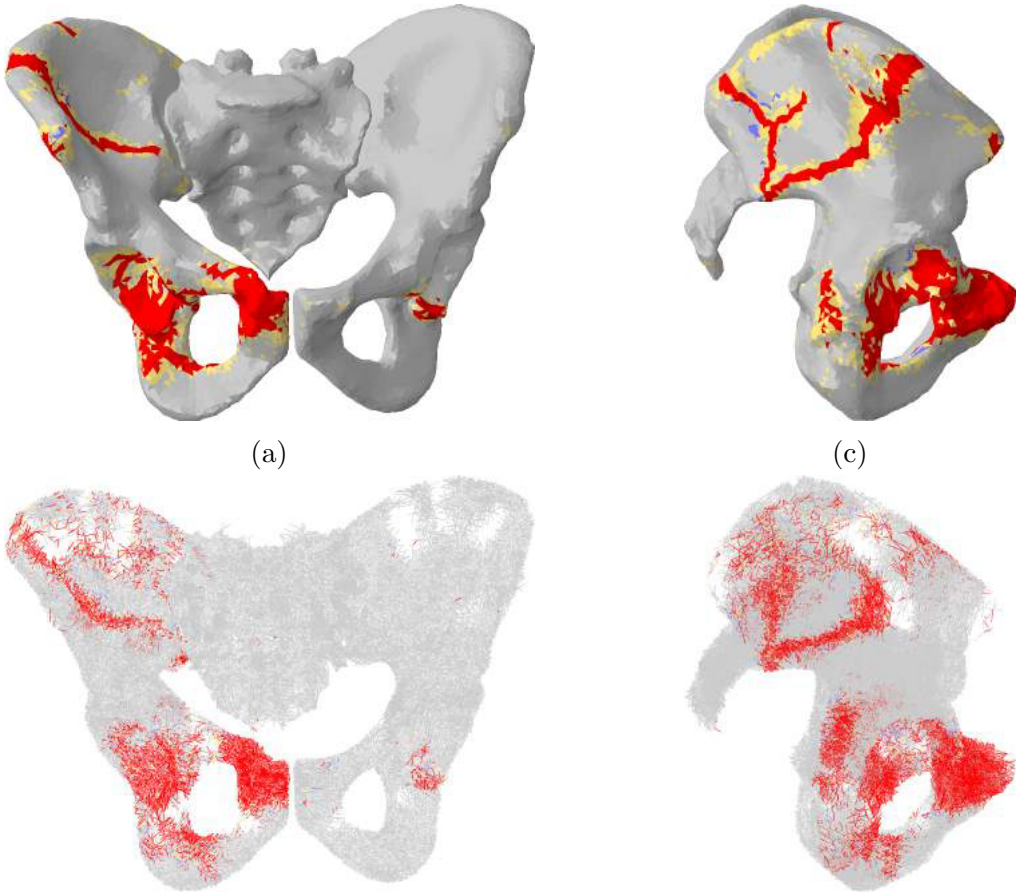
7.2.2 Results

The fracture patterns predicted by the two models are shown in Figures 7.3 and 7.4 for displacement rates of 4 m/s and 8 m/s, respectively.

In the first scenario, fracture was initiated in the impacted inferior acetabulum, which then progressed towards the inferior pubic ramus. As the simulation progressed, clusters of failed elements appeared in the superior pubic ramus and across the superior ilium posteriorly. The model predicted a damaged acetabulum, fractured ipsilateral pubic rami and a fracture line along the superior ilium. On the contralateral side, failed elements were found on the inferior acetabulum.

In the second scenario, when the pelvis was impacted with a greater velocity, fracture was initiated in the inferior acetabulum, similar to the slower case. Fractures at the inferior and superior pubic rami occured at a later stage in the simulation due to the damage to the inferior acetabulum spreading towards the superior acetabulum, in contrast to the lower velocity scenario. A similar fracture line across the superior ilium posteriorly was also predicted towards the end of the simulation. In addition, the attachment region of the inguinal ligament on the ipsilateral ilium was damaged. Contralaterally, failed elements were predicted on the inferior acetabulum and attachment region of the ingiunal ligament in the ilium.

In both cases, the fracture patterns predicted by the model were consisted with observations made by Young et al. (1986).



(a) (c)

(b) (d)

Figure 7.3: Frontal and side view predicted fracture pattern in lateral compression scenario with an impact velocity of 4m/s. Failed elements are shown in red, elements yielded in tension are shown in light yellow and elements yielded in compression are shown in light blue.

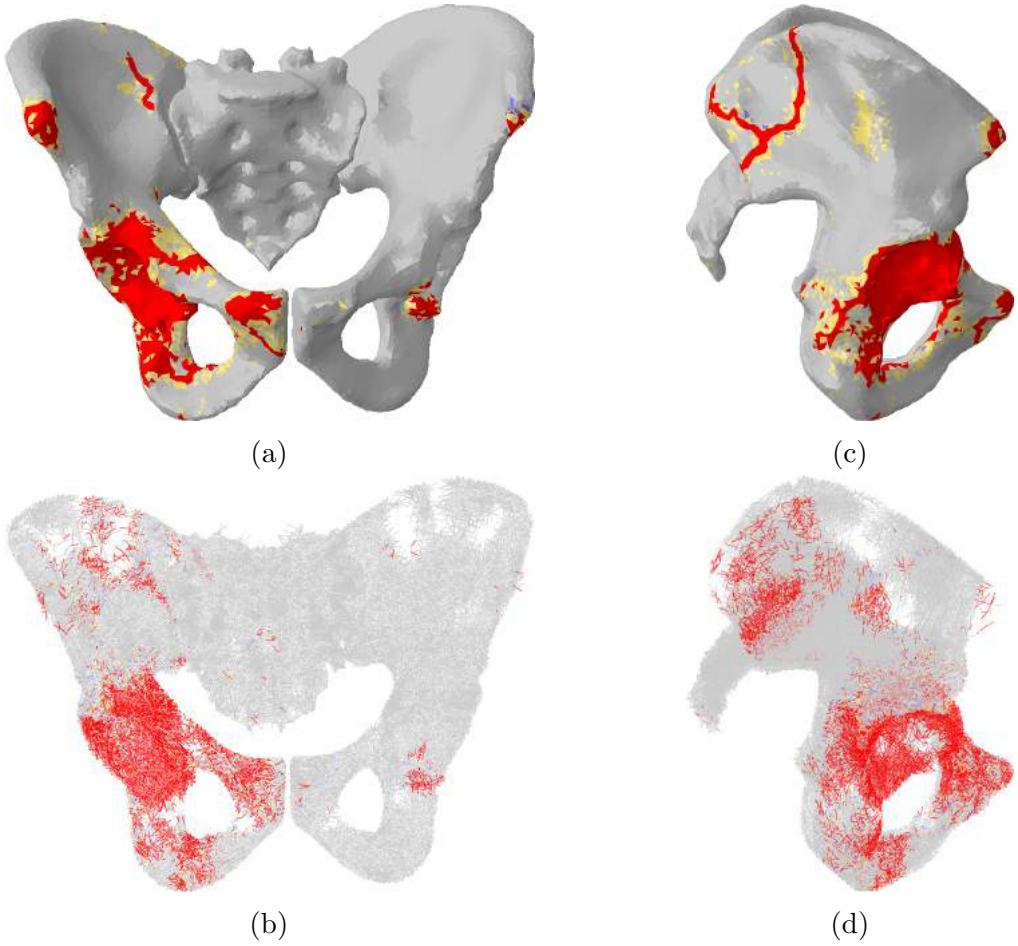


Figure 7.4: Frontal and side view predicted fracture pattern in lateral compression scenario with an impact velocity of 8 m/s. Failed elements are shown in red, elements yielded in tension are shown in light yellow and elements yielded in compression are shown in light blue.

Reaction force components at the sacral boundary condition plotted against time are shown in Figure 7.5. Peak forces in the direction of impact were 7.62 kN and 7.38 kN for 4 m/s and 8m/s displacement rates, respectively. Although the displacement vector was set along the z axis, comparable reaction forces were predicted in the x and y directions, suggesting that, after contact initiation at the hip joint, the direction of the load transferred changes.

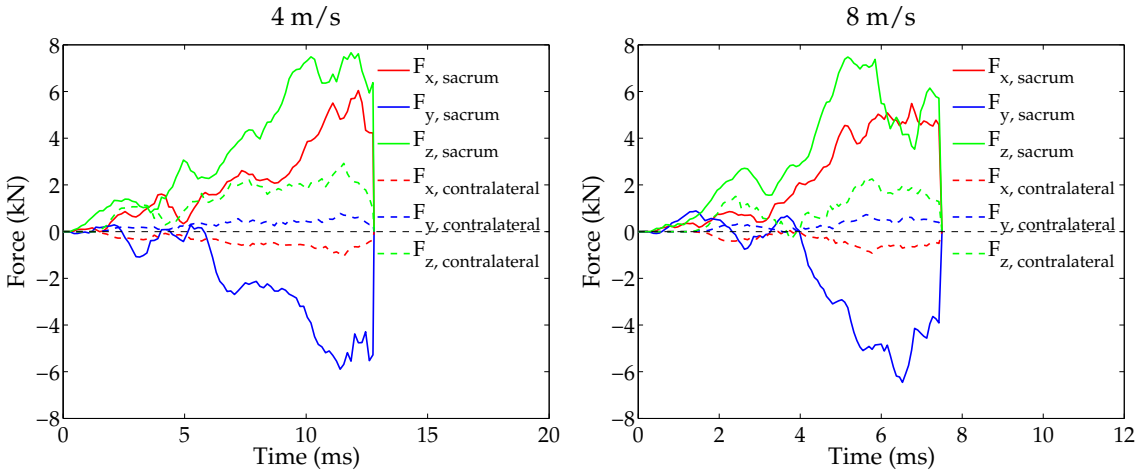
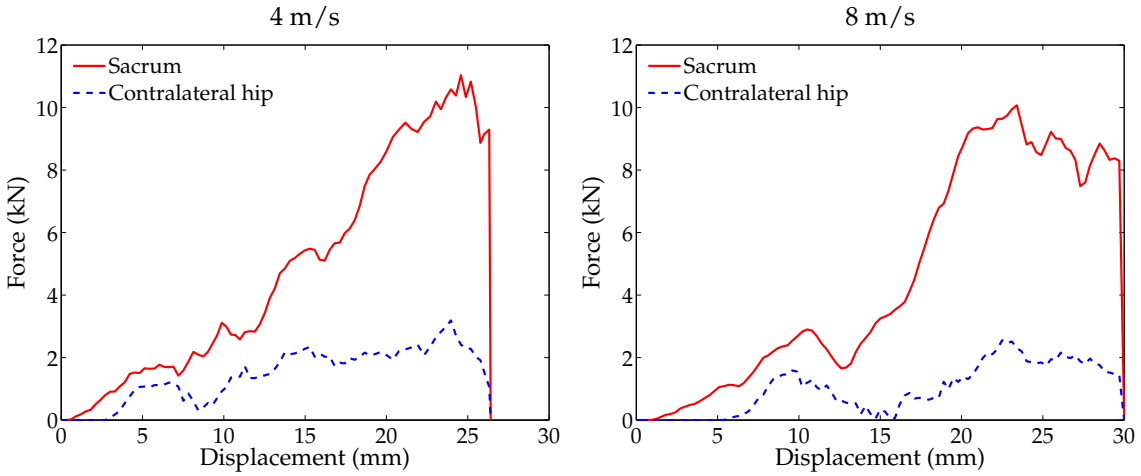


Figure 7.5: Force-time plots for both scenarios. Components of reaction force at the sacrum are shown in solid lines and in dash lines at the contralateral femur.

The resultant reaction force-displacement curves for both scenarios are shown in Figure 7.6. The model predicted fracture occuring in the acetabulum at 4.8 kN and 3.3 kN for 4 m/s and 8 m/s respectively. Fracture at the pubic rami occured at load of 9.2 kN and 9.6 kN for 4 m/s and 8 m/s, respectively. Further displacement causing an internal rotation of the impacted hemi-pelvis led to fracture lines occuring in the ilium in both cases. The peak resultant force predicted at the sacrum in the first case (4 m/s) was 11.04 kN and 10.07 kN in the second case (8 m/s). Similar observations were made by Dawson et al. (1999) in terms of the force at which the pubic rami and ilium fracture. However, their model predicted fracture in the acetabulum at a force of approximately 12 kN. A limitation of the structural model is the relatively low resolution in the proximity of joints, which can lead to underpredicting fracture loads at the joints.



(a) (b)

Figure 7.6: Force-displacement plots for both scenarios. Reaction force at the sacrum is shown in solid red and in dash blue at the contralateral femur.

7.3 Vertical shear

Vertical shear fractures of the pelvis are usually caused by a vertical load transferred through the hip towards the lumbar spine, as described in Chapter 2, §2.4. A typical civilian scenario associated with this type of injury are purposeful falls from height, where the casualty lands feet first. As opposed to lateral compression, there is little data in the literature assessing numerically or experimentally axial loading on a standing pelvic ring. A number of clinical studies showed that the height of fall is proportional with probability of fatal injury (Bertocci et al., 2004; Dickinson et al., 2012). Bruno et al. (2014) investigated outcomes from purposeful falls and found that pelvic ring injuries occured at the three pelvic joints more frequently with increasing height, with the sacroiliac joints more commonly affected.

7.3.1 Loading and boundary conditions

The scenario simulating vertical shear comprised of a similar assembly to lateral compression, with both the left and right proximal femurs included in the model to simulate load transfer through the hip joint to the pelvis. The coordinate frames used in §7.2 were applied to the pelvis and femurs. Contact between each femur and the pelvis was modelled as described in §7.2.

To simulate this injury scenario, two cases were simulated. In the first case, displacement was applied vertically through the right femur, with boundary conditions enforced at the top of the sacrum through the load applicator and the contralateral femur to simulate unilateral damage, indicative of one foot striking before the other. In addition, the ipsilateral femur was restricted from movement in the z direction. The model configuration is shown in Figure 7.7.

In the second case, displacement was applied vertically through both femoral shafts, with boundary conditions enforced at the top of the sacrum to simulate bilat-

eral damage, indicative of both feet striking the ground simultaneously. The model configuration is shown in Figure 7.8. Similar to lateral compression, two displacement rates were simulated to investigate the potential effect of strain rate on fracture outcome and load.

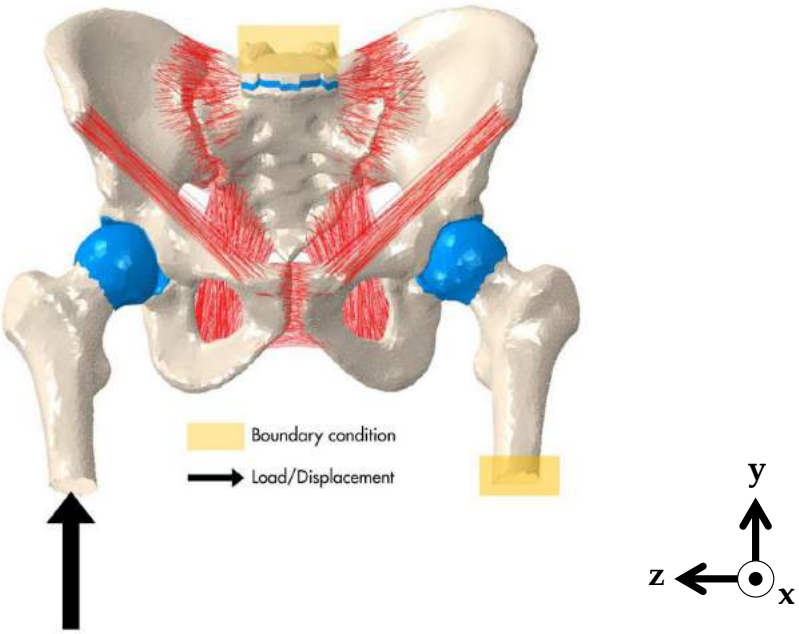


Figure 7.7: Boundary and loading conditions applied to the model to simulate unilateral vertical shear fracture

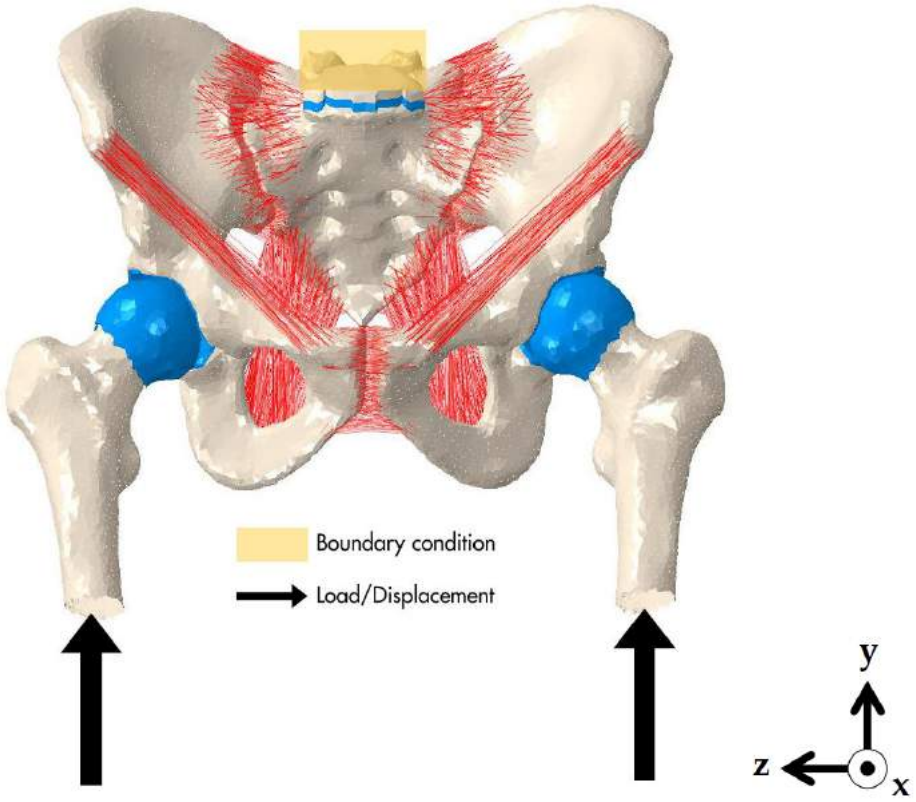


Figure 7.8: Boundary and loading conditions applied to the model to simulate bilateral vertical shear fracture

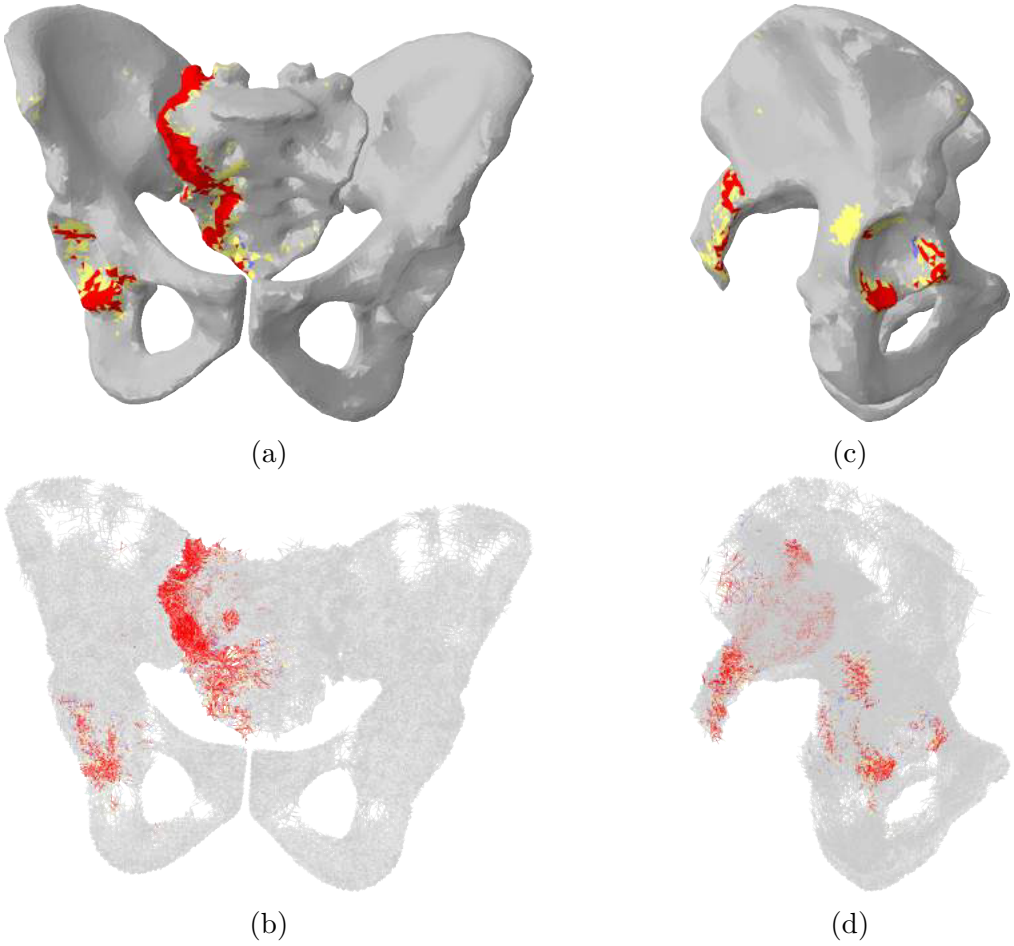
7.3.2 Results

7.3.2.1 Unilateral impact

The fracture patterns predicted by the two models are shown in Figures 7.9 and 7.10 for 4 m/s and 8 m/s, respectively.

In the first scenario, failed elements first appeared in the acetabulum. As the displacement progressed, a fracture line was initiated on the ipsilateral side of the sacrum and progressed around the sacroiliac joint, leading to a mechanical instability in the pelvic ring.

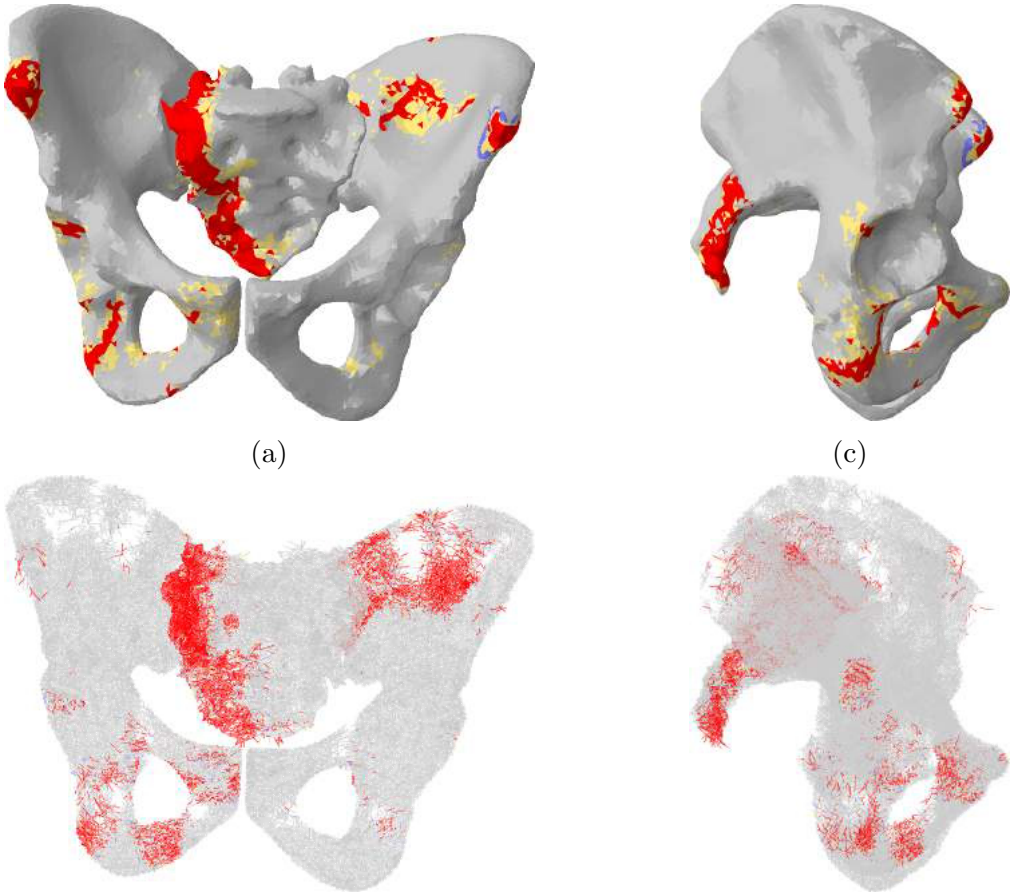
The second model predicted similar damage in the acetabulum and around the ipsilateral sacroiliac joint on the sacrum. Due to a greater displacement rate, additional fracture lines and areas with failed elements appeared in the pubic fossa, contralateral superior ilium and inguinal ligament attachment regions on both ilia.



(a) (c)

(b) (d)

Figure 7.9: Frontal and side view predicted fracture pattern in vertical shear scenario. Failed elements are shown in red, elements yielded in tension are shown in light yellow and elements yielded in compression are shown in light blue.



(a) (c)

(b) (d)

Figure 7.10: Frontal and side view predicted fracture pattern in vertical shear scenario. Failed elements are shown in red, elements yielded in tension are shown in light yellow and elements yielded in compression are shown in light blue.

Reaction force components at the sacral boundary condition plotted against time are shown in Figure 7.11. Although the dominant component was in the direction of the applied displacement, the other two components reached peak values of up to 10 kN, suggesting that the loading scenario is more complex than a purely axial loading case. For both displacement rates, the reaction forces in the anterior-posterior and medio-lateral directions were similar.

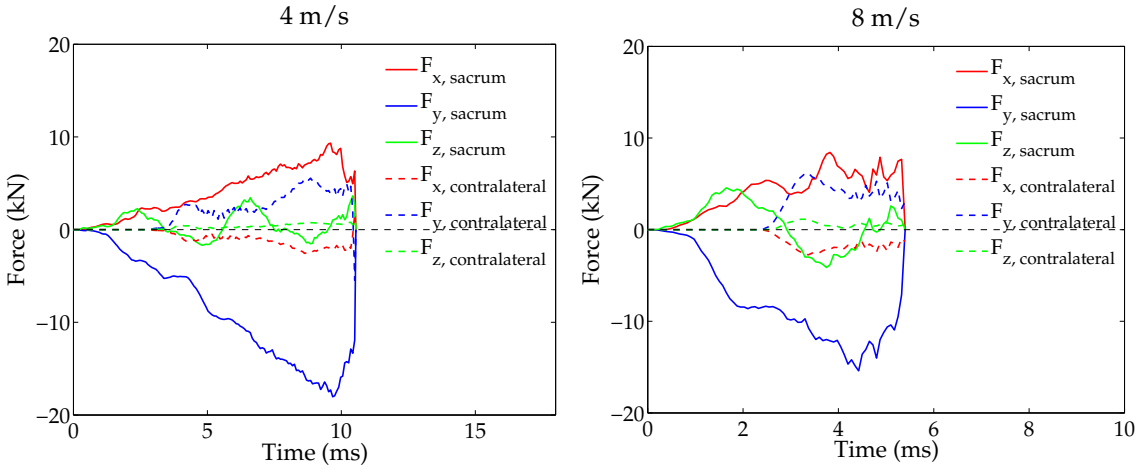


Figure 7.11: Force-time plots for both scenarios. Components of reaction force at the sacrum are shown in solid lines and in dash lines at the contralateral femur.

The force-displacement curves for both scenarios are shown in Figure 7.12. The peak resultant force predicted at the sacrum in the first case (4 m/s) was 20.78 kN and 16.68 kN in the second case (8 m/s). Although the damage was greater for the higher displacement rate case, the peak load was greater for the lower impact velocity case. An explanation can be that elements failing earlier in the 8 m/s case have lead to a change in the load transferred to the pelvis, increasing the stresses on the contralateral side. This difference is also highlighted by the reaction force at the contralateral femur, as in the 8 m/s case it reaches a peak value of approximately 5 kN earlier in the simulation than in the slower velocity case.

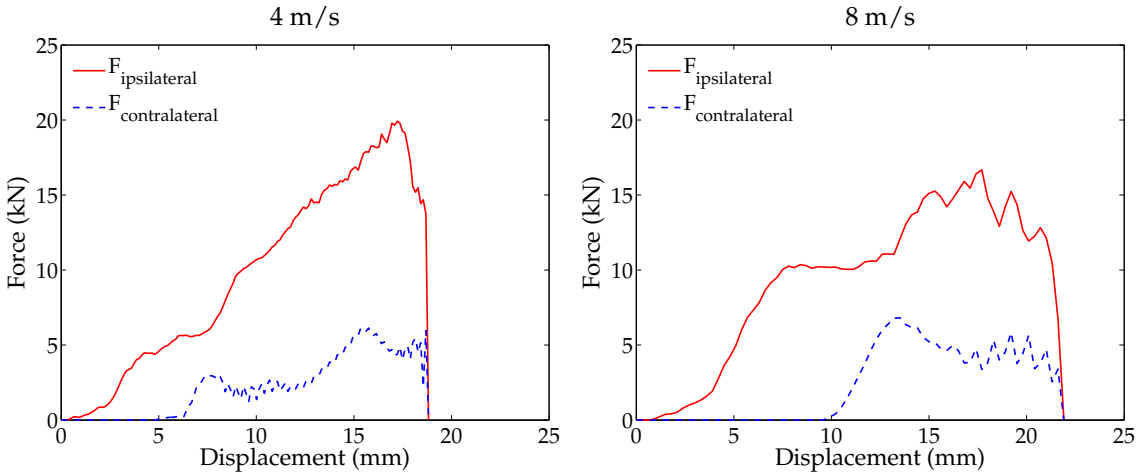


Figure 7.12: Force-displacement plots for both scenarios. Reaction force at the sacrum is shown in red and in dash blue at the contralateral femur.

7.3.2.2 Bilateral impact

In the case of bilateral impact, the fracture patterns predicted by the model for displacement rate of 8 m/s are shown in Figure 7.13. Failed elements appeared first in the acetabular regions. As the displacement increased, the sacroiliac regions began to fail, followed by fracture lines developing across both pubic rami.

Although the displacement rates were identical on both sides, the fracture patterns are not symmetrical. The right acetabulum sustained more damage, whereas on the left side of the pelvis, a greater number of failed elements were found in the sacroiliac region. An explanation for the fracture patterns predicted by the bilateral impact model can be provided by the asymmetric structure of the adapted pelvis, leading to differences in the manner that load is transferred from the acetabulum through to the sacrum.

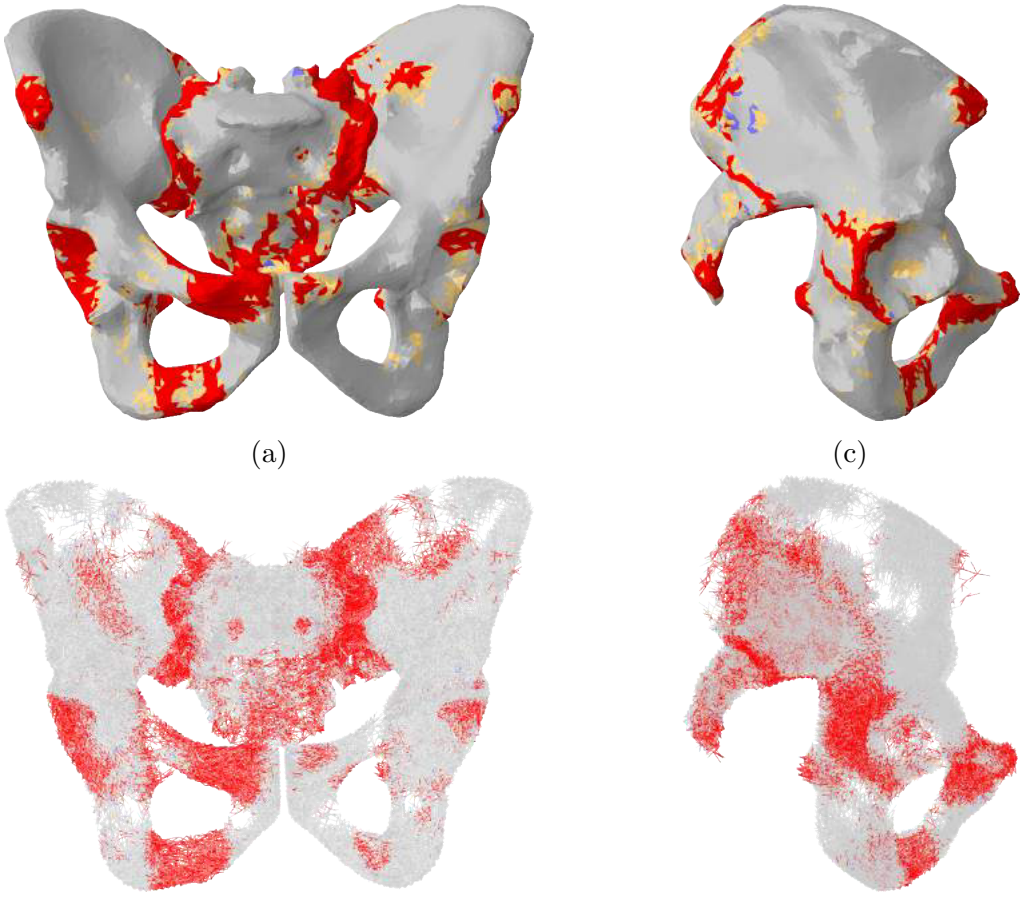
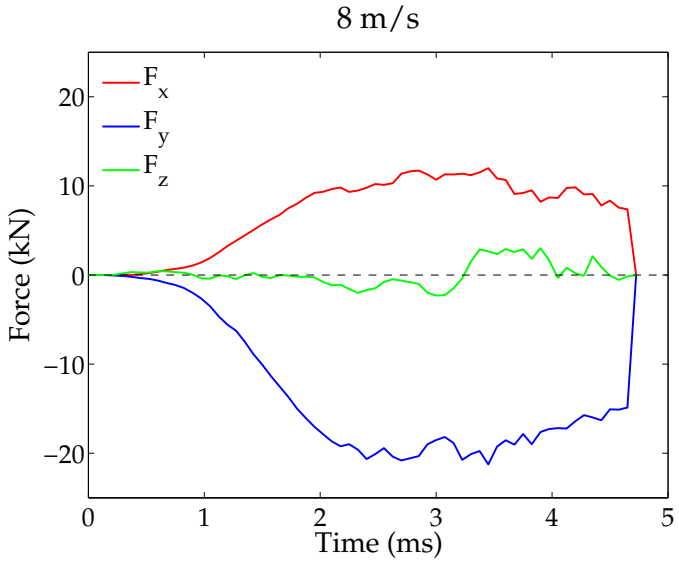


Figure 7.13: Frontal and side view predicted fracture pattern in vertical shear scenario. Failed elements are shown in red, elements yielded in tension are shown in light yellow and elements yielded in compression are shown in light blue.

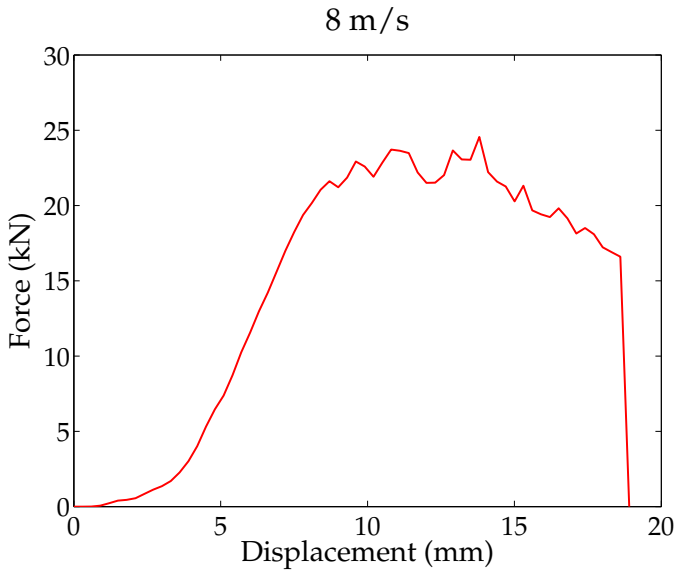
Reaction force components at the sacral boundary condition are shown in Figure 7.14. The peak magnitudes of the x and y components of the reaction force were greater than in the unilateral case. Due to the bilateral nature of the loading conditions, the z component did not vary as much as for the unilateral case. This can explain the nature of the fracture patterns and further damage at the pubic rami due to a more axial loading scenario.



(a)

Figure 7.14: Reaction force components at the sacral boundary condition for bilateral vertical shear.

The force-displacement curve for bilateral vertical shear is shown in Figure 7.15. The peak resultant force predicted at the sacrum was 24.5 kN, higher than the unilateral case for the same displacement rate. The fracture patterns and peak loads predicted by the model for unilateral and bilateral impact suggest that impacting the pelvis with both femurs leads to greater damage and a more complex fracture type.



(a)

Figure 7.15: Force-displacement for bilateral vertical shear.

7.4 Anterior posterior compression

As described in Chapter 2, §2.4, anterior posterior fractures are generally caused by a load driven through the femoral shaft in a seated position (eg. frontal vehicle crash).

Experimental studies investigating injuries from frontal crashes were initially focused on the knee and femur (Viano, 1977; Viano et al., 1978), while others did not achieve pelvic fractures even with high loads (Powell et al., 1975; Donnelly and Roberts, 1987; Brun-Cassan et al., 1982). Rupp et al. (2003) suggested that the characteristics of experimental loading conditions used in previous experimental tests were limiting the transfer of loads to the hip. They performed tests on the knee-thigh-hip complex and found that hip fractures occured at loads of approximately 6 kN (Rupp et al., 2002, 2003). Salzar et al. (2006) assessed whether the injury tolerance of the hip depended on the anatomical configuration of the thigh-hip complex. They tested eight cadavers in six seated positions by varying the flexion-extension and abduction-adduction angles and recorded peak axial forces and forces at fracture initiation.

7.4.1 Loading and boundary conditions

To simulate an anterior posterior compression mechanism, both femurs were rotated around the z-axis such that the final configuration corresponds to a seated position. Displacement was applied at two velocities (4m/s and 8m/s) through one femoral shaft axially (unilateral impact) and through both femoral shafts axially (bilateral) to replicate a frontal crash scenario where the passenger's knee and thigh are accelerated towards the dashboard. Regions of the posterior sacrum and posterior superior iliac spine (PSIS) were fixed in all degrees of freedom while the femurs were restricted form movement in the z direction. In the unilateral case, the unimpacted femur was restricted from movement in all three directions. The model setup is shown in Figure

7.16.

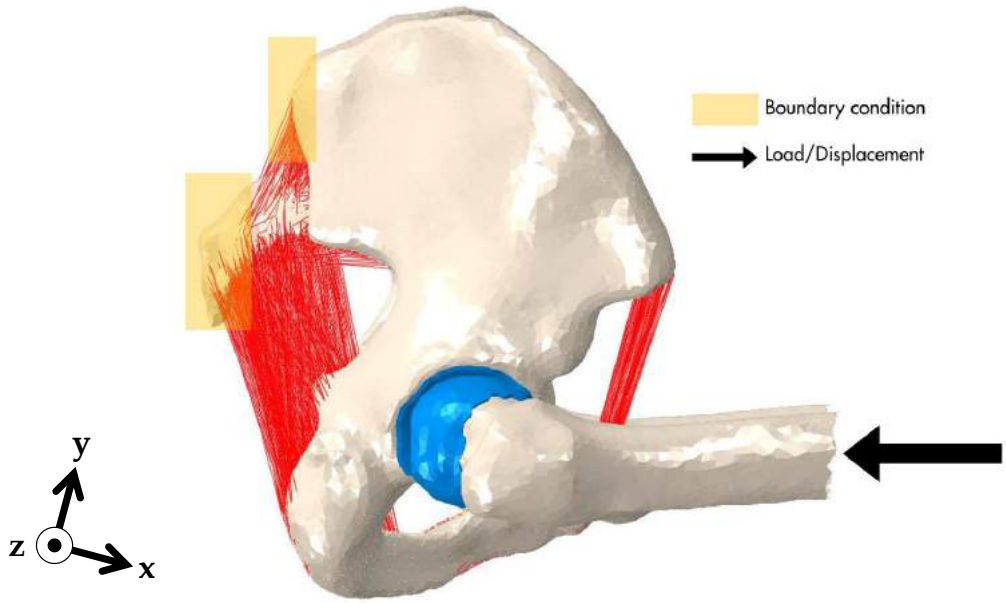


Figure 7.16: Boundary and loading conditions applied to the model to simulate anterior posterior compression fracture

7.4.2 Results

7.4.2.1 Bilateral impact

The fracture patterns predicted by the two models for bilateral impact are shown in Figures 7.17 and 7.18 for 4 m/s and 8 m/s, respectively. The 4 m/s model predicted acetabular damage on both sides, followed by failed elements around the PSIS, inferior and superior sacrum. For a displacement rate of 8 m/s, failed elements appeared on the acetabular regions and around the PSIS early in the simulation, followed by damage in the inferior and superior sacrum, albeit to a lesser extent than the model with a lower displacement rate.

Both models predicted fractures in the acetabular region, consistent with previous experimental studies (Rupp et al., 2002; Salzar et al., 2006). Failed elements at the

PSIS and posterior sacrum were not consistent with results reported in literature, suggesting that the boundary conditions applied on the models might over constrain it for this type of loading scenario.

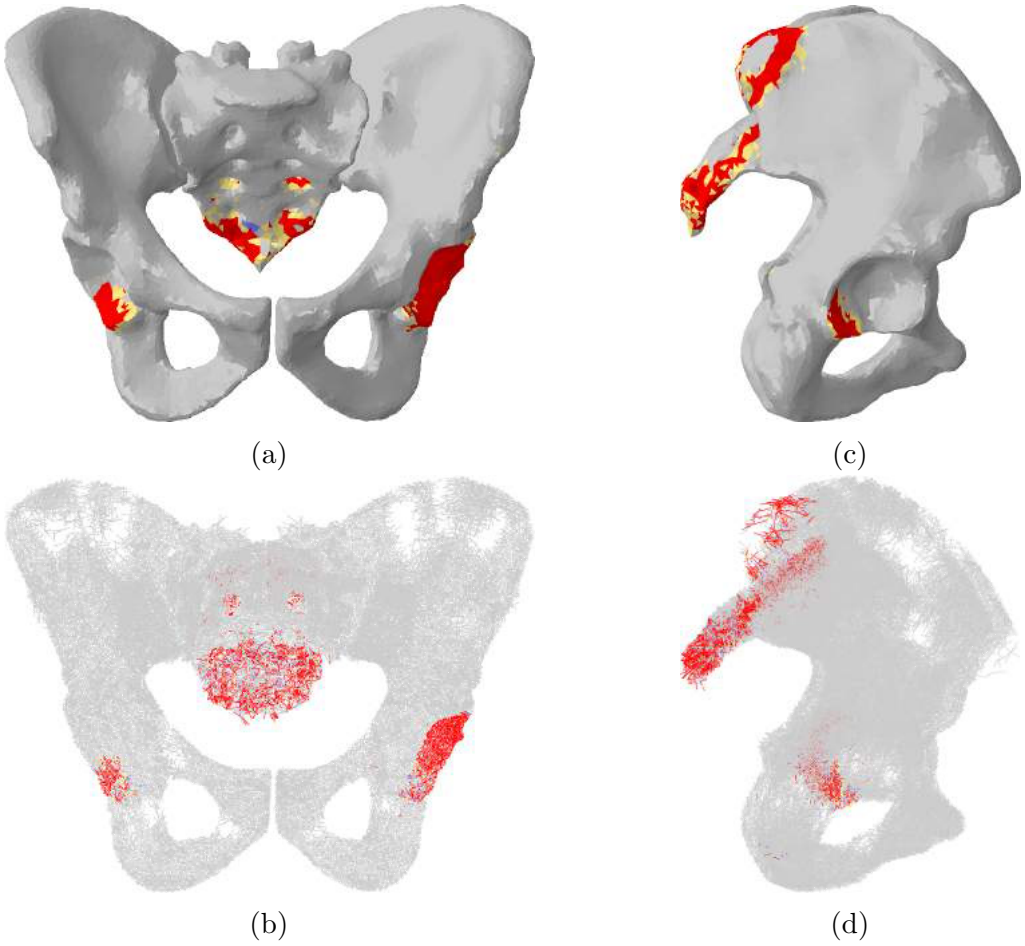


Figure 7.17: Frontal and side view predicted fracture pattern in anterior posterior compression scenario. Failed elements are shown in red, elements yielded in tension are shown in light yellow and elements yielded in compression are shown in light blue.

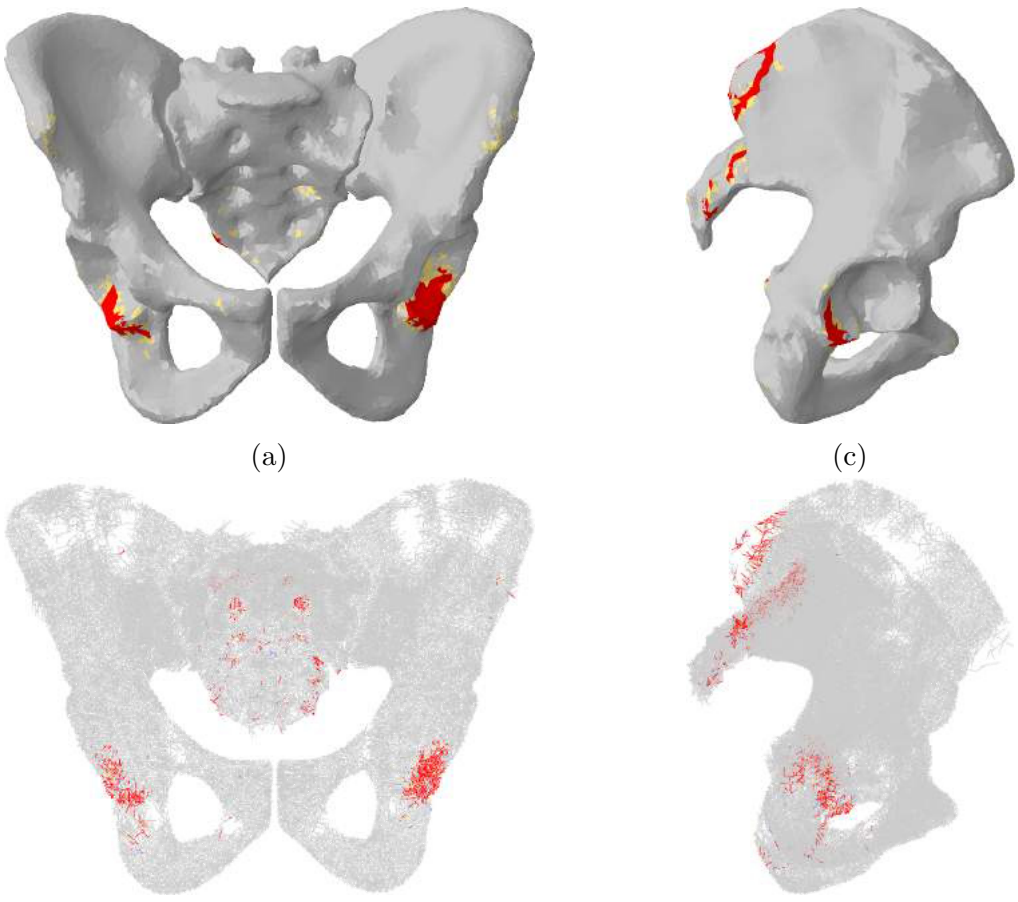


Figure 7.18: Frontal and side view predicted fracture pattern in anterior posterior compression scenario. Failed elements are shown in red, elements yielded in tension are shown in light yellow and elements yielded in compression are shown in light blue.

Reaction force components at the fixed boundary condition plotted against time are shown in Figure 7.19. The dominant component was in the x direction, with peak values reaching 6 kN in both cases. Due to the bilateral nature of the impact, the reaction force in the z direction was much smaller compared to the other two components.

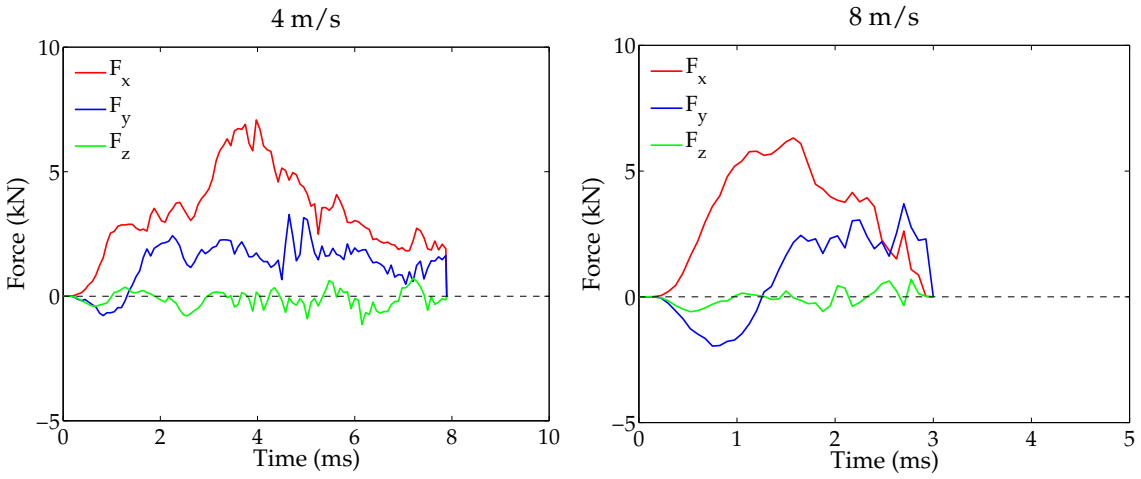


Figure 7.19: Force-time plots for both scenarios.

The force-displacement curves for both scenarios are shown in Figure 7.28. The peak resultant force predicted at the sacrum in the first case (4 m/s) was 7.29 kN and 6.68 kN in the second case (8 m/s). Both predicted peak forces were comparable to results reported in experimental studies (Rupp et al., 2002, 2003; Salzar et al., 2006).

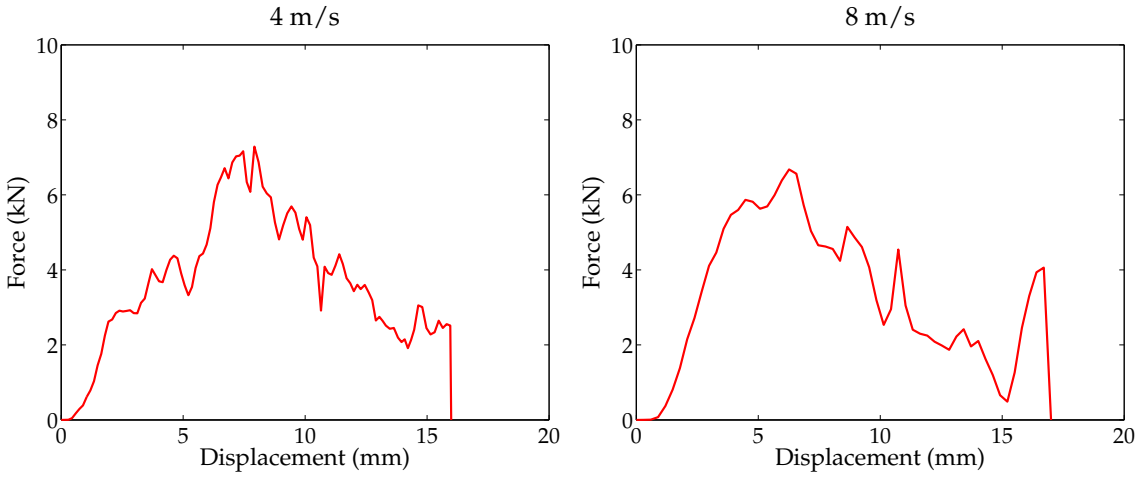


Figure 7.20: Force-displacement plots for both scenarios.

7.4.2.2 Unilateral impact

The fracture patterns predicted by the two models for unilateral impact are shown in Figures 7.21 and 7.22 for 4 m/s and 8 m/s, respectively. The first model predicted a small number of yielded elements before the rotation of the pelvis meant that the displaced femur was not transferring loads to the hip.

For a displacement rate of 8 m/s, failed elements appeared on the ipsilateral acetabular region and around the PSIS, with a small number of yielded elements present at the inferior sacrum.

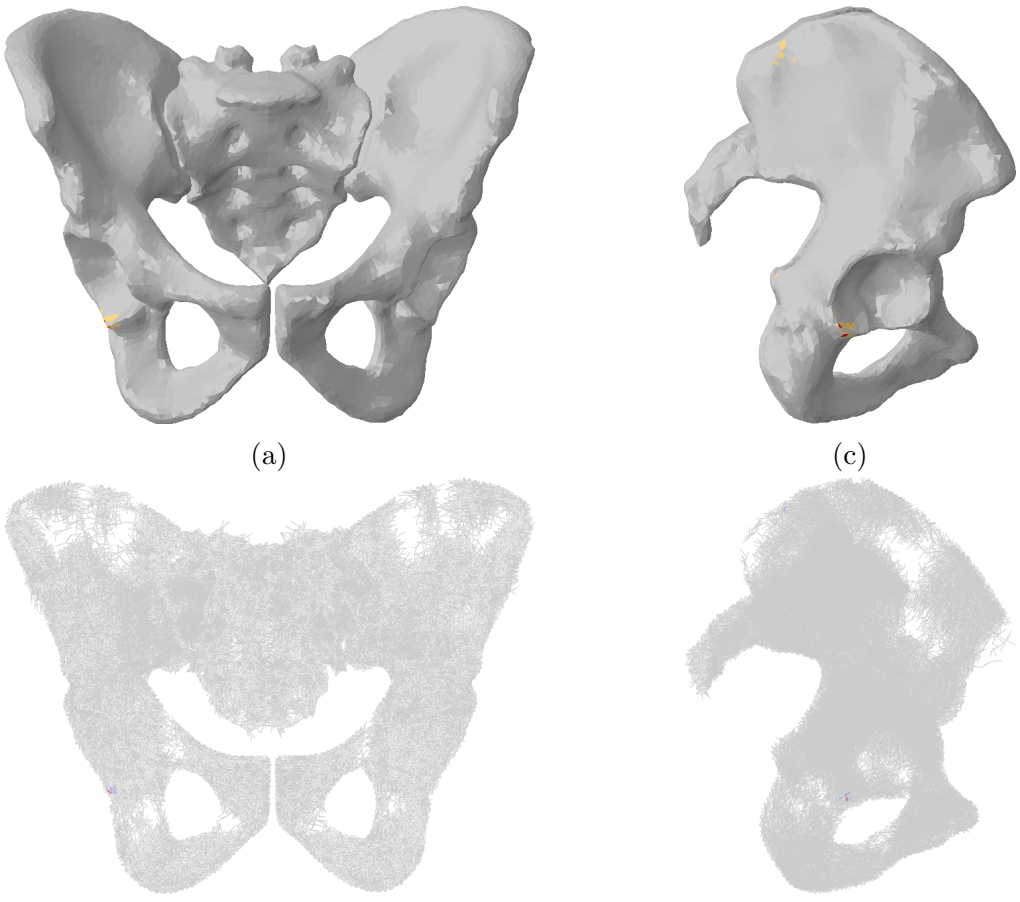


Figure 7.21: Frontal and side view predicted fracture pattern in anterior posterior compression scenario. Failed elements are shown in red, elements yielded in tension are shown in light yellow and elements yielded in compression are shown in light blue.

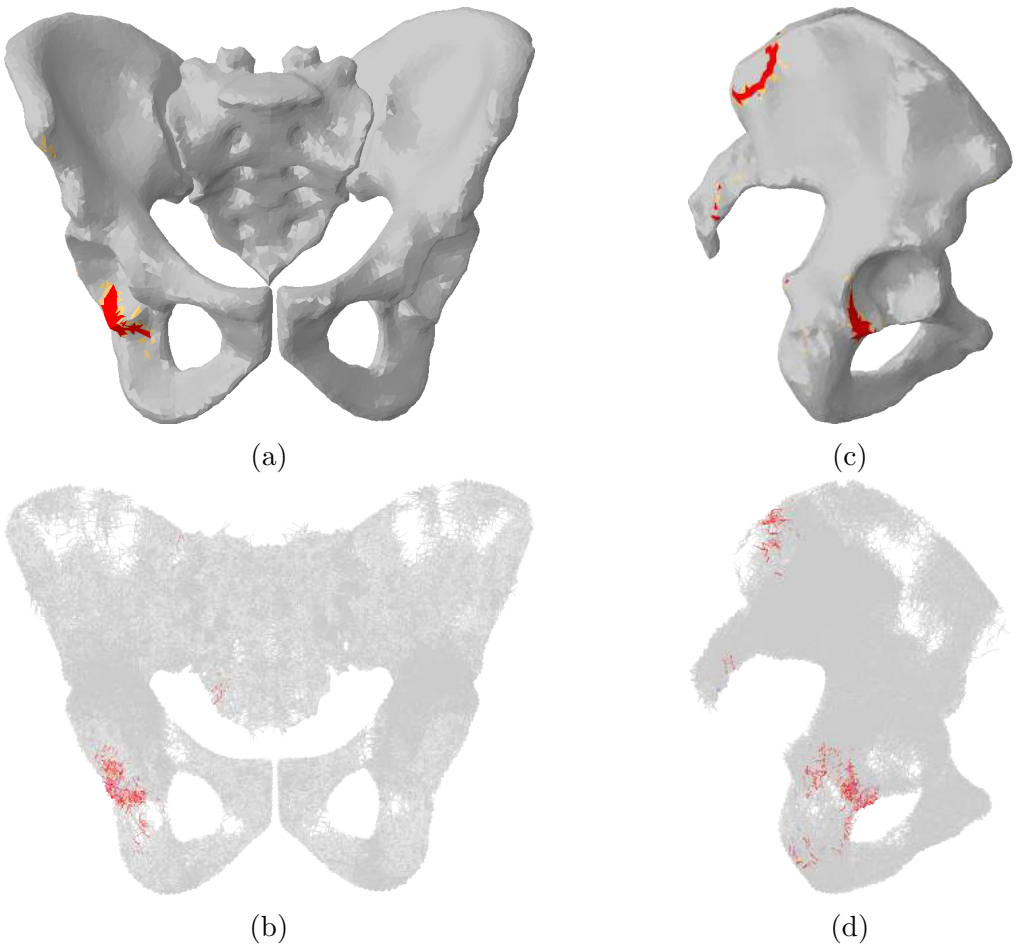
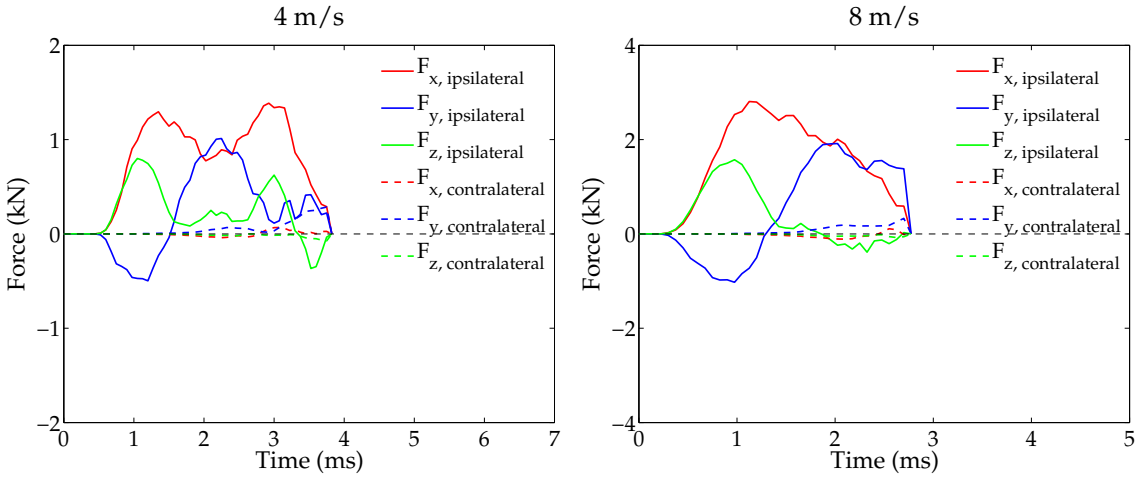


Figure 7.22: Frontal and side view predicted fracture pattern in anterior posterior compression scenario. Failed elements are shown in red, elements yielded in tension are shown in light yellow and elements yielded in compression are shown in light blue.

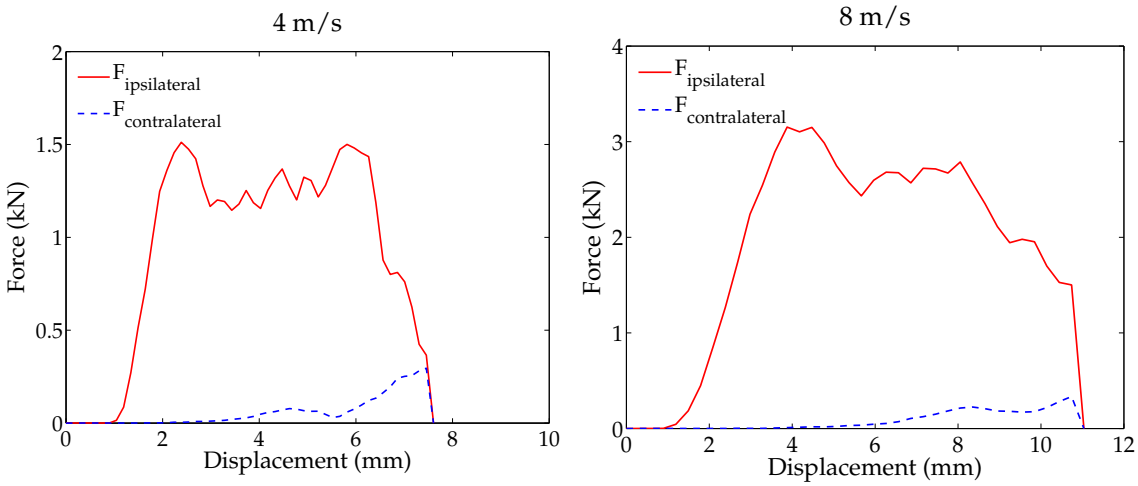
Reaction force components at the fixed boundary condition and the contralateral femur plotted against time are shown in Figure 7.23. The dominant component was in the x direction, with peak values reaching 1.5 kN and 3 kN for 4 m/s and 8 m/s, respectively. The low values of reaction forces at the contralateral femur and lack of failed elements on the contralateral side indicate that most of the load is taken by the sacrum and ipsilateral side.



(a) (b)

Figure 7.23: Force-time plots for both scenarios.

The force-displacement curves for both scenarios are shown in Figure 7.24. The peak resultant force predicted at the sacrum in the first case (4 m/s) was 1.5 kN and 3.2 kN in the second case (8 m/s). Both predicted peak forces were smaller than the corresponding bilateral cases.

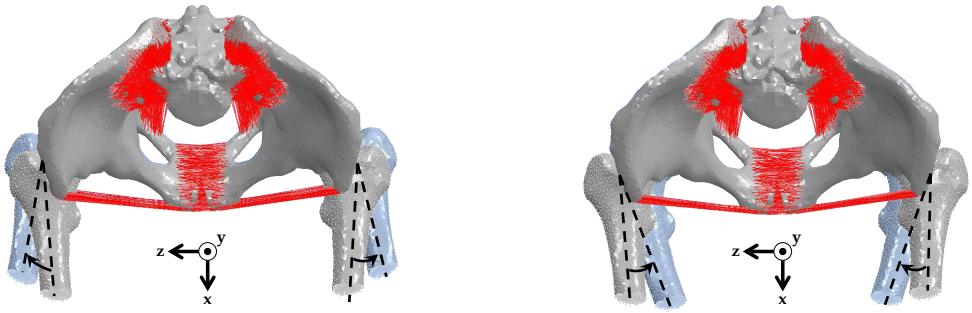


(a) (b)

Figure 7.24: Force-displacement plots for both scenarios.

7.4.3 Postures

In addition to investigating the predicted response to axial loading in a neutral seated position, the model was used to assess the influence of postures on predicted fracture patterns and fracture loads for bilateral impact. Two scenarios were proposed, in which both femurs were abducted and adducted by 20 degrees, respectively. The resulting configurations are shown in Figure 7.25. The loading and boundary conditions applied were identical to the neutral configuration. A displacement rate of 8 m/s was applied to both femoral shafts.



(a) (b)

Figure 7.25: Posture obtained by abducting (a) or adducting (b) both femurs by 20 degrees (light blue) shown in comparison to baseline posture (grey)

The fracture patterns predicted by the two models are shown in Figure 7.26 for abduction and in Figure 7.27 for adduction. In both postures failed elements were found in the acetabular regions and on the posterior side of the pelvis, similar to results predicted in the neutral configuration for the corresponding displacement rate.

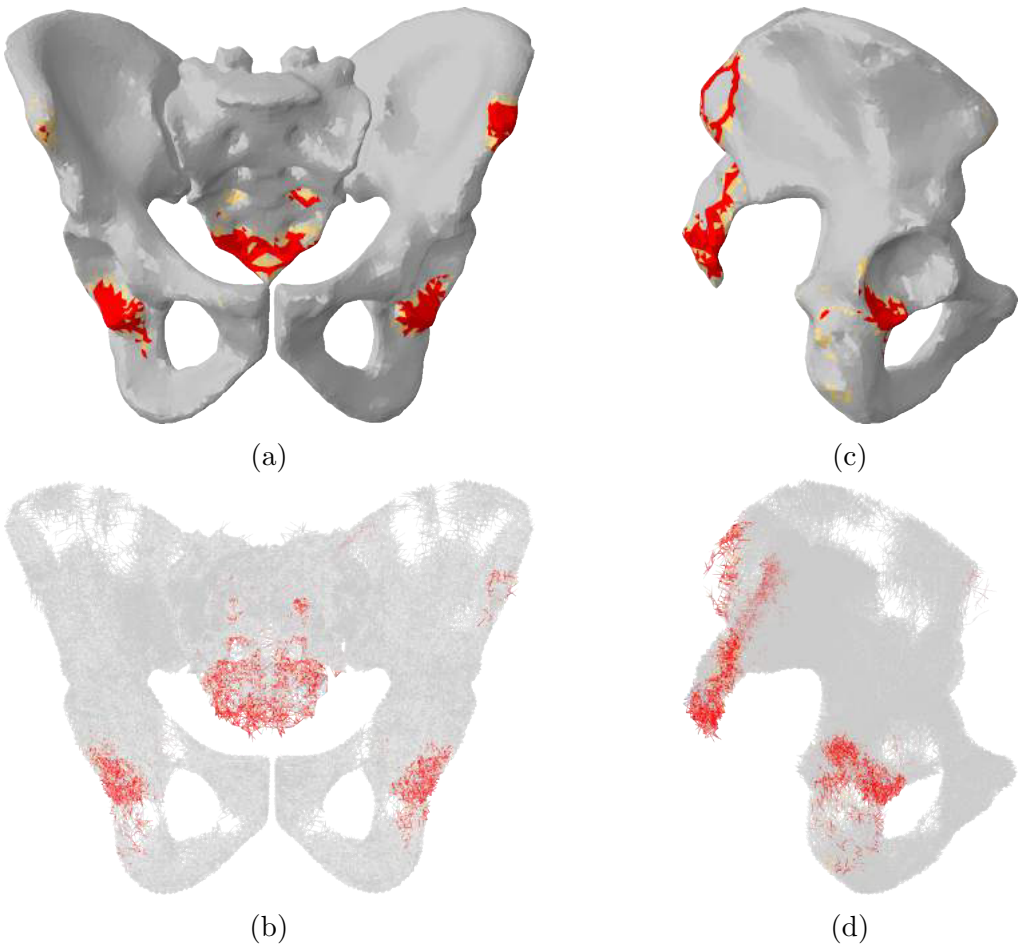


Figure 7.26: Frontal and side view predicted fracture pattern in anterior posterior compression abducted scenario. Failed elements are shown in red, elements yielded in tension are shown in light yellow and elements yielded in compression are shown in light blue.

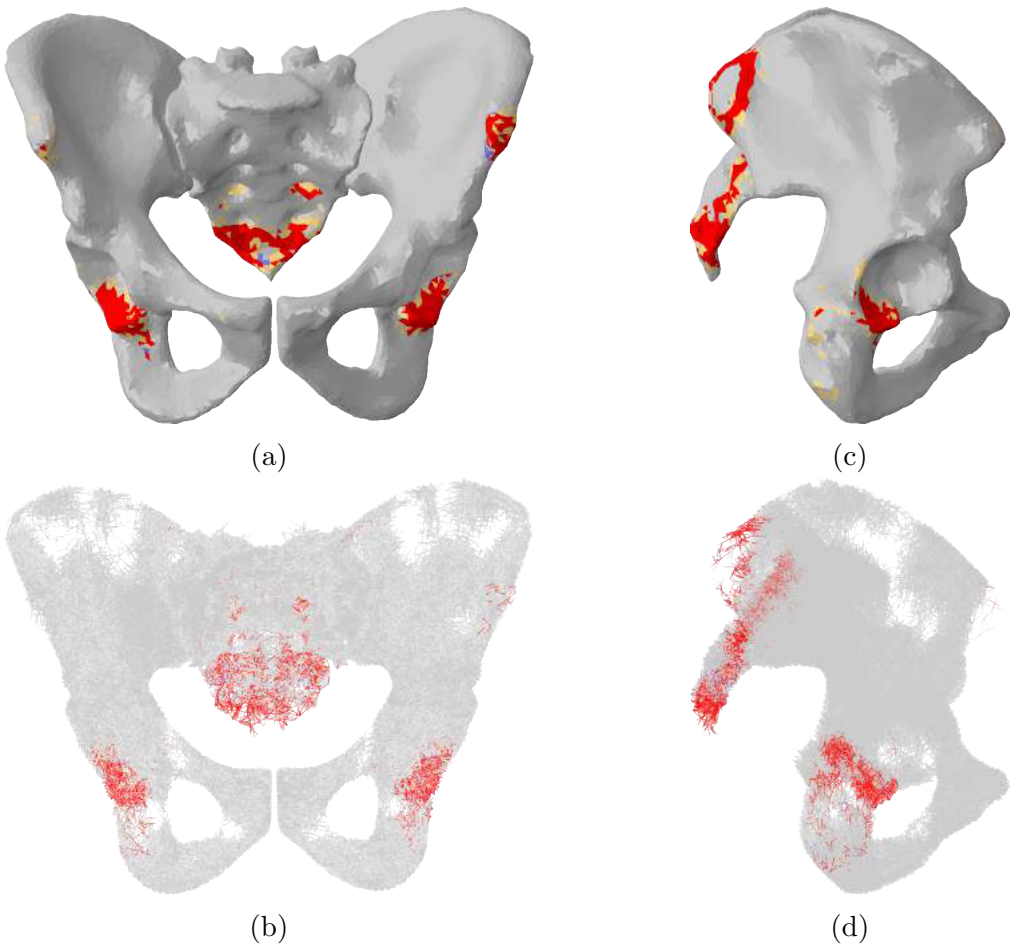
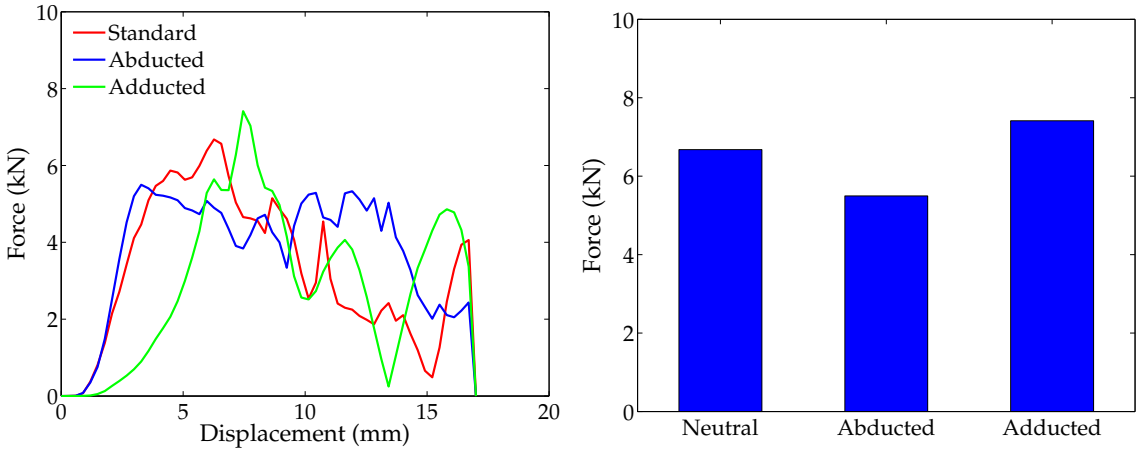


Figure 7.27: Frontal and side view predicted fracture pattern in anterior posterior compression adducted scenario. Failed elements are shown in red, elements yielded in tension are shown in light yellow and elements yielded in compression are shown in light blue.

Reaction forces at the applied boundary conditions plotted against displacement and peak predicted forces for the neutral, abducted and adducted configurations are shown in Figure 7.28. The predicted peak forces are 17 % lower and 11 % higher in the abducted and adducted configurations with respect to the neutral configuration, suggesting a higher injury threshold of the pelvis in an adducted position. However, the predicted forces at fracture initiation were 6 % and 4 % lower for abduction and adduction compared to the neutral configuration and are in agreement with previous observations that abduction or adduction decreases the fracture tolerance of the pelvis (Rupp et al., 2003).



(a) (b)

Figure 7.28: Force-displacement plots (a) and peak forces (b) for neutral, abducted and adducted configurations. In (a), circles indicate moment of fracture initiation.

7.5 Concluding remarks

The damage elasto-plasticity failure model presented in this Chapter in combination with the structural model of the pelvic ring presented in Chapter 4 were used to predict fracture patterns and loads for three dynamic injury scenarios that lead to pelvic fractures commonly seen in high energy automotive crashes or falls from a high altitude. The fracture patterns predicted by the model in the three cases studied showed broad trends that were previously reported in literature in terms of fracture outcome. Predicted peak loads were similar to literature findings for lateral compression and anterior posterior compression. In addition, the ability of the model to predict both fracture initiation and progression can provide further information on the mechanism of injury.

A number of limitations of the fracture model have to be acknowledged. The lack of other body segments could play an important role in the predicted fracture loads as the enforced boundary conditions might not be sufficiently reasonable for the investigated cases. For high strain rate cases, the effect of the added mass of other body segments could have a significant effect on the dynamics of the pelvic ring. In addition, driving the displacement through the femoral head added further constraints which could have had an impact on predicting fracture progression.

Inclusion of the soft tissue surrounding the pelvis could also improve its accuracy in predicting the patterns and loads associated with injury. The rupture of ligaments and joints was not modelled, which could explain the predicted fracture at the tail of the sacrum for the vertical shear and anterior posterior compression cases. Expanding the material model to the ligaments and joints could improve the injury predictions at the locations neighbouring their insertion points.

In terms of computational cost, the simulations had runtimes of approximately 24 hours on a standard workstation. It should be noted that the models used in all scenarios were comprised of a complete pelvic ring and both proximal femurs. Simplified

setups using only the pelvic ring and simplified contact conditions at the region of impact would increase the computational efficiency further. A pilot model using only the pelvic ring and a spherical impactor to simulate dynamic lateral compression had a runtime of approximately five hours.

The strain-rate dependent material model enabled the assessment of an injury scenario for different impact velocities or bone ages. In this Chapter, the effect of impact velocity was investigated for two rates of loading bone with an age of 30 years. However, the data presented in §7.1.2 cover bone ages from 20 to 100 years and strain rates from 0.08 s^{-1} to 29 s^{-1}, hence the material model could be used to investigate the effect of a wider range of bone ages and strain rates on fracture outcome.

Finally, the damage elasto-plasticity material model can be used in conjunction with a continuum model, such as the isotropic model presented in Chapter 5. The results of a pilot study of lateral compression using the isotropic continuum model are included in the Appendix.

8

Conclusions

8.1 Summary of achievements

The aims of this doctoral thesis were to develop a set of FE models of the pelvic construct to predict its bone architecture as a consequence of a physiologically relevant mechanical loading environment through the use of different modelling approaches. Furthermore, one of the FE models was used in conjunction with a damage elasto-plasticity material model to predict fracture progression and patterns for a number of injury scenarios commonly associated with complex pelvic injuries.

The first part of this thesis focused on the development of a structural model of the pelvic ring at the mesoscale, where cortical and trabecular bone were modelled using shell elements and truss elements, respectively. The adaptation pipeline used a strain based bone remodelling algorithm, where joint contact forces, muscle forces and inertial forces experienced during common daily physical activities (walking, stair ascent, stair descent, sit-to-stand and stand-to-sit) drove the iterative adaptation of bone structure towards a target strain value. The resulting model presented a bone architecture that compared well qualitatively with previous findings in literature and CT slices in terms of trabecular trajectories and cortical thickness distribution.

In addition, the structural model was compared to a CT imaging data derived continuum model in terms of mechanical response to a simple loading scenario akin to a standing posture. The results showed that the structural model compared well with the CT derived model in the regions where bone structure was more developed. Regions where the structural model was less stiff were found in areas where structural elements were either thin or inexistent. In contrast, the continuum model had a minimum Young's modulus value throughout its volume due to bone marrow having a grayscale value.

In the second part of this thesis, two continuum predictive modelling technique were presented. An orthotropic and an isotropic FE model were developed using continuum elements and where no distinction was made between cortical and trabecular

bone. Both models were adapted in response to the same loading environment applied to the structural model using strain driven adaptation algorithms. The spatial variation of material properties and an equivalent density distribution were assessed qualitatively and showed that both models had similar features comparable to the CT scan derived model. In addition, a quantitative comparison between the predictive models and the CT derived model was performed, highlighting that the orthotropic model had a mechanical response much closer to the CT derived model.

Three additional models were developed using a combination of structural and continuum elements to assess the impact of distinguishing between cortical and trabecular bone in the case of the isotropic and orthotropic models and the role of background stiffness in the case of the structural model.

A set of sensitivity analyses were conducted to investigate the effect of mesh density and material properties on the structural and continuum models and to assess the robustness of the adaptation algorithms used to predict bone architecture. Both adaptation pipelines were found to be robust, with the most important factor being the target strain value, the main adaptation driver. The material properties of the joints and ligaments holding the three pelvic bones together had a small effect on the resulting bone architecture.

The mesh resolution assessment revealed that the continuum mesh was more sensitive to element size than the structural mesh, with a 50% finer mesh resulting in a 45 % and 2.04 % increase in bone volume with respect to the baseline resolution used in this study for the two models. The increase in computational costs for the two models was similar, suggesting that, at the mesoscale, using a structural mesh is a better tradeoff between resolution of architectural fetures and computational efficiency.

The final part of the thesis focused on using a damage elasto-plasticity material model in conjunction with the optimised structural model to predict fracture initiation, progression and load for three high energy injury scenarios commonly associated with complex pelvic injuries: lateral compression, vertical shear and anterior-posterior

compression. The modelling approach was based on elements changing their stiffness upon reaching strain values associated with yield or complete failure. This method enabled the prediction of fracture onset and progression, providing more in depth information on the fracture mechanisms associated with each injury scenario.

8.2 Current limitations

The methods used throughout this thesis and models developed present a number of limitations that are summarised in this Section.

The musculoskeletal approach used to derive the loading environment applied to the FE model had a number of limitations. The loads are derived from a system of rigid bodies, meaning that when they are translated into a deformable FE model, the equilibrium conditions are not satisfied. The full impact of muscle forces on the FE model was not captured as they were not applied over the full attachment area and compressive forces applied by muscles onto bone were note taken into account. The high number of muscle actuators in the musculoskeletal model partially overcame this drawback. In addition, sub-sampling the load cases to reduce the number of steps in the FE model and maintain computational efficiency was done based only on the variation of joint contact forces. The resulting set of time points was used to extract corresponding muscle forces, potentially missing higher muscle forces at time points not present in the final sample.

A limitation of the bone adaptation algorithms used in this thesis is the lack of a time component as part of the bone remodelling process. Thus, the models predicted only the remodelled state and not the transition between phases. In addition, the frequency and duration of activities were not taken into account. Although using a homogeneous set of activities can be justified by the notion that bone remodelling takes place on a longer time scale, including frequency, duration and intensity of activities into a dynamic remodelling process could provide insight into skeletal conditions

such as osteoporosis.

The FE models were developed to include only the pelvic bones, ligaments and joints. A potential limitation is the lack of internal organs and soft tissue within the pelvic ring. Compressive loads caused by the components surrounding pelvic bone could have an impact on localised adaptation. The structural model was built using low order finite elements with an idealised mechanical behaviour. This can become a limitation when dealing with contact modelling or load distribution. The continuum models were developed at a scale which does not enable the modelling of bone void, which can play an important role in the overall mechanical behaviour and resulting architecture of bone. The use of a larger scale mesh can be justified by the high increase in computational cost associated with microscale continuum modelling, limiting the application of this approach.

Limitations concerning the CT scan derived FE model were the lack of calibration when deriving space varying material properties and the resolution of the resulting model. The lack of high resolution imaging data for the complete pelvic ring means that the clinical CT scan derived model may be prone to errors in quantifying bone morphology. As such, the comparisons between the adaptive models and the CT scan derived model were fairly generic and mainly served to show that the predictive models were showing similar rough trends in terms of bone morphology as observed in clinical data. The possibility of distinguishing between cortical and trabecular bone in an accurate manner could provide more in depth information on bone architecture and serve as a more appropriate tool of assessing the biofidelity of the structural and combined continuum models.

Finally, a more comprehensive validation of the predictive models could be done by quantitatively comparing the trajectories in the structural model or the dominant axes in the continuum orthotropic model with high resolution imaging data. Although volumetric regions can be chosen to compare local particularities of trabecular bone, an investigation of the complete pelvic ring would be more beneficial in assessing the

reliability of the developed models.

8.3 Future work and applications

The models developed in this thesis provide insight into the bone architecture and mechanical behaviour of the pelvic ring, a complex set of bones which hasn't been studied as extensively as long bones. A deeper understanding of the capabilities of different modelling approaches used in skeletal biomechanics was required to enable the use of models tailored for specific applications within the field.

Immediate future work can be aimed at quantitatively comparing the local bone morphology predicted by the structural and continuum orthtropic models against analogous high resolution medical imaging data. In addition, the models could be potentially improved by having an envelope of loading conditions derived from multiple subjects of similar anthropometric characteristics rather than a unique set of loading conditions. This could provide further insight in particularities of pelvic bone morphology and whether some of the structures developed are linked with the gait of the subject or are trends that can be observed in all cases. A similar alteration could be done by using multiple medical imaging data to assess the effect of external geometry on the predictions of the models.

The structural approach used to model the pelvic construct presented in Chapter 4 has the potential to be a more appropriate predictor of bone structure, as other studies have suggested the existence of underlying motifs that may represent a blueprint for bone structural form (Reznikov et al., 2016). This 3D structural approach to bone assessment and remodelling would enable quantitative investigations of such structures by comparing trabecular trajectories and inter-trabecular angles in bone regions of interest against micro-CT imaging data.

The predictive models presented in Chapters 4 and 5 could be used as part of re-

habilitation programs to inform what type of physical activity is required to stimulate bone formation in the region of interest with the caveat that the isotropic approach only predicts bone mineral density with no potentially important directional properties of bone. The structural approach could be considered more appropriate due to its lower sensitivity to mesh density.

The efficacy of different rehabilitation programs could be assessed by modifying the loading conditions applied on the adaptive model. The resulting bone structures would provide information on which rehabilitation program is more appropriate for the case that is being studied. Including a time component in the adaptation pipelines could provide useful information on the required intensity.

Similarly, the adaptation pipelines could be tailored to predict evolution of skeletal diseases such as osteoporosis, by modifying the target strain, remodelling rate or activity spectrum. Simulating bone remodelling with a reduced activity spectrum and a target strain or remodelling rate modified to represent osteoporotic bone could provide potentially valuable information on how the bone structure could change due to the disease. This information could then be used as an initial guide to define a prevention or treatment plan.

In addition, the developed structural model could enable additive manufacturing of massive endoprostheses and scaffolds that can be designed to allow bone regeneration in regions of the pelvis affected by trauma or disease while providing suitable mechanical properties to the regions. The structural nature of the model would allow for additive manufacturing of structurally optimised endoprostheses, promoting bone growth in regions where otherwise bone would not regrow.

The fracture model presented in Chapter 7 showed potential to be a useful tool in investigating the effect of boundary and loading conditions, strain rates and bone age for a given injury scenario. Experimental design and testing could be streamlined and the quantity of cadaveric specimens could be minimised by using the fracture model to assess a wide envelope of loading and boundary conditions a-priori. Although the

material model used to simulate fracture was shown to behave appropriately, the role of other body segments in resulting fracture patterns and loads and the complex boundary conditions occuring in the injury scenarios presented in this thesis require further understanding and work. Further work can be done to improve the application of the boundary conditions and to include a material model to predict ligament and joint rupture.

Finally, the structural model enables additive manufacturing of experimental surrogates that can be calibrated in terms of mechanical properties to match the behaviour of bone under severe loading and potentially replace the use of cadaveric specimens. This technique has has been successfully implemented on long bones in this research group as part of a project funded by DSTL.

Furthermore, the ability of the model to predict fracture progression suggests that it can be developed as an essential tool in investigating the effect that bone fracture can have on the integrity of blood vessels and organs surrounding it during high energy injury scenarios such as underbody blast or high speed automotive collisions. The blood vessels and organs of interest could be integrated in the pelvic model. The model's ability to simulate fracture progression could provide information on the displacements and strains occurring on the organs/vessels during impact. In addition, future mechanical characteristation of such tissues could enable the use of a damage model to simulate potential organ/vessel rupture during fracture of the pelvis.

Finally, it is hoped that the models and discussion presented in this thesis provide a platform for a deeper understanding of the morphological and mechanical particularities of the bony pelvis and the different computational approaches that can be used to model bone behaviour.

Appendix

A1 Additional data on structural, continuum and hybrid models

Case	Trabecular (mm^3)	Cortical (mm^3)	Total (mm^3)
Full	132307	162007	294310
Walking	134001	99992	233990
Stair ascent	136504	103034	239540
Stair descent	152171	87540	239710
Sit to stand	93027	40144	133170
Stand to sit	87133	35949	123080

Table A1: Comparison between trabecular, cortical and total bone volumes for each structural model adapted to a different activity

A2 Fracture chapter animations

The animations of each fracture model are available in an online repository (link). Links for each animation are provided below:

Lateral compression - 4 m/s: link

Lateral compression - 8 m/s: link

Vertical shear - unilateral - 4 m/s: link

Vertical shear - unilateral - 8 m/s: link

Vertical shear - bilateral - 8 m/s: link

Anterior posterior compression - bilateral - 4 m/s: link

Anterior posterior compression - bilateral - 8 m/s: link

Anterior posterior compression - unilateral - 4 m/s: link

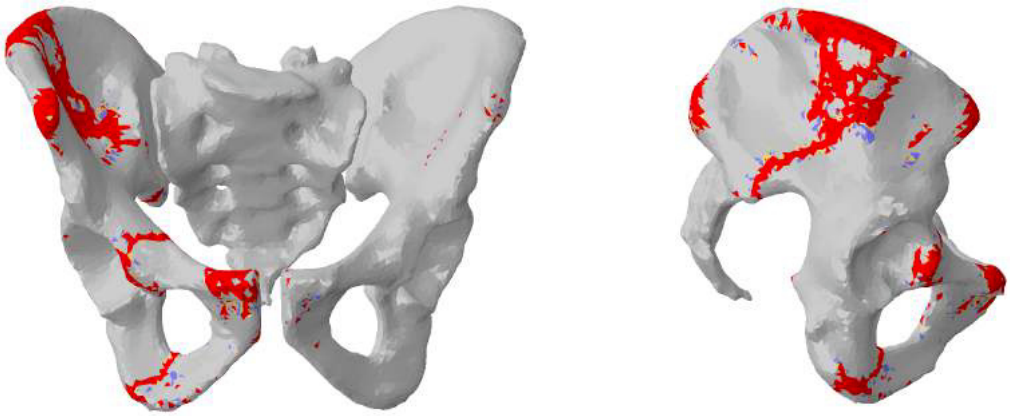
Anterior posterior compression - unilateral - 8 m/s: link

Anterior posterior compression - adduction - 8 m/s: link

Anterior posterior compression - abduction - 8 m/s: link

A3 Continuum fracture model

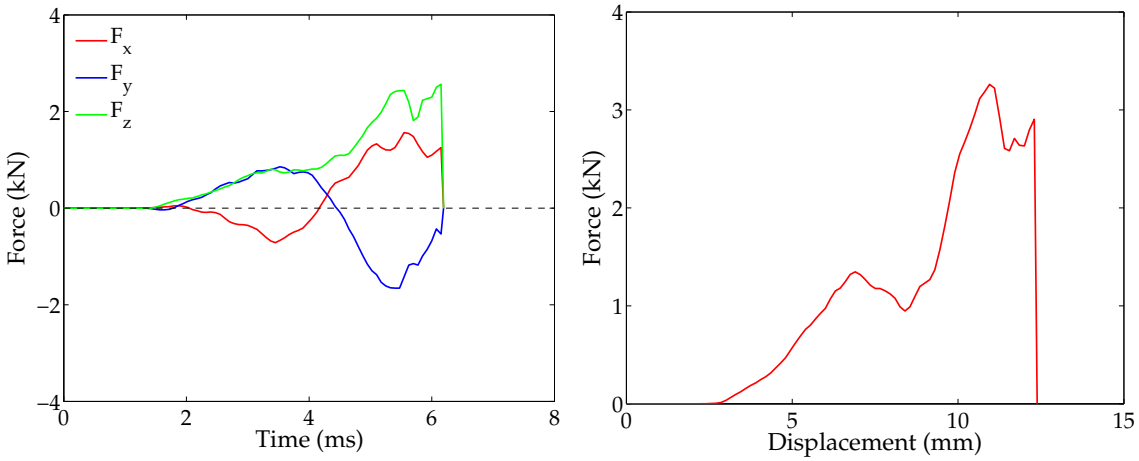
A lateral compression scenario similar to the scenario applied on the structural model, presented in Chapter 7, was applied to a converged isotropic continuum model of the pelvic construct, presented in Chapter 5. The damage elasto-plasticity material model was adjusted slightly to be compatible with the use of continuum elements as opposed to structural elements. The material properties of the elements of the continuum model were discretised in 100 categories to reduce the computational cost. Thus, 100 damage material models were implemented in the FE model using a FORTRAN subroutine. The fracture pattern predicted by the continuum model for a lateral compression scenario at a dispalcement rate of 4 m/s is shown in Figure A1.



(a) (b)

Figure A1: Frontal and side view predicted fracture pattern in lateral compression scenario using an isotropic continuum model. Failed elements are shown in red, elements yielded in tension are shown in light yellow and elements yielded in compression are shown in light blue.

The reaction force components and resultant reaction force plotted against time and displacement, respectively, are shown in Figure A2.



(a) (b)

Figure A2: Force-time (a) and force-displacement (b) plots for lateral compression of isotropic continuum model

References

Aamodt, A., Lund-Larsen, J., Eine, J., Andersen, E., Benum, P., and Husby, O. S. (1997). In vivo measurements show tensile axial strain in the proximal lateral aspect of the human femur. *Journal of Orthopaedic Research*, 15(6):927–931.

Ahlborg, H. G., Johnell, O., Turner, C. H., Rannevik, G., and Karlsson, M. K. (2003). Bone loss and bone size after menopause. *New England Journal of Medicine*, 349(4):327–334.

Almeida, E. S. and Spilker, R. L. (1998). Finite element formulations for hyperelastic transversely isotropic biphasic soft tissues. *Computer Methods in Applied Mechanics and Engineering*, 151(3-4):513–538.

Alton, T. B. and Gee, A. O. (2014). Classifications in brief: young and burgess classification of pelvic ring injuries.

Anderson, A. E., Ellis, B. J., Maas, S. A., Peters, C. L., and Weiss, J. A. (2008). Validation of Finite Element Predictions of Cartilage Contact Pressure in the Human Hip Joint. *Journal of Biomechanical Engineering*, 130(5):51008.

Anderson, A. E., Peters, C. L., Tuttle, B. D., and Weiss, J. a. (2005). Subject-Specific Finite Element Model of the Pelvis: Development, Validation and Sensitivity Studies. *Journal of Biomechanical Engineering*, 127(3):364.

Anderson, F. C. and Pandy, M. G. (2001). Static and dynamic optimization solutions for gait are practically equivalent. *Journal of biomechanics*, 34(2):153–161.

Andreoli, A., Monteleone, M., Van Loan, M., Promenzio, L., Tarantino, U., and De Lorenzo, A. (2001). Effects of different sports on bone density and muscle mass in highly trained athletes. *Medicine & Science in Sports & Exercise*, 33(4):507–511.

Arbelaez, R., Dakin, G., Molziv, F., Alonso, J., Eberhardt, A., and Mann, K. (1998). Pelvic injury in simulated side impact: effects of loading rate on fracture etiology. *ASME Advances In Bioengineering*, pages 171–172.

Balogh, Z., King, K. L., Mackay, P., McDougall, D., Mackenzie, S., Evans, J. A., Lyons, T., and Deane, S. A. (2007). The epidemiology of pelvic ring fractures: a

population-based study. *Journal of Trauma and Acute Care Surgery*, 63(5):1066–1073.

Barre, A. and Armand, S. (2014). Biomechanical ToolKit: Open-source framework to visualize and process biomechanical data. *Computer methods and programs in biomedicine*, 114(1):80–87.

Beason, D. P., Dakin, G. J., Alonso, J. E., Lopez, R. R., and Eberhardt, A. W. (2001). Bone mineral density correlates with fracture loads in pelvic lateral impacts. *ASME-PUBLICATIONS-BED*, 50:883–884.

Beason, D. P., Dakin, G. J., Lopez, R. R., Alonso, J. E., Bandak, F. A., and Eberhardt, A. W. (2003). Bone mineral density correlates with fracture load in experimental side impacts of the pelvis. *Journal of Biomechanics*, 36(2):219–227.

Bennell, K., Malcolm, S., Khan, K., Thomas, S., Reid, S., Brukner, P., Ebeling, P., and Wark, J. (1997). Bone mass and bone turnover in power athletes, endurance athletes, and controls: a 12-month longitudinal study. *Bone*, 20(5):477–484.

Bergmann, G., Deuretzabacher, G., Heller, M., Graichen, F., Rohlmann, A., Strauss, J., and Duda, G. N. (2001). Hip forces and gait patterns from rountine activities. *Journal of Biomechanics*, 34:859–871.

Bertocci, G. E., Pierce, M. C., Deemer, E., Aguel, F., Janosky, J. E., and Vogeley, E. (2004). Influence of fall height and impact surface on biomechanics of feet-first free falls in children. *Injury*, 35(4):417–424.

Bland, J. M. and Altman, D. G. (1999). Measuring agreement in method comparison studies. *Statistical methods in medical research*, 8(2):135–160.

Bloomfield, S. A. (1997). Changes in musculoskeletal structure and function with prolonged bed rest. *Medicine and science in sports and exercise*, 29(2):197–206.

Boyle, C. and Kim, I. Y. (2011). Three-dimensional micro-level computational study of wolff's law via trabecular bone remodeling in the human proximal femur using design space topology optimization. *Journal of biomechanics*, 44(5):935–942.

Brun-Cassan, F., Leung, Y., Tarriere, C., Fayon, A., Patel, M. M., Got, C., and Hureau, J. (1982). Determination of knee-femur-pelvis tolerance from the simulation of car frontal impacts. In *Proceedings of the International Research Council on the Biomechanics of Injury conference*, volume 10, pages 101–115. International Research Council on Biomechanics of Injury.

Bruno, C. M., Alessio, B., Alberto, B., and Cristina, C. (2014). The injury pattern in fatal suicidal falls from a height: an examination of 307 cases. *Forensic science international*, 244:57–62.

Burger, H., De Laet, C., Van Daele, P., Weel, A., Witteman, J., Hofman, A., and Pols, H. (1998). Risk factors for increased bone loss in an elderly population the rotterdam study. *American journal of epidemiology*, 147(9):871–879.

Burgess, A. R., Eastridge, B. J., Young, J. W., Ellison, T. S., Ellison Jr, P. S., Poka, A., Bathon, G. H., and Brumback, R. J. (1990). Pelvic ring disruptions: effective classification system and treatment protocols. *The Journal of trauma*, 30(7):848.

Burstein, A. H., Reilly, D. T., and Martens, M. (1976). Aging of bone tissue: mechanical properties. *The Journal of bone and joint surgery. American volume*, 58(1):82–86.

Carter, D. R., Beaupré, G. S., Giori, N. J., and Helms, J. A. (1998). Mechanobiology of skeletal regeneration. *Clinical orthopaedics and related research*, 355:S41–S55.

Carter, D. R. and Hayes, W. C. (1976). Bone compressive strength: the influence of density and strain rate. *Science*, 194(4270):1174–1176.

Carter, D. R., Vasu, R., and Harris, W. H. (1982). Stress distributions in the acetabular region-II. Effects of cement thickness and metal backing of the total hip acetabular component. *Journal of Biomechanics*, 15(3):165–170.

Cavanaugh, J. M., Walilko, T. J., Malhotra, A., Zhu, Y., and King, A. I. (1990). Biomechanical Response and Injury Tolerance of the Pelvis in Twelve Sled Side Impacts. Technical report, SAE Technical Paper.

Cesari, D. and Ramet, M. (1982). Pelvic tolerance and protection criteria in side impact. Technical report, SAE Technical Paper.

Cesari, D., Ramet, M., and Clair, P.-Y. (1980). Evaluation of pelvic fracture tolerance in side impact. Technical report, SAE Technical Paper.

Chong, K., DeCoster, T., Osler, T., and Robinson, B. (1997). Pelvic fractures and mortality. *The Iowa orthopaedic journal*, 17:110.

Ciarelli, M., Goldstein, S., Kuhn, J., Cody, D., and Brown, M. (1991). Evaluation of orthogonal mechanical properties and density of human trabecular bone from the major metaphyseal regions with materials testing and computed tomography. *Journal of Orthopaedic Research*, 9(5):674–682.

Cilingir, A. C., Ucar, V., and Kazan, R. (2007). Three-dimensional anatomic finite element modelling of hemi-arthroplasty of human hip joint. *Trends in Biomaterials and Artificial Organs*, 21(1):63–72.

Clarke, S., Phillips, A., and Bull, A. (2013). Evaluating a suitable level of model complexity for finite element analysis of the intact acetabulum. *Computer methods in biomechanics and biomedical engineering*, 16(7):717–724.

Correnti, V. (1955). *Le basi morfomeccaniche della struttura dell'osso iliaco.*

Cowin, S. and Mehrabadi, M. (1989). Identification of the elastic symmetry of bone and other materials. *Journal of Biomechanics*, 22(6-7):503–515.

Cowin, S. C. and Van Buskirk, W. C. (1986). Thermodynamic restrictions on the elastic constants of bone. *Journal of biomechanics*, 19(1):85–87.

Cryer, H. M., Miller, F. B., Evers, B. M., Rouben, L. R., and Seligson, D. L. (1988). Pelvic fracture classification: correlation with hemorrhage. *The Journal of trauma*, 28(7):973–980.

Culmann, K. (1866). Die graphische statik, mayer and zeller, zurich.

Dakin, G. J., Arbelaez, R. a., Molz, F. J., Alonso, J. E., Mann, K. a., and Eberhardt, a. W. (2001). Elastic and viscoelastic properties of the human pubic symphysis joint: effects of lateral impact joint loading. *Journal of biomechanical engineering*, 123(3):218–226.

Dalal, S. A., Burgess, A. R., Siegel, J. H., Young, J. W., Brumback, R. J., Poka, A., Dunham, C. M., Gens, D., and Bathon, H. (1989). Pelvic fracture in multiple trauma: classification by mechanism is key to pattern of organ injury, resuscitative requirements, and outcome. *The Journal of trauma*, 29(7):981–1000.

Dalstra, M. (1993). *Biomechanical aspects of the pelvic bone and design criteria for acetabular prostheses*. [Sl: sn].

Dalstra, M., Huiskes, R., Odgaard, A., and van Erning, L. (1993). Mechanical and textural properties of pelvic trabecular bone. *Journal of Biomechanics*, 26(4-5):523–535.

Dalstra, M., Huiskes, R., and Section, B. (1995a). Load Transfer Across the Pelvic. *Biomechanics*, 28(6).

Dalstra, M., Huiskes, R., and van Erning, L. (1995b). Development and validation of a three-dimensional finite element model of the pelvic bone. *Journal of biomechanical engineering*, 117(3):272–278.

Dawson, J. M., Khmelniker, B. V., and McAndrew, M. P. (1999). Analysis of the structural behavior of the pelvis during lateral impact using the finite element method. *Accident Analysis & Prevention*, 31(1-2):109–119.

Delp, S., Anderson, F., Arnold, A., Loan, P., Habib, A., John, C., Guendelman, E., and Thelen, D. (2007). OpenSim: Open source to create and analyze dynamic simulations of movement. *IEEE transactions on bio-medical engineering*, 54(11):1940–1950.

Dickinson, A., Roberts, M., Kumar, A., Weaver, A., and Lockey, D. (2012). Falls from height: injury and mortality. *Journal of the Royal Army Medical Corps*, 158(2):123–127.

Donaldson, C. L., Hulley, S. B., Vogel, J. M., Hattner, R. S., Bayers, J. H., and McMillan, D. E. (1970). Effect of prolonged bed rest on bone mineral. *Metabolism*, 19(12):1071–1084.

Donnelly, B. R. and Roberts, D. P. (1987). Comparison of cadaver and hybrid iii dummy response to axial impacts of the femur. Technical report, SAE Technical Paper.

Drinkwater, B. (1993). Exercise in the prevention of osteoporosis. *Osteoporosis International*, 3(1):169–171.

Dumas, R., Chèze, L., and Verriest, J. P. (2007). Adjustments to McConville et al. and Young et al. body segment inertial parameters. *Journal of Biomechanics*, 40(3):543–553.

Ehlers, W. and Markert, B. (2001). A Linear Viscoelastic Biphasic Model for Soft Tissues Based on the Theory of Porous Media. *Journal of Biomechanical Engineering*, 123(5):418.

Eng, J. J. and Winter, D. A. (1995). Kinetic analysis of the lower limbs during walking: what information can be gained from a three-dimensional model? *Journal of biomechanics*, 28(6):753–758.

Evans, F. (1976). Age changes in mechanical properties and histology of human compact bone. *Yearb Phys Anthropol*, 20:1361–1372.

Fernandez, J., Sartori, M., Lloyd, D., Munro, J., and Shim, V. (2014). Bone remodelling in the natural acetabulum is influenced by muscle force-induced bone stress. *International journal for numerical methods in biomedical engineering*, 30(1):28–41.

Frost, H. M. (1987). Bone mass and the mechanostat: a proposal. *The anatomical record*, 219(1):1–9.

Frost, H. M. (2003). Bone's mechanostat: a 2003 update. *The Anatomical Record Part A: Discoveries in Molecular, Cellular, and Evolutionary Biology*, 275(2):1081–1101.

Galilei, G. (1638). Discorsi e dimostrazioni matematiche, intorno à due nuove scienze attenenti alla mecanica & i movimenti locali. *Leida, Italy*.

Geraldes, D. and Phillips, A. (2010). A novel 3d strain-adaptive continuum orthotropic bone remodelling algorithm: prediction of bone architecture in the femur. In *6th World Congress of Biomechanics (WCB 2010). August 1-6, 2010 Singapore*, pages 772–775. Springer.

Geraldes, D. M., Modenese, L., and Phillips, A. T. (2016). Consideration of multiple load cases is critical in modelling orthotropic bone adaptation in the femur. *Biomechanics and modeling in mechanobiology*, 15(5):1029–1042.

Geraldes, D. M. and Phillips, A. (2014). A comparative study of orthotropic and isotropic bone adaptation in the femur. *International journal for numerical methods in biomedical engineering*, 30(9):873–889.

Ghosh, R., Pal, B., Ghosh, D., and Gupta, S. (2013). Finite element analysis of a hemi-pelvis: the effect of inclusion of cartilage layer on acetabular stresses and strain. *Computer methods in biomechanics and biomedical engineering*, 5842(December 2013):37–41.

Gibson, L. (1985). The mechanical behaviour of cancellous bone. *Journal of biomechanics*, 18(5):317–328.

Gibson, L. J. and Ashby, M. F. (1999). *Cellular solids: structure and properties*. Cambridge university press.

Goel, V. K., Valliappan, S., and Svensson, N. L. (1978). Stresses in the normal pelvis. *Computers in Biology and Medicine*, 8(2):91–104.

Goldstein, S. A., Wilson, D. L., Sonstegard, D. A., and Matthews, L. S. (1983). The mechanical properties of human tibial trabecular bone as a function of metaphyseal location. *Journal of biomechanics*, 16(12):965–969.

Guillemot, H., Besnault, B., Robin, S., Got, C., Le Coz, J. Y., Lavaste, F., and Lassau, J.-P. (1997). Pelvic injuries in side impact collisions: a field accident analysis and dynamic tests on isolated pelvic bones. Technical report, SAE Technical Paper.

Guillemot, H., Got, C., Besnault, B., Lavaste, F., Robin, S., Le Coz, J. Y., and Lassau, J.-P. (1998). Pelvic behavior in side collisions: static and dynamic tests on isolated pelvic bones. In *Proceedings of the 16th International Technical Conference of the Enhanced Safety of Vehicles, Windsor, ON, Canada*, pages 1412–1424.

Hammer, N., Steinke, H., Böhme, J., Stadler, J., Josten, C., and Spanel-Borowski, K. (2010). Description of the iliolumbar ligament for computer-assisted reconstruction. *Annals of Anatomy-Anatomischer Anzeiger*, 192(3):162–167.

Hammer, N., Steinke, H., Slowik, V., Josten, C., Stadler, J., Böhme, J., and Spanel-Borowski, K. (2009). The sacrotuberous and the sacrospinous ligament–a virtual reconstruction. *Annals of Anatomy-Anatomischer Anzeiger*, 191(4):417–425.

Hannan, M. T., Felson, D. T., Dawson-Hughes, B., Tucker, K. L., Cupples, L. A., Wilson, P. W., and Kiel, D. P. (2000). Risk factors for longitudinal bone loss in elderly men and women: the framingham osteoporosis study. *Journal of Bone and Mineral Research*, 15(4):710–720.

Hansen, U., Zioupos, P., Simpson, R., Currey, J. D., and Hynd, D. (2008). The effect of strain rate on the mechanical properties of human cortical bone. *Journal of biomechanical engineering*, 130(1):011011.

Heller, M., Bergmann, G., Deuretzbacher, G., Dürselen, L., Pohl, M., Claes, L., Haas, N., and Duda, G. (2001). Musculo-skeletal loading conditions at the hip during walking and stair climbing. *Journal of biomechanics*, 34(7):883–893.

Hill, P. and Orth, M. (1998). Bone remodelling. *Journal of Orthodontics*, 25(2):101–107.

Horsman, M. D. K., Koopman, H., der Helm, F. C. T., Prosé, L. P., and Veeger, H. E. J. (2007). Morphological muscle and joint parameters for musculoskeletal modelling of the lower extremity. *Clinical biomechanics*, 22(2):239–247.

Huiskes, R. (1987). Finite element analysis of acetabular reconstruction. Noncemented threaded cups. *Acta orthopaedica Scandinavica*, 58(6):620–5.

Jacob, H., Huggler, A., Dietschi, C., and Schreiber, A. (1976). Mechanical function of subchondral bone as experimentally determined on the acetabulum of the human pelvis. *Journal of biomechanics*, 9(10):625IN1627–626IN2.

Joseph, L., Kan, S. H., Wahner, H. W., Riggs, B. L., et al. (1988). Lifetime fracture risk: an approach to hip fracture risk assessment based on bone mineral density and age. *Journal of clinical epidemiology*, 41(10):985–994.

Kado, D. M., Browner, W. S., Blackwell, T., Gore, R., and Cummings, S. R. (2000). Rate of bone loss is associated with mortality in older women: a prospective study. *Journal of Bone and Mineral Research*, 15(10):1974–1980.

Kannus, P., Haapasalo, H., Sankelo, M., Sievanen, H., Pasanen, M., Heinonen, A., Oja, P., and Vuori, I. (1995). Effect of starting age of physical activity on bone mass in the dominant arm of tennis and squash players. *Annals of internal medicine*, 123(1):27–31.

Keaveny, T. M., Morgan, E. F., Yeh, O. C., et al. (2004). Bone mechanics. *Standard handbook of biomedical engineering and design*, pages 1–24.

Keaveny, T. M., Wachtel, E. F., Ford, C. M., and Hayes, W. C. (1994). Differences between the tensile and compressive strengths of bovine tibial trabecular bone depend on modulus. *Journal of biomechanics*, 27(9):1137–1146.

Keller, T. S. (1994). Predicting the compressive mechanical behavior of bone. *Journal of biomechanics*, 27(9):1159–1168.

Knets, I. (1977). Mechanics of biological tissues. a review. *Polymer Mechanics*, 13(3):434–441.

Koch, J. C. (1917). The laws of bone architecture. *Developmental Dynamics*, 21(2):177–298.

Kular, J., Tickner, J., Chim, S. M., and Xu, J. (2012). An overview of the regulation of bone remodelling at the cellular level. *Clinical biochemistry*, 45(12):863–873.

Landjerit, B., Jacquard-Simon, N., Thourot, M., and Massin, P. (1992). Physiological loadings on human pelvis: a comparison between numerical and experimental simulations. *Proc. ESB*, 8:195.

Lang, T., LeBlanc, A., Evans, H., Lu, Y., Genant, H., and Yu, A. (2004). Cortical and trabecular bone mineral loss from the spine and hip in long-duration spaceflight. *Journal of bone and mineral research*, 19(6):1006–1012.

LeBlanc, A., Schneider, V., Shackelford, L., West, S., Oganov, V., Bakulin, A., and Voronin, L. (2000). Bone mineral and lean tissue loss after long duration space flight. *J Musculoskelet Neuronal Interact*, 1(2):157–60.

Les, C., Keyak, J., Stover, S., Taylor, K., and Kaneps, A. (1994). Estimation of material properties in the equine metacarpus with use of quantitative computed tomography. *Journal of Orthopaedic Research*, 12(6):822–833.

Leung, A. S. O., Gordon, L. M., Skrinskas, T., Szwedowski, T., and Whyne, C. M. (2009). Effects of bone density alterations on strain patterns in the pelvis: application of a finite element model. *Proceedings of the Institution of Mechanical Engineers. Part H, Journal of engineering in medicine*, 223(8):965–979.

Li, Z., Alonso, J. E., Kim, J.-E., Davidson, J. S., Etheridge, B. S., and Eberhardt, A. W. (2006). Three-Dimensional Finite Element Models of the Human Pubic Symphysis with Viscohyperelastic Soft Tissues. *Annals of Biomedical Engineering*, 34(9):1452–1462.

Li, Z., Kim, J.-E., Davidson, J. S., Etheridge, B. S., Alonso, J. E., and Eberhardt, A. W. (2007). Biomechanical response of the pubic symphysis in lateral pelvic impacts: a finite element study. *Journal of biomechanics*, 40(12):2758–2766.

Lindahl, O. and Lindgren, A. G. (1967). Cortical bone in man 1. variation of the amount and density with age and sex. *Acta Orthopaedica Scandinavica*, 38(1-4):133–140.

Lu, T. W. and O'Connor, J. J. (1999). Bone position estimation from skin marker coordinates using global optimisation with joint constraints. *Journal of Biomechanics*, 32(2):129–134.

Macchiarelli, R., Bondioli, L., Galichon, V., and Tobias, P. V. (1999). Hip bone trabecular architecture shows uniquely distinctive locomotor behaviour in South African australopithecines. *Journal of human evolution*, 36(2):211–232.

Mahato, N. K. (2010). Trabecular architecture in human sacra: Patterns observed in complete sacralisation and accessory articulation with the fifth lumbar vertebrae. *Journal of Morphological Sciences*, 27(1):19–22.

Majumder, S., Roychowdhury, A., and Pal, S. (2004). Dynamic response of the pelvis under side impact loada three-dimensional finite element approach. *International Journal of Crashworthiness*, 9(1):89–103.

Majumder, S., Roychowdhury, A., and Pal, S. (2007). Simulation of hip fracture in sideways fall using a 3D finite element model of pelvis-femur-soft tissue complex with simplified representation of whole body. *Medical Engineering and Physics*, 29(10):1167–1178.

Matsui, Y., Kajzer, J., Wittek, A., Ishikawa, H., Schroeder, G., and Bosch, U. (2003). Injury pattern and tolerance of human pelvis under lateral loading simulating car-pedestrian impact. Technical report, SAE Technical Paper.

McCalden, R. W., McGeough, J. A., Barker, M. B., et al. (1993). Age-related changes in the tensile properties of cortical bone. the relative importance of changes in porosity, mineralization, and microstructure. *JBJS*, 75(8):1193–1205.

Miller, Z., Fuchs, M. B., and Arcan, M. (2002). Trabecular bone adaptation with an orthotropic material model. *Journal of biomechanics*, 35(2):247–256.

Modenese, L. (2013). *Hip contact force prediction using a musculoskeletal model of the lower limb*. PhD thesis, Imperial College London.

Modenese, L., Gopalakrishnan, A., and Phillips, A. (2013). Application of a falsification strategy to a musculoskeletal model of the lower limb and accuracy of the predicted hip contact force vector. *Journal of Biomechanics*, 46(6):1193–1200.

Modenese, L. and Phillips, A. T. M. (2012). Prediction of hip contact forces and muscle activations during walking at different speeds. *Multibody System Dynamics*, 28(1-2):157–168.

Modenese, L., Phillips, A. T. M., and Bull, A. M. J. (2011). An open source lower limb model: Hip joint validation. *Journal of Biomechanics*, 44(12):2185–2193.

Molz, F. J., George, P. D., Go, L. S., Bidez, M. W., King, A. I., and Alonso, J. (1997). Simulated automotive side impact on the isolated human pelvis: Phase i: Development of a containment device phase ii: Analysis of pubic symphysis motion and overall pelvic compression. Technical report, SAE Technical Paper.

Moore, K. L., Agur, A. M. R., Dalley, A. F., Moore, K. L., and Others (2015). *Essential clinical anatomy*. Wolters Kluwer Health,.

Morlock, M., Schneider, E., Bluhm, A., Vollmer, M., Bergmann, G., Müller, V., and Honl, M. (2001). Duration and frequency of every day activities in total hip patients. *Journal of biomechanics*, 34(7):873–881.

Mossadegh, S., Sharma, D., Parker, P., and Midwinter, M. (2012). Developing a predictive anatomic scoring system for military perineal & pelvic blast injuries. *British Journal of Surgery*, 99:142–143.

Mucha, J. P. and Farnell, M. B. (1984). Analysis of pelvic fracture management. *The Journal of trauma*, 24(5):379–386.

Nägele, E., Kuhn, V., Vogt, H., Link, T. M., Müller, R., Lochmüller, E.-M., and Eckstein, F. (2004). Technical considerations for microstructural analysis of human trabecular bone from specimens excised from various skeletal sites. *Calcified tissue international*, 75(1):15–22.

Nguyen, T., Kelly, P., Sambrook, P., Gilbert, C., Pocock, N., and Eisman, J. (1994). Lifestyle factors and bone density in the elderly: implications for osteoporosis prevention. *Journal of Bone and Mineral Research*, 9(9):1339–1346.

Nguyen, T., Sambrook, P., and Eisman, J. (1998). Bone loss, physical activity, and weight change in elderly women: the dubbo osteoporosis epidemiology study. *Journal of bone and mineral research*, 13(9):1458–1467.

Nusholtz, G. S., Alem, N. M., and Melvin, J. W. (1982). Impact response and injury of the pelvis. Technical report, SAE Technical Paper.

Nusholtz, G. S. and Kaiker, P. S. (1986). Pelvic stress. *Journal of biomechanics*, 19(12):1003–1014.

Oonishi, H., Isha, H., and Hasegawa, T. (1983). Mechanical analysis of the human pelvis and its application to the artificial hip joint–by means of the three dimensional finite element method. *Journal of biomechanics*, 16(6):427–44.

Oonishi, H., Tatsumi, M., and Kawaguchi, A. (1986). Biomechanical studies on fixations of an artificial hip joint acetabular socket by means of 2d-fem. *Biological and biomechanical performance of biomaterials.(P Christel, A Meunier, and AJC Lee, eds.) Amsterdam: Elsevier Science Publishers BV*, pages 513–518.

Pedersen, D. R., Crowninshield, R. D., Brand, R. a., and Johnston, R. C. (1982). An axisymmetric model of acetabular components in total hip arthroplasty. *Journal of biomechanics*, 15(4):305–15.

Pedersen, P. (1989). On optimal orientation of orthotropic materials. *Structural and Multidisciplinary Optimization*, 1(2):101–106.

Peretz, A. M., Hipp, J. A., and Heggeness, M. H. (1998). The internal bony architecture of the sacrum. *Spine*, 23(9):971–974.

Phillips, A., Pankaj, P., Howie, C., Usmani, A., and Simpson, A. (2007). Finite element modelling of the pelvis: Inclusion of muscular and ligamentous boundary conditions. *Medical Engineering & Physics*, 29(7):739–748.

Phillips, A. T. M. (2012). Structural optimisation: biomechanics of the femur. *Proceedings of the ICE - Engineering and Computational Mechanics*, 165:147–154.

Phillips, A. T. M., Pankaj, P., Howie, C. R., Usmani, A. S., and Simpson, A. H. R. W. (2006). 3D non-linear analysis of the acetabular construct following impaction grafting. *Computer methods in biomechanics and biomedical engineering*, 9(3):125–33.

Phillips, A. T. M., Pankaj, P., Usmani, A. S., and Howie, C. R. (2004). Numerical modelling of the acetabular construct following impaction grafting. *Proceedings of Computer Methods in Biomechanics and Biomedical Engineering, Madrid. FIRST Numerics, ISBN 0-9549670-0-3*.

Phillips, A. T. M., Villette, C. C., and Modenese, L. (2015). Femoral bone mesoscale structural architecture prediction using musculoskeletal and finite element modelling. *International Biomechanics*, 2(1):43–61.

Pidaparti, R. and Turner, C. (1997). Cancellous bone architecture: advantages of nonorthogonal trabecular alignment under multidirectional joint loading. *Journal of biomechanics*, 30(9):979–983.

Plummer, J. W., Bidez, M. W., and Alonso, J. (1996). Parametric finite element studies of the human pelvis: the influence of load magnitude and duration on pelvic tolerance during side impact. Technical report, SAE Technical Paper.

Plummer, J. W., Eberhardt, A. W., Alonso, J., and Mann, K. A. (1998). Parametric tests of the human pelvis: the influence of load rate and boundary condition on peak stress location during simulated side impact. *ASME-PUBLICATIONS-BED*, 39:165–166.

Pohlemann, T., Gänsslen, A., Schellwald, O., Culemann, U., and Tscherne, H. (1996). Outcome after pelvic ring injuries. *Injury*, 27:31–38.

Pollock, M. L., Mengelkoch, L. J., Graves, J. E., Lowenthal, D. T., Limacher, M. C., Foster, C., and Wilmore, J. H. (1997). Twenty-year follow-up of aerobic power and body composition of older track athletes. *Journal of Applied Physiology*, 82(5):1508–1516.

Poole, G., Ward, E., Griswold, J., Muakkassa, F., and Hsu, H. (1992). Complications of pelvic fractures from blunt trauma. *The American surgeon*, 58(4):225–231.

Powell, W. R., Ojala, S. J., Advani, S. H., and Martin, R. B. (1975). Cadaver femur responses to longitudinal impacts. Technical report, SAE Technical Paper.

Prevrhal, S., Engelke, K., and Kalender, W. a. (1999). Accuracy limits for the determination of cortical width and density: the influence of object size and CT imaging parameters. *Physics in medicine and biology*, 44(3):751–764.

Prot, M., Cloete, T., Saletti, D., and Laporte, S. (2016). The behavior of cancellous bone from quasi-static to dynamic strain rates with emphasis on the intermediate regime. *Journal of biomechanics*, 49(7):1050–1057.

Rapperport, D., Carter, D., and Schurman, D. (1985). Contact finite element stress analysis of the hip joint. *Journal of orthopaedic research*, 3(4):435–446.

Reilly, D. T. and Burstein, A. H. (1975). The elastic and ultimate properties of compact bone tissue. *Journal of biomechanics*, 8(6):393–405.

Renaudin, F., Guillemot, H., Lavaste, F., and Skalli, N. (1993a). Mechanical behaviour of pelvic bone in axial loading. In *PROCEEDINGS OF 26TH INTERNATIONAL SYMPOSIUM ON AUTOMOTIVE TECHNOLOGY AND AUTOMATION (ISATA). DEDICATED CONFERENCE ON ROAD AND VEHICLE SAFETY.*

Renaudin, F., Guillemot, H., Lavaste, F., Skalli, W., Lesage, F., and Pecheux, C. (1993b). A 3d finite element model of pelvis in side impact. Technical report, SAE Technical Paper.

Reznikov, N., Chase, H., Brumfeld, V., Shahar, R., and Weiner, S. (2015). The 3d structure of the collagen fibril network in human trabecular bone: relation to trabecular organization. *Bone*, 71:189–195.

Reznikov, N., Chase, H., Zvi, Y. B., Tarle, V., Singer, M., Brumfeld, V., Shahar, R., and Weiner, S. (2016). Inter-trabecular angle: a parameter of trabecular bone architecture in the human proximal femur that reveals underlying topological motifs. *Acta biomaterialia*, 44:65–72.

Reznikov, N., Shahar, R., and Weiner, S. (2014). Bone hierarchical structure in three dimensions. *Acta biomaterialia*, 10(9):3815–3826.

Rho, J.-Y., Kuhn-Spearing, L., and Zioupos, P. (1998). Mechanical properties and the hierarchical structure of bone. *Medical engineering & physics*, 20(2):92–102.

Riggs, B. L., O'fallon, W. M., Muhs, J., O'connor, M. K., Kumar, R., and Melton, L. J. (1998). Long-term effects of calcium supplementation on serum parathyroid hormone level, bone turnover, and bone loss in elderly women. *Journal of Bone and Mineral Research*, 13(2):168–174.

Robling, A. G., Castillo, A. B., and Turner, C. H. (2006). Biomechanical and molecular regulation of bone remodeling. *Annu. Rev. Biomed. Eng.*, 8:455–498.

Roesler, H. (1987). The history of some fundamental concepts in bone biomechanics. *Journal of biomechanics*, 20(11-12):1025–1034.

Rucci, N. (2008). Molecular biology of bone remodelling. *Clinical cases in mineral and bone metabolism*, 5(1):49.

Rupp, J. D., Reed, M. P., Jeffreys, T. A., and Schneider, L. W. (2003). Effects of hip posture on the frontal impact tolerance of the human hip joint. *Stapp car crash journal*, 47:21.

Rupp, J. D., Reed, M. P., Van Ee, C. A., Kuppa, S., Wang, S. C., Goulet, J. A., and Schneider, L. W. (2002). The tolerance of the human hip to dynamic knee loading. Technical report, SAE Technical Paper.

Rybicki, E., Simonen, F., and Weis, E. (1972). On the mathematical analysis of stress in the human femur. *Journal of biomechanics*, 5(2):203–215.

Salzar, R. S., Dale Bass, C. R., Kent, R., Millington, S., Davis, M., Lucas, S., Rudd, R., Folk, B., Donnellan, L., Murakami, D., et al. (2006). Development of injury criteria for pelvic fracture in frontal crashes. *Traffic injury prevention*, 7(3):299–305.

Salzar, R. S., Genovese, D., Bass, C. R., Bolton, J. R., Guillemot, H., Damon, A. M., and Crandall, J. R. (2009). Load path distribution within the pelvic structure under lateral loading. *International journal of crashworthiness*, 14(1):99–110.

Sathy, A. K., Starr, A. J., Smith, W. R., Elliott, A., Agudelo, J., Reinert, C. M., and Minei, J. P. (2009). The effect of pelvic fracture on mortality after trauma: an analysis of 63,000 trauma patients. *JBJS*, 91(12):2803–2810.

Schuller, H., Dalstra, M., Huiskes, R., and Marti, R. (1993). Total hip reconstruction in acetabular dysplasia. A finite element study. *The Journal of Bone and Joint Surgery Br*, 75B(3):468–474.

Shefelbine, S. J., Augat, P., Claes, L., and Simon, U. (2005). Trabecular bone fracture healing simulation with finite element analysis and fuzzy logic. *Journal of biomechanics*, 38(12):2440–2450.

Skedros, J. G. and Baucom, S. L. (2007). Mathematical analysis of trabecular trajectories in apparent trajectorial structures: the unfortunate historical emphasis on the human proximal femur. *Journal of theoretical biology*, 244(1):15–45.

Steele, K. M., DeMers, M. S., Schwartz, M. H., and Delp, S. L. (2012). Compressive tibiofemoral force during crouch gait. *Gait and Posture*, 35(4):556–560.

Suh, J. K. and Bai, S. (1998). Finite element formulation of biphasic poroviscoelastic model for articular cartilage. *Journal of biomechanical engineering*, 120(2):195–201.

Sverdlova, N. S. and Witzel, U. (2010). Principles of determination and verification of muscle forces in the human musculoskeletal system: muscle forces to minimise bending stress. *Journal of biomechanics*, 43(3):387–396.

Taddei, F., Schileo, E., Helgason, B., Cristofolini, L., and Viceconti, M. (2007). The material mapping strategy influences the accuracy of ct-based finite element models of bones: an evaluation against experimental measurements. *Medical engineering & physics*, 29(9):973–979.

Taylor, M., Tanner, K., Freeman, M., and Yettram, A. (1996). Stress and strain distribution within the intact femur: compression or bending? *Medical engineering & physics*, 18(2):122–131.

Thompson, M. S., Northmore-Ball, M. D., and Tanner, K. E. (2002). Effects of acetabular resurfacing component material and fixation on the strain distribution in the pelvis. *Proceedings of the Institution of Mechanical Engineers. Part H, Journal of engineering in medicine*, 216(4):237–245.

Tile, M. and Pennal, G. F. (1980). Pelvic disruption: principles of management. *Clinical orthopaedics and related research*, (151):56–64.

Turner, C. H., Rho, J., Takano, Y., Tsui, T. Y., and Pharr, G. M. (1999). The elastic properties of trabecular and cortical bone tissues are similar: Results from two microscopic measurement techniques. *Journal of Biomechanics*, 32(4):437–441.

Turner, M. (1956). Stiffness and deflection analysis of complex structures. *journal of the Aeronautical Sciences*, 23(9):805–823.

van Arkel, R. J., Modenese, L., Phillips, A. T., and Jeffers, J. R. (2013). Hip abduction can prevent posterior edge loading of hip replacements. *Journal of Orthopaedic Research*, 31(8):1172–1179.

van Lenthe, G. H., Stauber, M., and Müller, R. (2006). Specimen-specific beam models for fast and accurate prediction of human trabecular bone mechanical properties. *Bone*, 39(6):1182–1189.

Van Vugt, A. and Van Kampen, A. (2006). An unstable pelvic ring: the killing fracture. *Bone & Joint Journal*, 88(4):427–433.

Vasu, R., Carter, D. R., and Harris, W. H. (1982). Stress distributions in the acetabular region-I. Before and after total joint replacement. *Journal of Biomechanics*, 15(3):155–157.

Viano, D. (1989). Biomechanical responses and injuries in blunt lateral impact. In *STAPP Car Crash Conference, 33rd, 1989, Washington, DC, USA*, number P-227.

Viano, D. C. (1977). Considerations for a femur injury criterion. *SAE Transactions*, pages 3192–3204.

Viano, D. C., Culver, C. C., Haut, R. C., Melvin, J. W., Bender, M., Culver, R. H., and Levine, R. S. (1978). Bolster impacts to the knee and tibia of human cadavers and an anthropomorphic dummy. *SAE Transactions*, pages 3253–3263.

Viano, D. C., Lau, I. V., Asbury, C., King, A. I., and Begeman, P. (1989). Biomechanics of the human chest, abdomen, and pelvis in lateral impact. *Accident Analysis & Prevention*, 21(6):553–574.

Villette, C. (2016). *Structural Meso and Microscale Finite Element Based Approaches for the Prediction of Bone Architecture and Fracture*. PhD thesis, Imperial College London.

Villette, C. C. and Phillips, A. T. M. (2018). Rate and age-dependent damage elasticity forumlation for efficient hip fracture simulations. *Medical Engineering and Physics*.

Vrahas, M., Hern, T. C., Diangelo, D., Kellam, J., and Tile, M. (1995). Ligamentous contributions to pelvic stability. *Orthopedics*, 18(3):271–274.

Winter, D. A. (2009). *Biomechanics and motor control of human movement*. John Wiley & Sons.

Winter, D. A., Sidwall, H. G., and Hobson, D. A. (1974). Measurement and reduction of noise in kinematics of locomotion. *Journal of biomechanics*, 7(2):157–159.

Wu, G., Siegler, S., Allard, P., Kirtley, C., Leardini, A., Rosenbaum, D., Whittle, M., D'Lima, D. D., Cristofolini, L., Witte, H., Schmid, O., and Stokes, I. (2002). ISB recommendation on definitions of joint coordinate system of various joints for the reporting of human joint motionpart I: ankle, hip, and spine. *Journal of Biomechanics*, 35(4):543–548.

Young, J., Burgess, A., Brumback, R., and Poka, A. (1986). Pelvic fractures: value of plain radiography in early assessment and management. *Radiology*, 160(2):445–451.

Zant, N. P., Heaton-Adegbile, P., Hussell, J. G., and Tong, J. (2008). In vitro fatigue failure of cemented acetabular replacements: a hip simulator study. *Journal of biomechanical engineering*, 130(2):021019.

Zhang, Q. H., Wang, J. Y., Lupton, C., Heaton-Adegbile, P., Guo, Z. X., Liu, Q., and Tong, J. (2010). A subject-specific pelvic bone model and its application to cemented acetabular replacements. *Journal of Biomechanics*, 43(14):2722–2727.

Zheng, N., Watson, L. G., and Yong-Hing, K. (1997). Biomechanical modelling of the human sacroiliac joint. *Medical & Biological Engineering & Computing*, 35(2):77–82.

Zhu, J., Cavanaugh, J., and King, A. (1993). Pelvic biomechanical response and padding benefits in side impact based on a cadaveric test series. Technical report, SAE Technical Paper.

Zienkiewicz, O. C. and Cheung, Y. K. (1967). *The finite element method in structural and continuum mechanics: numerical solution of problems in structural and continuum mechanics*, volume 1. McGraw-Hill.

Zienkiewicz, O. C., Taylor, R. L., and Taylor, R. L. (2000). *The finite element method: solid mechanics*, volume 2. Butterworth-heinemann.

Zienkiewicz, O. C., Taylor, R. L., Zienkiewicz, O. C., and Taylor, R. L. (1977). *The finite element method*, volume 3. McGraw-hill London.

Zioupos, P. and Currey, J. (1998). Changes in the stiffness, strength, and toughness of human cortical bone with age. *Bone*, 22(1):57–66.